University of Southampton

Faculty of Social Sciences
School of Mathematical Sciences

Frequency-Domain Approach to Self-Force in Hyperbolic Scattering

by

Christopher Luke Whittall
ORCiD: 0000-0003-2152-6004

A thesis for the degree of
Doctor of Philosophy

October 2024

University of Southampton

Abstract

Faculty of Social Sciences
School of Mathematical Sciences

Doctor of Philosophy

Frequency-Domain Approach to Self-Force in Hyperbolic Scattering

by Christopher Luke Whittall

Gravitational self-force is a well-established method for modelling the dynamics of binary systems in general relativity when one object is significantly less massive than the other. Existing study has focused primarily on the dynamics of bound systems, driven by a desire to model astrophysically relevant extreme mass ratio inspirals. In recent years, however, it has come to be understood that self-force can play a vital role in an ongoing cross-disciplinary effort to study black hole scattering, enabling explorations of the interface between different modelling approaches and advancing the post-Minkowskian and effective-one-body approaches to general relativistic 2-body motion.

In this thesis we investigate a method for calculating the self-force along hyperbolic orbits. Whilst some progress has previously been made towards this aim by working in the time-domain, our purpose will be the development of a frequency-domain approach. Frequency domain self-force methods are common for bound systems, where they provide superior performance compared to time-domain codes, but there are several challenges when moving to unbound systems. To investigate and overcome these, we will use a scalar-field toy model, which captures all of the essential challenges but is simpler to implement, and restrict ourselves to the case of a non-rotating, Schwarzschild black hole. Problems will be encountered with the standard method of extended homogeneous solutions, which cannot be fully applied to the unbound problem, and which suffers growing errors at early and late times. We will also face and overcome difficulties numerically evaluating oscillatory integrals which stretch to radial infinity. We develop solutions to each of these issues in turn, and present example results from our numerical implementation. We then illustrate how strong-field self-force scatter results can be used to resum weak-field post-Minkowskian results, extending the latter's domain of validity. We find that our frequency-domain approach is critical for high-precision strong-field calculations at high velocities. Initial work on an analytical calculation to obtain the self-force at early and late times is also presented. To conclude, we discuss the future development of the techniques developed herein, and the outlook for the self-force scatter programme at large.

Contents

List of Figures **ix**

List of Tables **xi**

Declaration of Authorship **xiii**

Acknowledgements **xv**

Definitions and Abbreviations **xix**

1 Introduction **1**
1.1 The gravitational wave era . . . 1
1.2 Gravitational wave source modeling . . . 6
1.2.1 Compact binary targets for LISA . . . 7
1.2.2 Modelling approaches . . . 9
1.3 Gravitational self-force . . . 12
1.4 Black hole scattering . . . 17
1.5 Outline . . . 20
1.5.1 Structure . . . 21
1.5.2 Summary of own contribution . . . 23
1.5.3 Conventions . . . 23

2 Mathematical preliminaries **25**
2.1 Scatter geodesics in the Schwarzschild spacetime . . . 25
2.2 Scalar-field model . . . 30
2.2.1 Scalar-field self force . . . 30
2.2.2 Mode-sum regularisation . . . 31
2.2.3 Conservative and dissipative forces . . . 34
2.3 First-order self-force correction to the scatter angle . . . 36
2.3.1 PM expansion of $\delta\varphi^{(1)}$ . . . 38
2.4 Frequency-domain solution for the scalar field with a scattering source . . . 40
2.4.1 Mode decomposition . . . 40
2.4.2 Homogeneous solutions . . . 42
2.4.3 The inhomogeneous solution . . . 44
2.4.4 Method of extended homogeneous solutions . . . 47

3 Frequency modes of the extended homogeneous solutions **49**
3.1 Normalisation integrals . . . 49

3.1.1 Truncating the normalisation integral . . . 49
3.1.2 Tail correction scheme . . . 50
3.1.3 Integration by parts . . . 53
3.2 Numerical method . . . 56
3.2.1 Homogeneous solutions . . . 56
3.2.2 Normalisation integrals . . . 57
3.3 Numerical results for $C^{-}_{\ell m\omega}$ . . . 59
3.3.1 Effect of IBP and tail corrections . . . 60
3.3.2 Performance . . . 62
3.3.3 General features . . . 63
3.3.4 Quasinormal modes . . . 64
3.3.5 Zeros in the spectrum . . . 66

4 Time-domain reconstruction and the scalar-field self-force 67
4.1 Efficient time-domain reconstruction . . . 67
4.2 Overall approach . . . 68
4.3 Scalar-field self-force: initial results . . . 70
4.3.1 Large-ℓ behaviour and code validation . . . 70
4.3.2 Self-force along the orbit . . . 72
4.4 Adaptive truncation of ℓ-mode summation . . . 74
4.5 Example scatter angle calculation . . . 76
4.6 Cancellation problem . . . 79

5 Scattering near the transition to plunge and the resummation of post-Minkowskian series 83
5.1 Scatter geodesics: transition to plunge . . . 83
5.2 Scatter angle in the limit of transition to plunge . . . 86
5.2.1 Convergence of integrals . . . 88
5.3 Resumming post-Minkowskian expansions using strong-field self-force results . . . 89
5.4 Self-force calculations along near-critical geodesics . . . 91
5.4.1 High-velocity limit . . . 92
5.4.2 Numerical method . . . 93
5.4.2.1 Time-domain self-force calculation . . . 94
5.4.2.2 Frequency-domain self-force calculation . . . 94
5.4.2.3 Hybrid scatter angle calculation . . . 95
5.4.3 Selected self-force results . . . 96
5.5 Calculating $A_1(v)$ by extrapolation . . . 98
5.6 PM resummation: results . . . 100

6 Large radius asymptotics of the self-force: analytical calculation 103
6.1 Scalar-field equation in Eddington-Finkelstein coordinates . . . 105
6.2 Perturbative treatment of the (1+1)D field equation . . . 106
6.2.1 Hierarchichal expansion of the scalar field . . . 106
6.2.2 The Green's function . . . 107
6.3 Evaluating Φ_0^R on Γ near i^+ . . . 109
6.3.1 Derivation of ψ_0 . . . 109
6.3.1.1 External evaluation point . . . 110

6.3.1.2 Internal evaluation point . . . 111
6.3.2 Late time expansions . . . 112
6.3.3 The retarded field Φ_0 . . . 114
6.3.3.1 Contribution from $\psi^{\rm II}_{0>}$ . . . 114
6.3.3.2 Contribution from $\psi^{\rm I}_{0>}$ . . . 117
6.3.3.3 The retarded field Φ_0^ℓ . . . 118
6.3.4 The Detweiler-Whiting regular field Φ_0^R . . . 118
6.3.4.1 Explicit summation over ℓ . . . 119
6.4 Evaluating the self-force F^0_α near i^+ . . . 121
6.4.1 The azimuthal component F^0_φ . . . 122
6.4.2 The components F^0_U and F^0_V: contribution from region II . . . 123
6.4.3 The components F^0_U and F^0_V: contribution from region I . . . 124
6.4.3.1 V derivative . . . 124
6.4.3.2 U derivative . . . 125
6.4.4 The components F^0_t and F^0_r . . . 127
6.4.4.1 Explicit summation over ℓ . . . 128
6.4.5 Numerical validation . . . 129
6.5 Calculation of ψ_1: setup and outlook . . . 130
6.5.1 Strategy . . . 130
6.5.2 Outlook . . . 133

7 Conclusions **135**
7.1 Outlook . . . 136
7.1.1 Large radius asymptotics of the self-force . . . 137
7.1.2 Self-force calculations along the critical orbit . . . 137
7.1.3 Extension to gravity . . . 138
7.1.4 Alternatives to the use of EHS . . . 138
7.1.5 Beyond . . . 139

Appendix A Expansion of geodesic quantities at large radius **141**

Appendix B Post-Minkowskian expansion of the scalar-field scatter angle correction **145**

Appendix C Boundary conditions for homogeneous solutions **147**

Appendix D Constants appearing in the tail correction scheme **149**

Appendix E Near-separatrix behaviour of $\delta\varphi^{(0)}$ **151**

References **153**

List of Figures

1.1 Gravitational wave event GW150914 . . . 2
1.2 Operating principles of a simple laser interferometer . . . 4
1.3 Sensitivity and frequency ranges of different gravitational wave detectors . 6
1.4 Example bound geodesic in the Kerr spacetime . . . 8
1.5 Different approaches for modelling binary systems in general relativity . . 9
1.6 Modelling methods used as inputs to the EOB framework . . . 11
1.7 Regions in the method of matched asymptotic expansions . . . 14

2.1 Example scatter geodesic with parameters $(E, r_{\min}) = (1.1, 4M)$ . . . 29
2.2 1SF scatter angle corrections as a function of impact parameter at fixed velocity $v = 0.2$ . . . 38
2.3 Comparison between numerical SF and analytical PM values for the 1SF scatter angle correction. . . . 39

3.1 Illustration of the truncation problem in the normalisation integrals $C^{-}_{\ell m\omega}$ 50
3.2 Effect of IBP and corrections on suppressing high-frequency noise in the calculation of $C^{-}_{\ell m\omega}$ . . . 60
3.3 Cancellation between surface term and integral in calculation of $C^{(r)-}_{\ell m\omega}$ using IBP . . . 61
3.4 Timings of $C^{-}_{\ell m\omega}$ using different methods of calculation. . . . 62
3.5 Selection of $C^{-}_{\ell m\omega}$ spectra for a variety of mode numbers and geodesic orbits. 63
3.6 Quasinormal mode features in the $C^{-}_{\ell m\omega}$ spectra . . . 64
3.7 QNM features in the $C^{-}_{\ell m\omega}$ spectrum for a near-critical geodesic. . . . 65

4.1 Self-force regularisation plot for the t-component of the force at $r_p = 6M$ along the inbound leg of the geodesic orbit with parameters $E = 1.1$ and $r_{\min} = 4M$ . . . 71
4.2 Self-force along the geodesic orbit with parameters $E = 1.1$ and $r_{\min} = 4M$ ($\ell_{\max} = 15$) . . . 73
4.3 Self-force along the geodesic orbit with parameters $E = 1.1$ and $r_{\min} = 4M$ (dynamic $\ell_{\max}$) . . . 75
4.4 Fourier integrand $\mathcal{J}^{\ell m}_t$ as a function of frequency at different orbital positions . . . 79
4.5 Degree of cancellation in the reconstruction of the t-component of the self-force . . . 81

5.1 Transition to plunge: effective potential description . . . 84
5.2 Scatter geodesics in the limit $\delta b \to 0$ for $v = 0.5$ . . . 85

5.3 Impact of the geodesic order resummation on the 4PM expression for $\delta\varphi^{(0)}$ at $v = 0.5$. 91
5.4 Self-force regularisation plot for the t-component of the force at given points along the inbound leg of certain geodesic orbits with velocity $v = 0.2$ and $v = 0.8$ 93
5.5 Self-force component $F_\varphi^{\rm self}$ for the orbit $b = 6.71257M$, $v = 0.7$, as calculated using FD, TD and Hybrid methods. 96
5.6 Self-force component $F_\varphi^{\rm self}$ for the orbit $b = 20.3825M$, $v = 0.2$ as calculated using FD, TD and Hybrid methods 97
5.7 Total, conservative and dissipative scatter angle corrections in the limit $\delta b \to 0$ for $v = 0.5$. 98
5.8 Values of the singularity coefficients $A_1(v)$, $A_1^{\rm cons}(v)$ and $A_1^{\rm diss}(v)$ 99
5.9 Impact of the self-force inspired resummation on 4PM expressions for $\delta\varphi^{(1)}_{\rm cons}$ and $\delta\varphi^{(1)}_{\rm diss}$ at $v = 0.5$. 101
5.10 Comparing geodesic and 1SF order resummations for the total scatter angle at $v = 0.5$. 102

6.1 Penrose diagram for the $r > 2M$ patch of Schwarzschild spacetime containing a scatter orbit. 104
6.2 Regions of the retarded Green's function 107
6.3 Support of the geodesic source for an external field evaluation point. . . . 111
6.4 Support of the geodesic source for an internal field evaluation point. . . . 112
6.5 Comparison between the numerical and leading-order analytical results for the regularised $\ell = 2$ contribution to the self-force along an example orbit. 129
6.6 Splitting the wordline into early, late and strong-field portions. 131
6.7 Support of the (U', V') integration in Eq. (6.150) for $U'' \in \Gamma_\pm$. 132

List of Tables

5.1 Values of the singularity coefficients $A_1(v)$, $A_1^{\text{cons}}(v)$ and $A_1^{\text{diss}}(v)$. 100

Declaration of Authorship

I declare that this thesis and the work presented in it is my own and has been generated by me as the result of my own original research.

I confirm that:

1. This work was done wholly or mainly while in candidature for a research degree at this University;
2. Where any part of this thesis has previously been submitted for a degree or any other qualification at this University or any other institution, this has been clearly stated;
3. Where I have consulted the published work of others, this is always clearly attributed;
4. Where I have quoted from the work of others, the source is always given. With the exception of such quotations, this thesis is entirely my own work;
5. I have acknowledged all main sources of help;
6. Where the thesis is based on work done by myself jointly with others, I have made clear exactly what was done by others and what I have contributed myself;
7. Parts of this work have been published as:
   Christopher Whittall and Leor Barack. Frequency-domain approach to self-force in hyperbolic scattering. *Phys. Rev. D*, 108(6):064017, 2023

   Oliver Long, Christopher Whittall and Leor Barack. Black hole scattering near the transition to plunge: Self-force and resummation of post-Minkowskian theory. *Phys. Rev. D*, 110(4):044039, 2024

Signed: Date:

Acknowledgements

First and foremost, I would like to thank my supervisor Leor Barack for four years of exceptional guidance. I have been very lucky to benefit from his combination of patience, accessibility and razor sharp physical and mathematical insight. I must also confess particular gratefulness for his piloting expertise.

I would also like to thank my collaborator and former Southampton student, Oliver Long. More broadly, I have appreciated the friendly and supportive environment within the Southampton self-force group. Particular thanks goes to my co-supervisor Adam Pound, and my fellow students, past and present: Jack Lewis, Sam Upton, Andrew Spiers, Mekhi Dhesi and Ayush Roy.

The greatest personal contribution to my life, and therefore also to my work, in recent years belongs to Carmaline de Silva. Things have proceeded rather differently – and with much greater difficulty – than I could have imagined when I first accepted my offer from Southampton in early March 2020, but we have coped together and made plenty of good memories besides the bad. It is a privilege to be able to build my life with you.

I have benefitted greatly from the lifelong support of my family in all my endeavours. Notable educational memories include being taught Pythagorean triples by my sister Elisabeth, and regular childhood trips to the library with my grandmother Veronica. My father, Phil, has provided extensive moral, practical and logistical support for my studies, for which I will be forever grateful. The final dedication of this thesis, however, belongs to the most notable absence from its readership. No one did as much to support and encourage my love of science as you did, and none went to such lengths to share in it.

In loving memory of my mother, Julie

Definitions and Abbreviations

3G	3rd generation (detectors)
BBH	Binary black hole
BNS	Binary neutron star
EHS	Extended homogeneous solution
EMRI	Extreme mass ratio inspiral
EOB	Effective-one-body
FD	Frequency-domain
IBP	Integration by parts
IMRI	Intermediate mass ratio inspiral
ISCO	Innermost stable circular orbit
LVK	LIGO-Virgo-KAGRA
LIGO	Laser interferometer gravitational observatory
LISA	Laser interferometer space antenna
LH	Leading-hierarchical
LLT	Leading-late-time
MBH	Massive black hole
NR	Numerical relativity
PM	Post-Minkowskian
PN	Post-Newtonian
SF	Self-force
SNR	Signal-to-noise ratio
TD	Time-domain

Chapter 1

Introduction

1.1 The gravitational wave era

Shortly before 5AM local time on the 14th September 2015, a small disturbance was noted at the LIGO facility in Livingston, Louisiana. The sophisticated instruments contained within the site's 4km long arms had detected changes in their length of barely 1 part per 10^{21}, around one thousandth of the width of a proton. On the other side of the United States, Livingston's sister facility at Hanford, Washington, detected the same event 7ms later. Subsequent analysis would identify the origin of this disturbance as the merger of two black holes, with masses approximately 36 and 29 times that of the Sun, in a galaxy 1.3 billion light years away [1]. During the final seconds of their lives, as they spiralled towards each other at a significant fraction of the speed of light, the two black holes emitted the equivalent of 3 solar masses of energy in the form of gravitational waves. After driving the binary to its merger by removing energy and angular momentum from the system, the emitted gravitational waves continued to travel essentially unimpeded through space long after the final coalescence, bringing news of the cataclysm to distant observers.

The signal detected by LIGO – displayed in Fig. 1.1 and christened GW150914 – was our first direct detection of gravitational waves. In 1915, a mere 100 years before this 1.3 billion year old message reached Earth, Einstein introduced the definitive version of his theory of General Relativity [2]. The following year, Einstein discovered that when the field equations of general relativity were linearised in the limit of weak gravitational fields, they admitted solutions representing waves that propagate at the speed of light [3, 4]. Despite this, it was initially unclear whether these waves represented real physical phenomena. Weyl classified Einstein's waves into three types [5]. Eddington studied these waves, and concluded that two of the three types were unphysical modes whose propagation velocities actually depend on the coordinate system used [6]. On the other hand, Eddington confirmed that the third type propagate at the speed of light

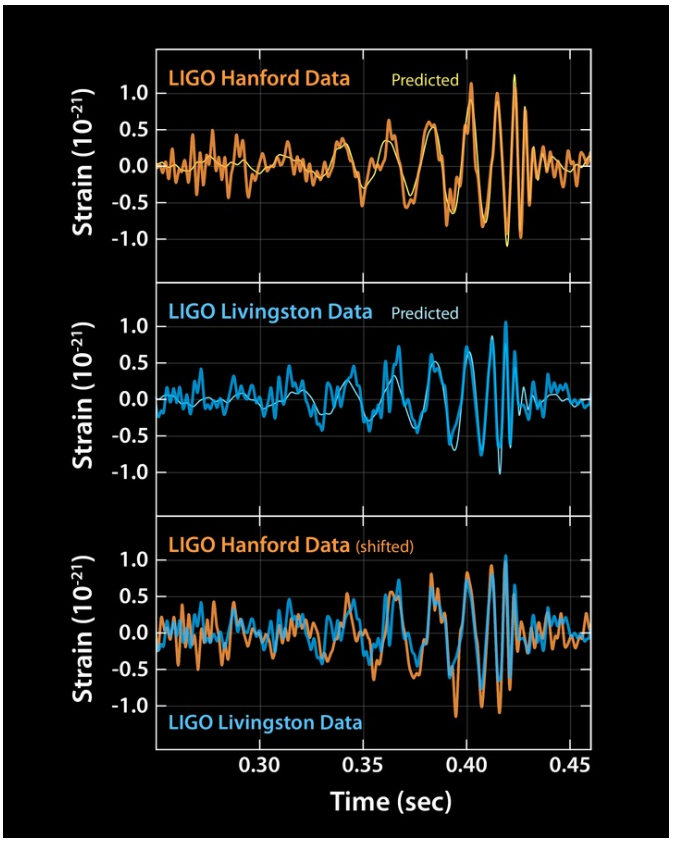

FIGURE 1.1: Gravitational wave signal GW150914. *Top row:* signal observed by LIGO Hanford, compared to theoretical prediction. *Middle row:* signal observed by LIGO Livingston, compared to theoretical prediction. *Bottom row:* side-by-side comparison of the two detector signals, aligned to account for the light-speed travel delay between the two sites. The data from the two detectors agree well with each other and with the predictions of general relativity. Image credit: Caltech/MIT/LIGO.

in all coordinate systems, but still he was not convinced of their existence. Einstein too remained sceptical, and in 1936 argued against the existence of plane gravitational waves alongside his assistant Nathan Rosen, but withdrew the manuscript in protest after receiving critical feedback from an anonymous referee [7]. With hints from Einstein's Princeton colleague Howard Robertson (who happened to be the anonymous referee), a modified version was published in a different journal a year later, establishing the existence of *cylindrical* gravitational waves [8]. The physical understanding of gravitational waves was boosted in 1956 by Felix Pirani, who developed a mathematical framework for interpreting physical effects using the Riemann tensor and tetrad formalism [9]. Pirani's ideas contributed to discussions on the nature of gravitational waves at the 1957 conference on gravitation at Chapel Hill, during which many of the initially sceptical theorists present were convinced of their existence [10].

With growing theoretical acceptance, the search for experimental evidence gained momentum. An important development occurred in 1974, when astronomers Russell Hulse and Joseph Taylor reported the discovery of PSR 1913+16 [11], a pulsar forming a binary system with what is now known to be another neutron star. Observations over the

following years allowed for increasingly accurate measurements of parameters such as the orbital period and its rate of change over time [12, 13]. These values were found to be in excellent agreement with energy being removed from the binary system by gravitational radiation, at precisely the rate predicted by general relativity [14, 15]. For their work leading to the first evidence for the existence of gravitational waves, Hulse and Taylor shared the 1993 Nobel Prize in Physics. But the radio astronomers had only detected *electromagnetic* radiation emitted by the pulsar, from which they extracted information about the binary dynamics and hence *indirectly* inferred the emission of gravitational radiation. It remained to directly detect the gravitational waves themselves.

In fact, Joseph Weber had already claimed such a detection in 1969, 5 years prior to Hulse and Taylor's announcement of PSR 1913+16 [16]. Weber was experimenting with resonant mass detectors, metal cylinders which, it was theorised, would exhibit measurable vibrations in response to passing gravitational waves. In this way, Weber claimed regular detection of gravitational waves, including anisotropic reception from the direction of the galactic centre [17]. Weber was also principal investigator for the Lunar Surface Gravimeter, deployed during the Apollo 17 landing mission in 1972, which he hoped would detect seismic events correlated with his observations in the laboratory [18]. In the event, the experiment failed to function correctly on the Moon and no relevant data could be collected. Weber's detections were likewise never replicated by his earthbound peers, despite significant efforts to do so. Concerns were also raised at the time as to whether the high rates of galactic mass loss implied by Weber's measurements were realistic or consistent with observations of the Milky Way [19, 20]. By the end of the 1970s, Weber's results were almost universally believed to be erroneous, but he receives personal recognition as an early pioneer of direct detection efforts [10].

The lack of confirmed detections did not derail the growing enthusiasm for gravitational wave experiments, and groups continued to pursue both resonant mass detectors and alternative approaches. Among these, the use of laser interferometers to detect gravitational waves had been formally proposed as early as the 1960s, but had not been immediately pursued [21–23]. As illustrated in Fig. 1.2, an interferometer exploits the interference of light beams to measure the relative change in length of two perpendicular arms caused by a passing gravitational wave. This approach was developed with smaller interferometers throughout the 1970s, and multiple proposals for large-scale detectors were developed in the following decades [10]. By the early 2000s, several major interferometers were under construction or in commissioning, including GEO600 (located in Germany) [24], LIGO (2 sites in the USA) [25] and Virgo (Italy) [26]. These instruments did not detect gravitational waves in their original science runs, and the latter two were upgraded to "advanced" configurations at the start of the 2010s.

The detection of GW150914 came just days into the first observing run (O1) of the

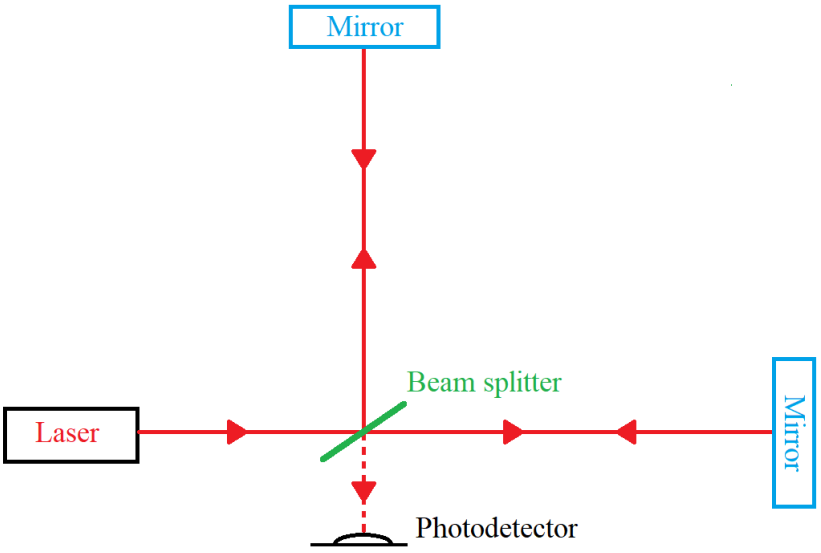

FIGURE 1.2: Operating principles of a simple laser interferometer. A laser produces a beam of monochromatic light, which is diverted into two perpendicular arms by a beam splitter. The light is reflected by mirrors at the end of each arm and returns to the beam splitter, where the two beams recombine and are directed towards a photodetector. When a gravitational wave passes the detector, it changes the length of the two arms by different amounts, altering the phase difference between the two beams where they recombine and hence changing the intensity of light incident on the photodetector.

advanced LIGO detector. [1] In addition to the first direct detection of gravitational waves, this event provided concrete evidence for the existence of black holes and allowed for unprecedented confirmation of the validity of general relativity in the strong-field regime [28]. The O1 run concluded in January 2016, having detected a total of 3 binary black hole (BBH) mergers [29, 30]. For their work on the LIGO detector, the 2017 Nobel Prize in Physics was awarded to Rainer Weiss, Barry Barish and Kip Thorne. The O2 run commenced at the end of November 2016 and continued until the end of August 2017, with the advanced Virgo detector joining for the final month of observations. A total of 7 BBH events (including the first three-detector event, GW170814 [31]) were identified from the O2 data [30]. In addition, on the 17th August 2017, the first gravitational waves were detected from a binary neutron star (BNS) merger [32]. This landmark signal, named GW170817, was followed 1.74s later by a short gamma ray burst (GRB) [33, 34]. Radiation from across the electromagnetic spectrum was subsequently detected by follow-up searches. Multi-messenger events of this nature allow for greater physical information to be obtained: the discovery of an optical counterpart consistent with the gravitational wave sky localisation enabled the host galaxy to be identified; BNS mergers were identified as the progenitors of at least some short GRBs; the difference between the speeds of light and gravity was constrained; and restrictions were placed on the neutron star equation of state [34–36].

[1] GW150914 occurred 3 days into stable data collection, but 4 days *before* the officially scheduled start of O1 [27].

A third pair of observing runs were completed in 2019-20, bringing the total to 90 detected events [37–39]. Highlights from O3 include the first confident detections of neutron star-black hole mergers [40]; the first BBH merger leading to the creation of an intermediate mass black hole [41]; the most asymmetric black hole binary observed thus far [42]; and a second observation of a likely BNS merger [43]. Notably, the Japanese KAGRA observatory conducted its first runs during the O3 period [44]. The network's O4 run began in May 2023, with some early results already announced [45]. Additional periods of upgrades and observations are planned for the LIGO-Virgo-KAGRA (LVK) network in the coming years, including the addition of a new LIGO antenna in India [46, 47]. Adding additional detectors to the network increases the amount of time that multiple detectors are collecting science data, increasing the detected event rates. Networks consisting of multiple detectors with greater geographic spread also allow for more precise sky localisation of gravitational wave events, critical for multi-messenger follow-up.

In the longer term, there is a proposal to install upgraded detectors, called LIGO Voyager, at the current LIGO sites [48]. New 3rd generation (3G) detectors with arm lengths of tens of kilometres, such as Cosmic Explorer (2 sites in the USA) [49] and the Einstein Telescope (Europe) [50], are also envisaged joining the network, perhaps as early as the 2030s.These detectors will be able to detect BBH and BNS mergers at much greater distances and in greater numbers, allowing us to build an accurate history of compact object populations and merger rates throughout cosmic history [51]. Highly precise multi-messenger observations of BNS mergers will provide an unprecedented window in to the properties of matter at extremely high densities. The 3G observatories will, however, largely remain sensitive only to the roughly $10 - 10^4$ Hz frequency range of their 2nd generation forebears. Expanding observations to different frequency bands, and hence different sources, is thus an important goal. Initial success in this direction has been achieved by pulsar timing arrays, radio telescopes that search for correlated delays in the arrival of pulses from a network of pulsars. In 2023, the NANOGrav collaboration (itself a part of the larger International Pulsar Timing Array) announced evidence in their 15 year observational data set for a gravitational wave background at nanohertz frequencies, consistent with that expected from a background of supermassive black hole binaries [52].

Another recent milestone is the formal adoption of the Laser Interferometer Space Antenna (LISA) mission by the European Space Agency in January 2024 [54, 55]. LISA will consist of 3 spacecraft in heliocentric orbit, forming an equilateral triangle interferometer with arms 2.5 million km long, and will be sensitive to gravitational waves with frequencies in the millihertz band (0.1 mHz - 1 Hz). The lower frequency range will make LISA sensitive to BBH systems containing supermassive and intermediate mass black holes, in contrast to the less massive stellar mass black holes typically observed by the LVK network. It may also be possible for LISA to detect some stellar mass

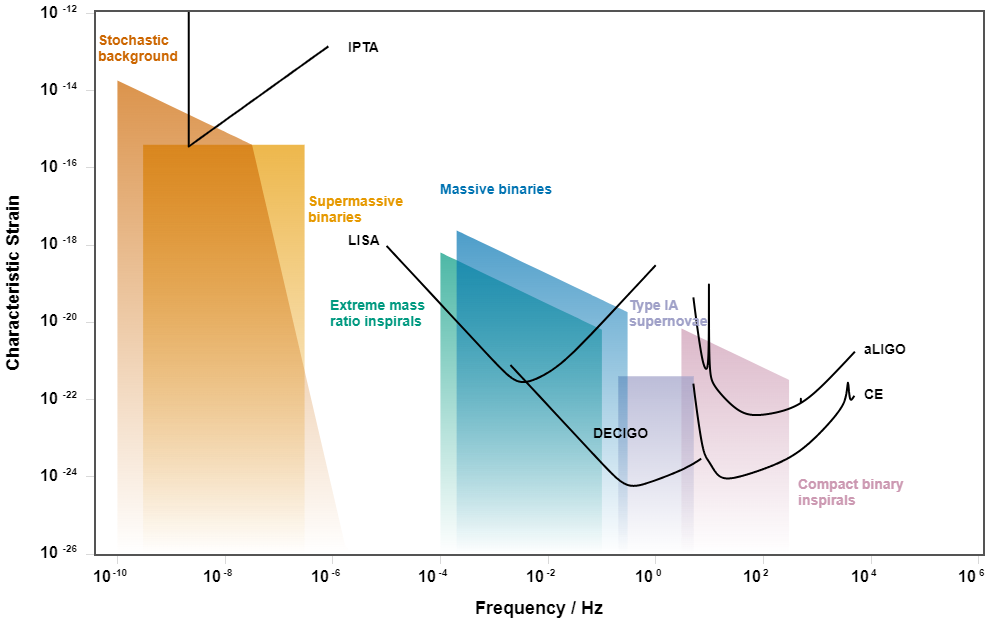

FIGURE 1.3: Strain sensitivity curves for different current and planned gravitational wave detectors: the International Pulsar Timing Array (IPTA), LISA, DECIGO, Advanced LIGO and Cosmic Explorer. Different detectors are sensitive to different frequency ranges, corresponding to different astrophysical sources. Image created using [53].

binaries earlier in their inspiral, when they are emitting gravitational waves in the mHz band. This opens the door to potential multi-band gravitational wave observations in which LISA provides prior warning and sky localisation for ground based detectors and electromagnetic follow-up. Other space based detector concepts include the Japanese decihertz proposal, DECIGO [56], and the Chinese millihertz band TianQin and Taiji programmes [57, 58]. Figure 1.3 displays strain sensitivity curves for a selection of current and future detectors, demonstrating how having a variety of instruments gives us better coverage of potential sources.

The detection of GW150914 marked the beginning of the era of gravitational wave astronomy. Nearly a decade later, the field is flourishing and beginning to answer important questions in both astro- and fundamental physics. These results build on over 100 years of work in theoretical relativity, numerical methods and detector technology. If we are to seize the opportunity presented by next-generation observatories, it is necessary to redouble these efforts.

1.2 Gravitational wave source modeling

To identify gravitational wave events and accurately extract the parameters of the source we commonly make use of matched filtering. Crucial to this process is the availability of highly accurate *waveform templates* which, given a set of source parameters, tell us

the theoretically predicted gravitational wave strain for that source. Members of our template bank may be correlated against the detector output to calculate the *signal-to-noise ratio* (SNR) for that template. If the SNR exceeds a given threshold, this may be considered a candidate detection requiring follow-up, and the template with highest SNR represents the best initial estimate for the source parameters [59]. During follow-up, the waveform templates are again required as part of a Bayesian framework to infer the posterior probability distribution on the source parameters.

Future detector developments pose two main challenges for waveform modelling. Firstly, as detector noise falls, so too do the resulting statistical measurement errors, and hence systematic errors in our waveform models potentially gain greater significance. Secondly, as new detectors probe new frequency bands and hence new sources, we need to expand the range of validity of our models to ensure full coverage of all expected targets. Current waveform models have proven largely adequate for the groundbreaking initial observations by the LIGO and Virgo detectors, but achieving the scientific potential of LISA and the 3G detectors is certain to demand significant improvements in both accuracy and parameter space coverage [60, 61].

In this section we review the main methods used to model general relativistic binary systems. Starting with a brief survey of some relevant astrophysical targets to illustrate the different regimes that must be covered, we will then outline the different modelling approaches one may take and discuss their respective domains of application.

1.2.1 Compact binary targets for LISA

The largest class of compact binary targets for LISA is likely to be the population of stellar-origin compact binaries in the Milky Way. Known as galactic binaries, these systems mostly consist of binary white dwarfs, with a much smaller number of systems containing neutron stars or a single black hole. The binary components will typically have roughly equal masses around 1 solar mass ($1M_\odot$). Such systems evolve only on timescales much longer than the planned duration of LISA's observations, and would thus appear as nearly-monochromatic sources in the LISA data stream. It is estimated there may be up to 10,000 individually resolvable white dwarf binaries, including roughly 30 "verification binaries" which have been identified in advance using electromagnetic observations [60]. LISA may also be able to detect some stellar origin black hole binaries outside of the Milky Way. Consisting of two black holes with masses in the range $(\text{few} - 100)M_\odot$, these systems are expected to have roughly symmetric mass ratios, between $1:1$ and $3:1$ [60]. Entering the mHz band several years before merger, it is estimated that during the LISA mission it may be possible to track the evolution of between 0 and a few dozen such systems across the LISA and ground-based bands, all the way until merger [62].

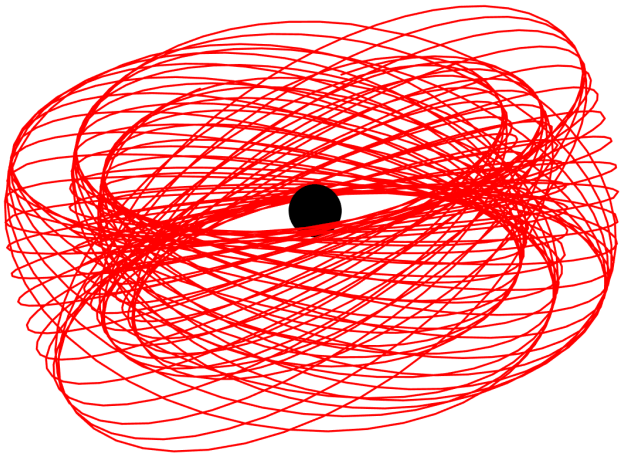

FIGURE 1.4: An example bound geodesic in the Kerr spacetime. The central Kerr black hole has mass M and angular momentum $J/M^2 = 0.2$, and the geodesic has eccentricity $e = 0.2$, semi-latus rectum $p = 10M$ and inclination $\iota = \pi/8$. Trajectory calculated using the KerrGeodesics package from the BHP Toolkit [63].

Another important class of targets are massive black hole (MBH) binaries. Containing two black holes in the mass range $(10^5 - 10^8)M_\odot$, these systems are expected to have roughly symmetric mass ratios in the range $(1 - 10) : 1$. Depending on the formation mechanisms assumed, LISA event rate estimates range from a few per year to a few tens over the 4 year initial mission [60]. Some MBH mergers may be exceptionally loud signals, with accumulated SNRs of over 1000 possible over the course of the inspiral and merger. Highly accurate waveform templates for these sources are thus required, as any errors may result in high-power residuals after subtracting the MBH signal from the data, complicating the analysis of the quieter sources left behind [59]. LISA is also expected to detect the merger of MBHs with intermediate mass black holes, defined to have masses between $100M_\odot$ and $10^4M_\odot$. Systems such as these, which have a mass ratio in the range $(10 - 10^4) : 1$, are known as intermediate mass-ratio inspirals (IMRIs); a second class of IMRI targets for LISA arise from the merger of stellar mass black holes with intermediate mass black holes.

Perhaps the most interesting LISA sources are the so-called extreme mass-ratio inspirals (EMRIs). A typical EMRI consists of a stellar mass compact body with mass $\mu \sim (1 - 100)M_\odot$ inspiralling and merging with an MBH of mass $M \sim (10^5 - 10^7)M_\odot$. We define the mass ratio to be $\eta := \mu/M$ (note we adopt the convention with $\eta \leq 1$), which for EMRIs will typically lie in the range $10^{-6} \lesssim \eta \lesssim 10^{-4}$. This extremely small mass ratio results in a clear separation of timescales in the EMRI problem. Gravitational wave emission alters the trajectory over the radiation reaction timescale $T_{\rm RR} \sim M/\eta$, which for EMRIs is much longer than the orbital time period $T_{\rm orb} \sim M$ [64]. This means that over orbital timescales the smaller object appears to be moving along a fixed geodesic in the spacetime of the MBH. For a rotating Kerr black hole these geodesics are tri-periodic (with separate radial, azimuthal and longitudinal periods) and generically ergodic, as

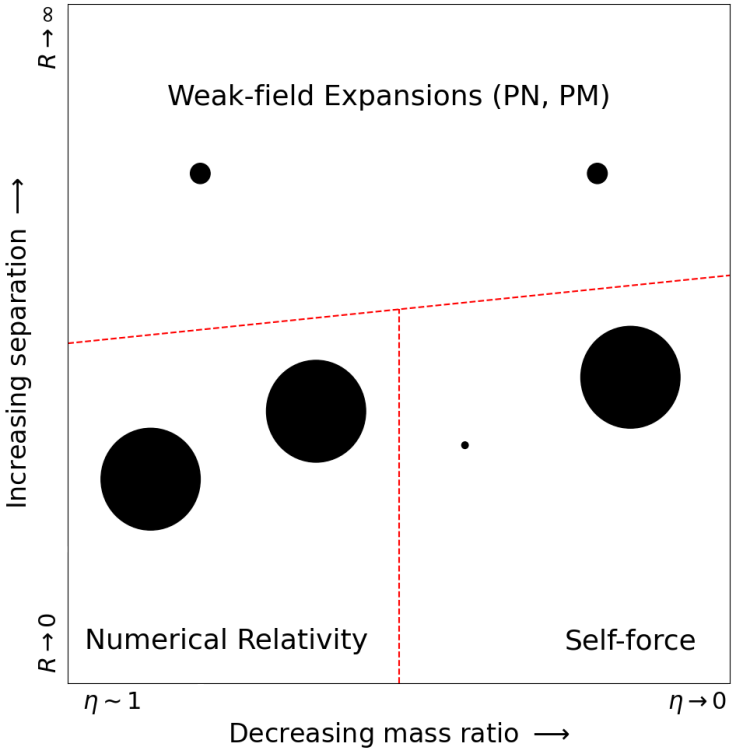

FIGURE 1.5: Illustration of the parameter space for compact binary modelling: separation (R) vs mass-ratio ($\eta \leq 1$). The post-Newtonian (PN) and post-Minkowskian (PM) approaches may be used to model widely separated binaries, and self-force may be used to model binaries with significant mass asymmetry. Numerical relativity is used to model roughly symmetric binaries close to merger, but becomes inefficient in the limit of large separations or small mass ratios.

illustrated in Fig. 1.4. Over the final several years before merger, the smaller object will trace out $T_{\rm RR}/T_{\rm orb} \sim 1/\eta \sim 10^5$ orbital cycles in close proximity to the massive black hole, emitting gravitational waves in the LISA band as it does so. The resulting gravitational waveforms will thus encode exquisite information about the strong-field region around the MBH, allowing us to place strong constraints on any deviation from the Kerr geometry and measure the mass and spin of the MBH with great precision [60]. It has been estimated that LISA will observe between a few and a few thousand EMRIs per year, depending on the astrophysical assumptions made, with SNRs up to $O(100)$ [65].

1.2.2 Modelling approaches

The two most important parameters informing our choice of modelling approach for a compact binary are the orbital separation R and the binary's mass ratio, $\eta \leq 1$. This parameter space, and the optimal choices of modelling approach for each region, are illustrated in Fig. 1.5. An important approach is *numerical relativity* (NR), in which the full non-linear Einstein equations are recast as an initial value problem and solved

numerically – see Ref. [66] for a review of 21st century breakthroughs and the state of the art techniques in this area. NR is able to model binaries in the strong-field regime, including the final inspiral and merger, but the calculations are highly computationally expensive. This issue becomes particularly pressing when there is a separation of scales within the problem, such as when the orbital separation is much larger than the objects, or when one component is significantly more massive than the other. This means that, in practice, NR is only suitable for modelling the late stages of roughly comparable mass binaries. For widely-separated systems such as galactic binaries and other targets earlier in their inspirals, the dynamics are well-described by weak-field approximations. The leading approach in this area is *post-Newtonian* (PN) theory, which relies on expansions in powers of the gravitational constant G and velocities v [67]. Alternatively, in *post-Minkowskian* (PM) theory one dispenses with the slow-velocity assumption and expands only in G [68]. The combination of NR and weak-field methods (primarily PN) has proven highly successful for modelling the stellar origin BBH and BNS mergers observed by LIGO and Virgo, and these approaches will remain the mainstay for other sufficiently symmetric LISA targets such as MBH binaries.

The most asymmetric event observed by LIGO and Virgo thus far was GW191219_163120, a suspected neutron star-black hole merger with a mass ratio $\eta \leq 0.041$ at the 90% credible level [39]. This already exceeds the limits of current routine NR simulations: the smallest mass-ratio included in the latest catalogue of numerical relativity simulations by the SXS collaboration, for example, is only $\eta = 0.1$ [69]. Other teams have successfully simulated a short inspiral and plunge for a binary with $\eta = 1/100$ [70], and a head-on collision between two black holes with mass-ratio $\eta = 1/1024$ [71], but these are currently only isolated experimental results. The fundamental challenge is the need to use a numerical grid which simultaneously resolves the length scale of both the large and small object, and to evolve the system over multiples of the long radiation-reaction timescale $T_{\rm RR} \sim 1/\eta$. When η becomes small, this results in a rapid growth in runtime proportional to $1/\eta^2$ [72]. Greater success simulating low mass ratio binaries may be expected with theoretical and computational developments, but NR will not be able to model the most asymmetric IMRIs and EMRIs that we expect to observe for the first time with LISA. For this, we turn to a form of black hole perturbation theory called *self-force* (SF) theory [73–76]. The self-force approach relies on an expansion in the mass-ratio, without any expansions in G or v. This results in an approximation which is valid in the strong-field and with arbitrary velocities, but only for binaries with sufficiently small mass ratio. Unlike PN, SF results are not in general given analytically, and the SF expanded field equations must be solved numerically. This process can require significant computational resources, but solving the perturbative self-force equations (which are linear and separable) is typically much less expensive than the NR simulations used in the comparable mass regime. PN results may continue to be used to model extreme mass ratio systems at large separation, including the use of combined

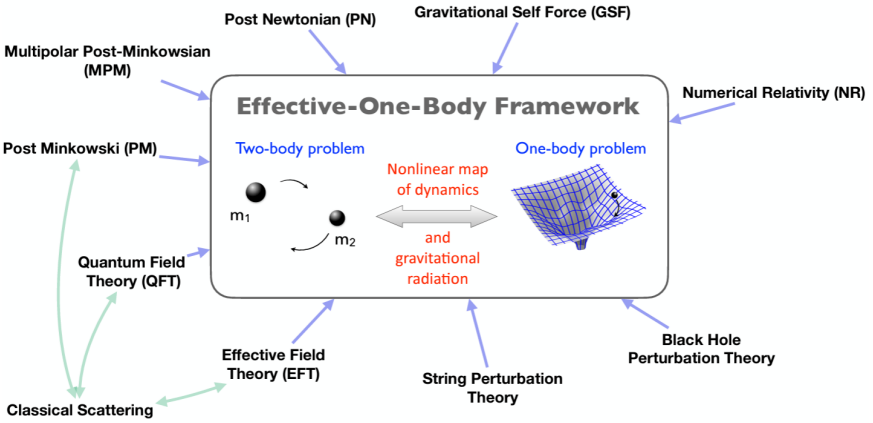

FIGURE 1.6: Approaches which inform development of effective-one-body (EOB) models. EOB combines information from different numerical and perturbative approaches to produce a universal model of binary inspiral, merger and ringdown. Image credit: [60]

PN-SF expansions that obtain higher-order PN results by restricting to first-order in the mass-ratio [77–82].

Before reviewing the foundations of self-force theory in greater detail, we consider how results from the above approaches are combined to generate waveforms for use in real-world gravitational wave searches and parameter estimation. In order to be of practical use, our waveform models need to be much faster to evaluate than the NR or SF calculations described above, which are far too slow to be evaluated on the fly. This requires the creation of secondary models which, informed by PN and numerical NR/SF calibration data, can give rapid predictions for the waveform for arbitrary parameters. An example is the IMRPhenom family [83–86] of *phenomenological* models, which play a key role in LVK data analysis [30, 38, 39]. In this approach, the waveform is split into sections (e.g. inspiral, merger-ringdown and the intermediate region between) and functions such as the (spherical harmonic mode) phase and amplitude in each section are described by physically motivated closed-form ansatze with undetermined coefficients [60]. These coefficients are fit to a bank of calibration waveforms constructed using, for example, PN and NR, and then interpolated across the parameter space.

Another important tool for obtaining gravitational waveforms is *effective-one-body* (EOB) theory [87]. This approach relies on a map between the real two-body dynamics and the motion of an effective test particle in a deformed black hole background. An EOB model then contains three essential ingredients: a Hamiltonian (containing certain a priori undetermined potentials) describing the conservative dynamics; a description of the radiation-reaction force; and a description of the gravitational waveform emitted during the inspiral, merger and remnant ringdown phases [88, 89]. Each of these contributions must be calibrated against the primary modelling approaches described above. This was originally achieved using resummed PN results, and later with information from

NR simulations [88, 89]. Modern EOB models may also incorporate information from self-force [90–99] or PM theory [100–105] in addition – see Fig. 1.6 for a summary of the different approaches that have been integrated into the EOB framework. EOB combines and resums the information from these different approaches, producing models which cover a larger region of parameter space than the primary methods alone [60], and which are much more rapid to evaluate than the expensive NR (or SF) calculations used for calibration.

1.3 Gravitational self-force

The basic principle of self-force theory is to expand all quantities as a series in the small mass ratio, identifying the perturbations as objects on the *background* spacetime of the large primary object. The motion of the smaller secondary object is represented by an effective worldline in the background, and the key goal is to obtain its equation of motion order-by-order in the mass ratio.

More concretely, suppose our primary object has mass M, and the small, secondary, object has mass $\mu \ll M$. The "physical" metric describing the combined spacetime of the two objects may be expanded

$$g^{\rm phys}_{\alpha\beta} = g_{\alpha\beta} + \eta h^{(1)}_{\alpha\beta} + \eta^2 h^{(2)}_{\alpha\beta} + ..., \tag{1.1}$$

where $g_{\alpha\beta}$ is the "background" metric describing the isolated primary body and, recall, $\eta := \mu/M \ll 1$. The physical metric obeys the Einstein field equations,

$$G_{\alpha\beta}[g^{\rm phys}] = 8\pi T_{\alpha\beta}, \tag{1.2}$$

where $G_{\alpha\beta}[g^{\rm phys}]$ is the Einstein tensor constructed from the metric $g^{\rm phys}_{\alpha\beta}$ and $T_{\alpha\beta}$ is the stress-energy tensor. Substituting Eq. (1.1) into Eq. (1.2), the left hand side becomes

$$G_{\alpha\beta}[g^{\rm phys}] = G_{\alpha\beta}[g] + \eta\delta G_{\alpha\beta}[h^{(1)}] + \eta^2\left(\delta G_{\alpha\beta}[h^{(2)}] + \delta^2 G_{\alpha\beta}[h^{(1)}, h^{(1)}]\right) + O(\eta^3), \tag{1.3}$$

where $\delta G_{\alpha\beta}[h]$ is a 2nd order linear differential operator acting on h and $\delta^2 G_{\alpha\beta}$ is a 2nd order quadratic differential operator with schematic form $\delta^2 G[h,h] \sim (\partial h)^2 + h\partial^2 h$ [75]. Assuming the stress-energy tensor may also be expanded as

$$T_{\alpha\beta} = T^{(0)}_{\alpha\beta} + \eta T^{(1)}_{\alpha\beta} + \eta^2 T^{(2)}_{\alpha\beta} + O(\eta^3), \tag{1.4}$$

Eq. (1.2) gives rise to a hierarchy of equations,

$$G_{\alpha\beta}[g] = 8\pi T^{(0)}_{\alpha\beta}, \tag{1.5}$$

$$\delta G_{\alpha\beta}[h^{(1)}] = 8\pi T^{(1)}_{\alpha\beta}, \tag{1.6}$$

$$\delta G_{\alpha\beta}[h^{(2)}] = 8\pi T^{(2)}_{\alpha\beta} - \delta^2 G_{\alpha\beta}[h^{(1)}, h^{(1)}], \tag{1.7}$$

and so on. We will assume the primary body is a black hole, meaning $T^{(0)}_{\alpha\beta} = 0$.

A significant early result in the development of gravitational self-force theory was the demonstration by D'Eath that, at first order in q, the metric perturbation outside a small body is equivalent to that obtained by solving Eq. (1.6) with a *point-particle* source [106],

$$T^{(1)}_{\alpha\beta}(x) = \mu \int u_\alpha u_\beta \frac{\delta^4(x - x_p(\tau))}{\sqrt{-g}} d\tau, \tag{1.8}$$

where $x_p(\tau)$ is an effective worldline describing the motion of the smaller object in the background spacetime, τ is the small body's proper time in that spacetime, and $u^\alpha := dx^\alpha_p/d\tau$ is the small object's 4-velocity. This result applies even when the small body is a black hole, for which the true stress-energy vanishes. The existence of a point-particle description at first order is notable because, in general, point particles do not make sense as a concept in general relativity. Due to their nonlinear nature, the Einstein field equations do not admit solutions over any sensible space of functions when the stress-energy is a distribution supported on some worldline [107]. The physical origin of this problem is clear: any attempt to compress a finite mass into an infinitesimal volume would result in a collapse to form a black hole of finite diameter instead. Another important point to emphasise is that, although many self-force calculations start from Eqs. (1.6) & (1.8) without commenting on their origin, the validity of the effective point particle description they define has been rigorously derived and is not an assumption of the theory.

D'Eath's analysis made use of an important method in self-force, the method of *matched asymptotic expansions*. The presence of two disparate length scales $\mu \ll M$ in the problem allows us to expand the physical metric in two distinct limits. In the "near zone" $r \ll M$ (where r is the proper spatial distance from the small-body worldline), the metric appears to be that of the small object, with corrections arising from tidal perturbations by the primary object. In the "far zone" $r \gg \mu$, however, the metric appears to be that of the background, perturbed by small corrections arising from the small-body, which appears distant and point-*like* at this scale. Crucially, as illustrated in Fig. 1.7, both expansions remain valid in the "buffer region" $\mu \ll r \ll M$, and hence both expansions must agree here. Requiring that the two expansions match in the buffer region is a remarkably powerful technique, and it has been used to derive many key results in self-force theory, including the derivation of the equation of motion for the

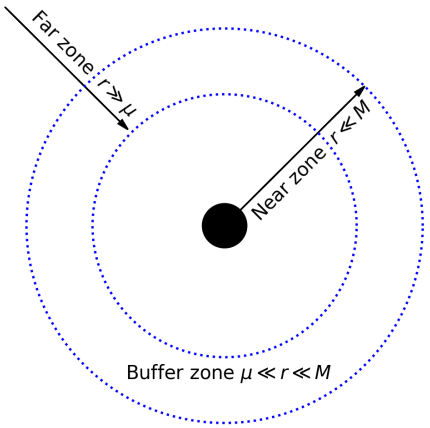

FIGURE 1.7: Illustration of the different regions around the small body in the method of matched asymptotic expansions. The near and far zones are the regions at distances $r \ll M$ and $r \gg \mu$ from the small body respectively. The separation of mass scales $\mu \ll M$ ensures the existence of a buffer zone $\mu \ll r \ll M$ between them.

small body at $O(\eta)$. Before we can present this result, however, we must introduce two more self-force concepts.

The first is the concept of gauge freedom in self-force theory. In general relativity, gauge freedom corresponds to the freedom to map our spacetime manifold to itself via a diffeomorphism without altering the physics (or, equivalently, freedom to choose our coordinate systems). In self-force, gauge freedom arises from the redundancy in our choice of identification map between the physical and background spacetimes [108]. A gauge transformation may be described by a "small" coordinate transformation, $x^\alpha \mapsto x^\alpha + \eta\xi^\alpha + O(\eta^2)$, under which [75]

$$h^{(1)}_{\alpha\beta} \mapsto h^{(1)}_{\alpha\beta} - \nabla_\alpha \xi_\beta - \nabla_\beta \xi_\alpha, \tag{1.9}$$

where ∇_α is the Levi-Civita connection compatible with the background metric. For the remainder of this section we assume the gauge freedom has been exploited to choose the Lorenz gauge, obeying the condition $\nabla^\alpha \left(h_{\alpha\beta} - \frac{1}{2} g^{\mu\nu} h_{\mu\nu} g_{\alpha\beta}\right) = 0$.

The second concept is the decomposition of the metric perturbation into pieces which are, respectively, singular and regular in the vicinity of the small body. An example of this is the construction introduced by Detweiler and Whiting in Ref. [109], where they showed that the first order metric perturbation may be split in the form

$$h^{(1)}_{\alpha\beta} = h^{\mathrm{S1}}_{\alpha\beta} + h^{\mathrm{R1}}_{\alpha\beta}, \tag{1.10}$$

where $h^{\mathrm{S1}}_{\alpha\beta}$ and $h^{\mathrm{R1}}_{\alpha\beta}$ are defined in terms of certain Green's functions such that they have the following properties. The singular field $h^{\mathrm{S1}}_{\alpha\beta}$ is a particular solution to Eq. (1.6) with a point particle source and hence has the same singularity structure as the full (retarded)

solution in the vicinity of the small body,

$$h^{\mathrm{S1}}_{\alpha\beta} \sim \frac{\mu}{r}. \tag{1.11}$$

The regular field $h^{\mathrm{R1}}_{\alpha\beta}$, on the other hand, is a solution to the vacuum linearised Einstein equation,

$$\delta G_{\alpha\beta}[h^{\mathrm{R1}}] = 0, \tag{1.12}$$

and is (as the name would suggest) regular everywhere, including on the small body's worldline. The motion of the small body is affected only by the regular field; for a non-spinning small body, the equation of motion is given by

$$\frac{D^2 x_p^\alpha}{d\tau^2} = -\frac{\eta}{2} g^{\alpha\beta}\left(2h^{\mathrm{R1}}_{\beta\rho;\sigma} - h^{\mathrm{R1}}_{\rho\sigma;\beta}\right) u^\rho u^\sigma + O(q^2) := F^\alpha_{\mathrm{self}}/\mu, \tag{1.13}$$

where semicolons denote covariant derivatives and $D/d\tau := u^\beta \nabla_\beta$. The quantity on the right hand side of Eq. (1.13) defines the (first-order) gravitational self-force, F^α_{self}. The formula is known as the MiSaTaQuWa equation after the groups of Mino, Sasaki and Tanaka, who first derived it using matched asymptotic expansions [110], and Quinn and Wald, who independently derived it using an axiomatic approach [111] a short time later. Both teams originally made use of an alternative singular/regular split for the metric perturbation, with the formulation in terms of Detweiler-Whiting fields introduced at the same time as that decomposition in Ref. [109].

We note that Eq. (1.13) is consistent with the standard equivalence principle of general relativity: at zeroth order in the mass ratio, any sufficiently small body (regardless of its internal structure) moves along a geodesic in the background spacetime. Indeed, this fact is not assumed in self-force theory, and self-force may thus be considered to provide a *derivation* of the geodesic postulate. Furthermore, Eq. (1.13) suggests a generalisation of the equivalence principle. Introducing the first order effective metric $g^{\mathrm{eff}}_{\alpha\beta} := g_{\alpha\beta} + \eta h^{\mathrm{R1}}_{\alpha\beta}$, the MiSaTaQuWa equation becomes [109]

$$\frac{\tilde{D}^2 x_p^\alpha}{d\tilde{\tau}^2} = O(\eta^2), \tag{1.14}$$

where objects with a tilde are defined with respect to the effective metric. In other words, at first order in the mass-ratio an arbitrary small body moves along a geodesic in a certain effective vacuum spacetime. As elegant as this result is, however, it is important to remember that $h^{\mathrm{R1}}_{\alpha\beta}$, and hence $g^{\mathrm{eff}}_{\alpha\beta}$, is not a physical quantity. The split into regular and singular pieces is not unique, and only the combination $h^{(1)}_{\alpha\beta} = h^{\mathrm{R1}}_{\alpha\beta} + h^{\mathrm{S1}}_{\alpha\beta}$ can be considered truly physical [75].

The Detweiler-Whiting construction does not extend to second order, but it is still possible to define convenient splits $h^{(2)}_{\alpha\beta} = h^{\mathrm{S2}}_{\alpha\beta} + h^{\mathrm{R2}}_{\alpha\beta}$. One such approach introduced by

Pound in Ref. [112] ensures that the second order effective metric $g^{\rm eff}_{\alpha\beta} := g_{\alpha\beta} + \eta h^{\rm R1}_{\alpha\beta} + \eta^2 h^{\rm R2}_{\alpha\beta}$ obeys the vacuum Einstein equation through second order,

$$G_{\alpha\beta}[g^{\rm eff}] = O(\eta^3). \tag{1.15}$$

With this choice of regular field, Pound showed that at second order the equation of motion is given by

$$\frac{D^2 x^\alpha_p}{d\tau^2} = -\frac{1}{2}\left(g^{\alpha\beta} - h^{\alpha\beta}_{\rm R}\right)\left(2h^{\rm R}_{\beta\rho;\sigma} - h^{\rm R}_{\rho\sigma;\beta}\right)u^\rho u^\sigma + O(\eta^3), \tag{1.16}$$

where $h^{\rm R}_{\alpha\beta} := \eta h^{\rm R1}_{\alpha\beta} + \eta^2 h^{\rm R2}_{\alpha\beta}$ is the total second order regular field. The $O(\eta^2)$ part of the right hand side is known as the second-order self-force (per unit μ). This may be recast in terms of $g^{\rm eff}_{\alpha\beta}$,

$$\frac{\tilde{D}^2 x^\alpha_p}{d\tilde{\tau}^2} = O(\eta^3), \tag{1.17}$$

establishing that the generalised equivalence principle also holds at second self-force order.

The development of self-force theory in recent decades has been driven primarily by the need to accurately model EMRIs for LISA. In Ref. [64], Hinderer and Flanagan showed that the orbital phases φ_A of an EMRI take the form

$$\varphi_A = \frac{1}{\eta}\left(\varphi^{(0)}_A + \eta\varphi^{(1)}_A + O(\eta^2)\right), \tag{1.18}$$

where the "adiabatic" term $\varphi^{(0)}_A$ depends on the first-order *dissipative* (see Sec. 2.2.3) self-force, and the first "post-adiabatic" term $\varphi^{(1)}_A$ depends on the full first-order self-force, plus the dissipative piece of the second order self-force. Accurately tracking the waveform phase to sub-radian accuracy is critical for LISA data analysis, thus we require the orbital phases correct to first post-adiabatic order, and hence must calculate the second-order self-force. At first-order, the gravitational self-force has been calculated along generic (i.e. eccentric and inclined) bound geodesics in the Kerr spacetime [113, 114]. Second order self-force calculations are significantly less mature, but early examples include the calculation of the binding energy [115] and gravitational wave energy flux [116] for a quasicircular binary with a Schwarzschild primary, and most recently a waveform for a full quasicircular inspiral into a Schwarzschild black hole [117]. Extending these calculations to eccentric orbits and a Kerr primary [118, 119] are important goals of the self-force programme.

1.4 Black hole scattering

The potential compact binary sources for LISA discussed in Sec. 1.2.1 are all examples of *bound* systems, in which the objects have insufficient orbital energy to escape to infinity, remaining instead a finite distance apart until they eventually merge. This thesis, however, is interested in a distinct problem – that of *scattering* motion. During a scatter encounter, two initially distant objects approach each other closely but, having sufficient energy and angular momentum, avoid merging and begin to separate once more, never to interact again.

Extreme mass ratio scatter events (the class of scattering systems that may be directly modelled using self-force methods) are not considered one of the primary observational targets for LISA, although a small number of detections may be possible [60]. The reason for this is clear if one compares the dynamics to those of an EMRI with similar component properties. As discussed previously, an EMRI may emit $1/\eta \sim 10^5$ gravitational wavecycles in the LISA frequency band prior to merger, allowing us to accumulate SNR over these many cycles despite the relatively low amplitude (compared to, say, an MBH binary.) Scatter events, meanwhile, will emit strongly only during the closest period of the encounter, appearing as a gravitational wave *burst* rather than a multi-year EMRI. With this relatively short period of emission, an extreme mass ratio burst would only be identifiable in the LISA data stream if it had much greater amplitude than the comparable EMRI, which in turn requires the scatter system to be located much closer. The study in Ref. [120] estimated that on average around 2 bursts may be detected from the galactic centre during a notional 2 year mission. Looking at potential extragalactic sources, Ref. [121] concluded that detections may be possible out to distances ~ 100 Mpc but, when considering parameter estimation for sources in a selection of potential nearby host galaxies, they found that only binaries with very small closest separation would yield useful information about the primary black hole. In any case, the inclusion of the self-force is much less important for modelling astrophysical scatter events than for EMRIs, because the duration of the observed burst is much shorter than the radiation-reaction timescale. Consequently, waveform generation for extreme mass ratio bursts is not an important inspiration for our work. In fact, several other compelling motivations exist.

The first is pure theoretical interest. Scatter orbits are good natural probes of the strong-field region outside black holes, able to penetrate deep into the region inside the innermost stable circular orbit (ISCO) and stay there for long periods, even at low velocities and with minimal tuning of the initial conditions. By contrast, bound systems will generically plunge after crossing the ISCO. The scatter problem, with motion beginning and ending in the asymptotically flat region, also admits "in" and "out" states with well-defined energy and angular momentum, free of the gauge ambiguities which complicate the interpretation of physical effects for bound orbits.

Another important motivation was the realisation that the gravitational *scatter angle* completely determines the EOB Hamiltonian, and hence the entire conservative 2-body dynamics [100, 101]. The self-force approach constitutes one way to obtain the scatter angle (as an expansion in the mass ratio), and this is an important objective motivating the development of gravitational self-force calculations along scatter orbits. In the meantime, there has been significant interest in the use of the PM expansion [100, 101, 122, 123], an approach which has benefitted in recent years from the introduction of established techniques from outside the usual gravitational physics community. Among the new methods adopted are advanced quantum amplitude techniques such as generalised unitarity [124, 125] and double copy [126–128], which have been used to develop "dictionaries" that translate quantum scattering amplitudes to classical gravitational dynamics. This has led to rapid advances in the PM theory of two-body dynamics [129–132], culminating in the derivation of the conservative 2-body Hamiltonian at 4th PM (4PM, $O(G^4)$) order [133], and more recently the 5PM conservative scatter angle correct at first-order in the mass ratio [134]. These are supplemented by similar calculations using effective field theory (EFT) [135–140]. There has also been work towards including radiative effects [131, 141, 142].

As well as directly calibrating EOB, self-force scatter calculations can play a role in PM calculations. As noted by Damour in Ref. [122], self-force calculations give relatively easy access to higher order PM terms in the scatter problem. Remarkably, the scatter angle of geodesics is sufficient to determine the full conservative 2-body dynamics (at *all* mass ratios) of structureless point particles to 2PM order on a Schwarzschild background, whilst knowing the first-order self-force correction to the scatter angle (that is to say the part of the correction linear in the small mass ratio η) is sufficient to determine the full conservative 4PM dynamics. A second-order self-force calculation could push this further to 6PM order. The origin of self-force's determinative power lies in the particular polynomial dependence of PM coefficients on the masses, combined with the expected mass-exchange symmetry. As a simple example, consider the scattering of two particles with masses ${m_i}^2$, during which each experiences an impulse $\Delta p_i^\mu := p^\mu_{i,\text{final}} - p^\mu_{i,\text{initial}}$. The momentum transfer $Q := \sqrt{\eta_{\mu\nu}\Delta p_1^\mu \Delta p_2^\nu}$ has a PM expansion of the form [122]

$$Q = \frac{2Gm_1m_2}{b}\left[Q^{1\text{PM}}(v) + \left(Q_1^{2\text{PM}}(v)\frac{Gm_1}{b} + Q_2^{2\text{PM}}(v)\frac{Gm_2}{b}\right) + O(G^3)\right], \tag{1.19}$$

where b is the impact parameter (distance of closest approach in the absence of gravitational interaction) and v is the initial relative velocity. At each PM order the coefficients are homogeneous polynomials of the two masses. In the self-force limit $m_2 \ll m_1$, the 2PM order term involving $Q_2^{2\text{PM}}$ is formally first order in the mass-ratio, being suppressed by a factor of $\eta = m_2/m_1$ relative to the $Q_1^{2\text{PM}}$ term. However, the mass exchange symmetry $m_1 \leftrightarrow m_2$ requires $Q_1^{2\text{PM}} = Q_2^{2\text{PM}}$, so that the full 2PM term is in

[2] Note the use of m_1 and m_2 for the masses rather than our previous notation, μ and M. We do this to emphasise that Eq. (1.19) is completely general, without any restrictions on the mass ratio.

fact completely determined by its geodesic order piece. In general, the expansion correct to nPM order may be completely determined by an $\lfloor \frac{n-1}{2} \rfloor$ order self-force calculation [122].

Self-force results for the scatter angle can be compared to PM results in an overlapping domain of validity, providing useful checks on both schemes. Given the first-order gravitational self-force correction to the scatter angle, one could completely verify the state of the art 4PM and 5PM-1SF analytical results; in the future, an extension to second-order self-force might allow the full 6PM dynamics to be determined earlier than possible using analytical means. Furthermore, self-force results remain exact in the strong-field limit (at a given order in the mass-ratio), and may thus be used to benchmark or calibrate PM results in this regime. We will explore the idea of using strong-field self-force information to extend the range of validity of weak-field PM results in Chapter 5.

Effective-one-body models incorporating self-force scatter angle data may be used to provide waveforms for *bound* compact binary systems. By calibrating EOB with SF-informed, mass-symmetrised, PM results, we may even help to model the dynamics and gravitational wave emission of comparable mass binaries (such as MBH or stellar-origin binaries), not just EMRIs. An alternative way to obtain bound orbit information from scatter calculations is provided by so-called "boundary to bound" maps, derived using effective field theory [143]. These maps have typically been developed in the context of PM theory, and formulations exist to map between (PM expanded) observables such as the scatter angle and bound orbit periastron advance [143], radiative fluxes [144], and most recently direct maps between scatter and bound orbit waveforms [145]. Relations between *exact* scatter and bound orbit observables have also been derived for geodesic orbits in the Kerr spacetime [146], and work is underway to extend this to higher orders in the self-force expansion [147]. If these self-force boundary to bound maps can be successfully developed, self-force scatter calculations would provide an additional (or alternative) approach to obtain bound orbit self-force information.

A first step towards a full self-force calculation of the scatter angle was taken by Long and Barack in Ref. [148], which demonstrated a method to reconstruct the linear metric perturbation sourced by a point mass moving along a fixed hyperbolic geodesic in the Schwarzschild spacetime, in a gauge suitable for self-force calculations. To demonstrate the practicality of their approach, they developed a time-domain numerical scheme for obtaining the scalar-like "Hertz potential", from which the metric perturbation (and hence self-force) can be derived. But that initial work stopped short of a calculation of the self-force itself. In a subsequent work by the same authors [149], a first calculation of the self-force correction to the scatter angle was carried out, albeit in a scalar-field toy model. This numerical calculation was performed using an adapted version of the time-domain computational platform developed in Ref. [148]. In addition to these numerical results, the scalar (as well as electromagnetic and gravitational) self-force corrections to the scatter angle were derived analytically at leading (2PM) order by Gralla and Lobo

in Ref. [150]. The leading-order (3PM) piece of the dissipative gravitational and scalar-field self-force scatter angle corrections were first written down in Ref. [149]. Knowledge of the scalar-field self-force correction to the scatter angle was subsequently improved to 4PM order using scattering amplitude methods, showing impressive agreement with the self-force results [151].

1.5 Outline

The purpose of this thesis is to develop *frequency-domain* numerical methods to calculate the self-force along fixed hyperbolic scatter geodesics. Frequency-domain methods are ubiquitous for self-force calculations along bound geodesics, being valued for their ability to give highly accurate results at relatively high speed by reducing the governing partial differential equations to ordinary differential equations. For example, the state-of-the-art code developed in Refs. [113, 114], which is able to compute the 1st order gravitational self-force along generic bound geodesics in a Kerr background, solves the Teukolsky equation in the frequency-domain to obtain the necessary Hertz potential. Frequency-domain methods are hoped to retain much of their advantage over time-domain codes when applied to unbound orbits, but several significant challenges to this extension are clear a priori.

An obvious difference between the bound and scatter orbit problems lies in the nature of the frequency spectrum. As noted in Sec. 1.2.1, bound geodesics in the Kerr spacetime are tri-periodic, giving rise to a *discrete* frequency spectrum for the scalar-field. Scatter orbits, however, lack any periodicity, leaving us with a *continuous* frequency spectrum for the scalar-field. In general this requires us to evaluate a greater number of frequency modes than an equivalent bound orbit calculation. It will be important therefore to take any steps we can to minimise the number of modes we must calculate, and in particular to maximise the re-use of frequency-domain quantities where possible. The calculation of the frequency modes themselves is also complicated for unbound orbits. A mainstay of frequency-domain self-force calculations is the method of *extended homogeneous solutions* (EHS) [152], in which the time-domain field is reconstructed piecewise from frequency modes of certain homogeneous solutions to the field equation. This approach avoids the problematic Gibbs ringing that confounds a naive attempt to reconstruct the time-domain field from the inhomogeneous frequency-domain solution, but, importantly, the usual EHS construction relies on the radial compactness of the particle's orbit. This condition fails to be satisfied for scatter orbits, and the applicability or otherwise of EHS will have to be established.

Other problems will only be discovered along the way. To investigate and resolve all these difficulties, and in line with the existing scalar-field scatter angle calculations performed in the time-domain, we make use of a scalar field model in a background Schwarzschild

spacetime. This model will capture the essential difficulties of the self-force scatter problem, while remaining simpler to implement overall than an equivalent calculation in gravity. The use of scalar-field toy models to develop new self-force techniques is a well-established strategy, and a number of frequency-domain scalar-field self-force codes exist for bound orbits (see examples in Refs. [153–156]). The approach of Ref. [154], in particular, inspired our initial numerical method. We note also that a frequency-domain method was used in Refs. [157, 158] to calculate the gravitational radiation from a point mass scattered off a Schwarzschild black hole. That work made use of the Regge-Wheeler-Zerilli formalism, in which information about the gravitational perturbation is encoded in a scalar-like field that obeys an equation very similar to that of our scalar-field model (to be introduced in Sec. 2.2). Crucially, however, that work considered only asymptotic waveforms and fluxes, which did not require the use of EHS.

1.5.1 Structure

The structure of this thesis is as follows. Chapter 2 provides the mathematical preliminaries for our approach, beginning with an introduction to hyperbolic scatter geodesics in the Schwarzschild spacetime. Our scalar-field self-force model is then described, and the method of mode-sum regularisation by which we will calculate the self-force is explained. The self-force correction to the scatter angle is defined, and existing numerical SF and analytical PM results reviewed. The frequency-domain scalar-field equation with a scattering source is obtained, and its inhomogeneous solution found using variation of parameters. The chapter concludes by presenting the EHS method, in the context of our scatter problem. Notably, we confirm that an EHS may be used to reconstruct the time-domain field in the "internal" region $r \leq r_p(\tau)$, where r is the Schwarzschild radial coordinate, and $r_p(\tau)$ is the radial position along the geodesic, parameterised by proper time τ. The usual construction fails in the external region, $r \geq r_p(\tau)$, but we are still able to proceed with the self-force calculation using a one-sided mode-sum regularisation procedure which only requires the values of the field and its derivatives as $r \to r_p(\tau)$ from below.

Chapter 3 concerns the numerical calculation of the frequency modes of the internal EHS. This requires us to evaluate certain normalisation integrals $C^{-}_{\ell m\omega}$ (one for each frequency-harmonic mode), which are obtained by numerically evaluating radial integrals along the orbit, which stretches to radial infinity. These integrals exhibit slow, oscillatory convergence, rendering them slow to evaluate, and making the error from the necessary finite-radius truncation hard to control. Two complementary analytical solutions are developed to minimise this truncation error. *Integration by parts* is used to increase the decay rate of the integrand, reducing the truncation error at a given finite truncation radius. The *tail correction scheme* uses a large-radius expansion of the integrand to approximate the value of the neglected tail. The numerical method for evaluating the

integrals is described, including the use of quadrature routines specialised towards highly oscillatory integrands. Finally, example numerical results are used to illustrate the success of our methods.

Our all-up numerical method for calculating the self-force along a given scatter geodesic is presented in Chapter 4. Efficient time-domain reconstruction is achieved by calculating discretised $C^{-}_{\ell m\omega}$ data in advance, and interpolating to obtain the values at the intermediate frequencies we require when evaluating the Fourier integrals for the time-domain field. All stages of our calculation can be significantly accelerated using parallel computing. With an efficient method at hand, we present initial numerical results. Validation is obtained by comparing the numerical results with the analytically known regularisation parameters, and by comparisons with the extant time-domain code of Ref. [149]. The conclusions of these tests are that our frequency-domain code is highly accurate in the strong-field region near to the periapsis of our example orbit, giving access to high angular ℓ-modes, and exceeding the precision of the time-domain code as hoped. Distressingly, however, the frequency-domain code is observed to deteriorate rapidly at larger radii along the orbit. This issue is traced to cancellation between low-frequency modes of the EHS; this problem has been previously noted in bound-orbit gravitational self-force calculations [113], but affects our scatter calculation even more severely. As an interim measure, we adopt an adaptive truncation algorithm which detects the onset of anomalous ℓ-mode behaviour, and truncates the self-force mode-sum early to prevent their inclusion. This preserves the high precision of the frequency-domain code near to periapsis, but transforms the catastrophic deterioration previously seen at large radii in to a much more gradual reduction in accuracy due to the progressively earlier truncation of the mode-sum.

In Chapter 5 we apply our method to calculate the self-force along *near-critical* geodesics, which lie close to the transition between scattering and plunging behaviour. It is discovered that in the limit of high-velocities, the large-ℓ contributions to the self-force become increasingly significant in the vicinity of periapsis, modes which only our frequency-domain code can provide. A hybrid method is thus developed, utilising the frequency-domain code in the central region where it has high-precision access to the large-ℓ modes of the field, before transitioning to the time-domain code of Ref. [149] as the accuracy of the frequency-domain method falls at larger radii. We extract a certain parameter characterising the divergence of the scatter angle correction in the limit of the transition to plunge. This information is then used to inform a resummation of the post-Minkowskian expansion of the scatter angle, resulting in a semi-analytic model which is fast to evaluate and uniformly accurate across both the strong and weak field (at first-order in the scalar-field self-force expansion parameter).

Ongoing work to obtain analytical results for the self-force at early and late times along the orbit is discussed in Chapter 6. Chapter 7 then concludes this thesis with a summary of our successful progress towards frequency-domain self-force calculations along

scatter geodesics, and the limitations of our approach that still remain. Several avenues for future work are highlighted, and the broader direction of self-force scatter research (including the extension to gravity) is discussed briefly.

1.5.2 Summary of own contribution

Chapters 2-4 of this thesis are based upon my work, published in Ref. [159] with my supervisor Leor Barack. Chapter 2 contains primarily review material, except for the derivation of the frequency-domain solution with a scatter source in Sec. 2.4, which is my own original work. Chapters 3 and 4 are my own work.

Chapter 5 is based upon collaborative work with Oliver Long and Leor Barack, published in Ref. [160]. My primary contributions to this chapter were: the self-force calculation using the frequency-domain code, the development of the hybrid TD/FD approach, and the estimation of the singularity coefficient and its errors.

Chapter 6 is primarily my own original work, except for the review of the hierarchical expansion and its Green's function.

1.5.3 Conventions

Throughout this thesis we work in natural units with $G = 1 = c$ and metric signature $(-,+,+,+)$. The central object is represented by a background Schwarzschild spacetime of mass M, which, in Schwarzschild coordinates $x^\alpha = (t, r, \theta, \varphi)$, has the line element

$$ds^2 = -f(r)dt^2 + f(r)^{-1}dr^2 + r^2 d\Omega^2, \tag{1.20}$$

where $f(r) := 1 - 2M/r$, and $d\Omega^2 := d\theta^2 + \sin^2\theta\, d\varphi^2$ is the metric on a unit 2-sphere. The Levi-Civita connection compatible with this metric is denoted ∇_μ. The smaller object is described by a pointlike particle endowed with mass $\mu \ll M$ and "small" scalar charge $q \ll \sqrt{\mu M}$. Its trajectory is described by a worldline $x_p^\alpha(\tau)$ in the background spacetime, parameterized by proper time τ, with 4-velocity $u^\alpha(\tau) := dx_p^\alpha/d\tau$.

Chapter 2

Mathematical preliminaries

In this chapter we outline the mathematical details of our model and the key concepts and methods we will be using. Our first objective is to summarise timelike scatter geodesics in the Schwarzschild spacetime, describing different choices of orbital parameters and the means to convert between them. We will then give an overview of our scalar-field model, including a description of the method of mode-sum regularisation used to calculate the self-force. The self-force correction to the scatter angle is introduced, and its known properties reviewed. Finally, we derive the solution of the scalar-field equation sourced by a scalar charge moving along a scatter geodesic using frequency-domain techniques, highlighting the limitations of the standard method of extended homogeneous solutions when applied to the scatter problem.

2.1 Scatter geodesics in the Schwarzschild spacetime

In the test particle limit $\mu/M \to 0$ and $q^2/(\mu M) \to 0$, the small object moves along a timelike geodesic in the background Schwarzschild spacetime, which, without loss of generality, may be taken to lie in the equatorial plane, $\theta = \pi/2$. The timelike and azimuthal Killing vectors give rise to conserved quantities E (specific energy) and L (specific angular momentum), respectively given by

$$E = f(r_p)\dot{t}_p, \tag{2.1}$$

$$L = r_p^2\dot{\varphi}_p, \tag{2.2}$$

where overdots denote derivatives with respect to proper time. The normalisation of the 4-velocity, $u^\alpha u_\alpha = -1$, gives rise to an effective potential equation for the radial motion,

$$\dot{r}_p = \pm\sqrt{E^2 - V(r_p; L)}, \tag{2.3}$$

with effective potential

$$V(r;L) := f(r)\left(1+\frac{L^2}{r^2}\right). \tag{2.4}$$

We are interested in the scattering problem, in which $r_p \to \infty$ as $t \to \pm\infty$, which requires $E > 1$. Note that the 3-velocity at infinity, $v^i := \frac{dx_p^i}{dt}\big|_{r\to\infty}$ $(i = r, \theta, \phi)$, has magnitude

$$v := \sqrt{(v^r)^2 + ((rv^\varphi)_\infty)^2} = \frac{\sqrt{E^2-1}}{E}, \tag{2.5}$$

leading to

$$E = (1-v^2)^{-1/2}, \tag{2.6}$$

the standard Lorentz factor. The particle scatters back to infinity if, and only if, $L > L_{\rm c}(E)$, where

$$L_{\rm c}(E) = \frac{M}{Ev}\sqrt{(27E^4 + 9\nu E^3 - 36E^2 - 8\nu E + 8)/2}, \tag{2.7}$$

with $\nu := \sqrt{9E^2-8}$.

We may use the first integrals E and L to parameterise our orbit, or we may choose to replace L with the *impact parameter* b:

$$b := \lim_{\tau\to-\infty} r_p(\tau)\sin|\varphi_p(\tau) - \varphi_p(-\infty)| = \frac{L}{\sqrt{E^2-1}}. \tag{2.8}$$

Likewise, we may replace E with v using Eq. (2.6). The orbit (b, v) is then a scatter orbit provided

$$b > b_{\rm c}(E) := \frac{L_{\rm c}(E)}{\sqrt{E^2-1}}. \tag{2.9}$$

For a given $E > 1$ and $L > L_{\rm c}(E)$, the cubic equation

$$\dot{r}_p^2 = E^2 - V(r;L) = 0 \tag{2.10}$$

has three real roots r_1, r_2 and $r_{\rm min}$, with $r_1 < 0$ and $2M < r_2 < r_{\rm min}$. These are given explicitly by [161]

$$r_1 = \frac{6M}{1-2\zeta\sin\left(\frac{\pi}{6}+\xi\right)}, \tag{2.11}$$

$$r_2 = \frac{6M}{1+2\zeta\cos\xi}, \tag{2.12}$$

$$r_{\rm min} = \frac{6M}{1-2\zeta\sin\left(\frac{\pi}{6}-\xi\right)}, \tag{2.13}$$

where $\zeta := \sqrt{1 - 12M^2/L^2}$ and

$$\xi := \frac{1}{3} \arccos\left(\frac{1 + (36 - 54E^2)M^2/L^2}{\zeta^3}\right). \tag{2.14}$$

The root $r_{\min}$ is the periapsis radius for the orbit, and may be calculated from E and L using Eq. (2.13). At the same time, Eq. (2.10) allows one to determine L for a given $r_{\min}$ and $E > 1$. The pair $(E, r_{\min})$ provides an alternative parameterisation for the orbit.

The orbital turning points also give rise to another parameterisation, in terms of an eccentricity $e > 1$ and a semi-latus rectum p, defined by the relations

$$r_1 = \frac{Mp}{1 - e}, \quad r_{\min} = \frac{Mp}{1 + e}. \tag{2.15}$$

Substituting Eqs. (2.15) into Eq. (2.10) and solving for E and L, one finds the same relations as in the bound case,

$$E^2 = \frac{(p-2)^2 - 4e^2}{p(p - 3 - e^2)}, \qquad L^2 = \frac{p^2 M^2}{p - 3 - e^2}. \tag{2.16}$$

To invert Eqs. (2.16), it is easiest to first use Eq. (2.15) to write p in terms of $r_{\min}$ and e, and then solve the second equation in (2.16) to find

$$e = \frac{L^2 r_{\min} - 2M r_{\min}^2}{2M(L^2 + r_{\min}^2)} + \frac{\sqrt{L^4(r_{\min}^2 + 4M r_{\min} - 12M^2) - 16L^2M^2 r_{\min}^2}}{2M(L^2 + r_{\min}^2)}. \tag{2.17}$$

Using Eq. (2.13), we thus get $e(E, L)$, and hence also $p(E, L) = r_{\min}(1 + e)/M$ using Eq. (2.15).

With the (e, p) parameterisation, the radial motion is described in the familiar Keplerian-like form [162, 163],

$$r_p(\chi) = \frac{Mp}{1 + e\cos\chi}, \tag{2.18}$$

in terms of the relativistic anomaly χ. This anomaly takes values in $-\chi_\infty < \chi < \chi_\infty$, where $\chi_\infty := \arccos(-1/e)$ corresponds to the particle returning to infinity, and $\chi = 0$ corresponds to the periapsis passage. The (e, p) parameterisation is also convenient for calculating the other components of x_p^α, using χ as the parameter along the orbit. $t_p(\chi)$ can be obtained using Eqs. (2.1) and (2.3), and then substituting Eqs. (2.16) and (2.18):

$$\frac{dt_p}{d\chi} = \frac{\dot{t}_p}{\dot{r}_p}\frac{dr_p}{d\chi} = \frac{Mp^2}{(p - 2 - 2e\cos\chi)(1 + e\cos\chi)^2}\sqrt{\frac{(p-2)^2 - 4e^2}{p - 6 - 2e\cos\chi}}. \tag{2.19}$$

This equation can then be integrated numerically, subject to an initial condition, to give $t_p(\chi)$. In this work we chose to take $t_p = 0$ at periapsis ($\chi = 0$), which gives the

symmetry relation $t_p(-\chi) = -t_p(\chi)$. Similarly, we express

$$\frac{d\varphi_p}{d\chi} = \frac{\dot{\varphi}_p}{\dot{r}_p}\frac{dr_p}{d\chi}, \tag{2.20}$$

which, using Eqs. (2.2) and (2.3) and then substituting from Eqs. (2.16) and (2.18), gives

$$\frac{d\varphi_p}{d\chi} = \sqrt{\frac{p}{p-6-2e\cos\chi}}. \tag{2.21}$$

We can integrate this up to give

$$\varphi_p(\chi) = 2\sqrt{\frac{p}{p-6-2e}}\int_0^{\chi/2}\frac{d\theta}{\sqrt{1+k^2\sin^2\theta}} \tag{2.22}$$

$$= k\sqrt{\frac{p}{e}}\,\mathsf{EI}_1\left(\frac{\chi}{2}, -k^2\right), \tag{2.23}$$

where $k^2 := 4e/(p-6-2e)$, and $\mathsf{EI}_1(\phi, z)$ is the incomplete elliptic integral of the first kind with parameter z:

$$\mathsf{EI}_1(\phi, z) = \int_0^{\phi}\frac{d\theta}{\sqrt{1-z\sin^2\theta}}. \tag{2.24}$$

Note that we selected the initial condition $\varphi_p(\chi = 0) = 0$, which once again gives rise to a symmetry, $\varphi_p(-\chi) = -\varphi_p(\chi)$.

We define $\varphi_{\rm in}$ and $\varphi_{\rm out}$ to be the asymptotic values of φ_p as $\chi \to -\chi_\infty$ and $\chi \to \chi_\infty$ respectively. The *scatter angle* is then defined to be

$$\delta\varphi := \varphi_{\rm out} - \varphi_{\rm in} - \pi, \tag{2.25}$$

which for a geodesic trajectory is given by

$$\delta\varphi = 2k\sqrt{\frac{p}{e}}\,\mathsf{EI}_1\left(\frac{\chi_\infty}{2}, -k^2\right) - \pi. \tag{2.26}$$

Here we used Eq. (2.23) along with the identity $\mathsf{EI}_1(-\phi, z) = -\mathsf{EI}_1(\phi, z)$.

Finally, using r as a parameter along the outbound leg of the orbit ($\dot{r}_p > 0$), the relations $t_p(r)$ and $\varphi_p(r)$ admit useful large-r expansions in $1/r$. For example, for t_p we find

$$t_p(r) = t_0 + \frac{r}{v} + 2MB\log\left(\frac{r}{2M}\right) + 2M\sum_{n=1}^{\infty}C_n\left(\frac{2M}{r}\right)^n \tag{2.27}$$

as $r \to \infty$, where the constants B and C_n are given analytically in terms of E and L in Appendix A for $n \leq 5$. The constant t_0 is fixed by the boundary condition $t_p(r_{\rm min}) = 0$.

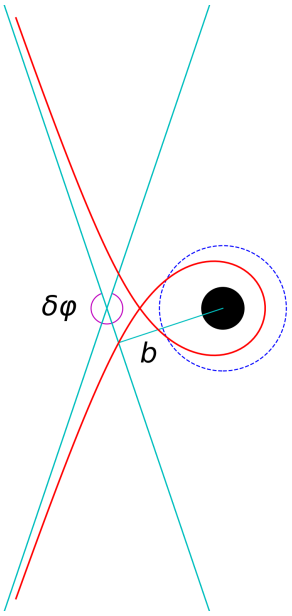

FIGURE 2.1: Geometric interpretation of the impact parameter b and the scatter angle $\delta\varphi$ (modulo 2π). The geodesic orbit displayed here has $E = 1.1$ and $r_{\rm min} = 4M$, corresponding to $L \approx 4.7666M$, $b \approx 10.4015M$, $v \approx 0.4166$, $e \approx 1.6273$ and $p \approx 10.5092$. The scatter angle is $\delta\varphi \approx 323°$. The view is in the equatorial plane, plotted on axes $x = r\cos\varphi$ and $y = r\sin\varphi$. The black hole (black disk) and the innermost stable circular orbit (blue circle) are to scale.

Likewise,

$$\varphi_p(r) = \varphi_\infty + \sum_{n=1}^{\infty} D_n \left(\frac{2M}{r}\right)^n \tag{2.28}$$

as $r \to \infty$, where $\varphi_\infty := \varphi_{\rm out} = -\varphi_{\rm in}$. The constants D_n are given analytically in Appendix A. Expressions along the inbound leg of the orbit may be obtained by using the symmetry relations $t_p(\chi) = -t_p(-\chi)$ and $\varphi_p(\chi) = -\varphi_p(-\chi)$. We will also make use of the large-r expansion for the radial component of the 4-velocity,

$$\left(\frac{dr_p}{d\tau}\right)^{-1} = \sum_{n=0}^{\infty} U_n \left(\frac{2M}{r}\right)^n , \tag{2.29}$$

as $r \to \infty$, where the first few coefficients U_n are given in Appendix A.

Above we have introduced several alternative parameterisations for scattering geodesics, and described the means to convert between them. In this thesis we will primarily make use of the $(E, r_{\rm min})$ and (v, b) parameterisations. The $(E, r_{\rm min})$ parameterisation is convenient because it allows one to control how relativistic the particle motion is at infinity (by varying E), and also how deep the orbit penetrates into the strong-field region (by varying $r_{\rm min}$). We will make use of this pair primarily when developing and demonstrating our numerical method. On the other hand, the parameters (v, b), being

defined as quantities at infinity (and hence free of gauge ambiguities in the gravitational problem), are the most convenient to use when considering the physical effects of the self-force. In particular, in Sec. 2.3 we will define the self-force correction to the scatter angle at fixed values of (v, b). Whichever parameterisation is used to describe an orbit, we will calculate and use the corresponding values of all parameters E, $r_{\min}$, v, b, L, e and p. A sample scattering orbit, with parameters $E = 1.1$ and $r_{\min} = 4M$, is depicted in Fig. 2.1.

2.2 Scalar-field model

In this section we will present the details of the scalar-field model, including the governing field equations and the definition of the scalar-field self-force. We will then summarise the standard method of mode-sum regularisation used to calculate the self-force from spherical harmonic modes of the retarded field, and also define the conservative and dissipative pieces of the self-force.

2.2.1 Scalar-field self force

The particle sources a scalar field Φ, which we assume is massless and minimally coupled. This field obeys the Klein-Gordon equation on the background Schwarzschild spacetime,

$$\nabla_\mu \nabla^\mu \Phi = -4\pi T, \tag{2.30}$$

where the scalar charge density is

$$T\left(x^\alpha\right) := q \int_{-\infty}^{+\infty} \delta^4\left(x^\alpha - x_p^\alpha(\tau)\right) \frac{d\tau}{\sqrt{-g(x)}}, \tag{2.31}$$

with g being the determinant of the Schwarzschild metric.

In analogy with Eq. (1.10), the full (retarded) scalar field may be decomposed as

$$\Phi = \Phi^R + \Phi^S, \tag{2.32}$$

where Φ^R and Φ^S are the Detweiler-Whiting regular and singular fields respectively, introduced in [109]. The regular field Φ^R is a certain vacuum solution to the scalar field equation, smooth everywhere, including at the particle's location. The singular field Φ^S is a particular solution of Eq. (2.30), singular at the worldline. Interaction with its own scalar field modifies the particle's trajectory according to [164]

$$u^\nu \nabla_\nu \left(\mu u^\mu\right) = q \nabla^\mu \Phi^R. \tag{2.33}$$

Note that we have not included the gravitational self-force acting on the particle, nor the effect of the scalar field's backreaction on the background spacetime.

We refer to the quantity on the right-hand side of Eq. (2.33) as the *scalar-field self-force*,

$$F^{\alpha}_{\rm self} := q\nabla^{\alpha}\Phi^{R} \propto q^2. \tag{2.34}$$

The singular field Φ^S does not appear; the self-force arises due to the interaction between the particle and its regular field only. Furthermore, the derivative on the right-hand side is not generically orthogonal to the 4-velocity, u^{μ}. The implications of this become clear if one splits Eq. (2.33) into parts parallel and perpendicular to u^{α}:

$$\frac{d\mu}{d\tau} = -qu_{\mu}\nabla^{\mu}\Phi^{R}, \tag{2.35}$$

$$\mu u^{\nu}\nabla_{\nu}u^{\mu} = q\left(g^{\mu\nu} + u^{\mu}u^{\nu}\right)\nabla_{\nu}\Phi^{R}. \tag{2.36}$$

From this we see that the component parallel to u^{α} is responsible for a variation in the particle's rest mass. Equation (2.35) can be integrated to give

$$\mu(\tau) = \mu_0 - q\Phi^{R}(\tau), \tag{2.37}$$

where μ_0 is a constant of integration. It is expected that $\Phi^R(-\infty) = \Phi^R(\infty)$, in which case there is no net mass change overall. Equation (2.36), meanwhile, can be rewritten as

$$u^{\nu}\nabla_{\nu}u^{\mu} = \eta_q F^{\mu}_{\perp}, \tag{2.38}$$

where $\eta_q := q^2/(\mu M) \ll 1$, and the perpendicular components of the self-force are defined by

$$\eta_q F^{\mu}_{\perp} := \frac{q}{\mu}\left(g^{\mu\nu} + u^{\mu}u^{\nu}\right)\nabla_{\nu}\Phi^{R}. \tag{2.39}$$

$F^{\mu}_{\perp}$ gives rise to the self-acceleration that alters the trajectory.

The purpose of this thesis is to use Eq. (2.33) to calculate the self-force that would be felt by a scalar charge moving along a fixed hyperbolic geodesic in a Schwarzschild background. Therefore, from now on it is to be understood that $x^{\alpha}_{p}(\tau)$ refers specifically to such a geodesic.

2.2.2 Mode-sum regularisation

The self-force will be calculated using the mode-sum regularisation procedure originally introduced by Barack and Ori for the scalar-field self-force in Ref. [165], and extended to the full gravitational self-force problem in Ref. [166]. As a first step to describe this

method, we use Eq. (2.32) to recast Eq. (2.33) as the *subtraction formula*,

$$F_\alpha^{\rm self}(\tau) = q \lim_{x\to x_p(\tau)} \left(\nabla_\alpha \Phi(x) - \nabla_\alpha \Phi^{\rm S}(x)\right) \tag{2.40}$$

Note that, unlike Φ^R, the fields Φ and Φ^S are individually divergent at the wordline and hence we must introduce this (well-defined) limit. The difficulty in a practical implementation of Eq. (2.40) is the need to take the limit of the difference of two divergent quantities. The mode-sum method resolves this issue by decomposing in a basis of spherical harmonics and performing the subtraction mode by finite mode.

More precisely, we rewrite Eq. (2.40) as

$$F_\alpha^{\rm self}(\tau) = \lim_{x\to x_p(\tau)} \left[F_\alpha^{\rm full}(x) - F_\alpha^{\rm S}(x)\right], \tag{2.41}$$

where the new fields are defined by

$$F_\alpha^{\rm full}(x) := q\nabla_\alpha \Phi(x), \quad F_\alpha^{\rm S}(x) := q\nabla_\alpha \Phi^S(x). \tag{2.42}$$

The fields $F_\alpha^{\rm full}$ and $F_\alpha^{\rm S}$ are divergent as $x \to x_p(\tau)$, but their difference is a smooth (in fact, analytic) function of x, even at the worldline. Working in Schwarzschild coordinates, we can treat each component as a scalar function and decompose into spherical harmonics defined on constant t, r surfaces in Schwarzschild coordinates:

$$F_\alpha^{\rm full/S}(x^\mu) = \sum_{\ell m} F_{\alpha,\ell m}^{\rm full/S}(t,r) Y_{\ell m}(\theta,\varphi). \tag{2.43}$$

The ℓ-mode contributions to the forces are defined by summing over m,

$$F_{\alpha,\ell}^{\rm full/S}(x) := \sum_{m=-\ell}^{\ell} F_{\alpha,\ell m}^{\rm full/S}(t,r) Y_{\ell m}(\theta,\varphi), \tag{2.44}$$

and they are finite, even at the worldline [165]. Equation (2.41) becomes

$$F_\alpha^{\rm self}(\tau) = \lim_{x\to x_p(\tau)} \sum_{\ell=0}^{\infty} \left[F_{\alpha,\ell}^{\rm full}(x) - F_{\alpha,\ell}^{\rm S}(x)\right]. \tag{2.45}$$

Since $F_\alpha^{\rm full}(x) - F_\alpha^{\rm S}(x)$ is a smooth function for all x, this sum is exponentially and uniformly convergent, even at $x = x_p(\tau)$. This allows us to exchange the order of the sum and limit, giving

$$F_\alpha^{\rm self}(\tau) = \sum_{\ell=0}^{\infty} \left[F_{\alpha,\ell}^{\rm full\pm}(x_p(\tau)) - F_{\alpha,\ell}^{\rm S\pm}(x_p(\tau))\right], \tag{2.46}$$

where the $\pm$ denotes whether the limit is taken from outside ($r \to r_p(\tau)^+$) or inside ($r \to r_p(\tau)^-$) the orbit. Note that the difference $F_{\alpha,\ell}^{\rm full\pm}(x_p(\tau)) - F_{\alpha,\ell}^{\rm S\pm}(x_p(\tau))$ does not

exhibit this directional ambiguity.

It can be shown that $F^{\rm S}_{\alpha,\ell}$ has the large-ℓ behaviour, [165]

$$F^{\rm S\pm}_{\alpha,\ell} = \mathcal{L}A^{\pm}_{\alpha} + B_\alpha + C_\alpha/\mathcal{L} + O\left(\mathcal{L}^{-2}\right), \tag{2.47}$$

where $\mathcal{L} := \ell + \frac{1}{2}$ and once again the positive (negative) sign is taken when the limit is taken from outside (inside) the orbit. Note that, by smoothness, the mode sum in Eq. (2.46) is expected to converge exponentially, and hence $F^{\rm full}_{\alpha,\ell}$ and $F^{\rm S}_{\alpha,\ell}$ must share the same large-ℓ expansion (2.47). Thus we rewrite Eq. (2.46) in the form

$$\begin{aligned} F^{\rm self}_{\alpha}(\tau) = \sum_{\ell=0}^{\infty}\Big[F^{\rm full\pm}_{\alpha,\ell}(x_p(\tau)) - \mathcal{L}A^{\pm}_{\alpha} - B_\alpha - C_\alpha/\mathcal{L}\Big] \\ - \sum_{\ell=0}^{\infty}\Big[F^{\rm S\pm}_{\alpha,\ell}(x_p(\tau)) - \mathcal{L}A^{\pm}_{\alpha} - B_\alpha - C_\alpha/\mathcal{L}\Big], \end{aligned} \tag{2.48}$$

where we have been able to split into two individually convergent sums. To be precise, the terms in each of the two series decay like $1/\mathcal{L}^2$ at large $\mathcal{L}$, and hence converge like $1/\ell$ overall. We thus arrive at the following *mode-sum* expression for the self-force

$$F^{\rm self}_{\alpha}(\tau) = \sum_{\ell=0}^{\infty}\Big[F^{\rm full\pm}_{\alpha,\ell}(x_p(\tau)) - \mathcal{L}A^{\pm}_{\alpha} - B_\alpha - C_\alpha/\mathcal{L}\Big] - D_\alpha, \tag{2.49}$$

where

$$D^{\alpha} := \sum_{l=0}^{\infty}\Big[F^{\alpha,l}_{S\pm}(x_p(\tau)) - \mathcal{L}A^{\alpha}_{\pm} - B^{\alpha} - C^{\alpha}/\mathcal{L}\Big]. \tag{2.50}$$

The ℓ-independent quantities $A^{\pm}_{\alpha}$, B_α, C_α and D_α are called the *regularisation parameters*.

Analytical expressions for the scalar field regularisation parameters in Schwarzschild were first derived in [167]. The non-vanishing components are:

$$A^{\pm}_{t} = \pm\frac{q^2\dot{r}_p}{(L^2+r_p^2)}, \qquad B_t - \frac{q^2 E r_p \dot{r}_p}{\pi(L^2+r_p^2)^{3/2}}(2\mathcal{E}-\mathcal{K}), \tag{2.51}$$

$$A^{\pm}_{r} = \mp\frac{q^2 E}{(1-2M/r_p)(L^2+r_p^2)}, \qquad B_r = \frac{q^2(\dot{r}_p^2-2E^2)\mathcal{K} + (\dot{r}_p^2+E^2)\mathcal{E}}{\pi r_p^2(1-2M/r_p)(1+L^2/r_p^2)^{3/2}}, \tag{2.52}$$

$$B_\varphi = \frac{q^2 r_p \dot{r}_p(\mathcal{K}-\mathcal{E})}{\pi L(r_p^2+L^2)^{1/2}}, \tag{2.53}$$

where $\mathcal{K} := \mathsf{EI}_1\big(\pi/2;\ L^2/(L^2+r_p^2)\big)$ (recalling EI_1 is the incomplete elliptic integral of the first kind, defined in Eq. (2.24)), and $\mathcal{E} := \mathsf{EI}_2\big(\pi/2;\ L^2/(L^2+r_p^2)\big)$, where

$$\mathsf{EI}_2(\phi, z) = \int_0^{\phi}\sqrt{1 - z\sin^2\theta}\, d\theta. \tag{2.54}$$

is the incomplete elliptic integral of the second kind. Note that $C_\alpha = D_\alpha = 0$ for a scalar field in the Schwarzschild spacetime.

The summand in Eq. (2.49) decays like $O(\ell^{-2})$, leaving a truncation error of $O(\ell_{\rm max}^{-1})$ when (in practical calculations) the mode-sum is truncated at $\ell = \ell_{\rm max}$. Fundamentally, this decay rate indicates the smoothness of the field we are reconstructing; the terms in the sum of Eq. (2.49) are not the ℓ-modes of $q\nabla_\alpha\Phi^{\rm R}$ (which decay exponentially due to the analyticity of the regular field), but rather the ℓ-modes of the regular field plus a piece of the singular field which vanishes on the worldline. To understand why, note that the form (2.47) is derived using a local expansion of $\Phi^{\rm S}$ in powers of the distance ϵ from the worldline, with the displayed terms accounting only for the terms up to and including $O(\epsilon^0)$ in $F_\alpha^{\rm S}(x)$ [167]. After subtracting the $A_\alpha^\pm$, B_α and C_α terms in the mode-sum (2.49), therefore, we leave behind pieces corresponding to the vanishing terms $\propto \epsilon^{n>0}$ in the local expansion of $F_\alpha^{\rm S}$. The ℓ-modes of the vanishing terms do not contribute to the SF, giving zero when summed over ℓ, but they decay only polynomially in ℓ and hence dominate the summand in Eq. (2.49) at large-ℓ. It has been shown that the higher-order terms in Eq. (2.47) may be written in the convenient form [168]

$$\frac{F_\alpha^{[2]}}{\left(\ell-\frac{1}{2}\right)\left(\ell+\frac{3}{2}\right)} + \frac{F_\alpha^{[4]}}{\left(\ell-\frac{3}{2}\right)\left(\ell-\frac{1}{2}\right)\left(\ell+\frac{3}{2}\right)\left(\ell+\frac{5}{2}\right)} + \cdots , \tag{2.55}$$

where the coefficients $F_\alpha^{[2n]}$ are known as *higher-order regularisation parameters*. The form of the polynomial terms in the denominators of Eq. (2.55) ensures that each term sums to zero individually in the sum over ℓ. By additionally subtracting the higher order parameters in the mode-sum (2.49), one can thus accelerate the convergence of the sum without altering its value [168]; if terms up to and including $F_\alpha^{[2n]}$ have been subtracted, the terms in the mode sum decay like $O\left(\ell^{-(2n+2)}\right)$, and the truncation error is $O\left(\ell_{\rm max}^{-(2n+1)}\right)$. Taking advantage of high-order local expansions for the Detweiler-Whiting singular field, the higher order regularisation parameters $F_\alpha^{[2n]}$ have been derived analytically for $n = 1, 2$ and 3 for the scalar-field self-force along generic geodesic orbits in the Schwarzschild spacetime [169, 170].

2.2.3 Conservative and dissipative forces

When considering the physical effects of the self-force, it can be convenient to decompose it into "conservative" (time-symmetric) and "dissipative" (time-antisymmetric) pieces,

$$F_\alpha^{\rm self} = F_\alpha^{\rm cons} + F_\alpha^{\rm diss} \tag{2.56}$$

[64, 171], defined by

$$F_\alpha^{\rm cons} = \frac{1}{2}\left[F_\alpha^{\rm self(ret)} + F_\alpha^{\rm self(adv)}\right], \tag{2.57}$$

$$F_\alpha^{\rm diss} = \frac{1}{2}\left[F_\alpha^{\rm self(ret)} - F_\alpha^{\rm self(adv)}\right]. \tag{2.58}$$

Here $F_\alpha^{\rm self(ret)}$ is the usual self-force constructed from the retarded scalar field, and $F_\alpha^{\rm self(adv)}$ is the self-force constructed in the same way the scalar field obeying advanced boundary conditions.

Helpfully, thanks to the symmmetries of Kerr geodesics, we do not have to actually calculate the advanced scalar field in order to calculate the conservative and dissipative pieces of the self-force. Treating the self-force as a function of the particle's four velocity at the evaluation point, it may be shown that [64]

$$F_\alpha^{\rm self(adv)}\left(\dot{t}_p, \dot{r}_p, \dot{\theta}_p, \dot{\varphi}_p\right) = \epsilon_\alpha F_\alpha^{\rm self(ret)}\left(\dot{t}_p, -\dot{r}_p, -\dot{\theta}_p, \dot{\varphi}_p\right), \tag{2.59}$$

where $\epsilon_\alpha = (-1, 1, 1, -1)$ in Boyer-Linqduist coordinates and there is no sum over α on the right hand side. For a particle moving along a Kerr geodesic that is either equatorial or inclined-circular, the orbital symmetries then allow us to rewrite Eq. (2.59) as a relation between the retarded and advanced forces along the geodesic, [64, 172]

$$F_\alpha^{\rm self(adv)}(\tau) = \epsilon_\alpha F_\alpha^{\rm self(ret)}(-\tau), \tag{2.60}$$

where we assumed the periapsis is at $\tau = 0$ for eccentric orbits. Note that all Schwarzschild geodesics may be taken to be equatorial, so Eq. (2.60) holds for all Schwarzschild geodesics, including our hyperbolic orbits. The use of the Kerr geodesic symmetries in this context was first noted by Mino in Ref. [172], where he showed that what we now call the dissipative force gives the correct time-averaged radiation-reaction force acting on a particle orbiting a Kerr black hole. Barack and Sago were the first to propose Eq. (2.60) as a practical method to compute the advanced, and hence conservative, force in Ref. [173], using it for their calculation of the conservative gravitational self-force shift to the ISCO around a Schwarzschild black hole.

The mode sums for the advanced and retarded self-force give mode sums for the conservative and dissipative pieces of the force [171],

$$F_\alpha^{\rm cons} = \sum_{\ell=0}^{\infty}\left[F_{\alpha,\ell}^{\rm full(cons)\pm} - \mathcal{L}A_\alpha^\pm - B_\alpha\right], \tag{2.61}$$

$$F_\alpha^{\rm diss} = \sum_{\ell=0}^{\infty} F_{\alpha,\ell}^{\rm full(diss)\pm}, \tag{2.62}$$

where, recall, $\mathcal{L} := \ell + \frac{1}{2}$ and

$$F^{\text{full(cons)}\pm}_{\alpha,\ell} = \frac{1}{2}\left[F^{\text{full(ret)}\pm}_{\alpha,\ell} + F^{\text{full(adv)}\pm}_{\alpha,\ell}\right], \tag{2.63}$$

$$F^{\text{full(diss)}\pm}_{\alpha,\ell} = \frac{1}{2}\left[F^{\text{full(ret)}\pm}_{\alpha,\ell} - F^{\text{full(adv)}\pm}_{\alpha,\ell}\right]. \tag{2.64}$$

In particular, we note that the terms in the mode-sum for F^{cons}_{α} require regularisation (with the same parameters) and decay at the same rate as the total self-force, while F^{diss}_{α} does not require regularisation and the mode sum converges exponentially [171]. The convergence of the mode sum for the conservative piece may be accelerated by subtracting higher-order regularisation parameters in the same way as for the total self-force.

2.3 First-order self-force correction to the scatter angle

The primary observable of interest is the scatter angle $\delta\varphi$. It was shown in Ref. [149] that the scatter angle admits a self-force expansion,

$$\delta\varphi = \delta\varphi^{(0)} + \eta_q \delta\varphi^{(1)} + O(\eta_q^2), \tag{2.65}$$

where $\delta\varphi^{(0)}$ is the geodesic scatter angle given in Eq. (2.26), and

$$\delta\varphi^{(1)} = \int_{-\chi_\infty}^{\chi_\infty} \left[\mathcal{G}_E(\chi) F_t^{\perp}(\chi) - \mathcal{G}_L(\chi) F_\varphi^{\perp}(\chi)\right] \tau_\chi d\chi \tag{2.66}$$

is the first-order self-force (1SF) correction to the scatter angle. In Eq. (2.66), $\tau_\chi := dt/d\chi$ is evaluated along the background geodesic and $F^{\perp}_{\alpha}$ is the projected self-force (as defined in Eq. (2.39)) that would be felt by a particle moving along the background geodesic. The functions $\mathcal{G}_{E/L}(\chi)$ are expressed in terms of the orbital parameters e and p of the background geodesic, and are the same for both the gravitational and scalar-field self-force; explicit expressions may be found in Sec. IV A of Ref. [149].

The relations between orbital parameters derived in Chapter 2.1 are only valid for geodesic orbits, so when expanding the self-force as in Eq. (2.65), it is important to be clear which pair of orbital parameters are being taken to be fixed. Fixing different choices of parameters yields different values of $\delta\varphi^{(1)}$. In Ref. [149], the parameters (v, b) are taken to be fixed, and Eq. (2.66) is correct for this convention.

It is possible to consider the effects of the conservative and dissipative self-force separately,

$$\delta\varphi^{(1)} = \delta\varphi^{(1)}_{\text{cons}} + \delta\varphi^{(1)}_{\text{diss}}, \tag{2.67}$$

where [149]

$$\delta\varphi^{(1)}_{\rm cons} = \int_0^{\chi_\infty} \left[\mathcal{G}^{\rm cons}_E(\chi) F_t^{\perp\rm cons}(\chi) - \mathcal{G}^{\rm cons}_L(\chi) F_\varphi^{\perp\rm cons}(\chi)\right] \tau_\chi d\chi, \tag{2.68}$$

$$\delta\varphi^{(1)}_{\rm diss} = \int_0^{\chi_\infty} \left[-\alpha_E E_\infty F_t^{\perp\rm diss}(\chi) + \alpha_L L_\infty F_\varphi^{\perp\rm diss}(\chi)\right] \tau_\chi d\chi, \tag{2.69}$$

and explicit forms of the functions $\mathcal{G}^{\rm cons}_{E/L}(\chi)$ and *constants* $\alpha_{E/L}$ may be found in Sec. IV B of Ref. [149]. Notice that, using the symmetries $F_\alpha^{\perp\rm cons}(\chi) = -F_\alpha^{\perp\rm cons}(-\chi)$ and $F_\alpha^{\perp\rm diss}(\chi) = F_\alpha^{\perp\rm diss}(-\chi)$ for $\alpha = t, \varphi$, it was possible to express Eqs. (2.68) & (2.69) as integrals along the outbound leg $\chi > 0$ only. Notice also that Eq. (2.69) is expressed in terms of E_∞ and L_∞, respectively the energy and angular momentum as $\tau \to -\infty$; under the action of the self-force, the energy and angular momentum cease to be constants of the motion. It is easily shown (for example in Sec. III of Ref. [149]) that, including the first order self-force, the energy and angular momentum evolve along the orbit according to

$$E(\chi) = E_\infty - \eta_q \int_{-\chi_\infty}^{\chi} F_t^\perp(\chi')\tau_\chi d\chi', \qquad L(\chi) = L_\infty + \eta_q \int_{-\chi_\infty}^{\chi} F_\varphi^\perp(\chi')\tau_\chi d\chi'. \tag{2.70}$$

Equation (2.69) may thus be rewritten as [149]

$$\delta\varphi^{(1)}_{\rm diss} = \frac{1}{2}\left(\alpha_E E_\infty E_{\rm rad} + \alpha_L L_\infty L_{\rm rad}\right), \tag{2.71}$$

where

$$E_{\rm rad} := -\int_{-\chi_\infty}^{+\chi_\infty} F_t^{\perp\rm diss}\tau_\chi d\chi, \qquad L_{\rm rad} := \int_{-\chi_\infty}^{+\chi_\infty} F_\varphi^{\perp\rm diss}\tau_\chi d\chi \tag{2.72}$$

are the total energy and angular momentum (per unit q^2/M) dissipated in gravitational waves respectively. Analogous results relating dissipative scatter angle effects to the total radiated energy and angular momentum have previously been derived in other perturbative approaches, notably PN [174] and PM [175].

The first numerical calculations of $\delta\varphi^{(1)}$ were carried out by Barack and Long in Ref. [149] using their time-domain numerical platform to calculate the scalar-field self-force. Example results, plotted as a function of b at fixed velocity $v = 0.2$, are displayed in Fig. 2.2. Several key features are immediately visible. First, the dissipative piece of the scatter angle correction is always found to be positive, while the conservative piece is always negative. It was expected that $\delta\varphi^{(1)}_{\rm diss}$ should be positive, because the effect of the dissipative self-force is to remove energy and angular momentum from the system, driving the particle deeper into the potential of the central black hole for longer, and hence increase the total deflection. The sign of $\delta\varphi^{(1)}_{\rm cons}$ was, however, not predicted on physical grounds a priori. We note that the first-order gravitational SF correction to the *periastron advance* for bound Schwarzschild geodesics was also found to be negative in Ref. [176], although comparisons are complicated by the different parameterisations

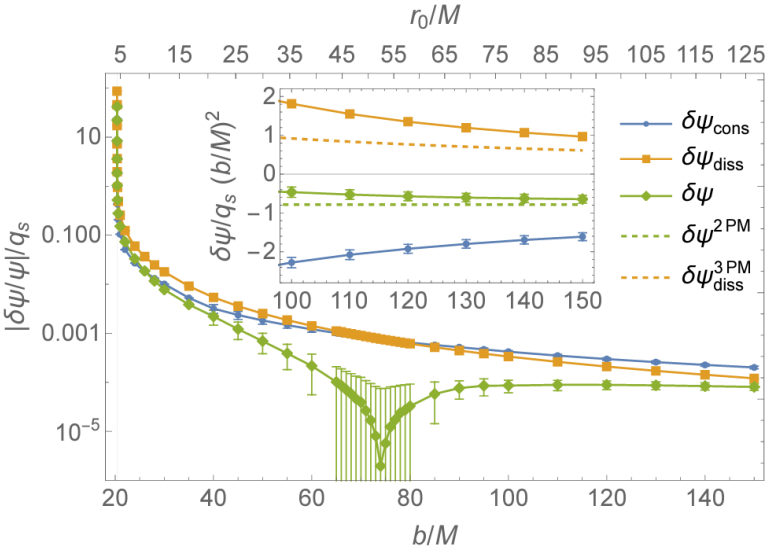

FIGURE 2.2: Example 1SF scatter angle correction results from Ref. [149], displayed as a function of b (lower axis) or $r_{\rm min}$ (upper axis) at fixed $v = 0.2$. Total, conservative and dissipative angles are displayed separately. In the notation of this thesis, $\psi = \delta\varphi^{(0)}$, $\delta\psi = \eta_q \delta\varphi^{(1)}$, $q_s = \eta_q$ and $r_0 = r_{\rm min}$. *Inset:* Magnified view of the PM regime $bv^2 \gg M$, comparing the numerical results to the analytical 2PM total and 3PM dissipative results. Image credit: [149]

used: the periastron advance correction was calculated at fixed (e, p), and the scatter angle correction at fixed (v, b). Second, we note that although the (positive) dissipative piece dominates over the (negative) conservative piece at small values of b, the dissipative decays more rapidly at large b and hence eventually the conservative piece becomes dominant. A consequence of this is that the total $\delta\varphi^{(1)}$ changes sign at an intermediate value of b. Finally, the total, conservative and dissipative scatter corrections all diverge in the limit $b \to b_c$, at a rate that was found to be [149]

$$\delta\varphi^{(1)} \sim \frac{1}{b - b_c}. \tag{2.73}$$

We will revisit this divergence in Chapter 5.

2.3.1 PM expansion of $\delta\varphi^{(1)}$

As mentioned in Chapter 1.4, comparisons with post-Minkowskian results are an important motivation for the self-force scattering programme. It is helpful therefore to introduce the PM expansion of $\delta\varphi^{(1)}$:

$$\delta\varphi^{(1)} = \sum_{k=2}^{\infty} \delta\varphi^{(1,k)}(v) \left(\frac{GM}{b}\right)^k, \tag{2.74}$$

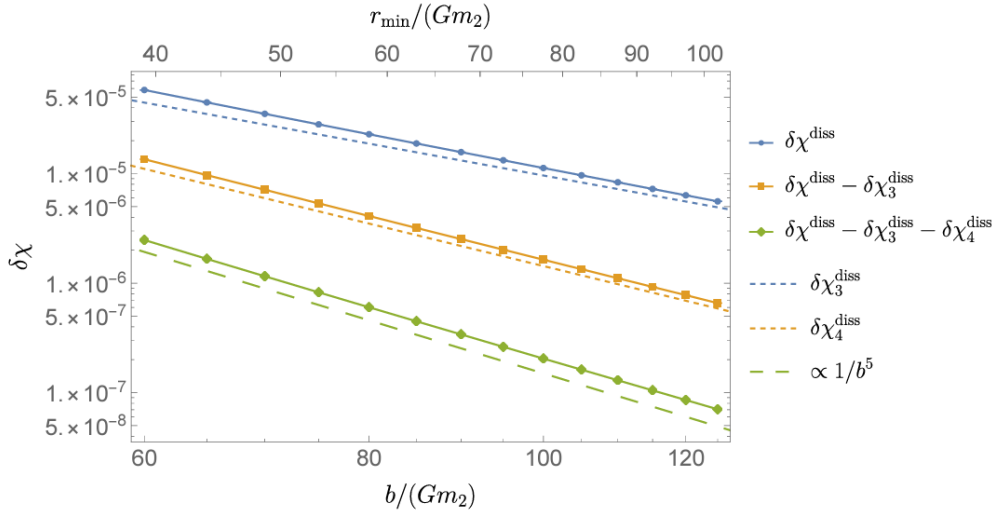

FIGURE 2.3: Comparison between numerical dissipative self-force scatter angle results and successive analytic PM approximations from Ref. [151]. The corrections are plotted as a function of b (lower axis) or $r_{\rm min}$ (upper axis) at fixed velocity $v = 0.5$. The numerical values for $\delta\varphi^{(1)}_{\rm diss}$ (blue dots) approach the 3PM prediction (blue dashed) as b increases. Subtracting the 3PM approximation results in a residual which approaches the analytic result for the 4PM term. Further subtracting this 4PM term results in a residual which decays at the expected 5PM ($\propto 1/b^5$) rate. In the notation of this thesis, $m_2 = M$, $\delta\chi = \delta\varphi^{(1)}$ and $\delta\chi^{\rm diss}_k = \delta\varphi^{(1,k)}_{\rm diss}(GM/b)^k$. Image credit: [151]

and analogous expansions for $\delta\varphi^{(1)}_{\rm cons/diss}$. We have temporarily re-introduced factors of G (previously set to unity) to aid power counting and enable comparisons with the PM results. For the scalar-field self-force, the leading-order non-zero coefficients are found to be

$$\delta\varphi^{(1,2)}_{\rm cons} = -\frac{\pi}{4}, \tag{2.75}$$

$$\delta\varphi^{(1,3)}_{\rm diss} = \frac{2E}{3}\frac{(1+v^2)^2}{v^3}, \tag{2.76}$$

i.e. the effect of the dissipative self-force enters the scatter angle only at 3PM order, explaining the more rapid decay observed for that piece in Fig. 2.2. The expression in Eq. (2.75) was first derived in Ref. [150], and Eq. (2.76) was first derived in Ref. [149] by substituting expressions for the PM-expanded self-force from [150] into (a PM expanded form of) Eq. (2.69). Numerical values of $\delta\varphi^{(1)}$ at large impact parameter and fixed $v = 0.2$ are compared to the 2PM (purely conservative) piece of $\delta\varphi^{(1)}$, and to the 3PM piece of $\delta\varphi^{(1)}_{\rm diss}$, in the inset of Fig. 2.2, showing increasing agreement with growing b.

Subsequently, expressions for $\delta\varphi^{(1,k)}_{\rm cons/diss}$ were derived up to and including 4PM order (i.e. $k = 4$) in Ref. [151], making use of quantum amplitude techniques. These were compared to numerical scalar-field self-force results at large impact parameters (again obtained using the time-domain platform of Ref. [149]), with good agreement found through 4PM order [151] – see Fig. 2.3 for an illustration. The analytical result for $\delta\varphi^{(1,4)}_{\rm cons}$ originally

obtained in [151] contained two undetermined constant parameters, which they calibrated against the numerical self-force data, demonstrating the capacity for numerical self-force calculations to resolve ambiguities in analytical results. The coefficients have more recently been determined through two independent methods: Matching of amplitude calculations in effective-field theory and black hole perturbation theory [177]; and a double PM/PN expansion of the self-force [178]. Expressions for all analytically known PM coefficients $\delta\varphi^{(1,k)}_{\text{cons/diss}}$ are given in Appendix B. These will be required when we explore the use of self-force to calibrate PM results in the strong field in Chapter 5.

2.4 Frequency-domain solution for the scalar field with a scattering source

In this section we solve the scalar field equation (2.30) with the source (2.31) corresponding to a scalar charge moving along a fixed scatter geodesic. We begin by fully decomposing the field and source into combined angular- and time-harmonic modes, and derive the ordinary differential equation they satisfy. The inhomogeneous solution obeying retarded boundary conditions is then constructed, and it is explained why, due to issues of slow convergence, this solution is not suitable for our self-force calculation. The method of extended homogeneous solutions is introduced to resolve this issue, but it is noted that, for a scattering source, this method may only be used to reconstruct the time-domain field in the region $r \leq r_p(t)$.

2.4.1 Mode decomposition

As a first step towards the solution of the scalar field equation (2.30), the scalar field and scalar charge density are decomposed into a basis of spherical harmonics $Y_{\ell m}(\theta, \varphi)$ defined on surfaces of constant t and r around the central black hole,

$$\Phi = \sum_{\ell m} \frac{1}{r} \psi_{\ell m}(t, r) Y_{\ell m}(\theta, \varphi), \tag{2.77}$$

$$T = \sum_{\ell m} T_{\ell m}(t, r) Y_{\ell m}(\theta, \varphi). \tag{2.78}$$

Equation (2.30) then becomes

$$-\frac{\partial^2 \psi_{\ell m}}{\partial t^2} + \frac{\partial^2 \psi_{\ell m}}{\partial r_*^2} - V_\ell(r) \psi_{\ell m} = -4\pi r f(r) T_{\ell m}, \tag{2.79}$$

where $r_* := r + 2M \log\left(\frac{r}{2M} - 1\right)$ is the Regge-Wheeler tortoise coordinate, and the potential $V_\ell(r)$ is defined by

$$V_\ell(r) := \left(\frac{\ell(\ell+1)}{r^2} + \frac{2M}{r^3}\right) f(r). \tag{2.80}$$

As a final step, we make a Fourier decomposition

$$\psi_{\ell m}(t,r) = \int_{-\infty}^{+\infty} d\omega\, e^{-i\omega t} \psi_{\ell m\omega}(r), \tag{2.81}$$

$$T_{\ell m}(t,r) = \int_{-\infty}^{+\infty} d\omega\, e^{-i\omega t} T_{\ell m\omega}(r), \tag{2.82}$$

to get the frequency-domain radial equation

$$\frac{d^2\psi_{\ell m\omega}}{dr_*^2} - (V_l(r) - \omega^2)\psi_{\ell m\omega} = -4\pi r f(r) T_{\ell m\omega}. \tag{2.83}$$

The source modes $T_{\ell m\omega}$ are obtained as follows. First, integrating in Eq. (2.31), we obtain

$$T\left(x^\alpha\right) = \frac{q}{r_p^2 u^t}\delta(r - r_p(t))\delta(\varphi - \varphi_p(t))\delta(\theta - \pi/2). \tag{2.84}$$

The spherical harmonics take the form $Y_{\ell m}(\theta,\varphi) = c_{\ell m} e^{im\varphi} P_{\ell m}(\cos\theta)$, where $c_{\ell m}$ are certain real constants and $P_{\ell m}$ are the associated Legendre polynomials. Using the orthogonality relations we have

$$T_{\ell m}(t,r) = \int d^2\Omega\, Y^*_{\ell m}(\theta,\varphi) T(t,r,\theta,\varphi), \tag{2.85}$$

where $*$ denotes complex conjugation, and substituting for T from Eq. (2.84), we obtain

$$T_{\ell m}(t,r) = d_{\ell m} e^{-im\varphi_p(t)} \frac{q}{r_p^2 u^t}\delta(r - r_p(t)), \tag{2.86}$$

where $d_{\ell m} := c_{\ell m} P_{\ell m}(0)$ is a constant. A Fourier transform now yields

$$T_{\ell m\omega} = \frac{1}{2\pi}\int_{-\infty}^{+\infty} dt\, d_{\ell m} e^{-im\varphi_p(t)} \frac{q}{r_p^2 u^t}\delta(r - r_p(t)) e^{i\omega t}. \tag{2.87}$$

Switching integration variable to r_p and using the orbital symmetries $t_p(-\chi) = -t_p(\chi)$ and $\varphi_p(-\chi) = -\varphi_p(\chi)$, gives

$$T_{\ell m\omega}(r) = \frac{q d_{\ell m}}{\pi}\int_{r_{\min}}^{+\infty} \frac{dr_p}{|\dot r_p|}\frac{\delta(r - r_p)}{r_p^2}\cos\left(\omega t_p(r_p) - m\varphi_p(r_p)\right) \tag{2.88}$$

$$= \frac{q d_{\ell m}}{\pi r^2 |\dot r_p(r)|}\cos\left(\omega t_p(r) - m\varphi_p(r)\right)\Theta(r - r_{\min}). \tag{2.89}$$

Finally, we note that conjugation symmetry relates some modes to others. Since Φ is a real scalar field, we have that $\Phi^* = \Phi$ and hence, using Eq. (2.77),

$$\Phi = \sum_{\ell m} \frac{1}{r} \psi^*_{\ell m} Y^*_{\ell m}. \tag{2.90}$$

Recalling the identity

$$Y^*_{\ell m}(\theta, \varphi) = (-1)^m Y_{\ell,-m}(\theta, \varphi), \tag{2.91}$$

we may rewrite Φ as

$$\Phi = \sum_{\ell m} \frac{1}{r} (-1)^m \psi^*_{\ell m} Y_{\ell,-m}, \tag{2.92}$$

and hence obtain

$$\psi_{\ell m}(t, r) = (-1)^m \psi^*_{\ell,-m}(t, r). \tag{2.93}$$

This means we only need to calculate modes with $m \geq 0$. Furthermore, when $\ell + m$ is odd, $d_{\ell m} = 0$ and hence the source $T_{\ell m}$ vanishes. From this we conclude that the modes of the retarded field with odd $\ell + m$ are identically zero, everywhere. Thus, for a given ℓ-mode we only need to calculate those modes with $m \geq 0$ and $\ell + m$ even, roughly one quarter as many as naively expected. The θ-derivative of the scalar field also vanishes on the equator by symmetry.

2.4.2 Homogeneous solutions

We first consider the solutions to the homogeneous form of Eq. (2.83),

$$\frac{d^2 \psi_{\ell m \omega}}{dr_*^2} - (V_l(r) - \omega^2) \psi_{\ell m \omega} = 0. \tag{2.94}$$

From Eq. (2.80), we see that $V_\ell(r) \to 0$ as $r_* \to \pm\infty$, i.e. at the horizon and infinity. In those limits, the radial equation reduces to a harmonic oscillator,

$$\frac{d^2 \psi_{\ell m \omega}}{dr_*^2} + \omega^2 \psi_{\ell m \omega} \approx 0, \tag{2.95}$$

whose solution is given by a superposition of sinusoidal modes $e^{i\omega r_*}$ and $e^{-i\omega r_*}$.

The physical, inhomogeneous, scalar field sourced by the particle should obey retarded boundary conditions with purely ingoing radiation at the horizon, and asymptotically outgoing radiation at infinity. In the frequency domain, using the Fourier conventions

of Eq. (2.81), this requirement translates to

$$\psi_{\ell m\omega} \sim e^{i\omega r_*} \quad \text{as } r_* \to +\infty, \tag{2.96}$$

$$\psi_{\ell m\omega} \sim e^{-i\omega r_*} \quad \text{as } r_* \to -\infty. \tag{2.97}$$

It is therefore convenient to define the basis of homogeneous solutions $\{\psi^-_{\ell\omega}, \psi^+_{\ell\omega}\}$, which for $\omega \neq 0$ are defined to be the solutions to the homogeneous equation (2.94) obeying the boundary conditions

$$\psi^\pm_{\ell\omega} \sim e^{\pm i\omega r_*} \quad \text{as } r_* \to \pm\infty. \tag{2.98}$$

We note that neither these boundary conditions nor the homogeneous equation (2.94) depend on the mode number m, so that the homogeneous solutions $\psi^\pm_{\ell\omega}(r)$ can be labelled only by ℓ and ω.

These homogeneous solutions may be expanded as a series in the appropriate wave zone. For example, as $r \to \infty$, we have

$$\psi^+_{\ell\omega}(r) = e^{i\omega r_*} \sum_{k=0}^{k_{\rm out}} c^\infty_k \left(\frac{2M}{r}\right)^k + O\left(\frac{2M}{r}\right)^{k_{\rm out}+1}, \tag{2.99}$$

where the coefficients $c^\infty_{k>0}$ depend on ℓ and ω, and are determined in terms of c^∞_0 using a recurrence relation described in Appendix C. We adopt an overall normalisation such that $c^\infty_0 = 1$. Likewise, in the near-horizon wave zone, $r \to 2M$, we have an expansion

$$\psi^-_{\ell\omega}(r) = e^{-i\omega r_*} \sum_{k=0}^{k_{\rm in}} c^{\rm eh}_k \left(\frac{r}{2M} - 1\right)^k + O\left(r - 2M\right)^{k_{\rm in}+1}. \tag{2.100}$$

The coefficients $c^{\rm eh}_{k>0}$ are determined from $c^{\rm eh}_0$ using another recurrence relation, also summarised in Appendix C. We choose a normalisation such that $c^{eh}_0 = 1$.

For $\omega = 0$, Eq. (2.94) can be rewritten in the form

$$\frac{d}{d\rho}\left[(1-\rho^2)\frac{dR_\ell}{d\rho}\right] + \ell(\ell+1)R_\ell = 0, \tag{2.101}$$

where $R_\ell := \psi_{\ell 0}/r$ and $\rho = (r-M)/M$. The general solution is

$$R_\ell(\rho) = a_\ell P_\ell(\rho) + b_\ell Q_\ell(\rho), \tag{2.102}$$

for arbitrary constants a_ℓ and b_ℓ. Here $P_\ell(\rho)$ is the Legendre polynomial, which is regular at all finite points but blows up as $\rho \to \pm\infty$ for $\ell > 0$, and $Q_\ell(\rho)$ is the Legendre function of the second kind, which decays at infinity but is singular at $\rho = 1$ ($r = 2M$). Thus for

$\omega = 0$ we take our basis of homogeneous solutions to be

$$\psi^-_{\ell 0}(r) := r P_\ell \left(\frac{r-M}{M}\right), \tag{2.103}$$

$$\psi^+_{\ell 0}(r) := r Q_\ell \left(\frac{r-M}{M}\right). \tag{2.104}$$

The large-r behavior of these solutions, needed for later discussion, is

$$\psi^-_{\ell 0}(r) \sim r^{\ell+1}, \qquad \psi^+_{\ell 0}(r) \sim r^{-\ell}. \tag{2.105}$$

2.4.3 The inhomogeneous solution

Solutions to the inhomogeneous frequency-domain equation (2.83) can be found using variation of parameters. One such solution is given by

$$\psi_{\ell m\omega}(r) = \psi^+_{\ell\omega}(r)\int_{r_{\rm min}}^{r} \frac{\psi^-_{\ell\omega}(r')S_{\ell m\omega}(r')}{W_{\ell\omega}}\frac{dr'}{f(r')} + \psi^-_{\ell\omega}(r)\int_{r}^{+\infty} \frac{\psi^+_{\ell\omega}(r')S_{\ell m\omega}(r')}{W_{\ell\omega}}\frac{dr'}{f(r')}, \tag{2.106}$$

where

$$S_{\ell m\omega} := -4\pi r f(r) T_{\ell m\omega} \tag{2.107}$$

is the source on the right-hand side of Eq. (2.83), and $W_{\ell\omega} := \psi^-_{\ell\omega}\frac{d\psi^+_{\ell\omega}}{dr_*} - \psi^+_{\ell\omega}\frac{d\psi^-_{\ell\omega}}{dr_*}$ is the Wronskian of the homogeneous solutions, which depends only on ℓ and ω, and not on r. For convenience we give names to the integrals in Eq. (2.106):

$$c^+_{\ell m\omega}(r) := \int_{r_{\rm min}}^{r} \frac{\psi^-_{\ell\omega}(r')S_{\ell m\omega}(r')}{W_{\ell\omega}}\frac{dr'}{f(r')}, \tag{2.108}$$

$$c^-_{\ell m\omega}(r) := \int_{r}^{+\infty} \frac{\psi^+_{\ell\omega}(r')S_{\ell m\omega}(r')}{W_{\ell\omega}}\frac{dr'}{f(r')}. \tag{2.109}$$

We will find that Eq. (2.106) gives the correct retarded solution to Eq. (2.83), except for the special case $\ell = 0 = \omega$ discussed below. We show this for the non-static $\omega \neq 0$ modes first, with the first task being to show that the integral defining $c^-_{\ell m\omega}$ converges. Substituting $T_{\ell m\omega}$ from Eq. (2.89), and recalling the expansions (2.27)-(2.29) and (2.98), the integrand of $c^-_{\ell m\omega}$ takes the schematic form

$$J^-_{\ell m\omega}(r) \sim e^{i\omega(1+1/v)r} r^{i\omega(1+B)-1} + e^{i\omega(1-1/v)r} r^{i\omega(1-B)-1} \tag{2.110}$$

as $r \to \infty$, where B is one of the constants appearing in expansion (2.27). The integral defining $c^-_{\ell m\omega}$ thus converges like sinusoidal oscillations/r at large radius. As we will see later, this slow oscillatory convergence is numerically challenging.

Next we check the boundary conditions. Since the source is supported only on $r \geq r_{\min}$, the integral $c^+_{lm\omega}(r)$ vanishes for $r \leq r_{\min}$. Thus, for $2M < r < r_{\min}$ we have

$$\psi_{\ell m\omega}(r) = C^-_{\ell m\omega}\psi^-_{\ell\omega}(r), \tag{2.111}$$

where we defined the normalisation integral

$$C^-_{\ell m\omega} := \int_{r_{\min}}^{+\infty} \frac{\psi^+_{\ell\omega}(r')S_{\ell m\omega}(r')}{W_{\ell\omega}f(r')}dr'. \tag{2.112}$$

Hence, as $r \longrightarrow 2M$,

$$\psi_{\ell m\omega}(r) \sim C^-_{\ell m\omega}e^{-i\omega r_*}, \tag{2.113}$$

as required.

Meanwhile, as $r \longrightarrow \infty$,

$$\psi^-_{lw}(r) \sim a_{\ell\omega}\, e^{i\omega r_*} + b_{\ell\omega}\, e^{-i\omega r_*}, \tag{2.114}$$

for some constants $a_{\ell\omega}$ and $b_{\ell\omega}$, and in particular it is bounded. Since $c^-_{\ell m\omega}(r) = O\left(r^{-1}\right)$ as $r \to \infty$, we have that

$$\lim_{r\to\infty} c^-_{\ell m\omega}(r)\psi^-_{\ell m\omega}(r) = 0. \tag{2.115}$$

Furthermore, as $r \to \infty$, $\psi^+_{\ell\omega}(r) \sim e^{i\omega r_*}$ and thus

$$\psi_{\ell m\omega}(r) \sim C^+_{\ell m\omega}e^{i\omega r_*}, \tag{2.116}$$

where

$$C^+_{\ell m\omega} := \int_{r_{\min}}^{+\infty} \frac{\psi^-_{\ell\omega}(r')S_{\ell m\omega}(r')}{W_{\ell\omega}f(r')}dr'. \tag{2.117}$$

This integral converges by a similar argument to that used for the convergence of $c^-_{\ell m\omega}(r)$. Thus we have shown that the solution (2.106) is the retarded inhomogeneous solution for the non-static modes.

The situation is more subtle for the static modes $\omega = 0$. As before we must first check that the integral defining $c^-_{\ell m\omega}$ is convergent and well-defined. The integrand of $c^-_{\ell m\omega}(r)$ now takes the form

$$J_{\ell m}(r) = \frac{\psi^+_{\ell 0}(r)\cos(m\varphi_p(r))}{r|\dot{r}_p(r)|}, \tag{2.118}$$

where we have neglected overall numerical factors. Using Eq. (2.105), we find that the integrand goes like $r^{-(\ell+1)}$ as $r \to \infty$, and does not oscillate. That is because $\varphi_p(r)$

tends to a finite limit, and $\psi^+_{\ell 0}$ is no longer asymptotically oscillatory. This means our integral converges for $\ell > 0$, but not for $\ell = 0$. The form of Eq. (2.106) will require modification for $\ell = 0$, and we will give further consideration to the large-r behaviour of the static $\ell = 0$ solution below. For now, we return to the task of checking the boundary conditions for $\ell > 0$ and $\omega = 0$.

When considering bound particle motion, the appropriate boundary condition for the static field is for it to be regular on the horizon, $r = 2M$, and decaying as $r \to \infty$. However, we find that these conditions cannot be imposed when the particle moves along a hyperbolic orbit, and instead we impose a condition of "greatest regularity", described below.

The horizon boundary condition is easiest to investigate: because the source is supported only on $r \geq r_{\min}$, the field is given by

$$\psi_{\ell m 0}(r) = r C^-_{\ell m 0} P_\ell \left(\frac{r - M}{M} \right) \tag{2.119}$$

for $2M < r \leq r_{\min}$, where $C^-_{\ell m 0}$ is as defined in Eq, (2.112) and we have substituted for $\psi^-_{\ell 0}$ from Eq. (2.103). The solution in Eq. (2.106) is therefore regular at the horizon.

The large-r behaviour is more subtle, because the factors $c^+_{\ell m 0}(r)$ and $\psi^-_{\ell 0}(r)$ grow as $r \to \infty$, while $c^-_{\ell m 0}(r)$ and $\psi^+_{\ell 0}(r)$ decay. This means that each term in Eq. (2.106) consists of a decaying factor and a growing factor. A careful analysis using Eq. (2.105) gives that, for $\ell > 0$,

$$c^\pm_{\ell m 0}(r) \psi^\pm_{\ell m 0}(r) \sim r \quad \text{as } r \to \infty, \tag{2.120}$$

so that the solution in Eq. (2.106) diverges at infinity unless there is cancellation between the two terms. A more detailed calculation confirms that total cancellation does not occur, and hence $\psi_{\ell m 0} \sim r$. Indeed, considering the dominant terms of Eq. (2.83) at large r,

$$\frac{d^2 \psi_{\ell m 0}}{dr^2} - \frac{\ell(\ell+1)}{r^2} \psi_{\ell m 0} = \frac{S_1}{r} \tag{2.121}$$

(where S_1 is a certain constant), we have the particular solution

$$\psi_{\ell m 0}(r) = -\frac{S_1 r}{\ell(\ell+1)}. \tag{2.122}$$

This is genuine behaviour; there is no homogeneous solution with matching large-r behaviour that we can subtract off to remove the divergence. For $\ell = 0$, a similar argument suggests that the behaviour is

$$\psi_{000} \sim r \log r \tag{2.123}$$

at large r, which is what one would obtain by truncating the logarithmically divergent integral $c^{-}_{000}(r)$ at a finite upper integration limit in the variation of parameters formula, Eq. (2.106).

In terms of the scalar field Φ itself [recall Eq. (2.77)], this behaviour translates to $\Phi^{\ell>0} \sim$ const and $\Phi^{\ell=0} \sim \log r$ as $r \to \infty$. Perhaps surprisingly, the static contributions to the scalar field do not fall off at infinity. Nonetheless Eq. (2.106) gives the most regular solution for $\omega = 0$ and $\ell > 0$, in the sense that any other solution would either be irregular on the horizon or diverge as $r \to \infty$. For $\omega = 0 = \ell$, Eq. (2.106) does not give the correct retarded solution (the integral in the second line is indefinite), but the true solution must diverge like $\psi_{000}(r) \sim r \log r$ as $r \to \infty$. This does not, however, mean that the time-domain solution diverges at infinity, and there is no sign of such behaviour in our numerical results.

2.4.4 Method of extended homogeneous solutions

The primary inputs for the mode-sum formula are the ℓm-modes of the time-domain scalar field and its derivatives at the particle. A naive attempt to obtain these from the frequency-domain field in Eq. (2.106) faces the problem of the Gibbs phenomenon, first discussed in this context in Ref. [152]. The presence of a Dirac delta function source, supported on the worldline, on the right hand side of Eq. (2.79) causes the derivatives $\psi_{\ell m,t}$ and $\psi_{\ell m,r}$ to be discontinuous at the worldline. A standard result from Fourier analysis says that the Fourier series/integrals for these derivatives will then converge to the correct value everywhere off the worldline, but will do so slowly [with terms decaying like $O\left(\omega^{-1}\right)$] and non-uniformly in the vicinity of the particle. On the worldline, the series would be expected to converge to the 2-sided average of the derivative.

The solution to this problem was developed in Ref. [152] for bound particle motion. It involves expressing the field on either side of the worldline [i.e. in $r \leq r_p(t)$ and $r \geq r_p(t)$] in terms of analytic, homogeneous, frequency modes that have exponentially convergent Fourier series. Here we present the argument used in [152], adapted to the unbound problem, to reconstruct the field in the interior region $r \leq r_p(t)$.

First one defines the *internal extended homogeneous solution*,

$$\tilde{\psi}^{-}_{\ell m\omega}(r) := C^{-}_{\ell m\omega}\psi^{-}_{\ell\omega}(r), \tag{2.124}$$

where the normalisation integral $C^{-}_{\ell m\omega}$ is as defined in Eq. (2.112). With this choice, the internal EHS is equal to the inhomogeneous field $\psi_{\ell m\omega}$ when $r \leq r_{\min}$. Denoting the corresponding time-domain EHS field by $\tilde{\psi}^{-}_{\ell m}(t, r)$, we thus have

$$\psi_{\ell m}(t, r) = \tilde{\psi}^{-}_{\ell m}(t, r) \quad \text{for } r \leq r_{\min}. \tag{2.125}$$

It was demonstrated in Ref. [152] that $C^{-}_{\ell m\omega}$ is expected to decay exponentially with ω, such that $\tilde{\psi}^{-}_{\ell m}(t,r)$ is analytic in both t and r. The inhomogeneous field $\psi_{\ell m}(t,r)$ is likewise expected to be analytic everywhere in $r < r_p(t)$, and agrees with $\tilde{\psi}^{-}_{\ell m}(t,r)$ in the open set $r < r_{\rm min}$. We must therefore have an equality throughout the domain,

$$\psi_{\ell m}(t,r) = \tilde{\psi}^{-}_{\ell m}(t,r) \quad \text{for } r < r_p(t). \tag{2.126}$$

Crucial to this argument is the existence of the vacuum region $r \leq r_{\rm min}$ where the inhomogeneous field coincides with a homogeneous solution. In the case of bound motion, there is also a vacuum region $r \geq r_{\rm max}$ that allows the definition of an external EHS field that may be used to reconstruct the field in the region $r \geq r_p(t)$. Such an external vacuum region does not exist for a hyperbolic orbit, and the EHS method is constrained to calculating only the time-domain scalar field in the region $r \leq r_p(t)$.

The mode-sum regularisation approach outlined in Chapter 2.2.2 is usually implemented using a two-side average of the limiting values corresponding to $x \to x_p^{\pm}$, which simplifies the form of the regularisation parameters. However, this is not strictly necessary, and it is possible to carry out the regularisation procedure "one-sided", making use of only the value of the scalar field derivatives taken from the direction $r < r_p(t)$. This is the approach we will be taking in this thesis.

We note here the small-frequency behaviour of $\tilde{\psi}^{-}_{\ell m\omega}(r)$, which will play a role later. For $r \ll \omega^{-1}$, the homogeneous solution $\psi^{-}_{\ell\omega}(r)$ behaves like the polynomially growing static solution in Eq. (2.105), growing approximately proportionally to $r^{\ell+1}$. We thus have that

$$\tilde{\psi}^{-}_{\ell m\omega}(r_p) \sim \left(\frac{r_p}{r_{\rm min}}\right)^{\ell+1} \psi_{\ell m\omega}(r_{\rm min}) \tag{2.127}$$

for $r_{\rm min} \leq r_p \ll \omega^{-1}$, where we made use of the fact that the internal EHS and the physical, inhomogeneous field coincide in $r \leq r_{\rm min}$. At small frequency the internal EHS field at the particle thus grows as a power law in r_p, and exponentially in ℓ. It was noted in Ref. [113] that this behaviour results in significant cancellation between low-frequency modes when the EHS method is used to reconstruct the time-domain field away from the orbital turning points, with subsequent loss of precision. This problem and its implications will be further explored in Chapter 4.6.

Chapter 3

Frequency modes of the extended homogeneous solutions

In this chapter we will explore the numerical challenges faced when evaluating the extended homogeneous solution $\tilde{\psi}^{-}_{\ell m\omega}(r)$ for a scattering source, and develop the theoretical tools and numerical methods to overcome them. The success of these tools is then demonstrated with example numerical results.

3.1 Normalisation integrals

When calculating the scalar-field self-force using the EHS method and one-sided regularisation, a key numerical task is to evaluate the normalisation integrals $C^{-}_{\ell m\omega}$ defined in Eq. (2.112). As discussed in Section 2.4.3, this integral displays marginal $\sim$ oscillations$/r$ convergence. In this section we will explore the consequences of truncating the normalisation integral at a finite radius, and develop two techniques to suppress the resulting truncation error. The *tail correction scheme* will involve a series of analytical approximations to the neglected tail of the integral, while *integration by parts* will be used to increase the decay rate of the original integrand.

3.1.1 Truncating the normalisation integral

In order to calculate the normalisation integral $C^{-}_{\ell m\omega}$ numerically, we wish to truncate it at some finite radius $r_{\rm max}$. Figure 3.1 displays some examples of $C^{-}_{\ell m\omega}$ spectra for the two geodesics with $(E, r_{\rm min}) = (1.1, 4M)$ and $(1.1, 10M)$. These integrals were calculated numerically using the numerical methods discussed in Sec. 3.2, truncating the integral at $r_{\rm max} = 2000M$. The modes $(\ell, m) = (2, 2)$ and $(10, 6)$ are displayed for both geodesics. We note that as we move away from the peak, high-frequency noise appears in the

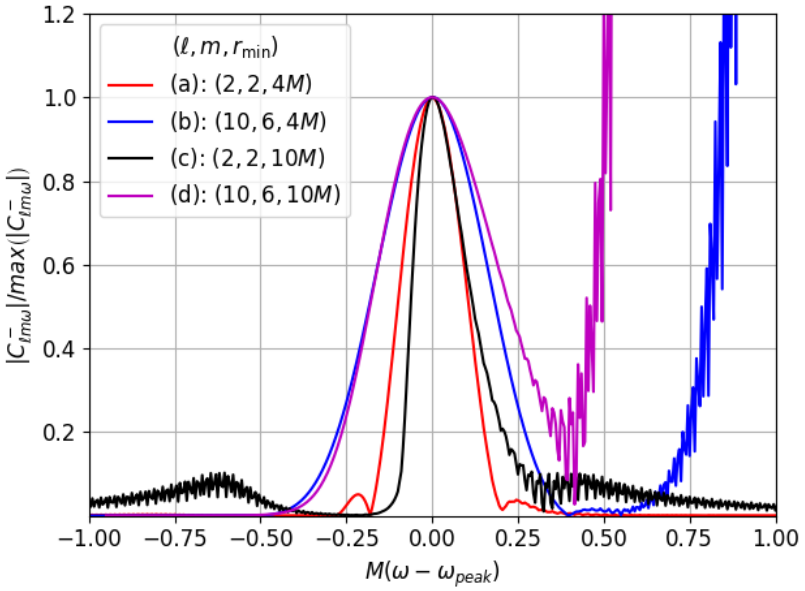

FIGURE 3.1: Example spectra of $|C^-_{\ell m\omega}|$, shifted by the peak frequency and normalised to unity at the peak. The modes $(\ell, m) = (2, 2)$ and $(10, 6)$ are illustrated, for the geodesics with fixed $E = 1.1$ and $r_{\min} \in \{4M, 10M\}$. The peak frequencies were $M\omega_{\text{peak}} \approx 0.29, 0.96, 0.095$ and 0.45 for modes (a)–(d), respectively. The numerical integrals were truncated at $r_{\max} = 2000M$. High-frequency noise is visible in the tails of the spectrum as a result of this truncation.

spectra and the numerical curves break away from the expected decaying trend. For a given energy and fixed $r_{\max}$, the problem is more acute for geodesics with larger $r_{\min}$ and at larger ℓ.

The high-frequency noise is not a numerical artefact, and can be traced to the truncation of $C^-_{\ell m\omega}$ at finite radius. Because of the marginal oscillations/r-type convergence, suppressing this issue by increasing $r_{\max}$ is impractical. Instead, we introduce two analytical mitigation techniques, with negligible increase in computational cost. The first technique is based on an analytical approximation of the large-r truncated tail of the $C^-_{\ell m\omega}$ integral, and the second uses integration by parts to improve the convergence of the integral. In the rest of this section we discuss each technique in turn, and in Sec. 3.3 we will illustrate their effectiveness in enabling a fast and efficient evaluation of $C^-_{\ell m\omega}$.

3.1.2 Tail correction scheme

We write $C^-_{\ell m\omega}$, defined in Eq. (2.112), in the form

$$C^-_{\ell m\omega} = -\frac{4qd_{\ell m}}{W_{\ell\omega}} \int_{r_{\min}}^{\infty} J_{\ell m\omega}(r)dr, \tag{3.1}$$

where

$$J_{\ell m\omega}(r) = \frac{1}{2}\sum_{\sigma=\pm 1}\frac{\psi^{+}_{\ell\omega}(r)\exp\left[i\sigma\left(\omega t_p(r) - m\varphi_p(r)\right)\right]}{r\,|\dot{r}_p(r)|}. \tag{3.2}$$

We seek to obtain a large-r asymptotic expansion for $J_{\ell m\omega}$. Starting with the homogeneous solution factor, we recall from Eq. (2.99) its asymptotic form,

$$\psi^{+}_{\ell\omega}(x) = e^{i\tilde{\omega}x_*}\sum_{k=0}^{\infty} c_k^{\infty} x^{-k}, \tag{3.3}$$

where for convenience we have introduced here $x := r/(2M)$, as well as $x_* := r_*/(2M)$ and $\tilde{\omega} := 2M\omega$. Using the identity

$$x_* = x + \log x - \sum_{n=1}^{\infty}\frac{1}{n}\,x^{-n}, \tag{3.4}$$

this becomes

$$\psi^{+}_{\ell\omega}(x) = e^{i\tilde{\omega}x}x^{i\tilde{\omega}}\left(1 + \sum_{n=1}^{\infty}\hat{c}_n^{\infty}x^{-n}\right), \tag{3.5}$$

where the new expansion coefficients, $\hat{c}_n^{\infty}$, can be written in terms of the old ones, c_n^{∞}. In Appendix D we give the explicit relations for $1 \le n \le 5$, which will suffice for our purpose.

We turn next to the phase factor in (3.2). Using Eqs. (2.27) and (2.28), we obtain

$$\omega t_p - m\varphi_p = \tilde{\omega}\left(\frac{x}{v} + B\log x\right) + \sum_{n\ge 0}\Delta_n x^{-n}, \tag{3.6}$$

where

$$\Delta_0 := \omega t_0 - m\varphi_\infty \quad \text{and} \quad \Delta_{n>0} := \tilde{\omega}C_n - mD_n, \tag{3.7}$$

with $B, t_0, \varphi_\infty, C_n$ and D_n being the coefficients appearing in the expansions (2.27) and (2.28). We further recall the large-r expansion of $1/|\dot{r}_p|$ from Eq. (2.29),

$$\frac{1}{|\dot{r}_p|} = \sum_{n=0}^{\infty} U_n x^{-n}. \tag{3.8}$$

The complex exponential function is then expanded as

$$\exp\left[i\sigma\sum_{n\ge 0}\Delta_n x^{-n}\right] = e^{i\Delta_0}\left[1 + \sum_{n\ge 1}H_{n\sigma}x^{-n}\right], \tag{3.9}$$

where expressions for $H_{n\sigma}$ are given in terms of Δ_n for $n \le 5$ in Appendix D.

Substituting the above expansions, Eq. (3.2) takes the form

$$J_{\ell m\omega}(x) = \frac{1}{2}\sum_{\sigma=\pm1}\sum_{n\geq 0}\lambda_{n\sigma}e^{i\tilde{\Omega}_\sigma x}x^{a_{n\sigma}-1}, \tag{3.10}$$

as $x \to \infty$, where

$$\tilde{\Omega}_\sigma := (1+\sigma/v)\tilde{\omega}, \tag{3.11}$$

$$a_{n\sigma} := i(1+\sigma B)\tilde{\omega} - n, \tag{3.12}$$

and

$$\lambda_{n\sigma} := \frac{1}{2M}e^{i\sigma\Delta_0}\sum_{q+r+s=n} U_q\hat{c}^\infty_r H_{s\sigma}, \tag{3.13}$$

where the sum is taken over non-negative integers q, r, s, and we define $H_{0\sigma} = 1 = \hat{c}^\infty_0$.

A key observation is that the expression in (3.10) can be integrated *analytically*, term by term:

$$\begin{aligned}\int_{x_{\rm max}}^{+\infty} & J_{\ell m\omega}(x')dx' \\ &= \frac{1}{2}\sum_{\sigma=\pm1}\sum_{n\geq 0}\lambda_{n\sigma}\left(-i\tilde{\Omega}_\sigma\right)^{-a_{n\sigma}}\Gamma[a_{n\sigma}, z_\sigma],\end{aligned} \tag{3.14}$$

where $x_{\rm max} = r_{\rm max}/2M$, $a_{n\sigma}$ depends on σ and n through Eq. (3.12), $z_\sigma := -i\tilde{\Omega}_\sigma x_{\rm max}$, and $\Gamma[a,z]$ is the upper incomplete gamma function, calculated in practice using the continued fraction representation,

$$\Gamma[a,z] = \cfrac{z^a e^{-a}}{z + \cfrac{1-a}{1 + \cfrac{1}{z + \cfrac{2-a}{1 + \cfrac{2}{z + \ddots}}}}}. \tag{3.15}$$

As $x_{\rm max} \to \infty$, the n-th term of the series in Eq. (3.14) has the asymptotic behaviour

$$|\Gamma[a_{n\sigma}, z_\sigma]| \sim \frac{1}{x^{n+1}_{\rm max}}. \tag{3.16}$$

The tail expression (3.14) may be added to a numerical integral that has been truncated at finite radius $r_{\rm max}$, to obtain a more accurate estimate of $C^-_{\ell m\omega}$. We define a *tail correction scheme of order* N as one obtained by truncating Eq. (3.14) at finite order $n = N-1$, and using this expression as an approximation to the tail of the integral

$C^{-}_{\ell m\omega}$. In this scheme, terms up to and including r^{-N} are included in the expansion of the integrand, and the error in the tail estimate is $O\left(r_{\rm max}^{-(N+1)}\right)$, where $r_{\rm max}$ is the radius at which the numerical portion of the integral is truncated. This error estimate is obtained by applying Eq. (3.16) to the first neglected term, $n = N$, of Eq. (3.14). For a correction scheme of order N, one requires the coefficients $\lambda_{n\sigma}$ up to and including $n = N - 1$. We have obtained these coefficients up to $n = 5$, sufficient to implement the tail correction scheme at orders up to $N = 6$.

3.1.3 Integration by parts

The key to the integration by parts (IBP) approach is to factorise the integrand $J_{\ell m\omega}$ in Eq. (3.1) into (a) a sinusoidal factor that may be integrated repeatedly, and (b) a decaying factor that may be practically differentiated without recourse to numerical differentiation, and which decays more rapidly each time it is differentiated. In this section, we will demonstrate the existence of such a factorisation, and thus show how IBP may be used to increase the rate of convergence of the integrals $C^{-}_{\ell m\omega}$.

First, however, we make a remark about the behaviour of the integrand $J_{lm\omega}$ at the lower boundary, $r = r_{\rm min}$. As can be seen from Eq. (3.2), there is a factor of $|\dot{r}_p| \propto (r - r_{\rm min})^{1/2}$ present in the denominator, which results in an integrable singularity. Although this does not prevent the integral converging, it is numerically problematic, and confounds an attempt at integration by parts, which may introduce a stronger, non-integrable singularity.

To handle this issue, we select some radius $r_{\rm cut} > r_{\rm min}$, and use the relativistic anomaly χ as the integration variable in the region $r_{\rm min} \leq r \leq r_{\rm cut}$. The use of χ as integration variable produces an integrand which is regular at $r_{\rm min}$, but which suffers from increasingly rapid, large amplitude oscillations as $\chi \to \chi_\infty$. It is therefore more practical to use r as the integration variable for the $r > r_{\rm cut}$ leg of the integral. A similar approach was adopted in Ref. [158]. The practical details of the integration, including the choice of $r_{\rm cut}$, will be discussed in Section 3.2.

We thus wish to apply IBP to the integral

$$C^{(r)-}_{\ell m\omega} := \int_{r_{\rm cut}}^{\infty} J_{\ell m\omega}(r')dr, \tag{3.17}$$

where the integrand $J_{\ell m\omega}$, recall, is given in Eq. (3.2). To obtain the sinusoidal factor we desire, we consider the phases of the oscillatory factors in the integrand, and remove the parts that grow linearly with r at large radii. Define

$$\Delta(r) := \omega t_p(r) - m\varphi_p(r) - \frac{\omega r}{v}, \tag{3.18}$$

and note that Eq. (3.6) implies

$$\Delta(r) = \tilde{\omega} B \log(x) + \sum_{n\geq 0} \Delta_n x^{-n} \tag{3.19}$$

as $r \to \infty$, where the coefficients Δ_n are the same as those defined in Sec. 3.1.2 for the correction scheme. Equation (3.19) then implies that

$$\frac{d}{dr}\Delta(r) = O\left(r^{-1}\right) \tag{3.20}$$

as $r \to \infty$. We rewrite Eq. (3.18) as

$$\Delta(r) = \omega \hat{t}_p(r) - m\varphi_p(r), \tag{3.21}$$

introducing the new time coordinate

$$\hat{t}_p(r) := t_p(r) - r/v, \tag{3.22}$$

which diverges logarithmically as $r \to \infty$. $\hat{t}_p$ can be calculated directly by integrating

$$\frac{d\hat{t}_p}{d\chi} = \frac{M}{(1+e\cos\chi)^2}\left[-\frac{pe\sin\chi}{v} + \frac{p^2}{p-2-2e\cos\chi}\sqrt{\frac{(p-2)^2-4e^2}{p-6-2e\cos\chi}}\right], \tag{3.23}$$

obtained using Eqs. (2.19) and (2.18). We also introduce the new field

$$P_{\ell\omega}(r) := e^{-iwr}\psi^+_{\ell\omega}(r), \tag{3.24}$$

which, using (2.94), satisfies

$$\frac{d^2P_{\ell\omega}}{dr_*^2} + 2i\omega f(r)\frac{dP_{\ell\omega}}{dr_*} + \left[-V_l + \omega^2 - \omega^2 f(r)^2 + \frac{2iM\omega}{r^2}f(r)\right]P_{\ell\omega}(r) = 0. \tag{3.25}$$

The large-r behaviour of $P_{\ell\omega}$ is easily deduced from that of $\psi^+_{\ell\omega}$ given in Eq. (2.99):

$$P_{\ell\omega} = \exp\left[2iM\omega\log\left(\frac{r}{2M}-1\right)\right]\sum_{k=0}^{\infty} c_k^{\infty}\left(\frac{2M}{r}\right)^k \tag{3.26}$$

as $r \to \infty$. Note $P_{\ell\omega}$ oscillates with only logarithmic phase at infinity.

With these definitions of $\Delta(r)$ and $P_{\ell\omega}(r)$, we obtain

$$C^{(r)-}_{\ell m\omega} = \frac{1}{2}\sum_{\sigma=\pm 1}\int_{r_{\rm cut}}^{+\infty} e^{i\Omega_\sigma r} K^{\sigma}_{\ell m\omega}(r)dr, \tag{3.27}$$

where

$$\Omega_\sigma := (1+\sigma/v)\omega \tag{3.28}$$

is related to Eq. (3.11) by $\Omega_\sigma = \tilde{\Omega}_\sigma/2M$, and

$$K^\sigma_{\ell m\omega}(r) := \frac{P_{\ell\omega}(r)e^{i\sigma\Delta(r)}}{r|\dot{r}_p(r)|}. \tag{3.29}$$

We note two properties of the function $K^\sigma_{\ell m\omega}$. First, we have closed form expressions for $\dot{r}_p(r)$ using Eq. (2.3), and also

$$\frac{d}{dr}\Delta(r) = \frac{\omega E}{f(r)\dot{r}_p(r)} - \frac{mL}{r^2\dot{r}_p(r)} - \frac{\omega}{v}, \tag{3.30}$$

both of which can be differentiated in closed analytical form any number of times. We can also determine $P_{\ell\omega}$ and $dP_{\ell\omega}/dr$ numerically, and then recursively determine any number of derivatives using the field equation (3.25). Thus we may practically differentiate $K^\sigma_{\ell m\omega}$ any given number of times using repeated applications of the product rule.

Second, each derivative of $K^\sigma_{\ell m\omega}$ decays one order more rapidly in r than the previous derivative:

$$K^{\sigma(N)}_{\ell m\omega} = O\left(\frac{1}{r^{N+1}}\right) \tag{3.31}$$

as $r \to \infty$, where we introduced the derivative notation $K^{\sigma(N)}_{\ell m\omega} := d^N K^\sigma_{\ell m\omega}/dr^N$. To show this, it suffices to show that each factor in Eq. (3.29) decays one order more rapidly each time it is differentiated. This is easily confirmed using the closed-form expressions for the derivatives of $e^{i\sigma\Delta}$ and of $1/(r|\dot{r}_p|)$. The result for the $P_{\ell\omega}$ factor follows from Eq. (3.26). Crucial to this result was the fact that the two oscillatory factors $e^{i\sigma\Delta}$ and $P_{\ell\omega}$ oscillate with only logarithmic phase as $r \to \infty$ and hence have decaying derivatives.

Equation (3.27) thus provides the desired factorisation of the integrand. Integrating by parts $N+1$ times gives

$$C^{(r)-}_{\ell m\omega} = \frac{1}{2}\sum_{\sigma=\pm1}\left\{\sum_{n=0}^{N}\left[\left(\frac{i}{\Omega_\sigma}\right)^{n+1} e^{i\Omega_\sigma r_{cut}} K^{\sigma(n)}_{\ell m\omega}(r_{cut})\right] + \left(\frac{i}{\Omega_\sigma}\right)^{N+1}\int_{r_{cut}}^{+\infty} e^{i\Omega_\sigma r} K^{\sigma(N+1)}_{\ell m\omega}(r)dr\right\}. \tag{3.32}$$

We can practically apply integration by parts any number of times, and hence achieve any polynomial rate of decay in the integrand. Using Eq. (3.31), we see that the integrand in Eq. (3.32) decays like $r^{-(N+2)}$ as $r \to \infty$. The limiting factor of the IBP method is the need to derive expressions for the necessary derivatives of $K^\sigma_{\ell m\omega}$ in advance, which becomes increasingly complicated at high orders. In practice we have only derived the expressions for derivatives up to and including $K^{\sigma(4)}_{\ell m\omega}$, allowing for four iterations of IBP and a truncation error of $O(r^{-5}_{\max})$.

It is possible to derive a tail correction scheme, analogous to Eq. (3.14), to approximate the tail of the integral in Eq. (3.32). Indeed, comparing the form of the integrand in Eq. (3.27) to the expansion in Eq. (3.10), we can read off the series expansion for $K^{\sigma}_{\ell m\omega}$ at large r:

$$K^{\sigma}_{\ell m\omega} = \sum_{n\geq 0} \lambda_{n\sigma} x^{a_{n\sigma}-1}, \tag{3.33}$$

where $x = r/(2M)$ as usual. Differentiating this term by term, we have

$$\left(\frac{i}{\Omega_\sigma}\right)^p K^{\sigma(p)}_{\ell m\omega} = \sum_{n\geq 0} \lambda_{np\sigma} x^{a_{n+p,\sigma}-1}, \tag{3.34}$$

where the new coefficients $\lambda_{np\sigma}$ are given by

$$\lambda_{np\sigma} = \left(\frac{i}{\tilde{\Omega}_\sigma}\right)^p \lambda_{n\sigma} \prod_{q=0}^{p-1} \left[a_{n+q,\sigma} - 1\right]. \tag{3.35}$$

The tail of the IBP integral may then be approximated using

$$\begin{aligned}\left(\frac{i}{\Omega_\sigma}\right)^p \int_{x_{\max}}^{+\infty} dx\, e^{i\Omega_\sigma r} K^{\sigma(p)}_{\ell m\omega} &\approx \frac{1}{2}\sum_{n=0}^{n_{\max}} \int_{x_{\max}}^{+\infty} dx\, \lambda_{np\sigma} e^{i\tilde{\Omega}_\sigma x} x^{a_{n+p,\sigma}-1} \\ &= \frac{1}{2}\sum_{n=0}^{n_{\max}} \lambda_{np\sigma} \left(-i\tilde{\Omega}_\sigma\right)^{-a_{n+p,\sigma}} \Gamma[a_{n+p,\sigma}, z_\sigma],\end{aligned} \tag{3.36}$$

where $a_{n\sigma}$ is as defined in Eq. (3.12) and again $z_\sigma = -i\tilde{\Omega}_\sigma x_{\max}$.

3.2 Numerical method

In this section we present the details of our numerical approach, implemented in C. We start with the numerical calculation of the homogeneous solutions $\psi^{\pm}_{\ell\omega}$, and then describe the quadrature routines used to calculate the normalisation integrals $C^{-}_{\ell m\omega}$, and the details of our application of the tail correction and IBP methods.

3.2.1 Homogeneous solutions

Boundary conditions for the homogeneous solution $\psi^{-}_{\ell\omega}$ and its radial derivative are provided by the series in Eq. (2.100). The coefficients $c^{\text{eh}}_{k>0}$ are obtained by recursively using the relation in Appendix C, with initial conditions $c^{\text{eh}}_{k<0} = 0$ and $c^{\text{eh}}_{0} = 1$. Successive terms in the series are calculated and added, stopping when the relative contribution of the last term falls below some threshold, usually taken to be 10^{-16}. The boundary conditions for $\psi^{-}_{\ell\omega}$ are specified at radius $r^{\text{in}}_{*} = -60M$. This value is limited by machine

precision when inverting the relation $r_*(r)$ to get $r(r_*)$; for $r_*^{\rm in} < -60M$, r begins to become indistinguishable from $2M$ at double precision. Despite this, we find that this choice of $r_*^{\rm in}$ is adequate for rapid convergence of series (2.100).

The field $\psi^-_{\ell\omega}$ is then obtained at radii $r_* > r_*^{\rm in}$ by evolving the initial data according to the homogeneous equation (2.94). This is done numerically using the Runge-Kutta Prince-Dormand (8,9) method `rk8pd` implemented in the GNU Scientific Library (GSL) [179], with a requested relative error tolerance of 10^{-12}.

The calculation of the field $P_{\ell\omega} = e^{-i\omega r}\psi^+_{\ell\omega}$ is similar. Boundary conditions are obtained from the series in Eq. (3.26) and its derivative, evaluated at some outer radius $r_*^{\rm out}$. The coefficients $c^\infty_{k>0}$ are once again obtained recursively using the relation described in Appendix C with initial conditions $c^\infty_{k<0} = 0$ and $c^\infty_0 = 1$. The series is once again truncated when the relative contribution of the last term falls below 10^{-16}. As noted in Ref. [154], however, the terms in series (3.26) can begin to increase again after initially decreasing. This lack of convergence is unsurprising; the expansion in Eq. (3.26) is only expected to converge in the wave zone $\omega r \gg 1$. For small frequency, the wave zone may lie beyond $r_*^{\rm out}$, in which case the series is not expected to converge. To resolve this we adopt a similar approach to Ref. [154], increasing $r_*^{\rm out}$ in steps of $2000M$ until convergence is achieved. For an initial value of $r_*^{\rm out}$ we usually choose a value slightly larger than $r_*(r_{\rm max})$, where $r_{\rm max}$ is the desired truncation radius for the normalisation integral $C^-_{\ell m\omega}$.

Once the boundary conditions for $P_{\ell\omega}$ have been calculated, the field at radii $r_* < r_*^{\rm out}$ is obtained by integrating Eq. (3.25) inwards with respect to r_*. Once again we use the `rk8pd` routine from the GSL, with a relative error tolerance of 10^{-12}.

3.2.2 Normalisation integrals

As discussed briefly in Chapter 3.1.3, the radial integration is divided in two. In the region $r_{\rm min} \leq r < r_{\rm cut}$ we use χ as the integration variable,

$$C^{(\chi)-}_{\ell m\omega} := \int_{\chi=0}^{\chi(r_{\rm cut})} J_{\ell m\omega}(r_p(\chi))\frac{dr_p}{d\chi}d\chi. \tag{3.37}$$

The section over $r_{\rm cut} \leq r \leq \infty$, which we earlier named $C^{(r)-}_{\ell m\omega}$, then uses r as the integration variable. $C^{(r)-}_{\ell m\omega}$ is calculated from Eq. (3.32) with the desired level of IBP applied; note that the integral is only to be truncated at finite radius $r_{\rm max}$ *after* integration by parts has been applied.

We make use of two quadrature routines from the GSL [179]. The first is the QAG general purpose adaptive integrator, which can be made to use Gauss-Kronrod rules with varying numbers of points. In particular, we make extensive use of QAG with

the 61pt Gauss-Kronrod rule, an approach we refer to as QAG61. The second method we used is based on the QAWO routine, an adaptive integrator based around a 25pt Clenshaw-Curtis rule tailored towards integrands with a sinusoidal weight function. Such a routine is well suited for calculating $C^{(r)-}_{\ell m\omega}$ because, as we have seen in Eqs. (3.27) and (3.32), the integrand can be factored into a sinusoidal factor and a factor that oscillates with only logarithmic phase.

When evaluating $J_{\ell m\omega}(r_p(\chi))$ in the integrand of $C^{(\chi)-}_{\ell m\omega}$, we require the geodesic functions $t_p(\chi)$ and $\varphi_p(\chi)$. These are calculated numerically by integrating Eqs. (2.19) and (2.21) using the QAG61 routine with a relative error tolerance of 10^{-12}. Evaluating $C^{(r)-}_{\ell m\omega}$ additionally requires the modified time coordinate $\hat{t}_p = t_p - r/v$, which we calculate directly by integrating Eq. (3.23) numerically using QAG61 with error tolerance 10^{-12}.

For a given ℓ, m and ω, the approach taken to evaluate the normalisation integrals $C^{-}_{\ell m\omega}$ with a given truncation radius $r_{\rm max}$ is then as follows:

1. The homogeneous solutions $\psi^-_{\ell\omega}$ and $P_{\ell\omega}$ are calculated using the method described in Sec. 3.2.1 and stored at a dense sample of points in an interval containing $[r_{\rm min}, r_{\rm max}]$. The Wronskian $W_{\ell\omega} = W[\psi^-_{\ell\omega}, \psi^+_{\ell\omega}]$ is also calculated. When, in subsequent steps, the homogeneous solutions are required at arbitrary radii $r_{\rm min} \leq r \leq r_{\rm max}$, these gridpoints are used as initial data and the homogeneous solution at the desired radius is obtained by integrating the appropriate field equation.

2. An initial choice of $r_{\rm cut} = 2r_{\rm min}$ is selected. The integral $C^{(\chi)-}_{\ell m\omega}$ is calculated numerically using the QAG61 routine. The relative error threshold is set at 10^{-10}.

3. If the integrator reports that it cannot achieve the error tolerance, $r_{\rm cut}$ is reduced to $1.5r_{\rm min}$ and step (2) is repeated. This estimate is then stored, whether or not the new relative error estimate is less than 10^{-10}.

4. The integral $C^{(r)-}_{\ell m\omega}$ is integrated by parts X times before being truncated at $r_{\rm max}$, and then evaluated numerically with a relative error threshold of 10^{-10}. This may be achieved using either the QAG61 or QAWO routine.

5. An order Y correction to the neglected tail (appropriate to the number of iterations of IBP) is then added.

The above algorithm involves two parameters, X and Y, which control the number of iterations of IBP and the order of the tail correction, respectively. We refer to such a method as *IBPXcorrY*. For example, IBP0corr0 uses neither integration by parts nor adds any approximation for the neglected tail, while IBP4corr5 uses 4 iterations of IBP and a 5th order correction.

One issue presents itself when attempting to use IBP at small frequencies. At small frequency, both the surface term and integral in Eq. (3.32) can grow very large, and

there is a significant degree of cancellation between them. This results in a loss of precision, which, for some ℓm modes, creates a noisy spike in the $C^-_{\ell m\omega}$ spectrum at small frequency. Fortunately, a simple solution is available to this problem. By introducing an additional breakpoint $r_{\rm split}$ between $r_{\rm cut}$ and $r_{\rm max}$, one can evaluate the integral without IBP (or using low order IBP) in the interval $r_{\rm cut} < r < r_{\rm split}$, and then use a higher order of IBP for $r > r_{\rm split}$. When $r_{\rm split} \gg r_{\rm cut}$, the error from cancellation between the surface term at $r_{\rm split}$ and the integral over $r > r_{\rm split}$ is much reduced. We refer to such split-order IBP methods as *IBPXYcorrZ*, where X and Y are the orders of the IBP used in the regions $r_{\rm cut} \leq r < r_{\rm split}$ and $r > r_{\rm split}$ respectively, and Z is the order of the tail correction applied. In practice we only make use of IBP04corrZ methods in this paper.

3.3 Numerical results for $C^-_{\ell m\omega}$

In this section we will examine the effectiveness of the methods we have developed to mitigate the high-frequency noise problem. Satisfied with the results, we will then examine the features of the $C^-_{\ell m\omega}$ spectra.

Before displaying the numerical results, it is worth discussing whether the $C^-_{\ell m\omega}$ spectra can be assigned physical meaning. The EHS $\tilde{\psi}^-_{\ell m\omega}(r)$ is not a physical field by itself, although, by construction, it does coincide with the true frequency modes of the physical scalar-field (given in Eq. (2.106)) when $r \leq r_{\rm min}$. More significantly, there is ambiguity in the definition of $C^-_{\ell m\omega}$; in principle, one may choose to exchange factors between $C^-_{\ell m\omega}$ and $\psi^-_{\ell\omega}(r)$, altering their individual values without changing their product. Put another way, the value of $C^-_{\ell m\omega}$ is only defined up to a change in the (arbitrary) normalisation of the homogeneous solution $\psi^-_{\ell\omega}(r)$. Indeed, formally – but not practically – one could even adopt a normalisation in which $C^-_{\ell m\omega} \equiv 1$. But we have not left the normalisation of $\psi^-_{\ell\omega}$ arbitrary during our numerical calculation, adopting instead the concrete choice $c_0^{\rm eh} = 1$ in Eq. (2.100). With this unit-normalised convention, one can assign a certain interpretation to the value of $C^-_{\ell m\omega}$ as follows. For $2M < r \leq r_p(t)$ we have

$$\psi_{\ell m}(t, r) = \int_{-\infty}^{+\infty} C^-_{\ell m\omega} \psi^-_{\ell\omega}(r) e^{-i\omega t}\, d\omega. \tag{3.38}$$

Taking $r \to 2M$ with $v := t + r_*$ fixed, and recalling $\psi^-_{\ell\omega} \sim e^{-i\omega r_*}$ as $r \to 2M$, this gives

$$\psi^{\mathcal{H}^+}_{\ell m}(v) = \int_{-\infty}^{+\infty} C^-_{\ell m\omega} e^{-i\omega v}\, d\omega, \tag{3.39}$$

i.e. $C^-_{\ell m\omega}$ is the Fourier transform with respect to advanced time of the spherical harmonic modes of the scalar field on the event horizon $\mathcal{H}^+$.

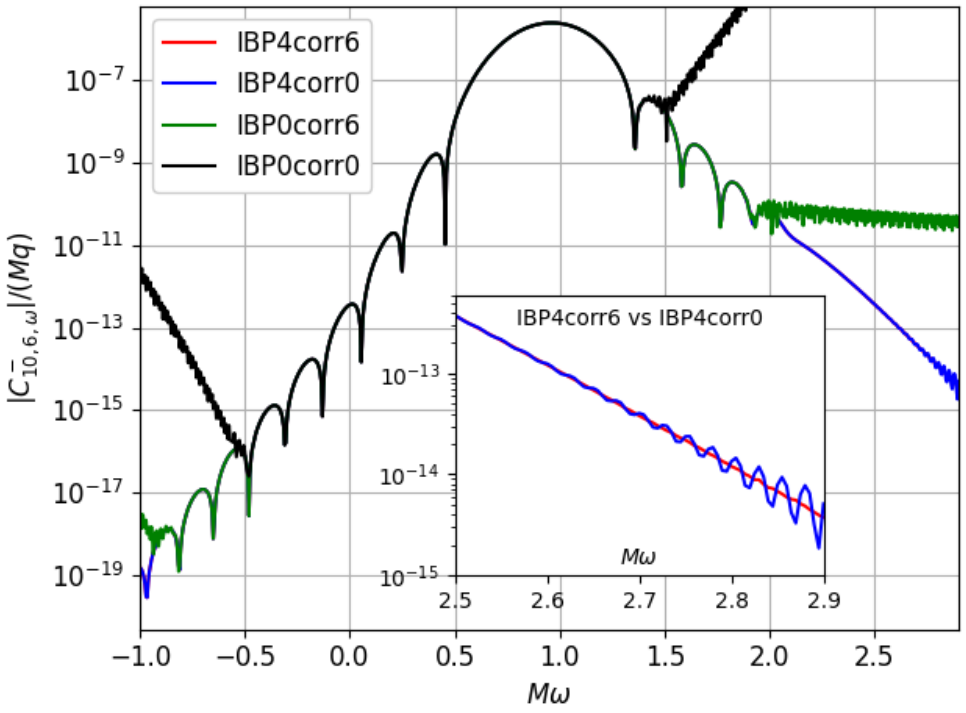

FIGURE 3.2: $C^-_{\ell m\omega}$ against frequency for the mode $(\ell, m) = (10, 6)$ and the geodesic with parameters $E = 1.1$ and $r_{\min} = 4M$, as calculated using the IBP0corr0, IBP0corr6, IBP4corr0 and IBP4corr6 methods. All numerical integrals were calculated using the QAWO quadrature routine and truncated at $r_{\max} = 2000M$. Tail corrections alone are sufficient to delay the onset of noise until further into the tail, but IBP4 is even more effective. Tail corrections provide a small, but non-zero, positive effect when using IBP4.

3.3.1 Effect of IBP and tail corrections

We begin by investigating the effect of varying the order of IBP and tail correction on the calculation of $C^-_{\ell m\omega}$. Figure 3.2 displays $C^-_{\ell m\omega}$ for the mode $(\ell, m) = (10, 6)$ and the geodesic $E = 1.1$ and $r_{\min} = 4M$, as calculated using different methods. Comparing the IBP0corr0 and IBP0corr6 results confirms that the correction scheme delays the onset of noise and hence allows a greater level of decay to be achieved, in this case gaining approximately 3 orders of magnitude greater decay to the right of the peak. This confirms the utility of the correction scheme, and the successful cancellation between the numerical integral and the tail correction also validates the implementation of the correction. One may confirm that using a lower-order correction produces a smaller, but still positive, improvement.

If instead we compare IBP0corr6 and IBP4corr0, we see that the IBP4 without tail corrections achieves a greater level of decay than corrections alone, by approximately 3 additional orders of magnitude to the right of the peak in this case. The inset compares IBP4corr0 and IBP4corr6 in the right-hand tail of the spectrum, showing that including

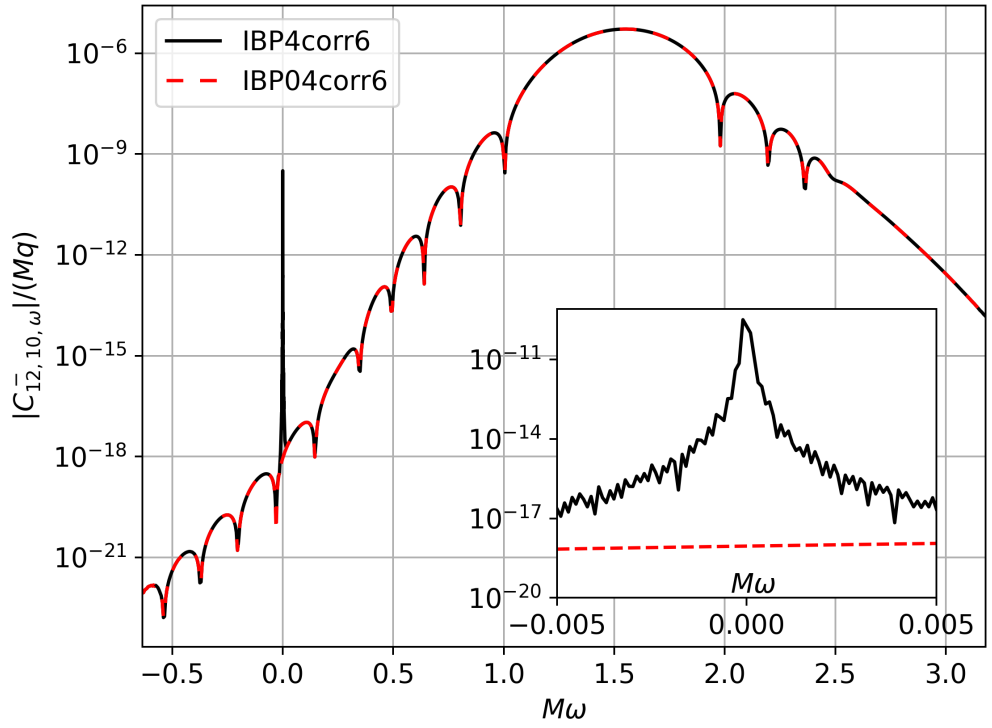

FIGURE 3.3: $C^{-}_{\ell m\omega}$ against frequency for the mode $(\ell, m) = (12, 10)$ and the geodesic with parameters $E = 1.1$ and $r_{\rm min} = 4M$, as calculated using the IBP4corr6 and IBP04corr6 methods. All numerical integrals were calculated using the QAWO routine and truncated at $r_{\rm max} = 2000M$. For the split-order IBP04corr6 method, the transition between IBP0 and IBP4 took place at $r_{\rm split} = 500M$. When using IBP4 for the entire integration region, a sharp spike centred on $\omega = 0$ is observed in the spectrum, which appears noisy when zoomed in (*inset*). The use of split-order IBP prevents this phenomenon in all instances it has been observed, and is adopted as standard at small frequency.

the tail corrections introduces further improvement. This improvement, however, is responsible for only a small proportion of the total improvement compared to IBP0corr0, and the effect of including tail corrections is much smaller with IBP4 than with IBP0. Despite this, we believe that continuing to include tail corrections when using IBP is justified on the grounds of improved accuracy (including a reduction in truncation error at intermediate frequencies) and negligible cost. The tail corrections are expressed in terms of gamma functions, which are near-instantaneous to compute compared to the numerical integrals.

Next we investigate the benefits of split-order IBP. Figure 3.3 displays $C^{-}_{\ell m\omega}$ for the mode $(\ell, m) = (12, 10)$, again for the geodesic with parameters $E = 1.1$ and $r_{\rm min} = 4M$, as calculated using the pure IBP4corr6 method and the split-order IBP04corr6 method. This example has been chosen because it displays the serious side effect of IBP raised in Sec. 3.2.2, where cancellation between the surface term and the numerical integral sometimes causes a sharp numerical blow-up at small-frequency. As illustrated in the figure, this issue does not occur when the use of IBP is delayed until larger radii (in

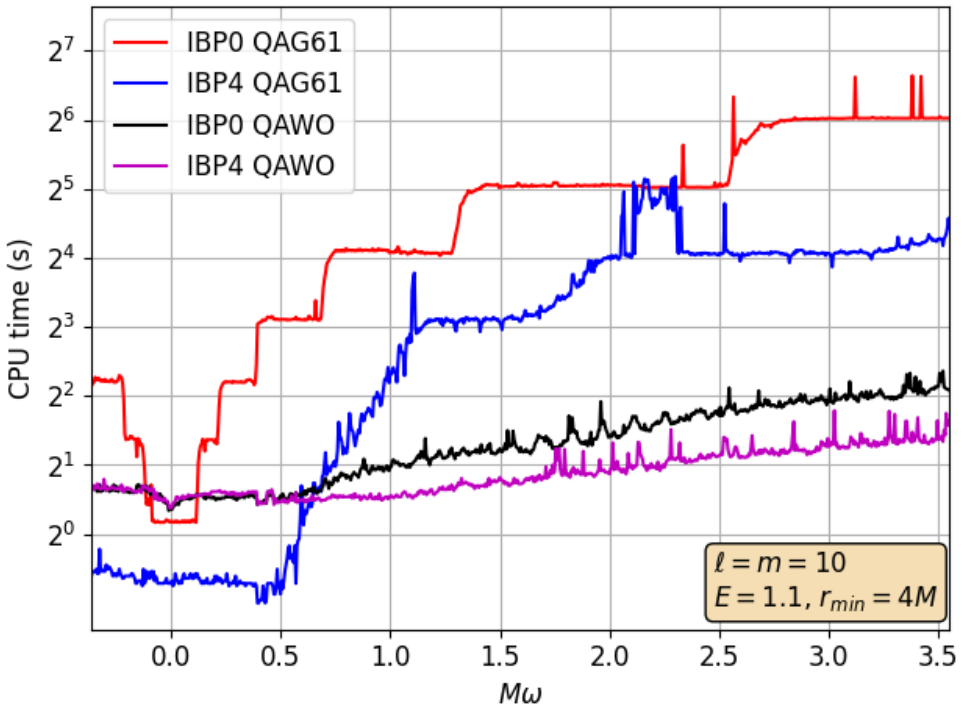

FIGURE 3.4: CPU time to calculate a single $C^{-}_{\ell m\omega}$ integral (truncated at $r_{\max} = 2000M$) as a function of frequency using different methods. The mode $\ell = m = 10$ was selected for the geodesic with parameters $E = 1.1$, $r_{\min} = 4M$, and the test was carried out on a laptop computer with Intel i7-11850H processor (8 cores at 2.5 GHz). Different orders of IBP (0 vs 4) and quadrature routines (QAG61 vs QAWO) for computing the $r \geq r_{\rm cut}$ portion of $C^{-}_{\ell m\omega}$ were tested. Using IBP has a modest time benefit in most circumstances, but the optimum quadrature routine depends on frequency.

this case $r_{\rm split} = 500M$). In fact, the use of split-order IBP has resolved the issue of small-frequency spikes in every instance they have been observed. Currently there is no means of predicting whether a particular ℓm mode will be affected by this rare but serious issue in advance of the calculation, so we instead adopt a cautious approach and use the split-order IBP04 method as the first-line method for all modes at small frequency (typically conservatively chosen to mean frequencies $|M\omega| < 0.05$).

3.3.2 Performance

Figure 3.4 displays the time taken to calculate $C^{-}_{10,10,\omega}$ as a function of ω for the geodesic with $E = 1.1$ and $r_{\min} = 4M$, using different choices of IBP order and quadrature routine to evaluate $C^{(r)-}_{\ell m\omega}$. At small frequencies, a single integral takes $\sim 1s$ when using QAG61 quadrature without any integration by parts, but this quickly rises in a stepwise fashion (almost doubling each step) and a single integral can exceed $60s$ at $|M\omega| \gtrsim 2.5$. Introducing IBP4 but maintaining QAG61 quadrature decreases the runtime to sub-$1s$ at small frequency, but the runtime still increases rapidly and may exceed $15s$ at the highest

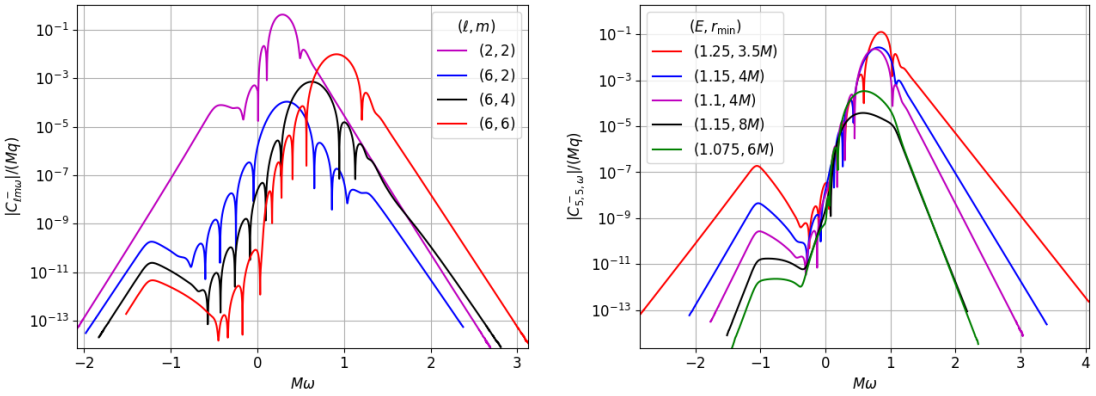

FIGURE 3.5: Selection of $C^{-}_{\ell m\omega}$ spectra for a variety of parameters. *Left panel*: different values of (ℓ, m) with fixed orbital parameters $E = 1.1$, $r_{\min} = 4M$. *Right panel*: fixed $\ell = m = 5$ for different scatter orbits. The IBP4corr6 method was used for frequencies $|M\omega| \geq 0.05$, and IBP04corr6 with $r_{\text{split}} = 500M$ was used for frequencies smaller than this. All numerical integrals were truncated at $r_{\max} = 2000M$. In all cases the displayed frequency range is the maximum one before noise is detected at the endpoints.

frequencies, a reduction of approximately 75% compared to IBP0. QAWO quadrature produces a significant reduction in runtime at high frequencies, keeping runtimes below approximately $5s$ in this test, but at lower frequencies the QAG61 routine is faster. This is not unexpected; when the (sub-)interval length falls below a few wavelengths, the QAWO routine defaults to a 15pt Gauss-Kronrod rule, which is lower order than the 61pt rule we use with the QAG61 routine [179]. Integration by parts produces an approximately 40% ($\sim 1.5s$) time saving when using QAWO quadrature at high frequencies, but makes little difference at low frequency.

For convenience we wish to adopt a single quadrature routine to evaluate $C^{(r)-}_{\ell m\omega}$, to be used at all frequencies. It is therefore sensible to make use of the QAWO routine, because this is the faster routine at the majority of frequencies we require, and because this routine makes the largest absolute time savings. From here on, $C^{(r)-}_{\ell m\omega}$ is always evaluated using the QAWO routine unless otherwise stated.

3.3.3 General features

The left panel of Fig. 3.5 displays sample $C^{-}_{\ell m\omega}$ spectra for different ℓm modes for the geodesic with parameters $E = 1.1$ and $r_{\min} = 4M$. For fixed ℓ and $m \geq 0$, the location of the peak frequency increases in approximate proportion to m, while the amplitude at peak also increases with m and decreases with ℓ. The exponential decay at large $|M\omega|$ is evident. The right panel of Fig. 3.5 instead shows the fixed mode $\ell = m = 5$ for a variety of different orbital parameters. Decreasing the periapsis radius increases the amplitude as expected. Increasing the energy results in a broader spectrum, but only a slight increase in the peak amplitude.

3.3.4 Quasinormal modes

A striking feature in Fig. 3.5 is the presence of "mountains" in the tail of the spectrum, defined by a sharp triangular peak that interrupts the overall decay trend. As can be seen in the left panel of Fig. 3.5, the location and profile of this feature is roughly independent of m for a given ℓ. The right panel meanwhile illustrates that this feature occurs in roughly the same location for a wide variety of orbital parameters, although its prominence is variable. These spectral features may occur at either positive or negative frequency, and occasionally both for the same mode.

These observed behaviors hint at the physical origin of the mountain feature. Indeed, our investigation reveals that the location of the mountain peak coincides with (plus or minus) the real part of the fundamental quasinormal mode frequency, suggesting these features may be associated with quasinormal excitation of the black hole. We note that for scalar perturbations in Schwarzschild, the quasinormal mode frequencies are independent of m, and of the orbital parameters, in line with the above observations. Quasinormal excitation phenomena have previously been observed in self-force calculations for highly eccentric bound orbits [156, 180], and subsequently in both gravitational and scalar calculations for scatter orbits [148, 149].

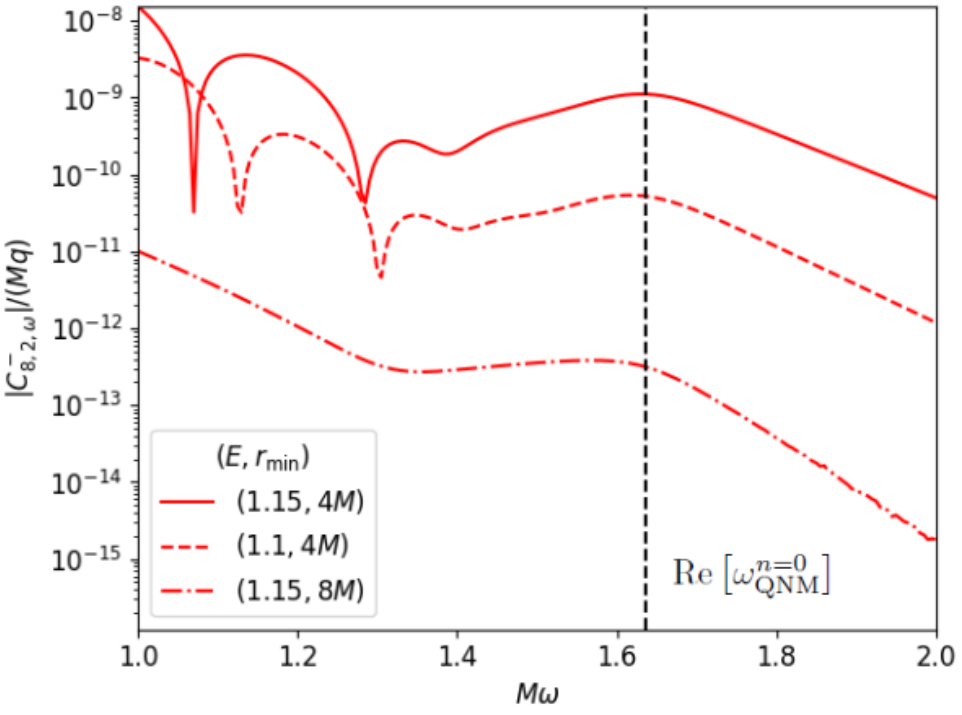

FIGURE 3.6: $C^{-}_{\ell m\omega}$ centred on the positive-frequency mountain feature for $(\ell, m) = (8, 2)$ and a selection of orbits. Indicated in vertical dashed line is the real part of the corresponding fundamental quasinormal frequency, $\mathrm{Re}(\omega^{n=0}_{\mathrm{QNM}}) \approx 1.63656/M$, which appears to coincide with the peak frequency. The mountain feature becomes more prominent when $r_{\min}$ is decreased.

Figure 3.6 illustrates mountains at positive frequency for $(\ell, m) = (8, 2)$ and a selection of orbits, also showing the value of real part of the fundamental quasinormal mode frequency $\omega^{n=0}_{\rm QNM}$. The figure demonstrates the close proximity between the peak and the fundamental quasinormal frequency. It also illustrates the increasing prominence of the quasinormal mode contribution as $r_{\rm min}$ decreases and the orbit further penetrates the strong-field region.

This phenomenon becomes particularly pronounced in the *near-critical* limit, where the impact parameter b lies close to the critical value $b_c(v)$ defined in Eq. (2.9). This is illustrated vividly in Fig. 3.7, which shows the $C^{-}_{\ell m\omega}$ spectrum for $(\ell, m) = (10, 2)$ for the geodesic with parameters $v = 0.8$ and $b = 6.07387M$, corresponding to $b - b_c(v) \approx 0.0005$. Along this orbit, the particle spends a prolonged period of time orbiting at around $r_{\rm min} \approx 3.18M$, eliciting strong quasinormal excitation. The resulting triangular peaks in the $C^{-}_{\ell m\omega}$ spectra can approach - and sometimes even exceed - the amplitude of the primary central peak.

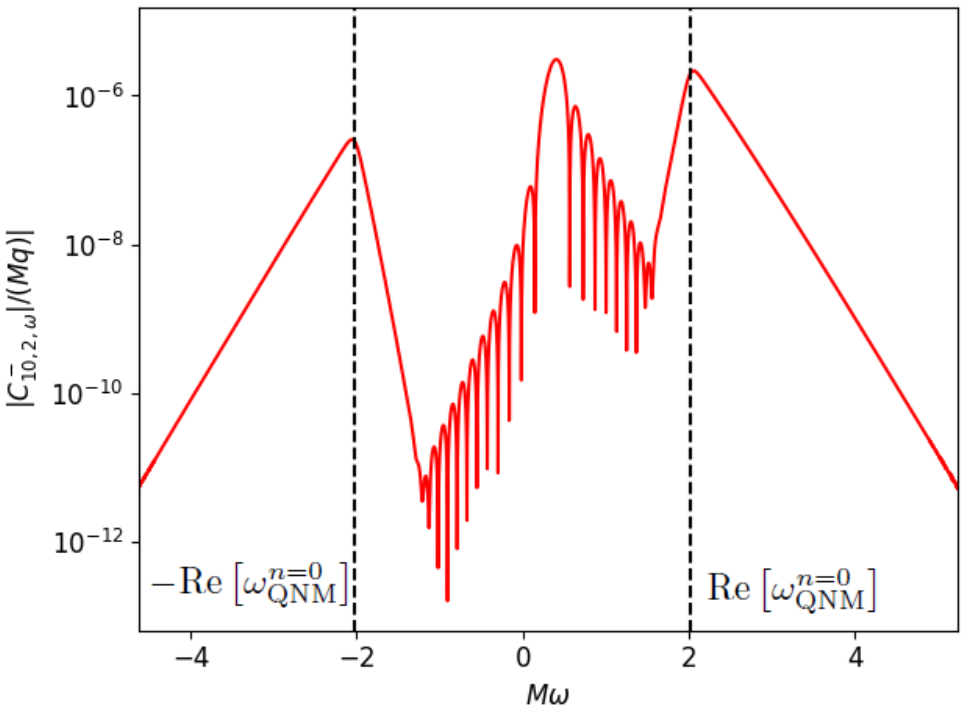

FIGURE 3.7: $C^{-}_{\ell m\omega}$ with $(\ell, m) = (10, 2)$ for the orbit with parameters $v = 0.8$ and $b = 6.07387M$ (corresponding to $E = 5/3$ and $r_{\rm min} \approx 3.18M$). Indicated in vertical dashed lines are plus and minus the real part of the fundamental $\ell = 10$ quasinormal frequency, $\mathrm{Re}(\omega^{n=0}_{\rm QNM}) \approx 2.02132/M$.

3.3.5 Zeros in the spectrum

Another notable feature in Fig. 3.5 are the locations where $|C^-_{\ell m\omega}|$ drops sharply, assumed to vanish. These points correspond to frequencies at which both the real and imaginary parts of $C^-_{\ell m\omega}$ appear to vanish simultaneously. Individual zeros of the real and imaginary parts are expected, but it is not clear what physical or mathematical mechanism is responsible for simultaneous zeros. Features suggestive of these zeroes have previously been observed in discrete spectra (see e.g. Fig. 1 in Ref. [113]), but we are not aware of any proposed explanations.

One possible explanation for this phenomenon comes from considering the behaviour of the homogeneous solutions $\psi^{\pm}_{\ell\omega}$ at low frequency. As described in Chapter 2.4.2, boundary conditions for $\psi^-_{\ell\omega}$ are specified near the horizon and then integrated outwards. For sufficiently small frequencies, there is a region $r \lesssim \omega^{-1}$ where the potential term in Eq. (2.94) dominates over the ω^2 term, and $\psi^-_{\ell\omega}$ behaves like a static solution, quickly approaching a (complex-valued) multiple of the polynomially growing real-valued solution $\psi^-_{\ell,\omega=0}$. Likewise, boundary data for $\psi^+_{\ell\omega}$ is specified in the large-r wave-zone, and it generically becomes proportional to the real-valued $\psi^+_{\ell,\omega=0}$ as we move inwards into the potential-dominated region.

Therefore, if ω is sufficiently small that a potential-dominated region exists, and if $r_{\min} \lesssim \omega^{-1}$, then there is a radial range $r_{\min} < r \lesssim \omega^{-1}$ where the homogeneous solutions may be approximated by (frequency-dependent) complex multiples of the respective static solution. It follows that the integrand in this region can be expressed as a real function of r multiplied by a frequency dependent complex constant. The integrand is largest in the potential-dominated region $r_{\min} < r \lesssim \omega^{-1}$ on account of the quasi-static polynomial growth of the homogeneous solutions, and thus the integral over this region is expected to provide the dominant contribution to $C^-_{\ell m\omega}$. The real-valued factor of the integrand is oscillatory, and thus the integral of this is an oscillatory function of ω too; where the real-valued integral vanishes, both real and imaginary parts of $C^-_{\ell m\omega}$ vanish simultaneously.

Chapter 4

Time-domain reconstruction and the scalar-field self-force

Having established a reliable and accurate method to calculate the frequency-modes of the extended homogeneous solution, we turn our attention to the problem of reconstructing the spherical harmonic modes of the time-domain field, and hence the self-force. Our approach relies on a multi-step process in which discretised $C^{-}_{\ell m\omega}$ data is generated first, and then intermediate frequencies are obtained using interpolation when evaluating the Fourier integrals for the time-domain field. Numerical results are presented using our method, showing excellent agreement with regularisation parameters up to at least $\ell = 25$ near to periapsis, and seemingly exceeding the precision of the time-domain code of Ref. [149] in this regime. Our frequency-domain method begins to break down rapidly at larger radii, however, due to an issue calculating modes with large values of ℓ. Without an immediate solution to this problem, we instead dynamically truncate the mode-sum in Eq. (2.49) to exclude problematic ℓ-modes when they are encountered, resulting in significantly improved large-r_p behaviour. In the final section of this chapter, we discuss the root cause of our difficulties at large r_p and large ℓ, and propose potential future directions to resolve this issue completely.

4.1 Efficient time-domain reconstruction

In order to calculate the ℓ-mode contributions to the t, r and φ derivatives of the scalar-field at a point x^{α}_{p} along the orbit, we have to numerically evaluate the inverse Fourier

integrals

$$\Phi_t^{\ell m-} := -\frac{1}{r_p}\int_{-\infty}^{+\infty} d\omega\, i\omega\, C^-_{\ell m\omega}\psi^-_{\ell\omega}(r_p)e^{-i\omega t_p}, \tag{4.1}$$

$$\Phi_r^{\ell m-} := \int_{-\infty}^{+\infty} d\omega\, C^-_{\ell m\omega}\partial_r\left(\frac{\psi^-_{\ell\omega}(r)}{r}\right)_{r=r_p} e^{-i\omega t_p}, \tag{4.2}$$

$$\Phi_\varphi^{\ell m-} := \frac{1}{r_p}\int_{-\infty}^{+\infty} d\omega\, im\, C^-_{\ell m\omega}\psi^-_{\ell\omega}(r_p)e^{-i\omega t_p}, \tag{4.3}$$

for $m \geq 0$ and $\ell + m$ even. Using the symmetry relation in Eq. (2.93), the ℓ-modes of the full force are then given by

$$F^{\text{full}-}_{\alpha,\ell} = q\Phi^{\ell 0-}_\alpha Y_{\ell 0}\left(\frac{\pi}{2},\varphi_p\right) + 2q\sum_{m>0}\text{Re}\left[\Phi^{\ell m-}_\alpha Y_{\ell m}\left(\frac{\pi}{2},\varphi_p\right)\right], \tag{4.4}$$

for $\alpha = t, r, \varphi$, where only modes with $\ell + m =$ even contribute.

The most obvious way to evaluate integrals (4.1)-(4.3) is to use an adaptive integrator such as the QAG61 routine we have made extensive use of. One issue with this approach is that an adaptive integrator will generically call different frequencies when evaluating different components, or when evaluating the integrals at different orbital positions. The oscillatory factors $\psi^-_{\ell\omega}(r_p)$ and $e^{-i\omega t_p}$ in the integrand may also require a denser sampling to resolve, particularly when $|t_p|$ is large, resulting in wasteful over-sampling of the normalisation integrals. Given that a single $C^-_{\ell m\omega}$ integral takes several seconds to compute in general (see Sec. 3.3.2), it would be a very lengthy process to calculate $C^-_{\ell m\omega}$ on the fly at every required frequency.

Interpolation provides one solution to this problem. In this approach, one first calculates the integrals $C^-_{\ell m\omega}$ at a dense sample of frequency nodes ω_n for the ℓm-modes required. The value of $C^-_{\ell m\omega}$ at an intermediate frequency ω can then be estimated using interpolation. We do this by identifying the node ω_N that lies nearest to ω, and then using the $2d$-degree polynomial that fits the data at the nodes ω_{N-d}, ω_{N-d+1}, ..., ω_{N+d}. This interpolation is carried out in practice using the `gsl_interp_polynomial` interpolator type included in the GSL [179] and a degree 8 polynomial.

Given a repository of $C^-_{\ell m\omega}$ data at an appropriately dense sample of frequencies, integrals (4.1)-(4.3) are then evaluated using the QAG61 routine with a relative error threshold of 10^{-8}. These are summed over m to get $F^{\text{full}-}_{\alpha,\ell}$ using Eq. (4.4).

4.2 Overall approach

The numerical method for calculating the normalisation integrals was outlined in Sec. 3.2.2, and in Sec. 4.1 we described how to efficiently calculate the ℓm-mode contributions to

the scalar field in the time domain, and hence the ℓ modes of the full force. We now outline how these blocks are combined to produce an end-to-end calculation of the self-force along an orbit with parameters $(E, r_{\rm min})$.

Step 1: We find the maximal frequency limits that may be used before high-frequency noise appears in the spectra of $C^-_{\ell m\omega}$. For a given ℓm mode, we begin calculating $C^-_{\ell m\omega}$ at $\omega = m\omega_{\rm circ}$, corresponding to the frequency of a circular geodesic of radius $r_{\rm min}$, namely $M\omega_{\rm circ} = (M/r_{\rm min})^{3/2}$. This frequency was used as an estimate of the peak frequency, and worked well in our tests. The frequency was then increased in steps $M\Delta\omega = 5 \times 10^{-3}$, and at each step the following procedure was applied:

1. If fewer than 6 data points $(\omega, C^-_{\ell m\omega})$ are available, continue.
2. If more than 6 data points are available, take the most recent 6 and calculate the gradients of the 5 chords in this interval.
3. Flag noise if there are 3 or more changes of sign between consecutive gradients.

Once noise is detected, the noisy interval was discarded, the maximal value of ω was recorded and the process halted. The same was then applied stepping backwards for $\omega < m\omega_{circ}$. This is repeated for all ℓm modes with $m \geq 0$ and $\ell + m =$ even, up to some $\ell = \ell_{\rm max}$. The values of the integrals and frequency limits were stored. To minimise duplicate evaluations of the homogeneous solutions $\psi^-_{\ell\omega}$ and $P_{\ell\omega}$ (which are m-independent), modes with the same value of ℓ but different m were calculated together.

Step 2: Additional $C^-_{\ell m\omega}$ data at intermediate frequencies may be calculated and stored if the desired frequency sampling density is higher than the one used in Step 1.

Step 3: Given the stored $C^-_{\ell m\omega}$ data for all modes up to $\ell = \ell_{\rm max}$, the corresponding ℓ-modes of the full force $F^{{\rm full}-}_{\alpha,\ell}$ may be calculated at any point along the orbit using the method of Chapter 4.1. For a given ℓ, the terms in the mode sum (2.49) are calculated by subtracting the regularisation terms up to and including $F^{[6]}_\alpha$. The self-force may then be approximated by summing the mode-sum up to $\ell = \ell_{\rm max}$.

Our calculation can be significantly accelerated by making use of parallelisation, which we achieved using the OpenMP library [181]. The calculation of integrals $C^-_{\ell m\omega}$ with different values of ℓ and ω have no common dependencies, which makes these labels ideal for parallelising over. However, in Step 1 above, the frequencies required are not known in advance, so Step 1 is only parallelised over ℓ. Step 2 may be parallelised over both ℓ and ω because the frequencies are known in advance, motivating the division between Steps 1 and 2. Parallelisation over m is also possible, but this then requires duplicate calculations of the homogeneous solutions, and therefore is only advisable if there remain additional unutilised cores after parallelising over ℓ and/or ω. Finally, the calculation of ℓm-mode contributions to the scalar-field derivatives for Step 3 may also

be parallelised over ℓ, m, orbital position or component; we were able to utilise all cores available to us by parallelising only over orbital position.

4.3 Scalar-field self-force: initial results

We illustrate the calculation of the self-force with the example of the geodesic orbit with parameters $E = 1.1$ and $r_{\rm min} = 4M$, which is displayed in Fig. 2.1. The coefficients $C^{-}_{\ell m\omega}$ were calculated for ℓ up to a maximum value $\ell_{\rm max} = 25$ using the IBP4corr6 method with $r_{\rm max} = 2000M$ for frequencies $|M\omega| \geq 0.05$, and IBP04corr6 with $r_{\rm split} = 500M$ and $r_{\rm max} = 2000M$ for $|M\omega| < 0.05$. The $C^{-}_{\ell m\omega}$ data was stored with density $M\Delta\omega = 1.25 \times 10^{-3}$. The ℓm-modes of the scalar field derivatives in the time-domain are obtained by integrating Eqs. (4.1)-(4.3) numerically and then constructing $F^{\rm full-}_{\alpha,\ell}$ using Eq. (4.4), as described in Chapter 4.1.

As a first test, we validate our code against the analytically known regularisation parameters, confirming that the terms in the mode sum (2.49) decay with ℓ at the expected rate. We then display the self-force along the orbit. At both stages we compare the results obtained using our frequency-domain (FD) code to those obtained with the time-domain code developed in Refs. [149], hereafter referred to simply as the time-domain (TD) code.

4.3.1 Large-ℓ behaviour and code validation

Figure 4.1 displays the regularised ℓ-mode contributions to the t component of the self-force at the point $r_p = 6M$ along the inbound leg of the orbit, with two different levels of regularisation applied. In the first set of data, represented by solid circles, the regularisation terms involving A_t and B_t have been subtracted from $F^{\rm full-}_{\alpha,\ell}$, as in the summand of Eq. (2.49). At large ℓ the terms of this series are known to behave like the higher-order regularisation terms in expression (2.55), decaying as ℓ^{-2}. Comparison with the reference line representing the first term in that expression confirms that our numerical results have the correct asymptotic behaviour, holding until at least $\ell = 25$.

The convergence of the mode-sum may be accelerated by subtracting the higher-order regularisation terms in expression (2.55) from the summand of Eq. (2.49). Once all terms up to and including $F_{[6]\alpha}$ have been subtracted, the terms of the mode sum should behave asymptotically as the first neglected term in expression (2.55), which is expected to decay as ℓ^{-8} (with a coefficient we don't currently have). The terms in the mode-sum with parameters up to and including $F_{[6]t}$ removed are represented in Fig. 4.1 with solid squares, and good agreement with the reference line proportional to ℓ^{-8} is seen all the way until $\ell = 25$, when the numerical data begins to deviate from the trend line.

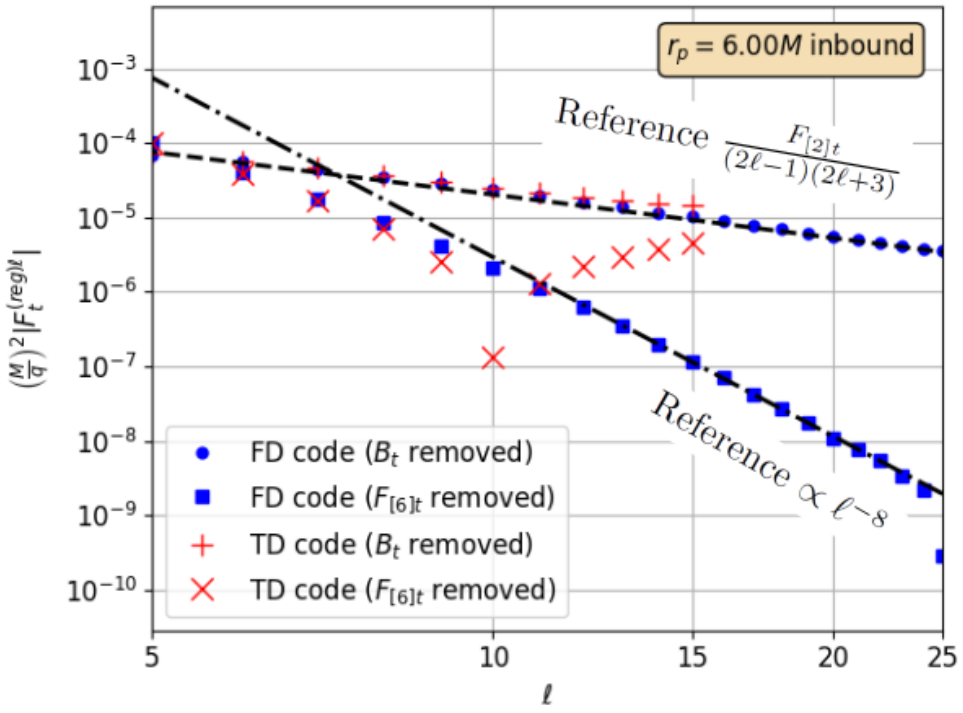

FIGURE 4.1: Regularised ℓ-mode contributions to the t component of the self-force at the point $r_p = 6M$ along the inbound leg of the orbit with parameters $E = 1.1$ and $r_{\min} = 4M$. The corresponding results from the time-domain code of Ref. [149] are also displayed for comparison for $5 \leq \ell \leq 15$. Two different levels of regularisation, subtracting parameters up to and including B_t or $F_{[6]t}$, are displayed. The B-regularised and $F_{[6]}$-regularised data agree well at large ℓ with the reference lines $\frac{F_{[2]t}}{(2\ell-1)(2\ell+3)}$ (dashed) and $\propto \ell^{-8}$ (dash-dot) respectively, validating our code. Note how the $F_{[6]t}$-regularised TD data becomes noise-dominated already at $\ell \sim 10$, while the corresponding FD data remains faithful down to $\ell \sim 24$. Evidently, the FD calculation is much more precise.

Obtaining the correct asymptotic behaviour is a strong internal check on the accuracy of our code. The ℓ-mode contributions to the full-force diverge like ℓ, so to achieve the expected decay rate requires delicate cancellation between the numerically calculated ℓ-mode and the regularisation terms, with a greater degree of cancellation required at larger ℓ and when greater numbers of regularisation parameters are subtracted. Once ℓ becomes large enough, the required degree of cancellation exceeds the precision of the numerical cancellation, and noise is expected to appear. In the example in Fig. 4.1, this is first observed for the $F_{[6]}$-regularised data at around $\ell = 25$.

Additional, external validation is provided by comparison with the TD results, displayed in red in Fig. 4.1. At small ℓ there is good agreement, but by $\ell = 10$ the $F_{[6]}$-regularised TD results have visibly broken away from the corresponding FD ones, with the latter continuing to approach the reference lines. By $\ell = 15$, this deviation is visible even in the B-regularised modes. Given the superior agreement with the regularisation parameters, it is evident that the FD code is significantly more accurate than the TD code at large-ℓ,

at least at this orbital position. This also enables the FD code to reach larger values of ℓ before noise appears in the regularised modes, allowing us to use larger values of $\ell_{\rm max}$ than the TD code, and thus reducing the error from truncating the mode-sum at finite ℓ.

4.3.2 Self-force along the orbit

Figure 4.2 displays the t, r and φ components of the self-force F_α^{self} as functions of time t and radius r along our sample orbit. We used $\ell_{\rm max} = 15$, to allow like-to-like comparison with existing TD results, which are also plotted for comparison. The self-force is, predictably, largest in the vicinity of periapsis ($r = r_{\rm min}$, $t = 0$), but the peaks are offset from the periapsis position. This behaviour was previously noted for the scalar-field self-force along scatter orbits in Ref. [149], and for bound orbits (e.g. Ref. [182]).

There is a good agreement between the FD and TD codes in the near-periapsis region $4M \leq r \lesssim 10M$ ($|t| \lesssim 37M$), where the results are visually indistinguishable. The insets to Fig. 4.2 display the relative difference (normalised by the results of the FD code) between the two methods for two different choices of the TD grid spacing h. With the higher TD resolution ($h = M/128$), the relative difference is between 10^{-3} and 10^{-2} in the post-periapsis, small radius region for the t and r components, and slightly larger than this shortly before periapsis. For the φ component, a tighter agreement of between 10^{-4} and 10^{-3} is achieved in this region. Near periapsis, the relative difference is sensitive to the resolution used in the TD code, suggesting that the FD code is more accurate here, consistent with our findings in Chapter 4.3.1. The relative difference gives an estimate of the relative numerical error in the TD calculation, and an upper bound on the numerical error of the FD calculation with this choice of $\ell_{\rm max}$. The closer agreement for $F_\varphi^{\rm self}$ may be attributed to the greater accuracy of the TD code for this component, which (unlike the t or r components) is obtained directly from the spherical harmonic modes of the scalar field themselves, without having to take numerical derivatives.

As we move outwards along the orbit, the agreement between the TD and FD results deteriorates, independently of the TD resolution. For $F_r^{\rm self}$ and $F_\varphi^{\rm self}$ this occurs at approximately $r = 10M$ ($t \sim 37M$), but agreement is maintained until around $r = 15M$ ($t \sim 50M$) for $F_t^{\rm self}$. Referring back to the main plots in Fig. 4.2, it is clear that the FD method is responsible, breaking sharply away from the smoothly decaying curve obtained using the TD method. An examination of the ℓ-mode contributions to the self-force at these larger radii shows that the regularised ℓ-modes in the tail of the mode sum cease to decay, and instead begin to blow up rapidly with ℓ. As the radius is increased, the problem affects successively lower values of ℓ. This phenomenon is associated with error messages from the numerical integrator, indicating that the inverse Fourier integrals (4.1)-(4.3) cannot be evaluated to the requested relative error tolerance of 10^{-8}.

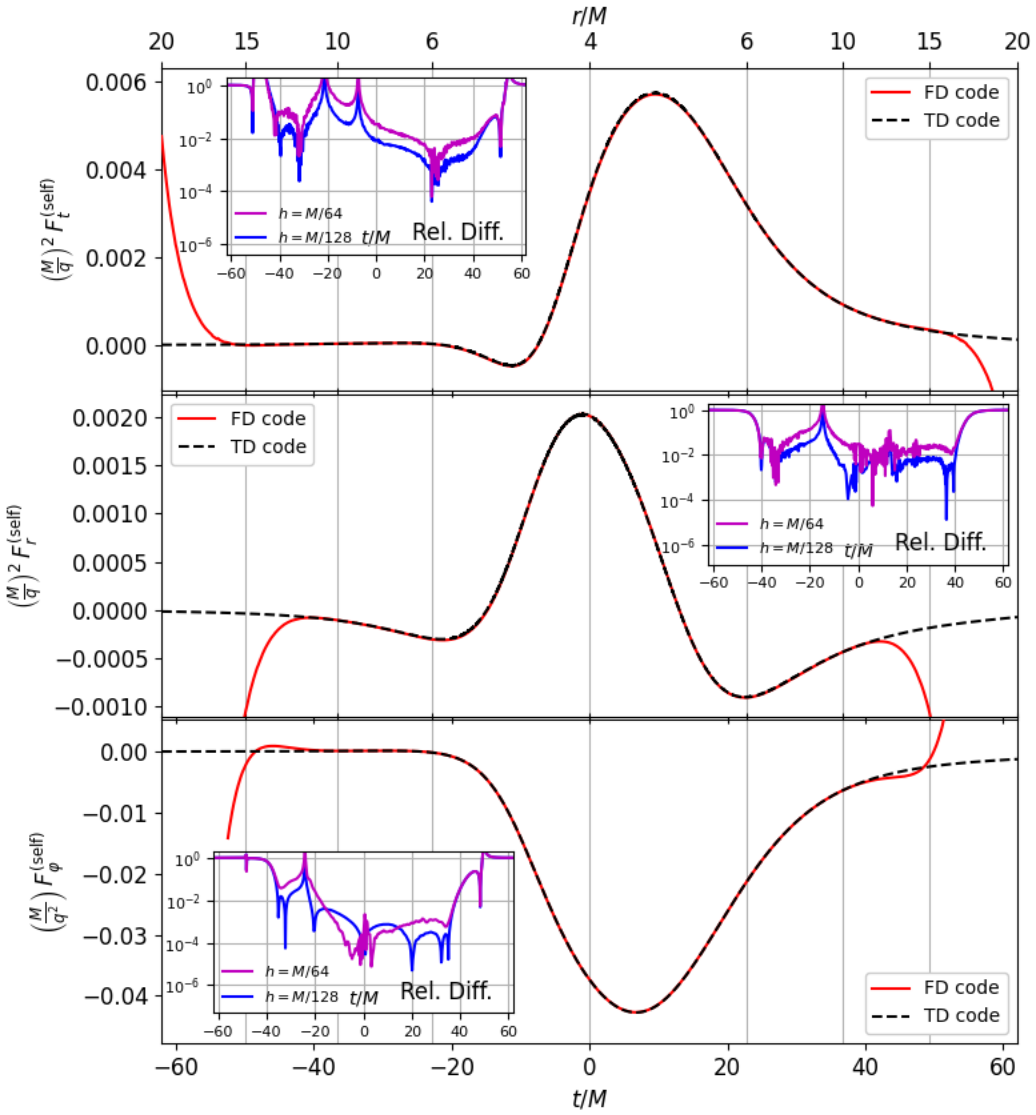

FIGURE 4.2: Components $F_t^{\rm self}$ (*top*), $F_r^{\rm self}$ (*middle*) and $F_\varphi^{\rm self}$ (*bottom*) of the scalar-field self-force along the orbit with parameters $E = 1.1$ and $r_{\rm min} = 4M$, plotted against time t (lower axis) and orbital radius r (upper axis). Results of the frequency-domain code developed in this paper (solid red) are compared to those of the time-domain code developed in Ref. [149] (dashed black, grid spacing $h = M/128$). Periapsis occurs at $t = 0$, $r = r_{\rm min} = 4M$, which is represented by the central vertical line. *Insets:* relative difference between the frequency-domain code and two runs of the time-domain code with different grid spacings $h = M/128$ and $h = M/64$, normalised by the frequency-domain results. A fiducial choice of $\ell_{\rm max} = 15$ and $F_{[6]}$ regularisation have been adopted for this test. There is good agreement between the two methods near periapsis, but the accuracy of the frequency-domain code deteriorates rapidly for $r_p \gtrsim 10M$.

The above results are reassuring, if mixed. The successful regularisation tests and agreement with TD results validate our new code, and eliminate the possibility of any serious errors in the calculation of FD quantities such as the $C^{-}_{\ell m\omega}$. We have illustrated the higher accuracy of the new FD code at small radii (compared to the existing TD implementation), where it exhibits superior large-ℓ performance and greater accuracy in the summed force. However, as r is increased, the code quickly loses accuracy at large ℓ. In practice, this means that, without directly addressing the problem, we are limited to $\ell_{\rm max}$ values that must be made smaller with increasing r, at a cost of increased truncation error.

In Section 4.6 we discuss the cause of the problem at large r and possible remedies for it. Since we are yet to develop a complete satisfactory cure, we proceed here with a temporary solution, involving a procedure for an adaptive adjustment of $\ell_{\rm max}$ as a function of r along the orbit.

4.4 Adaptive truncation of ℓ-mode summation

To detect when the terms of the mode-sum begin to rapidly lose accuracy, the following algorithm was applied. First, regularised ℓ-modes $F_\alpha^{({\rm reg})\ell}$ are calculated and added for $0 \leq \ell \leq \ell_{\rm min}$, where $\ell_{\rm min}$ takes some pre-selected value. Additional modes are then added so long as at least one of the following two criteria are met: Either $\left|F_\alpha^{({\rm reg})\ell}\right| < \sigma_1 \left|F_\alpha^{({\rm reg})\ell-1}\right|$; or there is precisely one change of sign among the successive ℓ-modes $F_\alpha^{({\rm reg})\ell-3}$, $F_\alpha^{({\rm reg})\ell-2}$, $F_\alpha^{({\rm reg})\ell-1}$ and $F_\alpha^{({\rm reg})\ell}$, and, in addition, $\left|F_\alpha^{({\rm reg})\ell}\right| < \sigma_2 \max\left(\left|F_\alpha^{({\rm reg})\ell-2}\right|, \left|F_\alpha^{({\rm reg})\ell-3}\right|\right)$. The second condition is designed to allow change-of-sign features to pass through the filter without triggering the truncation mechanism. Repeated changes of sign are taken to indicate noise or other difficulties in the ℓ-modes, and treated as a trigger for truncation. The constants $\sigma_{1,2}$ are safety factors to prevent the truncation mechanism from being falsely triggered by any legitimate small-scale features, such as "bounce-back" after a change of sign. Values of $\sigma_1 = 1.1$ and $\sigma_2 = 2$ were adopted. A minimum number of ℓ-modes, $\ell_{\rm min}$, are always included, so that the truncation mechanism is not triggered by transient small-ℓ behaviour. A piecewise value $\ell_{\rm min} = 10$ for $r_p \leq 10M$ and $\ell_{\rm min} = 5$ for $r_p > 10M$ was selected. The maximum possible value of $\ell_{\rm max}$ is set by the largest value of ℓ for which $C^{-}_{\ell m\omega}$ data is available, which in the present case was $\ell_{\rm max} = 25$.

$F_{[6]}$-regularised ℓ-mode contributions to the self-force were calculated in advance up to $\ell = 25$, 20 and 15 for $r_p \leq 6M$, $6M < r_p \leq 15M$ and $r_p > 15M$ respectively, at points along the orbit which are uniformly spaced in χ between $r_p = 50M$ (inbound) and $r_p = 50M$ (outbound). The truncation algorithm was then applied to determine the appropriate value of $\ell_{\rm max}$ at each location. The resulting self-force along the orbit is displayed in Fig. 4.3, with the TD results (still using $\ell_{\rm max} = 15$) for comparison.

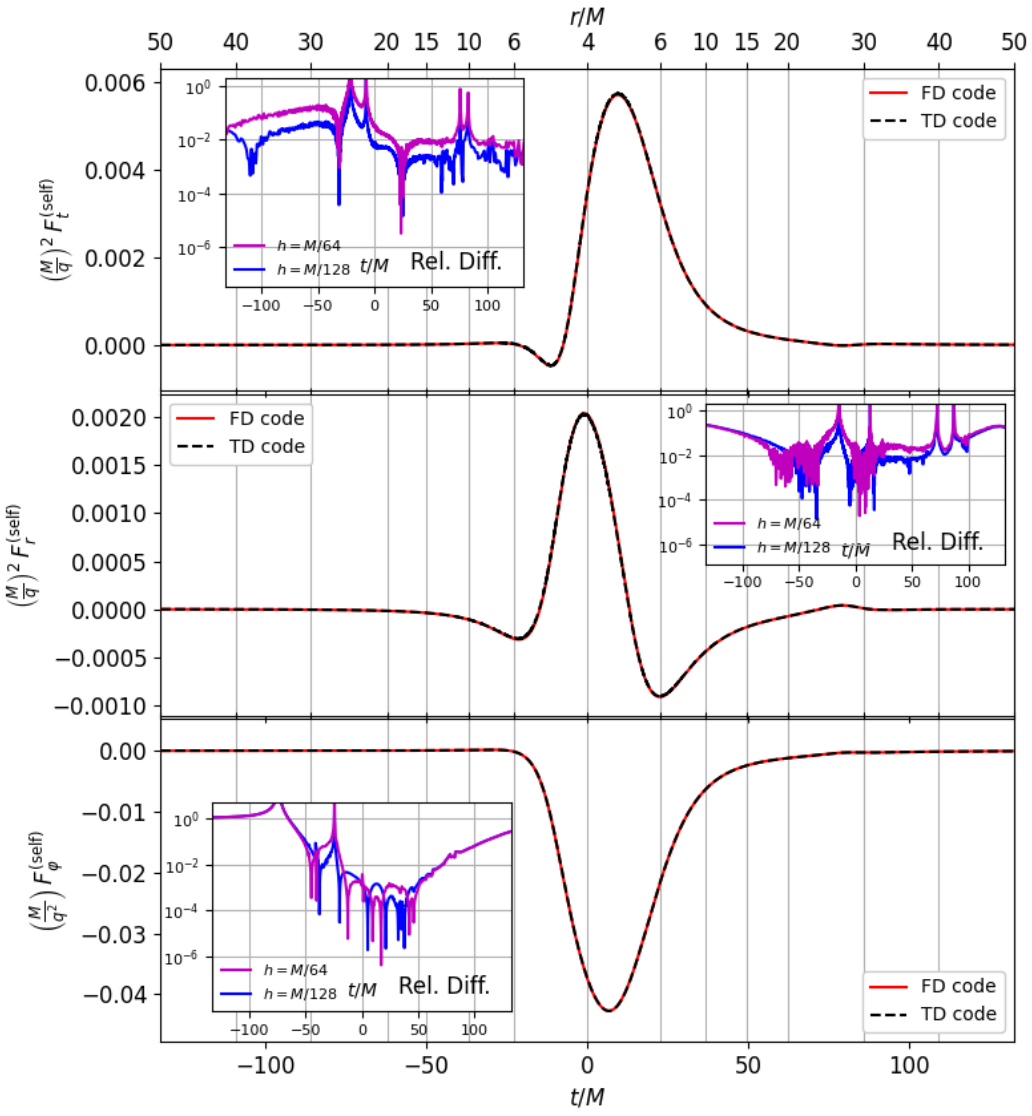

FIGURE 4.3: Same as Fig. 4.2, after applying the adaptive mode-sum truncation procedure described in the text. The time-domain data continues to use $\ell_{\max} = 15$. The improvement at large r is manifest.

We observe that the use of adaptive truncation of the mode sum prevents any visible blow-up in the FD calculation, out to at least $r = 50M$. This represents a significant improvement compared to the fiducial $\ell_{\rm max} = 15$ test in Fig. 4.2. The insets to Fig. 4.3 once again display the relative difference between the FD results and two TD runs with different resolutions ($h = M/128$ and $h = M/64$). For the t component of the force, the relative difference is sub-1% at late times, and $O(1)$-$O(10)$% at early times, with significant sensitivity to the TD resolution used. This once again suggests that the FD code is more accurate here, even at $r = 50M$. For the r and φ components, however, the relative difference is broadly insensitive to the TD resolution used, and the errors increase with radius, becoming $O(10)$% at late time, and even larger at very early time. To pin down the dominant source of numerical error in these domains would require a more detailed analysis of both FD and TD codes, which we have not performed here. We suspect, however, that the large-ℓ truncation error in the FD code is dominant at large r_p.

4.5 Example scatter angle calculation

We will now illustrate a full calculation of the self-force correction to the scatter angle, $\delta\varphi^{(1)}$, choosing our background geodesic to be the same orbit we considered in Sections 4.3 and 4.4. In those previous sections, we chose to define the orbit using specific choices for the energy and periapsis radius, namely $E = 1.1$ and $r_{\rm min} = 4M$, whereas the expression for $\delta\varphi^{(1)}$ given in Eq. (2.66) is for the scatter angle correction at fixed values of the parameters (v, b). It should be understood, therefore, that we will actually be calculating the scatter angle correction with fixed values of (v, b) exactly equal to those of the *geodesic* orbit with parameters $E = 1.1$ and $r_{\rm min} = 4M$. These values are given approximately by

$$b \approx 10.401M, \quad v \approx 0.41660. \tag{4.5}$$

We calculate $\delta\varphi^{(1)}_{\rm cons}$ and $\delta\varphi^{(1)}_{\rm diss}$ separately by numerically integrating Eqs. (2.68) and (2.69). Our scatter angle script takes as input the total, unprojected, self-force $F^{\rm self}_\alpha$ at $8N$ discrete locations, $\chi_n := nh_\chi$ for $n = \pm1, \pm2, ..., \pm4N$. Here N is an integer, h_χ is the spacing of the χ sample, and $\chi_{\rm max} := 4Nh_\chi$ is the value of χ where the integrals will be truncated. (The point $\chi = 0$ is not initially included in our sample because, although the entire integrand is bounded at $\chi = 0$, the factors $\mathcal{G}^{(\rm cons)}_{E/L}$ are individually singular there; instead, we obtain the value at $\chi = 0$ via extrapolation.) Given the unprojected self-force data, the script calculates the projection of the self-force orthogonal to the 4-velocity using Eq. (2.39), and then it separates it into conservative and dissipative pieces, $F^{\perp\rm cons}_\alpha$ and $F^{\perp\rm diss}_\alpha$, using Eqs. (2.57)-(2.60). The integrands in Eqs. (2.68) and (2.69) are then constructed at the $4N$ positions in $0 < \chi \leq \chi_{\rm max}$, and extended to $\chi = 0$

via extrapolation. The scatter-angle integrals (truncated at $\chi = \chi_{\max}$) are evaluated using Simpson's 1/3 rule, which requires an odd number of data points. Because $4N+1$ data points are available, 2 estimates of the integral may be obtained, one using step width h_χ, and another using step width $2h_\chi$. The former is used as the best estimate for the scatter angle, while the difference

$$\epsilon = \frac{1}{15}\left(\delta\varphi^{(1)}(2h_\chi) - \delta\varphi^{(1)}(h_\chi)\right) \tag{4.6}$$

provides an estimate of the quadrature error.

The self-force was calculated out to $r_p = 50M$ along both inbound and outbound legs of the orbit, with χ-spacing $h_\chi = \chi_{50}/1024$, where $\chi_{50} \approx 2.0776$ is defined by $r_p(\chi_{50}) = 50M$. This choice of h_χ is found to produce a quadrature error much smaller than other sources of error in our calculation (see below). The integrals (2.68) and (2.69) were truncated at $\chi_{\max} = \chi_{50}$. The resulting estimates for the scatter angle correction, expressed to 5 significant figures, were

$$\delta\varphi^{(1)}_{\rm cons} = -1.5032, \qquad \delta\varphi^{(1)}_{\rm diss} = 2.7034 \qquad (\text{FD}, r_{\max} = 50M), \tag{4.7}$$

with respective estimated quadrature errors $\epsilon_{\rm cons} \approx -1.1\times10^{-7}$ and $\epsilon_{\rm diss} \approx -7.9\times10^{-7}$.

For comparison, we apply the same method (with the same values of the χ-spacing h_χ and truncation point $\chi_{\max}$) to the self-force data obtained using the TD code of Ref. [149]. This approach yields estimates of

$$\delta\varphi^{(1)}_{\rm cons} = -1.5309, \qquad \delta\varphi^{(1)}_{\rm diss} = 2.6950 \qquad (\text{TD}, r_{\max} = 50M), \tag{4.8}$$

The difference relative to our estimates in Eq. (4.7) is approximately 1.8% (0.31%) in the conservative (dissipative) pieces. This discrepancy is significantly larger than the quadrature errors estimated above. In Chapter 4 it was found that the disagreement between the FD and TD self-force values was greatest at large radius, and thus it is expected that the large-radius portions of the integrals (2.68) and (2.69) contribute most significantly to the discrepancy in the scatter angle estimates. This may be investigated by truncating the integrals (2.68) and (2.69) at a smaller value of χ and examining the effect on the discrepancy. Using the same value of h_χ but a reduced truncation position $\chi_{\max} = 976h_\chi$ (corresponding to $r_p \approx 29.8M$), the FD self-force data provided estimates -1.4515 (2.6382) for the conservative (dissipative) piece of the scatter angle correction, compared to -1.4627 (2.6298) using the TD self-force data. The relative difference between the conservative parts has reduced significantly to 0.77%, but remains broadly unchanged at 0.32% for the dissipative part. This supports the idea that, in our tests, the discrepancy between the FD and TD conservative scatter angles is dominated by the loss of accuracy in the FD self-force at large radius, but the (smaller) discrepancy in the dissipative pieces may have a different root cause.

This test highlights another significant source of error in the estimates (4.7), that which arises from truncating the integrals (2.68) and (2.69) at $\chi < \chi_\infty$. To quantify this error, we change integration variable in Eq. (2.68),

$$\delta\varphi^{(1)}_{\rm cons} = \int_{r_{\rm min}}^{\infty} \left[\mathcal{G}^{(\rm cons)}_E(r_p) F_t^{\perp \rm cons}(r_p) - \mathcal{G}^{(\rm cons)}_L(r_p) F_\varphi^{\perp \rm cons}(r_p)\right] \frac{dr_p}{\dot{r}_p}, \tag{4.9}$$

and note that the self-force components decay like r_p^{-a} as $r_p \to \infty$, where $a = 3$ for $\alpha = t$ and r, and $a = 2$ for $\alpha = \varphi$ [149]. A simple asymptotic analysis shows that the full integrand in Eq. (4.9) decays like r_p^{-2}. Hence, when Eq. (2.68) is truncated at $\chi_{\rm max} < \chi_\infty$, the resulting truncation error behaves as $r_{\rm max}^{-1}$, where $r_{\rm max} = r_p(\chi_{\rm max})$. The same decay rate applies for the dissipative piece also.

Based on this reasoning, the relative truncation error in the scatter angle corrections may be approximated by $(r_{\rm min}/r_{\rm max})$. For truncation at $r_{\rm max} = 50M$, this would suggest an error of approximately $(4/50) = 0.08$. This is, of course, a very crude estimate, because the integrand is not a strict power-law function, and may also exhibit changes of sign. To better estimate the true truncation error in our calculation, we may compare to the values obtained in [149], where use was made of a larger truncation radius, with an analytic approximation for the large-r tail of the integral. This more precise calculation gave

$$\delta\varphi^{(1)}_{\rm cons} = -1.5957 \pm 0.0023, \qquad \delta\varphi^{(1)}_{\rm diss} = 2.7612 \pm 0.0026 \quad (\text{TD}, r_{\rm max} = \infty), \tag{4.10}$$

suggesting relative errors of approximately 4.1% and 2.5% in the truncated TD estimates (4.8). These are somewhat smaller than our crude $\sim 8\%$ estimate.

In summary, we see that the dominant source of error in our FD value (4.7) is the large-r truncation of the orbital integration. Mitigating this truncation error is challenging within our current FD framework. As we have discussed, increasing the truncation radius results in significant loss of accuracy. Indeed, even truncating at $r_p = 50M$ we found that the error associated with the large-r self-force may be as much as half the size of the truncation error for the conservative piece. Attempting to extrapolate the self-force to large radii is likewise more challenging for our FD code than it was for the TD code. If a tail is fitted to inaccurate large-radius self-force data, the accuracy of the extrapolation will be fundamentally limited. It is for this reason we find fitting a tail to our self-force data impractical. It is clear that high-precision scatter angle calculations will require improvements at large radius.

The next section will explore more deeply the reasons for our problems at large r, and suggest mitigations.

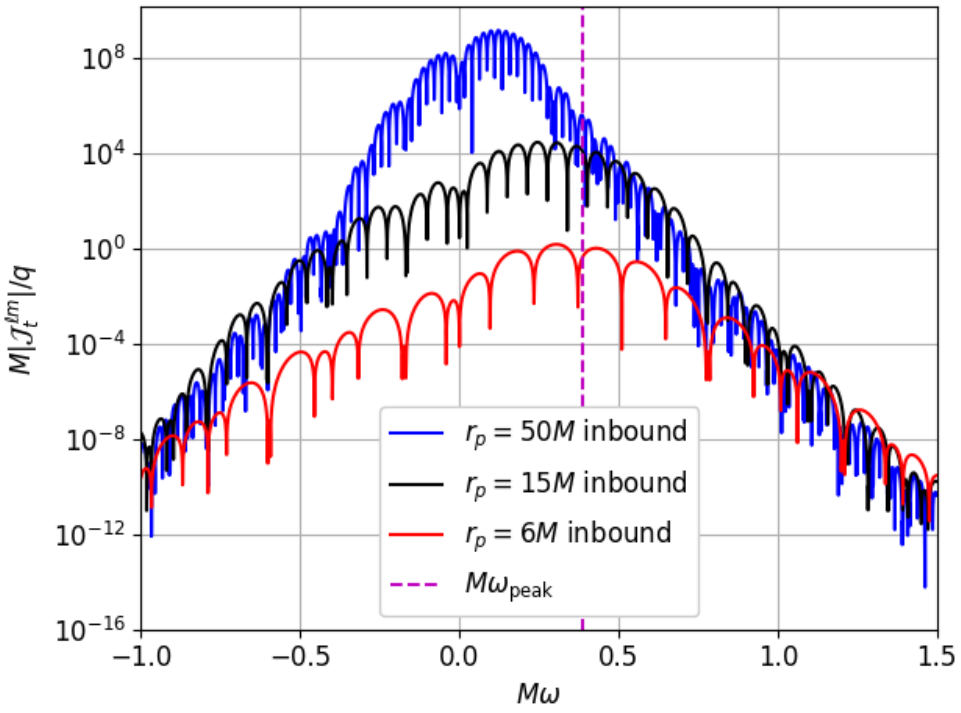

FIGURE 4.4: Integrand $\mathcal{J}_t^{\ell m}$ [as defined in Eq. (4.11)] plotted against ω for the mode $(\ell, m) = (10, 2)$ at selected radii along the inbound leg of the orbit with parameters $E = 1.1$ and $r_{\rm min} = 4M$. Also plotted is a vertical line representing the frequency $\omega_{\rm peak}$ at which $C^-_{10,2,\omega}$ peaks. The peak value of the integrand grows rapidly and is increasingly shifted towards $\omega = 0$ as the radius is increased, while the frequency of the oscillations also increases.

4.6 Cancellation problem

We seek to understand the origin of the observed loss of accuracy at large r and large ℓ. To this end, consider the integrand of the Fourier integral $\Phi_t^{\ell m-}$ in Eq. (4.1) as an example. In order to reconstruct $F^{\rm full-}_{t,\ell}$ using Eq. (4.4), the real-valued integrand of interest is

$$\mathcal{J}_t^{\ell m}(\omega) := -\mathrm{Re}\left[\frac{i\omega}{r_p} C^-_{\ell m\omega}\psi^-_{\ell\omega} e^{-iwt_p} Y_{\ell m}\left(\frac{\pi}{2}, \varphi_p\right)\right]. \tag{4.11}$$

In Fig. 4.4 we plot this quantity as a function of frequency at selected radii along the inbound leg of the orbit for the mode $(\ell, m) = (10, 2)$. The peak of $\mathcal{J}_t^{\ell m}$ is seen to shift away from that of $C^-_{\ell m\omega}$ and towards $\omega = 0$, where the homogeneous solution factor, $\psi^-_{\ell\omega}(r_p)$, peaks. This offset is small at small radii, but the peak grows rapidly and becomes increasingly shifted towards $\omega = 0$ as r_p is increased, due to the quasi-static growth of the homogeneous solution, $\psi^-_{\ell,\omega=0} \sim r^{\ell+1}$, at relatively small frequencies $\omega \ll \ell r^{-1}$. At the same time, the integrand oscillates at an increasing rate due to the

factors $\psi^{-}_{\ell\omega}(r_p)$ and $e^{-i\omega t_p}$, which have phases $\sim \omega r^p_*$ and ωt_p respectively. The same behavior is observed in the r and φ components too.

The ℓ-modes of the self-force, however, *decay* with radius. The conclusion is that there must be an increasing degree of cancellation in the Fourier integrals as the radius is increased. This increasing cancellation in the time-domain reconstruction due to the quasi-static growth of the EHS was first noted in Ref. [113], which studied the gravitational self-force on particles moving along eccentric, bound, Kerr geodesics. In that paper the author explained that the EHS modes with relatively small frequency exhibit unphysical amplitude variations along the orbit, by an amount that grows exponentially in ℓ. In the case of our scatter orbits, the unphysical growth of the EHS is encapsulated by Eq. (2.127), which makes the exponential dependence on ℓ clear.

The cancellation in the Fourier integral amplifies the error in the numerically calculated integrand, and we refer to this phenomenon as the *cancellation problem*. Once the loss of precision exceeds the precision of the underlying frequency-domain calculations, the cancellation in the numerical Fourier integrals cannot occur and our calculated self-force loses accuracy and begins to blow-up. The degree of cancellation (and hence the resulting loss of precision) may be quantified for the case of the t component by

$$\mathcal{R}^{\ell} := \max_{m} \left(\frac{\|\mathcal{J}^{\ell m}_t\|_1}{\left|\mathrm{Re}\left(\Phi^{\ell m -}_t Y_{\ell m}\right)\right|} \right), \tag{4.12}$$

where

$$\|f\|_1 := \int_{-\infty}^{+\infty} |f(\omega, r_p)|\, d\omega \tag{4.13}$$

is the L^1-norm over frequency at fixed orbital position. This quantity is plotted in Fig. 4.5, demonstrating the increased cancellation with r_p, and in particular reproducing the expected exponential growth with ℓ.

In Refs. [113] and [114] the author managed the cancellation problem by using arbitrary precision arithmetic, calculating frequency-modes at sufficiently high precision to ensure the desired level of accuracy even after the loss of precision during time-domain reconstruction. The key downside of this approach is the significantly increased computational cost that comes with higher precision arithmetic, which is particularly undesirable for hyperbolic orbits given the already reduced efficiency of frequency-domain methods in this regime. There are several other reasons why this approach is less effective in the scatter problem. First, we have seen that the scatter problem introduces a new source of error, arising from the truncation of the normalisation integrals $C^{-}_{\ell m\omega}$ at a finite radius. To benefit from improved-precision arithmetic would require a commensurate reduction in this truncation error, which, in turn, is likely to demand the use of new techniques, such as the derivation of higher-order IBP rules or the use of compactification [183, 184],

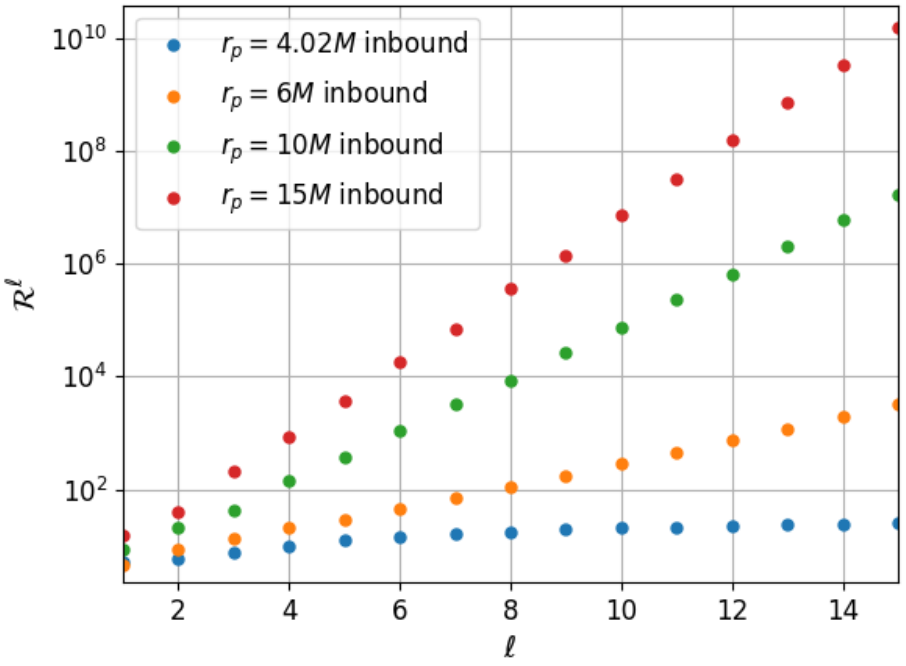

FIGURE 4.5: Degree of cancellation $\mathcal{R}^\ell$ [as defined in Eq. (4.12)] in the calculation of the Fourier integral $\Phi_t^{\ell m-}$ at selected points along the inbound leg of the orbit with parameters $E = 1.1$, $r_{\min} = 4M$. The degree of cancellation (and hence loss of precision) increases with r_p, and exponentially in ℓ.

with their own challenges and costs to bear. Second, achieving very high accuracy in the interpolation of $C^-_{\ell m\omega}$ will inevitably require the calculation of a larger number of frequency modes to use as data nodes, introducing extra cost and compounding the first issue. This is in contrast to the discrete-frequency bound case, where approximately the same number of frequencies are required even at radii where the cancellation problem is more severe.

We see several possible directions for mitigating the cancellation problem in future work. The most straightforward approach is to refine our existing double-precision code to improve the precision of the various frequency-domain quantities that go into the Fourier integrals, and hence delay the onset of breakdown. For example, adaptive placement of interpolation nodes for $C^-_{\ell m\omega}$ may be used to reduce interpolation error at those frequencies that contribute strongly to the cancellation, while reducing sample density to conserve computation time at frequencies in the tail of the spectrum, where the error requirement is less stringent. Another option is the use of semi-analytical results, based around small-ω expansions of the homogeneous solutions, to improve the accuracy of $C^-_{\ell m\omega}$ around $\omega = 0$. A more ambitious objective would be to use small-ω expansions of the homogeneous solutions to better understand the nature of the cancellation, with an aim to achieve part of the cancellation analytically.

In parallel to these direct mitigations of the cancellation problem, one should develop analytical approximations for the large-r tail of the self-force, which would reduce the need for a numerical calculation at large radius. This would also be beneficial for the TD approach, which also suffers from a loss of accuracy and efficiency at large radii. Work towards this objective will be presented in Chapter 6.

It should be reminded here that the cancellation problem is an inherent feature of the EHS approach, where unphysical, growing homogeneous solutions are extended into the source region. The problem would not occur in a calculation based on the standard variation-of-parameters formula, if a way was found to enable an efficient reconstruction of the TD field at the particle despite the Gibbs phenomena. Ultimately, therefore, a full satisfactory solution to the cancellation problem might need to involve a departure from the usual EHS approach. Alternatives would have to tackle the Gibbs phenomenon head-on. Ideas to be explored involve the application of spectral filtering to improve the convergence of the Fourier integral near the particle [185]; and/or the use of extrapolation to estimate the one-sided limits of the field derivatives based on values calculated away from the particle location, where the impact of the Gibbs phenomenon is less severe.

Chapter 5

Scattering near the transition to plunge and the resummation of post-Minkowskian series

In this chapter we turn our attention to scattering near the separatrix between scattering and plunging geodesics. In this limit, the correction $\delta\varphi^{(1)}$ is characterised by a single coefficient $A_1(v)$, which we extract numerically from calculations of the self-force along near-separatrix orbits. We then propose a method by which $A_1(v)$ may be used to *resum* analytical PM results, with the aim of improving their fidelity in the strong field regime. Our FD method turns out to be excellently suited to calculations of the self-force along orbits near to the separatrix. Observing the great significance of modes $\ell > 15$ in the vicinity of periapsis for larger velocities, modes which only our FD method can currently provide, we develop a hybrid TD/FD method to obtain the self-force along near-critical geodesics. Using this method, we illustrate the self-force in the near-separatrix limit, and extract the values of $A_1(v)$ at a selection of velocities. We conclude the chapter by exploring the effectiveness of our resummation scheme, finding a remarkable improvement in faithfulness compared to the plain PM expansion, in both the strong *and* weak field limits.

5.1 Scatter geodesics: transition to plunge

As explained in Sec. 2.1, a test particle starting at infinity with energy E and angular momentum L will scatter off the central black hole without being captured if, and only if, $L > L_c(E)$, where $L_c(E)$ is given in Eq. (2.7). For orbits with $L < L_c(E)$, instead of scattering and returning to infinity, the particle will instead *plunge* towards the central black hole, being captured at some finite proper time. The one-parameter curve in geodesic parameter space defined by $L = L_c(E)$ forms the *separatrix* between scattering

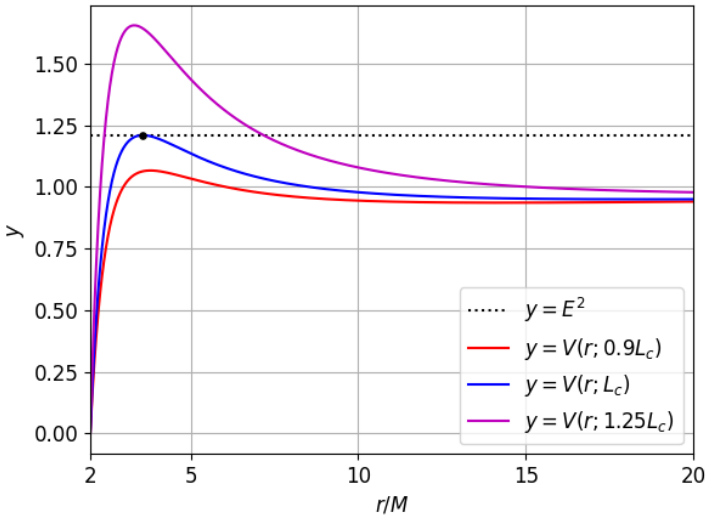

FIGURE 5.1: Effective potential for the radial motion [as defined in Eq. (2.4)] compared to E^2 for $E = 1.1$ and three different values of the angular momentum: $L = 0.9L_c(1.1)$, $L = L_c(1.1)$ and $L = 1.25L_c(1.1)$.

and plunging orbits. The origin of the transition to plunge may be explained using the effective potential description for the radial motion, Eq. (2.3),

$$\dot{r}_p = \pm\sqrt{E^2 - V(r_p; L)}, \tag{5.1}$$

where the effective potential $V(r; L)$ is given in Eq. (2.4). Figure 5.1 displays this potential, and the value of E^2, for $E = 1.1$ and three different choices of L. The figure illustrates that, for $L > L_c(E)$, a particle beginning its motion at infinity cannot overcome the potential barrier and will instead scatter back to infinity. For $L < L_c(E)$, however, the peak of the potential barrier lies below E^2, and thus the particle is able to reach $r = 2M$ and be captured. In the critical case $L = L_c(E)$, the peak of the potential lies exactly at the level of E^2, and a particle that initially moves inwards from infinity with this critical angular momentum will be captured into an (unstable) circular orbit as proper time $\tau \to \infty$.

The separatrix may also be described as $b = b_c(v)$ where, as usual, v is the velocity-at-infinity, b is the impact parameter, and

$$b_c(v) = \frac{M}{\sqrt{2}\,v^2}\sqrt{8v^4 + \beta - 1 + 4v^2(2\beta + 5)}, \tag{5.2}$$

with

$$\beta := \sqrt{1 + 8v^2}. \tag{5.3}$$

Equation (5.2) is easily obtained by substituting Eq. (2.7) into Eq. (2.9), and then re-expressing in terms of the velocity using $E = (1 - v^2)^{-1/2}$. Orbits with $b > b_c(v)$ scatter,

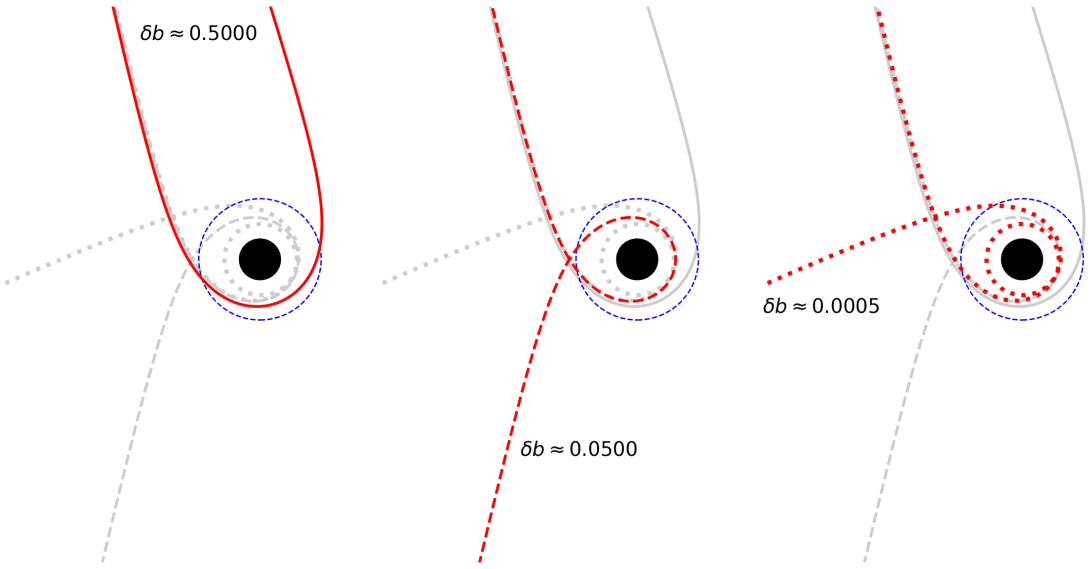

FIGURE 5.2: Scatter geodesics with $v = 0.5$ and: $b = 9.30734M$ (solid, highlighted *left*), $b = 8.85734M$ (dashed, highlighted *center*), and $b = 8.80784M$ (dotted, highlighted *right*). These correspond to values of $\delta b \approx 0.5$, 0.05 and 0.0005 respectively. The view is in the equatorial plane, plotted on axes $x = r\cos\varphi$ and $y = r\sin\varphi$, and each individual orbit has been rotated such that $\varphi_p = 5\pi/8$ when $r_p = 25M$ along the inbound leg. The black hole (black disk) and the ISCO (blue circle) are to scale.

and those with $b < b_c(v)$ plunge; the distance from the separatrix (at fixed v) may be parameterised by

$$\delta b := b - b_c(v), \tag{5.4}$$

with $\delta b > 0$ for scatter geodesics. Figure 5.2 displays three scatter geodesics with fixed $v = 0.5$ and different values of the impact parameter. For sufficiently small δb, one obtains *zoom-whirl* orbits, along which the particle performs a near-circular whirl before escaping back to infinity. As $\delta b \to 0^+$, the particle spends longer and longer on the whirl portion, which becomes increasingly circularised. This is consistent with our effective potential analysis, which concluded that an incoming particle will be captured into a circular orbit for $\delta b = 0$.

In fact, this is only half of the picture. The critical orbit $b = b_c(v)$ has two distinct branches, both of which are complete geodesics (in the sense that the proper time along each stretches from $-\infty$ to $+\infty$). We have already discussed the *inbound* branch, which begins with the particle moving inwards at early times ($\tau \to -\infty$) before being asymptotically captured into a circular orbit as $\tau \to +\infty$. The *outbound* branch, on the other hand, begins on a circular orbit at very early times, before escaping to radial infinity at late times.

5.2 Scatter angle in the limit of transition to plunge

It is evident that the geodesic scatter angle $\delta\varphi^{(0)}$ must diverge as the separatrix is approached and the trajectory tends closer and closer to the infinite whirl of the critical orbit. In fact, it can be established that $\delta\varphi^{(0)}$ diverges logarithmically:

$$\delta\varphi^{(0)} = A_0(v) \ln\left(\frac{\delta b}{b_c(v)}\right) + \text{const}(v) + \cdots , \tag{5.5}$$

where

$$A_0(v) = -\left(1 - \frac{12M^2(1-v^2)}{v^2 b_c(v)^2}\right)^{-1/4} . \tag{5.6}$$

This result is derived in Appendix E.

Moving on to include the effect of the self-force, there is some subtlety in the near-separatrix limit. Until now, we had assumed that, under the action of the self-force, the perturbed trajectory remained "close" to the background geodesic. This allowed us, for example, to calculate the scatter angle correction by evaluating the self-force and the scatter angle integral (2.66) along the background geodesic. In the near-separatrix limit, however, this assumption must break down; rather than continue on an infinite circular whirl, the emission of radiation means the SF-perturbed trajectory would either plunge into the black hole, or scatter back to infinity, after a finite whirl time. Despite this concern, our usual definition of $\delta\varphi^{(1)}$, in which we evaluate integral (2.66) along the background geodesic, remains perfectly well-defined in the near-separatrix limit. It may no longer be the case, however, that $\eta_q \delta\varphi^{(1)} \ll \delta\varphi^{(0)}$, even for "small" values of η_q. Indeed, it was found numerically in Ref. [149] that $\delta\varphi^{(1)}$ exhibits an even stronger divergence than $\delta\varphi^{(0)}$ as $\delta b \to 0$,

$$\delta\varphi^{(1)} \sim A_1(v) \left(\frac{b_c(v)}{\delta b}\right) , \tag{5.7}$$

where $A_1(v)$ is some function of v and $\sim$ denotes leading-order asymptotic equivalence as $\delta b \to 0$ (inclusive of all multiplicative factors on the right hand side). This ensures that for any fixed value of $\eta_q > 0$, the "correction" term $\eta_q \delta\varphi^{(1)}$ will always exceed the geodesic term $\delta\varphi^{(0)}$ for sufficiently small δb.

Our next task is to derive an expression for the coefficient $A_1(v)$ as an integral of the self-force along the critical orbit, analytically confirming the form of the divergence in Eq. (5.7) in the process. Considering first the dissipative piece, our starting point is the general formula for $\delta\varphi^{(1)}_{\text{diss}}$ in Eq. (2.69), which we rewrite as an integral over proper time $d\tau = \tau_\chi d\chi$. Our goal is to approximate this expression at small $\delta b = b - b_c(v)$ for an arbitrary v. To this end, we substitute $p = p_c(e) + \delta p = 6 + 2e + \delta p$ in $\alpha_{E,L}$, expand to leading order in δp (at fixed e), and then substitute for δp in terms of δb using the leading-order expression (E.5) from App. E. This procedure gives, at leading order in

δb,

$$\delta\varphi^{(1)}_{\rm diss} \sim \frac{1}{\delta b}\int_{-\infty}^{+\infty}\left(c_E F_t^{\perp\rm diss} + c_L F_\varphi^{\perp\rm diss}\right)d\tau, \tag{5.8}$$

with

$$c_E = -\frac{2(3-e)^{1/2}(3+e)^{5/2}M}{(e+1)^2\sqrt{e(e-1)}}, \tag{5.9}$$

$$c_L = -\frac{(3+e)(3-e)^{1/2}}{\sqrt{2e(e^2-1)}}. \tag{5.10}$$

Here the integrand is evaluated along the outbound branch of the critical geodesic with $b = b_c(v)$, whose periapsis is at $\tau \to -\infty$. We have thus reproduced Eq. (5.7), with

$$A_1^{\rm diss}(v) = \frac{1}{b_c(v)}\int_{-\infty}^{+\infty}\left(c_E F_t^{\perp\rm diss} + c_L F_\varphi^{\perp\rm diss}\right)d\tau. \tag{5.11}$$

One should resist temptation to write the integral here as $-c_E E_{\rm rad} + c_L L_{\rm rad}$ [recalling Eq. (2.71)], since both $E_{\rm rad}$ and $L_{\rm rad}$ diverge for a critical geodesic, due to the infinite whirl. The integral in Eq. (5.11), however, is well defined and finite. We discuss the convergence of this integral further below, in Sec. 5.2.1.

A similar procedure is applied to the conservative piece. Starting with Eq. (2.68), we expand the functions $\mathcal{G}_E^{\rm cons}(\tau)$ and $\mathcal{G}_L^{\rm cons}(\tau)$ (given explicitly in Ref. [149] in terms of p, e) in δp about $p_c(e) + \delta p = 6 + 2e$ at fixed e and τ, and then substitute for δp in terms of δb using the leading-order expression (E.5) from App. E. We find that the leading-order term in δb is τ-independent. In fact, the calculation yields an expression of a very similar form to that for $\delta\varphi^{(1)}_{\rm diss}$:

$$\delta\varphi^{(1)}_{\rm cons} \sim -\frac{1}{\delta b}\int_{-\infty}^{+\infty}\left(c_E F_t^{\perp\rm cons} + c_L F_\varphi^{\perp\rm cons}\right)d\tau, \tag{5.12}$$

with the same coefficients c_E and c_L as in Eq. (5.8). Thus

$$A_1^{\rm cons}(v) = -\frac{1}{b_c(v)}\int_{-\infty}^{+\infty}\left(c_E F_t^{\perp\rm cons} + c_L F_\varphi^{\perp\rm cons}\right)d\tau. \tag{5.13}$$

Again, the integration is done along the outbound branch of the critical orbit with velocity v. Its convergence is discussed in Sec. 5.2.1.

In Chapter 4, we obtained the conservative and dissipative forces along our given orbit from a calculation of only the retarded scalar-field along that orbit. We achieved this using the general Eq. (2.59), which relates the self-force arising from the advanced field at a given point to the self-force from the retarded field at a "conjugate" point with the same value of r_p, but opposite sign of $\dot{r}_p$. For the case of a critical orbit $b = b_c(v)$, the conjugate to a given point now lies on the opposite branch. A numerical calculation of the conservative and dissipative forces along a critical orbit thus requires a calculation

of the self-force along both critical branches (or, in principle, separate calculations of the advanced and retarded forces along a single branch instead).

Our immediate concern, however, is the reverse problem. Equations (5.11) and (5.13) give us expressions for $A_1^{\rm cons}$ and $A_1^{\rm diss}$ in terms of the conservative and dissipative forces evaluated along the outbound branch of the critical orbit, and we wish to add them to obtain the total coefficient $A_1(v) = A_1^{\rm cons}(v) + A_1^{\rm diss}(v)$ in terms of the total self-force, $F_\alpha^\perp$. Adding Eqs. (5.11) & (5.13), we get

$$A_1(v) = \frac{1}{b_c(v)} \int_{-\infty}^{+\infty} \Big[c_E \Big(F_t^{\perp \rm diss} - F_t^{\perp \rm cons} \Big) + c_L \Big(F_\varphi^{\perp \rm diss} - F_\varphi^{\perp \rm cons} \Big) \Big] d\tau, \tag{5.14}$$

where the self-forces and integral are again evaluated on the outbound branch. This cannot be immediately expressed in terms of an integral of the total $F_\alpha^\perp$. Instead, we use Eq. (2.59) with Eqs. (2.57) & (2.58) to note that for $\alpha = t, \varphi$, the value of $F_\alpha^{\perp \rm diss} - F_\alpha^{\perp \rm cons}$ at a given point along the outbound branch is equal to $F_\varphi^{\perp \rm diss} + F_\varphi^{\perp \rm cons} = F_\alpha^\perp$ at the conjugate point along the inbound branch. Equation (5.14) can thus be rewritten

$$A_1(v) = \frac{1}{b_c(v)} \int_{-\infty}^{+\infty} \Big(c_E F_t^\perp + c_L F_\varphi^\perp \Big) d\tau, \tag{5.15}$$

where the integral is now evaluated along the *inbound* branch. In Eq. (5.15), as in (5.11), the individual integrals over the c_E and c_L terms do not exist, but the integral of their sum does, as we explain next.

5.2.1 Convergence of integrals

At large radius, $F_t^\perp$ and $F_\varphi^\perp / r_p$ decay as $r_p^{-3} \sim \tau^{-3}$ [149], so the integrals in Eqs. (5.11)) and (5.13) converge well at their upper limits, and the one in (5.15) converges well at its lower limit. As mentioned, the convergence in the opposite limit, where the critical geodesic executes an infinite whirl, is more subtle, and requires some analysis.

We start with the conservative case. For a nearly circular orbit we have $F_\alpha^{\perp \rm cons} \propto \dot{r}_p$ for $\alpha = t, \varphi$ [186], so (5.13) can be written as

$$A_1^{\rm cons}(v) = -\frac{1}{b_c(v)} \int_{r_{\rm min}}^{+\infty} \Big(c_E \hat{F}_t^{\rm cons} + c_L \hat{F}_\varphi^{\rm cons} \Big) \, dr, \tag{5.16}$$

where $r_{\rm min}$ is the whirl (periapsis) radius, and $\hat{F}_\alpha^{\rm cons} := F_\alpha^{\perp \rm cons} / \dot{r}_p$ has a finite $r \to r_{\rm min}$ limit. In fact, each of the components are bounded everywhere in the integration domain, and fall off as $\hat{F}_t^{\rm cons} \sim r_p^{-3}$ and $\hat{F}_\varphi^{\rm cons} \sim r_p^{-2}$ at large r, so the integral in (5.16) exists.

The dissipative case is more delicate. The components $F_t^{\perp \rm diss}$ and $F_\varphi^{\perp \rm diss}$ do not vanish on the whirl radius, so the integrals of the corresponding terms in Eq. (5.11) do not

separately converge, and the same holds true also for the two separate full SF integrals in Eq. (5.15) (since the integrals of the conservative pieces do converge). However, the integral of the sum of c_E and c_L terms does converge, in both (5.11) and (5.15). To see this, note

$$\frac{c_L}{c_E} = \frac{1}{M}\left(\frac{1+e}{6+2e}\right)^{3/2} = \sqrt{\frac{M}{r_{\rm min}^3}} = \Omega_{\rm LSO}, \tag{5.17}$$

the angular frequency ($= \dot{\varphi}_p/\dot{t}_p$) of the whirl. Near the whirl radius we have $\dot{\varphi}_p/\dot{t}_p = \Omega_{\rm LSO} + O(\dot{r}_p)$, so, using $u^\alpha F_\alpha^\perp = 0$, it follows that, during the whirl,

$$\begin{aligned} c_E F_t^\perp + c_L F_\varphi^\perp &= c_E(F_t^\perp + \Omega_{\rm LSO} F_\varphi^\perp) \\ &= -c_E(\dot{r}_p/\dot{t}_p)F_r^\perp + O(\dot{r}_p). \end{aligned} \tag{5.18}$$

Thus the integrand in Eq. (5.15) is bounded everywhere (falling off as r_p^{-2} at infinity), and we conclude that the integral converges. Since the integral of the conservative piece converges also, we can conclude that, in Eq. (5.11), the integral of the dissipative piece alone also converges. Nonetheless, care must be taken if numerically evaluating the integrands in Eqs. (5.11) & (5.15) near the whirl radius, due the large degree of cancellation expected between the c_E and c_L terms.

5.3 Resumming post-Minkowskian expansions using strong-field self-force results

In this section, we propose a method for incorporating strong-field self-force information (in the form of the singularity coefficient $A_1(v)$) into post-Minkowskian results for the scatter angle, with the aim of extending the latter's validity to smaller values of b.

To this end, we introduce the function

$$\begin{aligned} \Psi(v,b) := A_0(v)\Bigg[&\log\left(1 - \frac{b_c(v)[1-\eta_q A_1(v)/A_0(v)]}{b}\right) \\ &+ \sum_{k=1}^{4}\frac{1}{k}\left(\frac{b_c(v)[1-\eta_q A_1(v)/A_0(v)]}{b}\right)^k\Bigg]. \end{aligned} \tag{5.19}$$

This function has the following significant properties:

(i) $\Psi = O(b^{-5})$ as $b \to \infty$. This follows from noting the counter-terms in the second line of Eq. (5.19) have been chosen to exactly cancel the leading terms in the large-b expansion of the logarithm.

(ii) In the geodesic limit $\eta_q \to 0$, Ψ possesses the same logarithmic singularity as $\delta\varphi^{(0)}$. More precisely, introducing the self-force expansion of Ψ,

$$\Psi = \Psi^{(0)} + \eta_q \Psi^{(1)} + O(\eta_q^2), \tag{5.20}$$

defined at fixed (v, b), we have that $\lim_{b\to b_c(v)} \left(\delta\varphi^{(0)} - \Psi^{(0)}\right)$ is finite.

(iii) At 1SF order, Ψ possesses the same $\sim 1/\delta b$ divergence as the scatter angle correction $\delta\varphi^{(1)}$,

$$\Psi^{(1)} \sim A_1(v) \left(\frac{b_c(v)}{\delta b}\right). \tag{5.21}$$

We note that the quantity $-\eta_q\, b_c(A_1/A_0)$ in Eq. (5.19) may be interpreted as the self-force correction to the critical impact parameter $b_c(v)$ (at fixed v).

We then define the *resummed* scatter angle,

$$\delta\tilde{\varphi}(v, b) := \delta\varphi_{\rm 4PM}(v, b) + \Psi(v, b), \tag{5.22}$$

where $\delta\varphi_{\rm 4PM}$ is the "plain" expansion for the scatter angle, correct to 4PM order. This resummed scatter angle then has the following properties:

1. Using property (i) above, $\delta\tilde{\varphi} - \delta\varphi_{\rm 4PM} = O(b^{-5})$ as $b \to \infty$.
2. Using property (ii) and the regularity of the plain 4PM scatter angle, for $\eta_q = 0$ the resummed angle has the same logarithmic divergence as $\delta\varphi^{(0)}$ near the separatrix.
3. Using property (iii), the 1SF term in the self-force expansion of $\delta\tilde{\varphi}$ has the same $A_1(v)b_c(v)/\delta b$ divergence as $\delta\varphi^{(1)}$ near the separatrix.

Putting these together, $\delta\tilde{\varphi}$ reproduces the $b \to \infty$ behaviour of $\delta\varphi$ correctly through 4PM order, whilst also matching the $b \to b_c(v)$ behaviour through first self-force order.

We may test the effectiveness of our resummation in the geodesic limit immediately, without the need for a self-force calculation. Figure 5.3 displays the plain and resummed 4PM expressions for $\delta\varphi^{(0)}$, alongside the exact value from Eq. (2.26). The plain 4PM expression clearly deviates from the exact expression in the $b \to b_c(v)$ limit, as the former does not pick up the logarithmic divergence. By design, the resummation forces better agreement near the separatrix, but we find that it also improves agreement remarkably at all values of b, even in the PM domain ($b \to \infty$).

In fact, a similar resummation utilising the logarithmic geodesic-order singularity was previously adopted in Ref. [103], with the successful aim of improving agreement between PM expansions for the scatter angle and the results from NR simulations. The novel feature of our proposal is the inclusion of the first-order self-force information

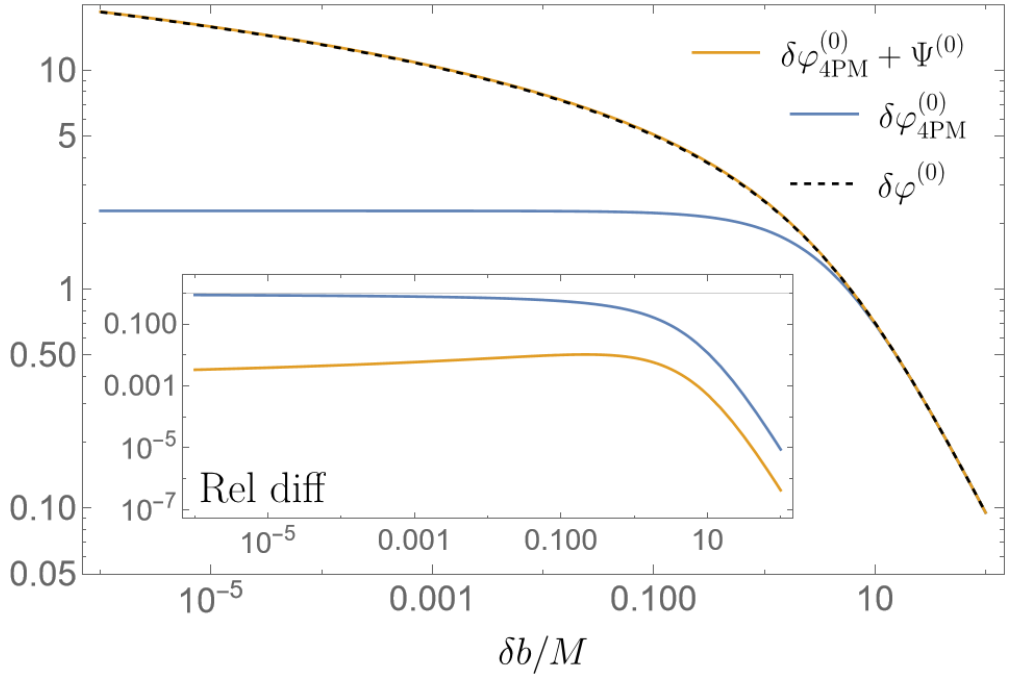

FIGURE 5.3: Comparisons between plain (blue) and resummed (orange) 4PM expressions for the geodesic scattering angle plotted as a function of δb at fixed $v = 0.5$. Also plotted is the exact expression for the geodesic scatter angle (dashed black) from Eq. (2.26). The resummation dramatically improves agreement with the exact result at all values of b. *Inset:* Differences relative to the exact geodesic scatter angle for the plain 4PM expression (blue) and resummed 4PM expression (orange). Modified from [160].

encoded in the singularity coefficient $A_1(v)$. Resumming PM results in this manner becomes particularly advantageous at 1SF order, where closed-form analytic expressions for the scatter angle are no longer available, and where numerical calculations are highly expensive. Rather than having to populate the full 2-dimensional (v, b) orbital parameter space, the semi-analytic resummed scatter angle only requires us to calculate the self-force for the 1-parameter family of geodesics with $b = b_c(v)$, significantly reducing the computational burden.

5.4 Self-force calculations along near-critical geodesics

We established in Sec. 5.2 that, in principle, the coefficient $A_1(v)$ can be obtained from a calculation of the self-force along the critical orbit $b = b_c(v)$. In practice, however, we have developed our frequency-domain code to handle non-critical orbits $b > b_c(v)$ only, and extending to $b = b_c(v)$ requires non-trivial modifications that we will discuss in Chapter 7. The time-domain code of Ref. [149] is currently restricted to non-critical orbits also. Consequently, rather than evaluate integral (5.15) directly, we will instead

calculate the self-force along a sequence of orbits with small $\delta b > 0$ (at fixed values of v), and then extract the coefficient $A_1(v)$ by numerically fitting Eq. (5.7) to the data.

In this section, therefore, we explore the calculation of the self-force along near critical geodesics. Calculations with the FD code immediately reveal the significance of large-ℓ modes in the high-velocity limit, motivating the development of a hybrid TD/FD approach which exploits the FD code's high-precision access to large-ℓ modes near to periapsis, while also retaining the TD code's better behaviour at large radius. We conclude the section by presenting selected numerical results for the scalar-field self-force along near-critical geodesics, highlighting the impact of the hybridisation and illustrating the features of the self-force in this regime.

5.4.1 High-velocity limit

In Sec. 4.3.1 we validated our self-force calculation by verifying that the terms in the mode-sum (2.49) decayed at the correct rate in ℓ. In that instance (as expected for all standard self-force calculations), the terms of the mode-sum were found to decay as ℓ^{-8} after subtracting the higher-order regularisation terms up to and including $F_{[6]}$ from Eq. (2.55). Fundamentally, as discussed in Sec. 2.2.2, the index of the power law reflects the residual non-smoothness of the field we are reconstructing, arising from the incomplete subtraction of the singular field.

While examining the results of our FD code, we have discovered an interesting new deviation from this standard behaviour, observed only in the near-separatrix, high-velocity limit. Figure 5.4 provides an illustration. It shows the $F_{[4]}$-regularised ℓ-mode contributions to the t-component of the self-force (i.e. the terms of the mode-sum (2.49) for $\alpha = t$, with parameters up to and including $F_{[4]}$ subtracted), at a certain point along a certain near-separatrix orbit with $v = 0.8$. For comparison, the same is also shown for a lower-velocity orbit with $v = 0.2$. The standard behaviour predicts that as $\ell \to \infty$, these ℓ-mode contributions should tend towards the first neglected term from Eq. (2.55), namely

$$\frac{F_{[6]t}}{(\ell - \frac{5}{2})(\ell - \frac{3}{2})(\ell - \frac{1}{2})(\ell + \frac{3}{2})(\ell + \frac{5}{2})(\ell + \frac{7}{2})}. \tag{5.23}$$

The parameter $F_{[6]t}$ is known analytically, and expression (5.23) is plotted for both the $v = 0.2$ and $v = 0.8$ orbits as reference. From the figure, we can see that for the $v = 0.2$ case the contributions approach the asymptotic prediction closely after $\ell \approx 15$. For $v = 0.8$, however, the magnitude of modal contributions picks up again at around $\ell = 14$ to form a broad "bump" in the angular spectrum. The ultimate ℓ^{-6} tail presumably develops only at greater values of ℓ, beyond the range accessible to us here. It is believed that this non-standard large-ℓ behaviour, corresponding to the presence of narrow angular features in the field, is associated with relativistic beaming of the scalar radiation

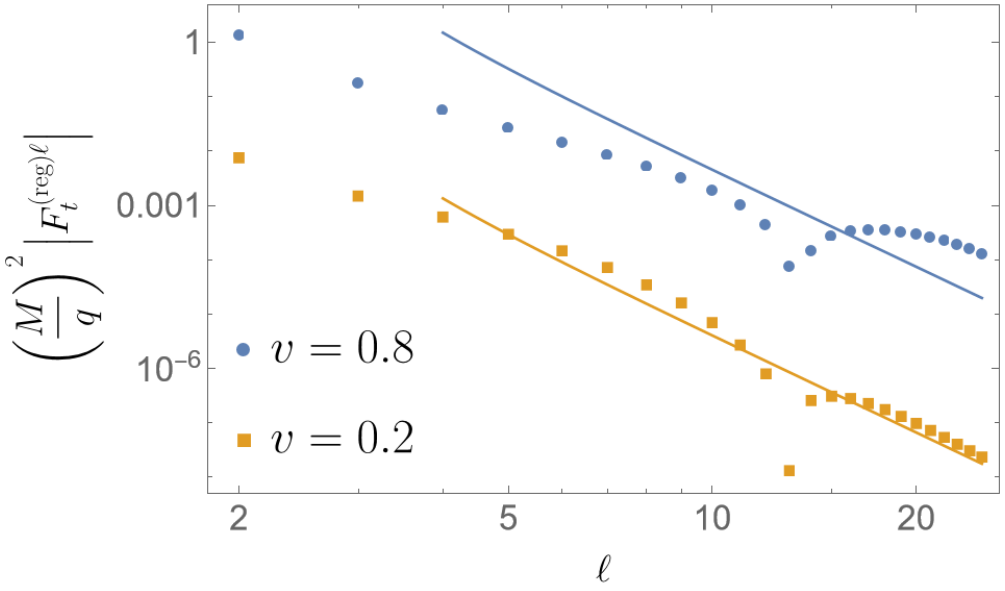

FIGURE 5.4: $F_{[4]}$-regularised ℓ-mode contributions to the t-component of the self-force at positions $r_p = 4.7M$ and $r_p = 4.2M$ along the outbound legs of the orbits with parameters $(v, b) = (0.8, 6.07387M)$ and $(0.2, 20.3825M)$, respectively (both orbits have $\delta b \approx 0.0005M$). Also plotted is the $F_{[6]}$ regularisation term for each case, towards which the $F_{[4]}$-regularised modes should tend as $\ell \to \infty$. The dips near $\ell = 13$ correspond to a sign change in both datasets. At high velocity, the ℓ-mode contributions take longer to settle down to the predicted asymptotic ℓ^{-6} decay, with distinct large-ℓ peaks visible at intermediate radii. Modified from [160].

emitted by the particle. Relativistic beaming was previously suggested in Ref. [187] as the likely explanation for behaviour they observed in the ℓ-mode contributions to various gravitational wave energy fluxes from different ultra-relativistic point particle sources. Beaming effects were also noted in gravitational waveforms during the (ultra-relativistic) near-horizon portion of quasicircular inspirals into near-extremal Kerr black holes in Ref. [188].

5.4.2 Numerical method

The broad ℓ-mode spectrum for high velocities noted in the previous section has important practical implications. When truncating the mode sum at $\ell_{\max} = 15$ (the practical limit of the TD code), the error compared to $\ell_{\max} = 25$ is observed to be on the order of several percent in the vicinity of periapsis in some instances. This is significantly larger than the other estimated numerical errors in either the TD or FD codes in that region. Fortunately, the problem is greatest in the immediate vicinity of the periastron, precisely where the FD method has high-precision access to large-ℓ modes. Conversely, the problem becomes less significant at large radii, where the TD code outperforms the FD code. This naturally suggests a hybrid TD/FD approach, which utilises the optimal code in each regime.

In this section we will describe how we achieve this hybridisation in practice, beginning with a summary of the workings of the TD code, describing the configuration of the FD code we used for the near-critical orbit calculations, and then discussing how the datasets from both codes were combined to create the best self-force model for a given orbit. We end by presenting some example self-force results, illustrating the features of the self-force along near-critical orbits and highlighting the impact of hybridisation.

5.4.2.1 Time-domain self-force calculation

The TD code developed in Ref. [149] obtains the spherical harmonic modes $\psi_{\ell m}(t,r)$ of the field using a characteristic evolution of the (1+1)d scalar-field equation (2.79). The initial value problem for each $\psi_{\ell m}$ is solved on a fixed grid of constant Eddington-Finkelstein coordinates $U = t - r_*$, $V = t + r_*$, using a second-order finite difference scheme. We do not describe the details of this scheme (which may be found in App. B of Ref. [149]), except to note that the delta-function source is implemented using "jump" conditions which are applied for each cell of the numerical grid crossed by the geodesic trajectory. Vanishing initial data $\psi_{\ell m} = 0$ is specified on the initial characteristic surfaces $U = U_0$, $V = V_0$. This initial data is unphysical, leading to a spike of spurious "junk" radiation, which propagates through the spacetime. The extraction of the physical modes $\psi_{\ell m}$ and their derivatives evaluated on the orbit must be delayed until after this junk has been allowed to dissipate.

A typical TD run uses a numerical grid split into cells of width $h = M/128$, and produces clean SF data for $r_{\rm min} \leq r_p \leq r_{\rm fin}$ (along both inbound and outbound legs of the orbit), where in these tests $r_{\rm fin}$ ranged from $450M$ to $1250M$. Since the runtime is $O(r_{\rm fin}^2)$, it is prohibitive to choose $r_{\rm fin}$ much larger than this value. Furthermore, the resolution of the grid must grow as ℓ increases, leading to a rapid degradation in computational performance. In practice this means that it is prohibitive for the TD code to routinely go beyond $\ell_{\rm max} = 15$.

5.4.2.2 Frequency-domain self-force calculation

For the calculations in this chapter, we use the same overall FD method used previously in Chapter 4. For each orbit, the values of the $C^-_{\ell m\omega}$ were pre-computed up to $\ell_{\rm max} = 25$ using the IBP4corr5 method with $r_{\rm max} = 2000M$ for $|M\omega| \geq 0.05$, and IBP04corr5 with the same $r_{\rm max}$ and $r_{\rm split} = 500M$ when $|M\omega| < 0.05$. The $C^-_{\ell m\omega}$ data was once again stored with density $M\Delta\omega = 1.25 \times 10^{-3}$.

We once again made use of adaptive ℓ-truncation in the mode-sum (2.49). The original algorithm introduced in Sec. 4.4 required some modifications in order to handle the large-ℓ peaks observed in Sec. 5.4.1, which would have otherwise triggered the early

truncation of the mode-sum. Preventing such a premature truncation is particularly important in light of the large contribution these peaks make to the total self-force. Our algorithm was thus modified in the following manner:

- A new clause was added which allowed the next regularised ℓ-mode to be included in the sum provided it was less than some ceiling. The value of this ceiling, $F_{\max}$, was updated on a rolling basis whenever $\ell \leq \ell_{\min}$ or $\left|F_\alpha^{(\mathrm{reg})\ell}\right| < \sigma_1 \left|F_\alpha^{(\mathrm{reg})\ell-1}\right|$, with the value

$$\min\left(F_{\max},\, 2\left|F_\alpha^{(\mathrm{reg})\ell-3}\right|^{1/2}\left|F_\alpha^{(\mathrm{reg})\ell-2}\right|^{1/3}\left|F_\alpha^{(\mathrm{reg})\ell-1}\right|^{1/6}\right). \tag{5.24}$$

- The clause allowing modes to be added following a single change of sign among the preceding four ℓ-modes was extended to the preceding five ℓ-modes.

- Minor changes were made to some parameters appearing in the algorithm. The safety factor σ_2 was increased from 2 to 5. Furthermore, rather than adopting a piecewise value of $\ell_{\min}$, we adopted a uniform value of $\ell_{\min} = 5$ instead.

The effectiveness of this algorithm will be demonstrated in Sec. 5.4.3.

Furthermore, the algorithm was implemented so that the dynamical ℓ-truncation was performed on the fly, at the same time as the calculation of the ℓ-modes themselves. This means that we can avoid wastefully calculating large numbers of modes which will ultimately be excluded anyway. This is in contrast to Sec. 4.4, where we pre-computed the modes with piecewise constant $\ell_{\max}$, and then used the dynamic algorithm to refine the truncation at each orbital position, discarding many un-used modes in the process. The computational saving of our new approach may be particularly significant, because the discarded modes are precisely those which involve high degrees of cancellation in the Fourier integrals, and thus take the longest to evaluate due to repeated interval bisections in the numerical quadrature.

5.4.2.3 Hybrid scatter angle calculation

For a given geodesic orbit, the TD-FD data hybridisation is performed in the following way. First, the TD and FD codes are run separately. The self-force is extracted from the TD code at radii $r_{\min} \leq r_p \leq r_{\mathrm{fin}}$, and it is also calculated at a grid of radii in $r_{\min} \leq r_p \leq 50M$ using the FD code. The output of the FD code includes the truncation value $\ell_{\max}$ used at each position, and from this we identify the largest radius r_{switch} such that $\ell_{\max} \geq 15$ for all components of the force at all radii $r_p \leq r_{\mathrm{switch}}$. For the orbits tested in this chapter, we always found $r_{\mathrm{switch}} < 50M$, justifying the appropriateness of our FD radial truncation. The scatter angle is then calculated by recasting Eq. (2.66) as an integral over radius r, and performing the sections over $r_{\min} \leq r \leq r_{\mathrm{switch}}$ and

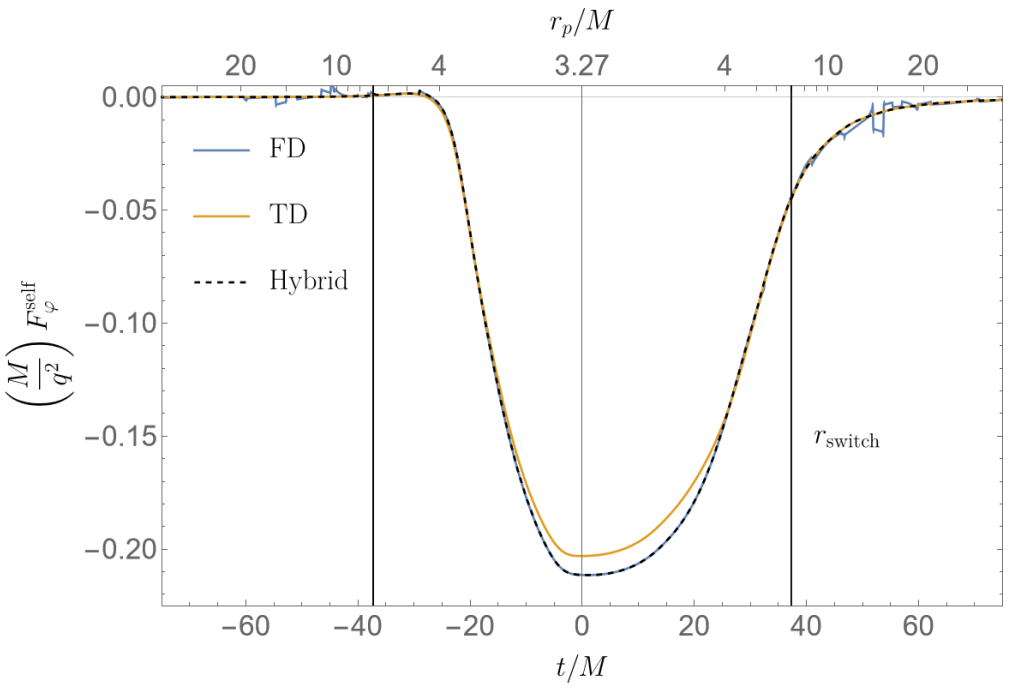

FIGURE 5.5: The azimuthal component of the unprojected self-force for the orbit with $(v, b) = (0.7, 6.71257M)$ (corresponding to $\delta b \approx 0.0005M$), as calculated using the FD (blue), TD (orange) and hybrid (dashed black) approaches. The vertical lines indicate the value of $r_{\rm switch} \approx 6.97M$ where the hybrid model transitions between the FD and TD data.

$r_{\rm switch} < r < r_{\rm fin}$ separately using self-force data from the FD and TD codes, respectively. This integration is performed using Mathematica's black-box `NIntegrate` function.

As a final step, we fit a polynomial in $1/r_p$ to the final 10-20% of the TD self-force data; this approximant is then used to estimate the $r > r_{\rm fin}$ contribution to the scatter angle integral. The range of the fit and the degree of the polynomial are varied, allowing us to estimate the error $\epsilon_{\rm tail}$ in the scatter angle arising from this tail fit. In Refs. [149, 151], which did not encounter the large-ℓ features observed at high-velocities in Sec. 5.4.1, $\epsilon_{\rm tail}$ was typically the dominant source of error in the scatter angle.

5.4.3 Selected self-force results

Figure 5.5 shows the unprojected self-force component $F_\varphi^{\rm self}$ for the orbit with parameters $v = 0.7$ and $b = 6.71257M$, corresponding to $\delta b \approx 0.0005$, as calculated using the FD, TD and hybrid approaches. The impact of the hybridisation is immediately clear. In the vicinity of periapsis ($t = 0$, $r_p = r_{\rm min} \approx 3.27M$), there is a clear naked eye difference between the FD and TD results, with a peak relative difference of 5.2%. This difference is caused almost entirely by the inclusion of $\ell > 15$ modes in the FD code, and the hybridisation is critical to ensure we include as much of this large contribution

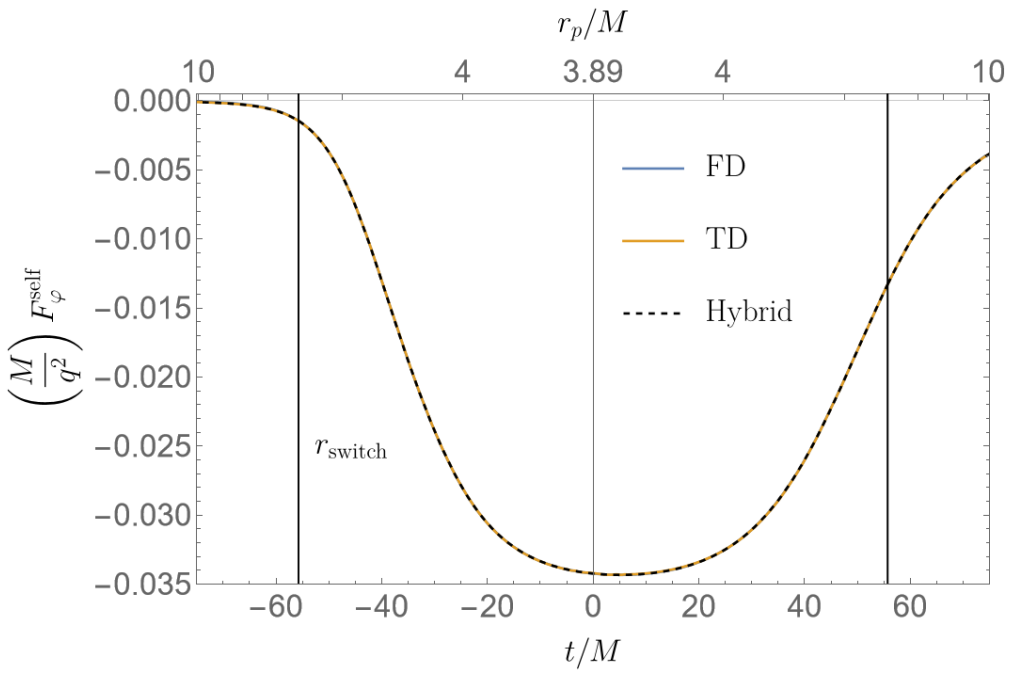

FIGURE 5.6: Same as Fig. 5.5, but for the orbit with $(v, b) = (0.2, 20.3825M)$ (again $\delta b \approx 0.0005M$). In this instance $r_{\rm switch} \approx 6.01M$.

as possible. As the radius r_p along the orbit increases, the gap between the TD and FD codes then closes.

At larger radii, the FD curve in Fig. 5.5 displays distinct jagged features after $r \sim r_{\rm switch}$, where the FD data may deviate significantly from the smooth TD curve. These features may be attributed to rapid variations in the value of $\ell_{\rm max}$, and in particular the instances of large deviation from the TD code are caused by the accidental inclusion of anomalous high-cancellation modes. The root cause of this problem lies in the amendments we made to our truncation algorithm in Sec. 5.4.2.2. The permissive nature of our updated algorithm, which allows any mode to be included so long as it does not exceed the rolling ceiling, increases the risk of including deviant modes as compared to the maximally strict algorithm of Sec. 4.4, which only allows modes to be included if they are decreasing (with a narrow exception to allow for routine changes of sign). The impact on our calculation, however, is minimal. As can be seen from the figure, the jagged features only begin to appear shortly around $r_{\rm switch}$, and there are no features of significant amplitude in the $r \leq r_{\rm switch}$ region (something which we carefully verified for all orbits used in the next section). The hybrid model is thus essentially unaffected. This is not luck or coincidence: the inclusion of deviant ℓ-modes does not become an issue until the cancellation problem has become well-established, by which point the FD code's $\ell_{\rm max}$ will have already fallen to around, or below, 15.

Figure 5.6 again displays the self-force component $F_\varphi^{\rm self}$, but this time for the orbit with $v = 0.2$ and $b = 20.3825M$ (again $\delta b \approx 0.0005$). As expected, the impact of hybridisation is much smaller at this lower velocity, and the TD and FD curves are visually coincident

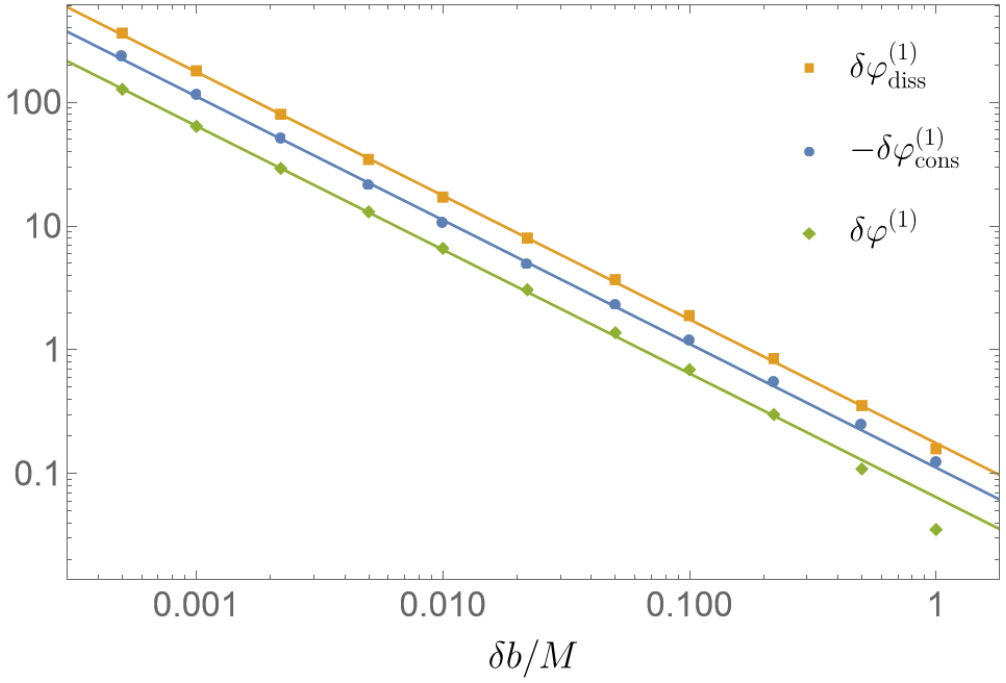

FIGURE 5.7: Strong-field numerical results for the dissipative (orange), conservative (blue), and total (green) pieces of the scattering angle for an initial velocity $v = 0.5$. The values were generated with the hybrid model, with error bars too small to be discerned on the scale of this plot. The solid lines are the extracted divergences of the form $\sim A_1(b_c/\delta b)$. The fitted values of A_1 are given in Table 5.1. Modified from [160].

throughout the range. Another notable feature is the distinct flattening of the self-force around periapsis. This is a generic feature of the self-force for small δb, being seen also in Fig. 5.5, and it arises from the particle's prolonged quasicircular whirl.

5.5 Calculating $A_1(v)$ by extrapolation

We fixed a grid of velocities in the range $0.15 \leq v \leq 0.7$ with spacing $\Delta v = 0.05$. At lower velocities, the transition to the asymptotic behavior $\delta\varphi^{(1)} \sim 1/\delta b$ is delayed until smaller values of δb, complicating the extrapolation. At higher velocities, it takes longer for the initial junk radiation to separate from the particle in the TD simulation, forcing us to start at a larger initial radius and hence increasing computational cost. For each velocity included in our sample, we ran the TD and FD codes to calculate the SF along each of the orbits with $b = b_c(v) + \delta b$, where δb takes values in $\{0.0005, 0.001, 0.0022, 0.005, 0.01, 0.022, 0.05, 0.1, 0.22, 0.5, 1\}$. The values of $\delta\varphi^{(1)}_{\rm cons}$ and $\delta\varphi^{(1)}_{\rm diss}$ were then calculated separately for each orbit using the hybrid method outlined in Sec. 5.4.2.3.

Figure 5.7 displays $\delta\varphi^{(1)}$, $\delta\varphi^{(1)}_{\rm cons}$ and $\delta\varphi^{(1)}_{\rm diss}$, plotted as functions of δb at fixed $v = 0.5$, illustrating the $1/\delta b$ divergence. For each value of v in our sample we fit the numerical dataset to the expression on the right hand side of Eq. (5.7), to obtain an estimate of $A_1(v)$. For this purpose we use Mathematica's `NonlinearModelFit` function, weighting

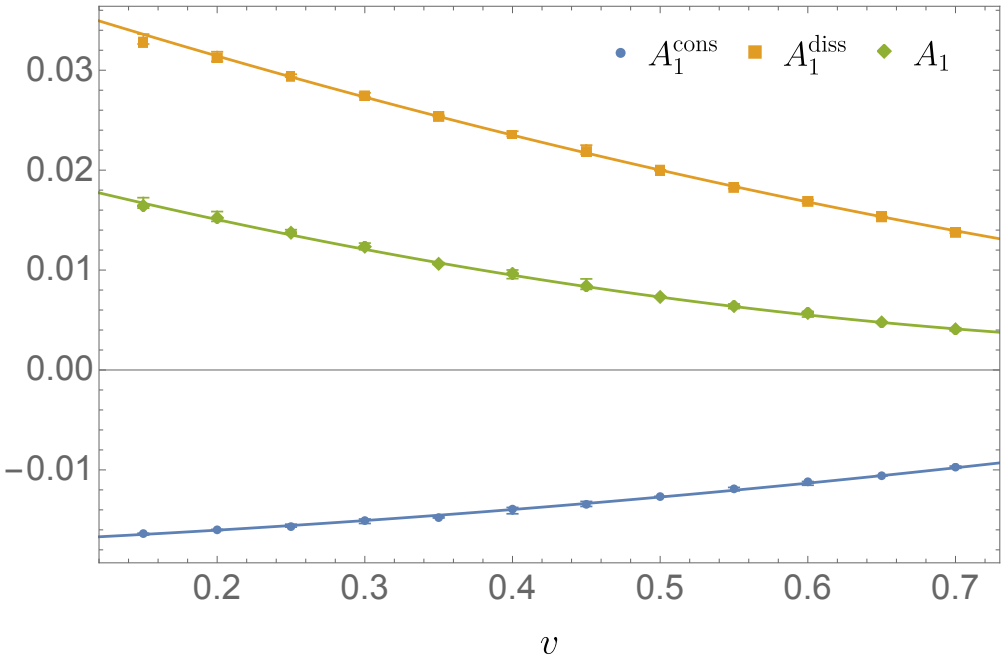

FIGURE 5.8: Values of the singularity parameter $A_1(v)$ for the conservative (blue), dissipative (orange), and total (green) pieces as a function of initial velocity v. The error bars on the values are shown but are barely visible on this scale. Shown in solid lines are the best-fit curves given in Eqs. (5.25)–(5.27).

each data point by $1/\epsilon_{\text{tail}}^2$, where, recall, ϵ_{tail} is the estimated error in the scattering angle due to the analytic fit to the SF at large radius. This routine returns an estimate for the value of $A_1(v)$, together with an estimate of the fitting error in this value. We perform the fit for the conservative and dissipative pieces separately, and then calculate $A_1(v) = A_1^{\text{diss}}(v) + A_1^{\text{cons}}(v)$. This approach is potentially more accurate, because, as illustrated in Fig. 5.7, the opposite signs of the conservative and dissipative contributions cause the total scattering angle to approach the asymptotic $1/\delta b$ behavior somewhat more slowly than for $\delta\varphi_{\text{cons}}^{(1)}$ and $\delta\varphi_{\text{diss}}^{(1)}$ individually.

Our fitting procedure is as follows. For each velocity, values of A_1^{diss} and A_1^{cons} are obtained by fitting to the N smallest values of δb in our sample, for $N = 3, ..., N_{\text{max}}$. We took $N_{\text{max}} = 8$ for $v \geq 0.3$, and $N_{\text{max}} = 6$ for $v < 0.3$ where the $\sim 1/\delta b$ trend is observed to break down at lower values of δb. A best estimate for each velocity was obtained by fitting a constant value to these individual fits, again using `NonlinearModelFit`, weighting the individual fits by the inverse squares of their estimated errors. The final error bar on A_1 (for each v) was conservatively estimated as the range between the largest and smallest values in our sample of individual fits, including their individual error bars.

v	A_1	$A_1^{\rm cons}$	$A_1^{\rm diss}$
0.15	0.01642^{+80}_{-22}	-0.01637^{+04}_{-14}	0.03280^{+80}_{-17}
0.20	0.01522^{+60}_{-35}	-0.01600^{+4}_{-6}	0.03122^{+60}_{-34}
0.25	0.01373^{+31}_{-11}	-0.01568^{+24}_{-05}	0.02941^{+19}_{-10}
0.30	0.01234^{+40}_{-31}	-0.01507^{+16}_{-29}	0.02741^{+33}_{-10}
0.35	0.01062^{+12}_{-07}	-0.01477^{+8}_{-4}	0.02539^{+9}_{-5}
0.40	0.0096^{+4}_{-5}	-0.01393^{+17}_{-50}	0.02357^{+32}_{-19}
0.45	0.00839^{+70}_{-32}	-0.01345^{+29}_{-21}	0.02184^{+70}_{-25}
0.50	0.00731^{+5}_{-4}	-0.012670^{+26}_{-27}	0.019978^{+50}_{-35}
0.55	0.00639^{+21}_{-25}	-0.01190^{+14}_{-20}	0.01829^{+16}_{-15}
0.60	0.00570^{+15}_{-40}	-0.01119^{+03}_{-35}	0.01689^{+15}_{-20}
0.65	0.004761^{+26}_{-26}	-0.010585^{+18}_{-18}	0.015345^{+19}_{-20}
0.70	0.00407^{+15}_{-15}	-0.00972^{+11}_{-11}	0.01379^{+11}_{-10}

TABLE 5.1: Calculated values of $A_1(v)$, $A_1^{\rm cons}(v)$ and $A_1^{\rm diss}(v)$, with estimated error bars on the last displayed decimals (e.g., 0.01642^{+80}_{-22} means $0.01642^{+0.00080}_{-0.00022}$). The error bars for $A_1(v)$ are obtained by adding the error bars of the conservative and dissipative pieces in quadrature.

The resulting values of $A_1(v)$, with error bars, are displayed in Fig. 5.8 and tabulated in Table 5.1. Also included in Fig. 5.8 are the best-fit curves

$$A_1(v) \approx 0.0222 - 0.0398v + 0.0199v^2, \tag{5.25}$$

$$A_1^{\rm cons}(v) \approx -0.0175 + 0.0060v + 0.0072v^2, \tag{5.26}$$

$$A_1^{\rm diss}(v) \approx 0.0406 - 0.0488v + 0.0154v^2, \tag{5.27}$$

obtained by fitting functions of the form $a + bv + cv^2$ to the numerical data, weighting each point by the inverse square of the size of its error bar.

5.6 PM resummation: results

With values of $A_1(v)$ in hand, we now test the performance of our resummed scatter angle (5.22), using the numerical self-force scatter angle calculation as a benchmark.

Figure 5.9 displays the numerical values of $\delta\varphi^{(1)}_{\rm cons}$ and $\delta\varphi^{(1)}_{\rm diss}$ as functions of δb at fixed $v = 0.5$, alongside the plain and resummed 4PM expressions for the same quantities. The plain 4PM expression agrees with the numerical self-force results to within a few percent or less in the weak-field ($\delta b \gtrsim 10M$), but the accuracy deteriorates rapidly as the impact parameter is reduced. The resummed PM expression, on the other hand, is uniformly accurate across the entire domain. Indeed, the resummation appears to even increase the agreement in the weak-field. Similar results are obtained for all other values of v sampled in our work.

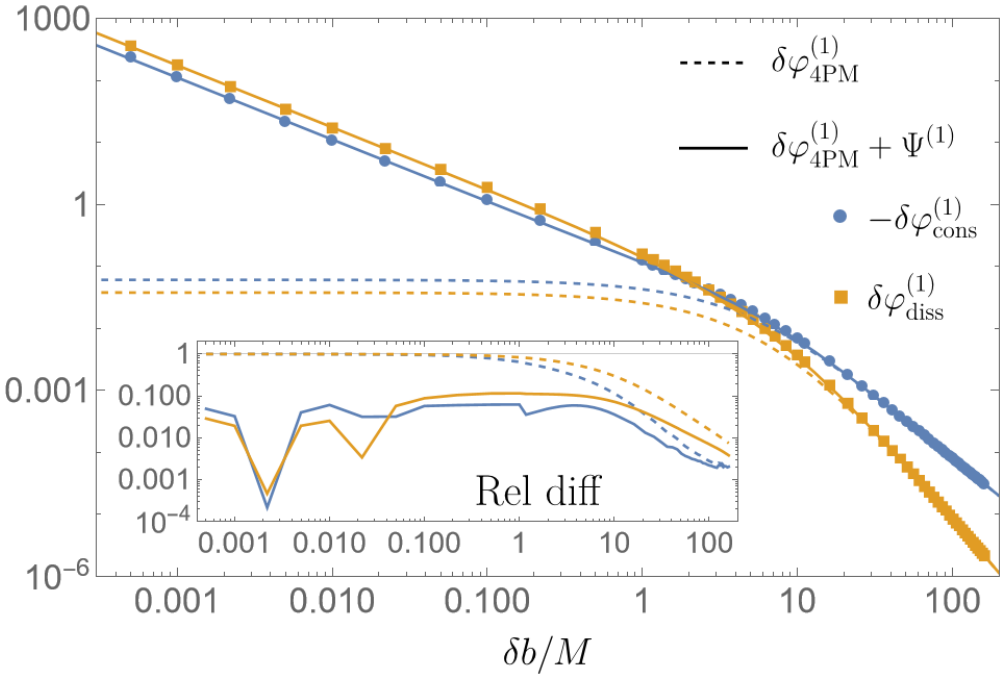

FIGURE 5.9: Comparisons between the plain (dashed) and resummed (solid) 4PM expressions for the conservative (blue) and dissipative (orange) contributions to the scalar-field self-force correction to the scatter angle at $v = 0.5$. *Inset:* relative difference between the PM results and the "exact" numerical self-force values. The resummation formula, given in Eq. (5.22), uses the values of $A_1^{\rm cons}$ and $A_1^{\rm diss}$ given in Table 5.1. The self-force scatter angle corrections were calculated using the hybrid method for $\delta b \leq M$, and using the TD code alone for $\delta b > M$. Numerical errors are too small to be visible on the scale of the main plot. Modified from [160].

We may also confirm the benefit from our novel inclusion of the 1SF terms in the resummation. Figure 5.10 shows the total angle $\delta\varphi^{\rm 1SF} := \delta\varphi^{(0)} + \eta_q \delta\varphi^{(1)}$ for fixed $\eta_q = 0.1$ and $v = 0.5$, alongside the corresponding 4PM expressions without any resummation, with geodesic order resummation, and with the full 1SF order resummation. Both resummations appear to increase the accuracy in the weak field by approximately an order of magnitude relative to the plain PM expressions. Differences between the resummations become manifest in the strong-field regime where the $1/\delta b$ divergence starts to dominate. The full resummation captures the scattering angle with at least $\sim 1\%$ precision, including in regions where the plain PM expansion completely breaks down.

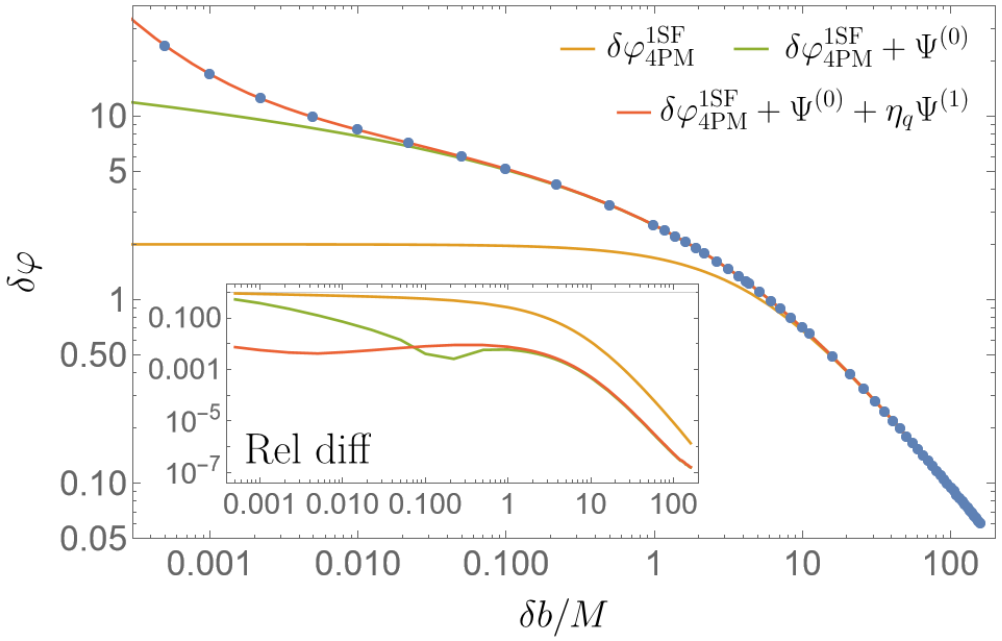

FIGURE 5.10: Total scatter angle (geodesic + 1SF correction) for $\eta_q = 0.1$ and $v = 0.5$. This figure compares the numerical self-force values (blue dots) to the 1SF truncation of the 4PM scatter angle, $\delta\varphi^{\rm 1SF}_{\rm 4PM}$, with no resummation (orange), geodesic order resummation only (green), and full 1SF resummation (red). *Inset:* relative difference between the PM results and the numerical values, interpolated over δb. The self-force scatter angle corrections were calculated using the hybrid method for $\delta b \leq M$, and using the TD code alone for $\delta b > M$. Numerical errors are too small to be visible on the scale of the main plot. Modified from [160].

Chapter 6

Large radius asymptotics of the self-force: analytical calculation

In this chapter we present an approach for calculating the self-force analytically as an expansion in $1/r_p$ at early and late times along the scatter orbit. The benefit of such a calculation is obvious in the context of our frequency-domain self-force calculations, in which we are unable to calculate the self-force accurately at $r_p \gg r_{\rm min}$. Having accurate analytical expressions whose domain of validity overlaps with that of the frequency-domain code would allow us to delegate to the analytical results at larger-r_p, enabling independent frequency-domain calculations of the self-force along the entire orbit without needing to hybridise with time-domain data as in Chapter 5. The analytical results would also be of direct benefit to time-domain methods too, allowing the simulation to be terminated at earlier times and thus reducing runtime. Analytical data can also be used to replace junk-contaminated data early in the simulation, improving accuracy, and perhaps runtime by reducing the amount of time one must spend waiting for the junk radiation to dissipate. Alternatively, one can tackle the junk radiation problem directly by extending our calculation of the scalar field to arbitrary positions at early times, giving an approximation to the physical initial data. Finally, whichever approach is taken, all numerical self-force calculations must ultimately be truncated at some finite radius, thus requiring an extrapolation of the self-force to infinity in order to accurately calculate the scatter angle. Presently, this can only be achieved numerically (as in Sec. 5.4.2.3), but analytical large-radius expansions will provide an alternate, more accurate, approach.

Our analytical calculation will be performed in the time-domain. We will work in terms of Eddington-Finkelstein (EF) coordinates,

$$U := t - r_*, \qquad V := t + r_*, \tag{6.1}$$

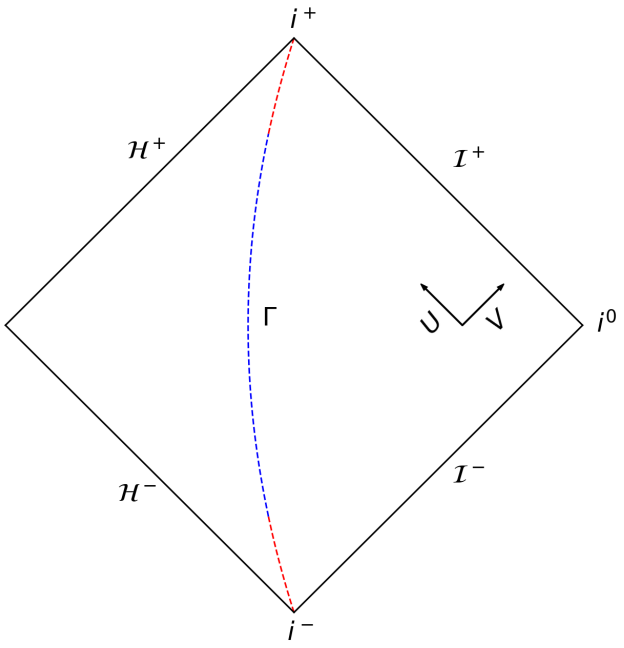

FIGURE 6.1: Penrose diagram for the $r > 2M$ coordinate patch of Schwarzschild spacetime containing a scatter orbit Γ. In this chapter we develop a framework for calculating the scalar-field self-force at early and late times (highlighted in red) along the orbit.

such that the Schwarzschild line element takes the form

$$ds^2 = -f(r)dUdV + r^2 d\Omega^2, \tag{6.2}$$

where, recall, $f(r) = (1 - 2M/r)$ and $d\Omega^2 = d\theta^2 + \sin^2\theta d\varphi^2$ is the metric on a unit 2-sphere. We will also make use of the metric determinant, given in these coordinates by

$$\sqrt{-g} = \frac{1}{2} f(r) r^2 \sin\theta. \tag{6.3}$$

The surfaces $U, V = \text{const}$ describe rays at 45° in the Penrose diagram for Schwarzschild spacetime, displayed in Fig. 6.1. Also illustrated in the figure is a schematic representation of a scatter geodesic orbit. Our objective is to approximate the self-force near past and future timelike infinity, $i^{\pm}$. In fact, for the purposes of simplicity we will only consider the i^+ limit here, corresponding to $U, V \to \infty$ along the orbit. The calculation for the i^- limit would proceed similarly. The scalar field equation in (1+1)D will be reformulated in terms of EF coordinates in Sec. 6.1. We then introduce our perturbative approach to solving the field equation, and give the appropriate Green's function. The leading-order terms in our expansion of the scalar-field ℓ-modes will be derived, and used to construct the regularised terms in the mode-sums for both the Detweiler-Whiting regular field and the self-force. The sum over ℓ is performed explicitly, yielding zero in both cases: the leading-order piece of the scalar-field does not contribute to the self-force.

Our leading-order results for the individual ℓ-modes are also validated by comparison to numerical data. We conclude by formulating our strategy for the next-to-leading order calculation for the scalar-field (from which we will obtain the leading-order self-force), the results of which remain at a preliminary stage.

6.1 Scalar-field equation in Eddington-Finkelstein coordinates

In EF coordinates, the (1+1)D scalar field equation (2.79) becomes

$$\frac{\partial^2\psi_{\ell m}}{\partial U\partial V}+\frac{1}{4}V_\ell(r)\psi_{\ell m}=\pi r f(r)T_{\ell m}, \tag{6.4}$$

where $V_\ell(r)$ is as given in Eq. (2.80). Rather than transform Eq. (2.86) to EF coordinates, it is easier to obtain $T_{\ell m}$ in terms of U,V from first principles, using the coordinate-invariant definition of T in Eq. (2.31). By the orthogonality of the spherical harmonics,

$$\begin{aligned}
\pi r f(r)T_{\ell m} &= \pi r f(r)\int d\Omega\, Y^*_{lm}(\theta,\varphi)T(x^\alpha_p(\tau))\\
&= \pi q r f(r)\int d\Omega\, Y^*_{lm}(\theta,\varphi)\int\frac{d\tau}{\sqrt{-g}}\,\delta^4(x^\alpha-x^\alpha_p(\tau))\\
&= \frac{2\pi q}{r_p(U)}\int d\tau\delta(V-V_p(\tau))\delta(U-U_p(\tau))\int d\theta\, d\varphi\, Y^*_{lm}(\theta,\varphi)\delta(\theta-\pi/2)\delta(\varphi-\varphi_p(\tau))\\
&= \frac{2\pi q}{r_p(U)\dot u_p(U)}\,\delta(V-V_p(U))\,Y^*_{lm}(\pi/2,\varphi_p(U)),
\end{aligned} \tag{6.5}$$

where we made use of Eq. (6.3) in the third line, and overdots denote $d/d\tau$ as usual. Notice also that we use U as parameter along the geodesic orbit, and $V_p(U)$, for example, is the relation between the V and U coordinates along that orbit. Equation (6.4) may thus be rewritten

$$\frac{\partial^2\psi_{\ell m}}{\partial U\partial V}+\frac{1}{4}V_\ell(r)\psi_{\ell m}=S_{\ell m}(U)\delta(V-V_p(U)), \tag{6.6}$$

where

$$S_{\ell m}(U):=\frac{2\pi q Y^*_{lm}(\pi/2,\varphi_p(U))}{r_p(U)\dot U_p(U)}. \tag{6.7}$$

The frequency modes $S_{\ell m\omega}$ defined in Eq. (2.107) are not exactly the frequency-modes of $S_{\ell m}$, but there is no possibility of confusion: in this chapter, any reference to $S_{\ell m}$ will unambiguously mean the functions defined in Eq. (6.7).

6.2 Perturbative treatment of the (1+1)D field equation

6.2.1 Hierarchichal expansion of the scalar field

Our perturbative treatment is based on the iterative expansion of the scalar field introduced in Ref. [189]. The first step is to introduce a cutoff R obeying $2M < R < r^*_{\rm min}$, and a new potential

$$V_0(r) := \begin{cases} \dfrac{\ell(\ell+1)}{4r_*^2}\,, & r_* \geq R, \quad \ell > 0, \\ 0\,, & r_* < R, \quad \ell > 0, \\ \delta(r_* - R)/M, & \ell = 0, \end{cases} \tag{6.8}$$

which approximates the asymptotic behaviour of the true potential $V_\ell(r)$ in the limits $r_* \to \pm\infty$. Consider next an expansion

$$\psi_{\ell m}(U,V) = \sum_{n=0}^{\infty} \psi_{\ell m,n}(U,V), \tag{6.9}$$

where the $\psi_{\ell m,n}$ obey the iterative equations

$$\partial^2_{UV}\psi_{\ell m,0} + V_0(r)\psi_{\ell m,0} = S(U)\delta(V - V_p(U)), \tag{6.10}$$

$$\partial^2_{UV}\psi_{\ell m,n} + V_0(r)\psi_{\ell m,n} = -\delta V(r)\psi_{\ell m,n-1} \qquad (\forall n > 0), \tag{6.11}$$

with

$$\delta V(r) := \frac{1}{4}V_\ell(r) - V_0(r). \tag{6.12}$$

Provided the sum converges, expansion (6.9) gives a solution to Eq. (6.6). Furthermore, if the $\psi_{\ell m,n}$ obey retarded boundary conditions individually, then so too will solution (6.9). We can thus construct the retarded scalar field by solving the hierarchy (6.10) and (6.11) with retarded boundary conditions at each level.

We note that expansion (6.9) does not immediately give us the large-radius expansion that we desire, so we must additionally expand each $\psi_{\ell m,n}$ in $1/r_p$. Using Eq. (6.11), and the fact that $\delta V \sim M$, dimensional considerations imply $\psi_{\ell m,n} \sim (M/L)\psi_{\ell m,n-1}$, where L is some length scale that does not scale with the mass. If r_p was the only other length scale in our problem, we could immediately conclude that each term in expansion (6.9) is suppressed by a factor M/r_p relative to the preceding term. This would be highly convenient, as it would ensure we can calculate the $1/r_p$ expansion of the field *exactly* to some order using a calculation of only *finitely* many $\psi_{\ell m,n}$, each individually expanded to the required order in $1/r_p$. Unfortunately, this argument fails because we have two additional length scales in our problem: the impact parameter b, and the cutoff R (the entire field $\psi_{\ell m}$ is independent of the arbitrary cutoff R, but the individual $\psi_{\ell m,n}$ need

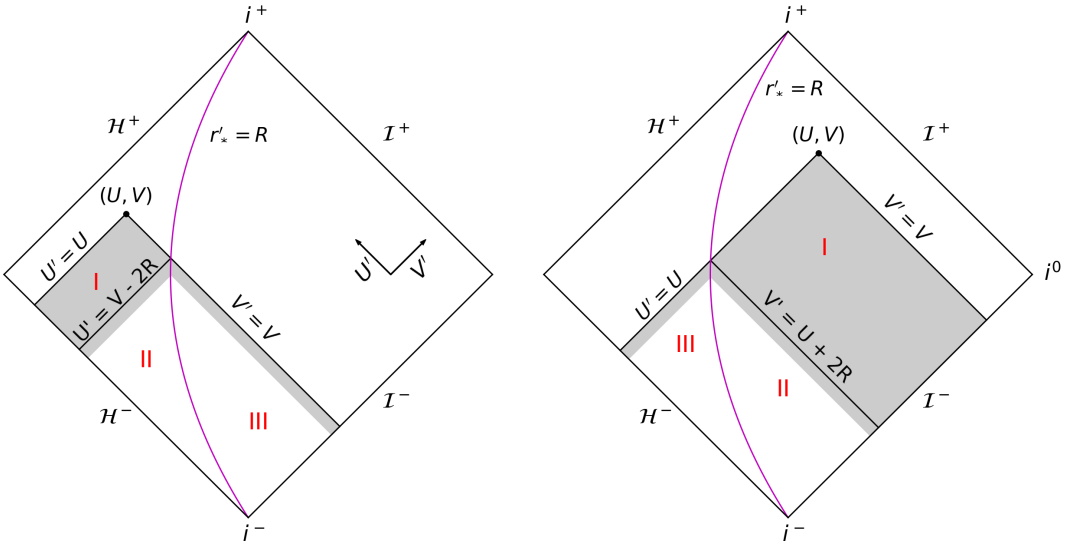

FIGURE 6.2: Regions of the retarded Green's function of $\partial_{UV} + V_0$ for a fixed field point (U, V) inside the sphere $r_* = R$ (left panel) and outside it (*right* panel). The primary support of the Green's function in each case is indicated by the shaded areas; it falls off exponentially in U or V going away from each shaded band to its past.

not be). Establishing that the $\psi_{\ell m,n}$ decay more rapidly in r_p with increasing n would thus require an explicit calculation, or a careful bounding argument. For the time being, we proceed with our calculation anyway, with the aim of demonstrating that at least $\psi_{\ell m,1}$ decays more rapidly than $\psi_{\ell m,0}$ along the way.

6.2.2 The Green's function

We find the retarded solutions to Eqs. (6.10) and (6.11) using a Green's function approach. The Green's function we require is the solution $G(U, V; U', V')$ of

$$G_{,UV} + V_0\, G = \delta(U - U')\, \delta(V - V') \tag{6.13}$$

which obeys the "retarded" conditions $G(U < U') = 0 = G(V < V')$. This Green's function was derived in Ref. [189]. The functional form of G depends on the positions of the the field point (U, V) and source point (U', V') with respect to the cutoff radius R. For field points outside R (i.e., $V - U > 2R$), we identify 3 regions I-III indicated in the left panel of Fig. 6.2, with corresponding Green's functions denoted $G^{\rm I}_>$, $G^{\rm II}_>$ and $G^{\rm III}_>$. For field points inside R (i.e., $V - U < 2R$), we identify 3 regions, again labelled I-III and indicated in the right panel of Fig. 6.2, with corresponding Green's functions denoted $G^{\rm I}_<$, $G^{\rm II}_<$ and $G^{\rm III}_<$.[1]

[1]Note this notation differs from that of [189], where Roman numerals were used to label regions defined for a fixed *source* point; our $G^{\rm I-III}_>$ correspond to Ref. [189]'s $G^{\rm A-C}$, and Ref. [189] has no notation equivalent to our $G^{\rm I-III}_<$.

For an external field point, Ref. [189] obtained [2]

$$G^{\mathrm{I}}_{>} = \sum_{n=0}^{\ell} A^{\ell}_{n} \frac{\partial^{n}_{U} g(U;U',V')}{(V-U)^{\ell-n}}, \tag{6.14}$$

where

$$g(U;U',V') = \frac{1}{\ell!}\left[\frac{(V'-U)(U-U')}{(V'-U')}\right]^{\ell}, \tag{6.15}$$

and

$$A^{\ell}_{n} = \frac{(2\ell-n)!}{n!(\ell-n)!}. \tag{6.16}$$

Note that for $\ell = 0$ this is simply $G^{\mathrm{I}}_{>} \equiv 1$. We also note that the sum over n can be evaluated explicitly to give

$$G^{\mathrm{I}}_{>}(U,V;U',V') = \frac{1}{\ell!}\frac{(V-U)^{\ell+1}}{(V'-U')^{\ell}}\frac{\partial^{\ell}}{\partial U^{\ell}}\left[\frac{(V'-U)^{\ell}(U-U')^{\ell}}{(V-U)^{\ell+1}}\right]. \tag{6.17}$$

The calculations in the present chapter do not currently make use of this simplification, but this may prove useful for subsequent calculations at higher orders. For regions II and III the expressions are

$$G^{\mathrm{II}}_{>} = \sum_{n,j=0}^{\ell}\sum_{i=1}^{\ell+1} \beta_{nji}\frac{(r'_{*}-R)^{\ell-j}R^{\ell+j-n}}{(r'_{*})^{\ell}\, r_{*}^{\ell-n}}\, E_i(U-V'+2R), \tag{6.18}$$

$$G^{\mathrm{III}}_{>} = \sum_{n}^{\ell}\sum_{i=1}^{\ell+1} \gamma_{ni}\left(\frac{R}{r_{*}}\right)^{\ell-n} E_i(U-U'), \tag{6.19}$$

where $r'_{*} = (V'-U')/2$, and β_{nji} and γ_{ni} are certain constant coefficients (depending on ℓ only) whose exact values will not be needed for our purposes. The symbol $E_i(x)$ represents $\exp(-\kappa_i x/R)$, where κ_i are certain complex numbers satisfying $\mathrm{Re}\,\kappa_i > 0$ for all i. Hence $E_i(x)$ decays exponentially in x. Results of this form are valid even for $\ell = 0$, where exact expressions are given in Eq. (61) of [189] .

For an internal field point, Ref. [189] obtained

$$G^{\mathrm{I}}_{<} \equiv 1, \tag{6.20}$$

$$G^{\mathrm{II}}_{<} = \sum_{i=1}^{\ell+1} \gamma_i E_i(V-U'-2R), \tag{6.21}$$

and

$$G^{\mathrm{III}}_{<} = \sum_{j=0}^{\ell}\sum_{i=1}^{\ell+1} \beta_{ji}\frac{(r'_{*}-R)^{\ell-j}R^{j}}{(r'_{*})^{\ell}}\, E_i(V-V'), \tag{6.22}$$

[2] Note that Eq. (6.14) and all subsequent expressions for the Green's function implicitly contain factors $\Theta(V-V')\Theta(U-U')$, where Θ is the Heaviside step function, to enforce the retarded condition $G(U,V;U',V') = 0$ whenever $U < U'$ or $V < V'$. We omit these factors for brevity, and enforce causality through the choice of integration limits.

where $\gamma_i := \sum_{n=0}^{\ell} \gamma_{ni}$ and $\beta_{ji} := \sum_{n=0}^{\ell} \beta_{nji}$. Again, it can be checked that these forms are valid also for $\ell = 0$.

6.3 Evaluating Φ_0^R on Γ near i^+

The objective of this section is to obtain the Detweiler-Whiting regular piece of the leading-late-time (LLT), leading-hierarchical (LH) scalar field evaluated on the scatter geodesic at late times. More precisely, we begin by deriving the retarded fields $\psi_{\ell m,0}$ in full generality, considering the different Green's function regions which contribute depending on the position of the field evaluation point. We then evaluate the $\psi_{\ell m,0}$ on the scatter geodesic Γ, and derive their LLT behaviour. The ℓ-mode contributions to the LH scalar field are defined to be

$$\Phi_0^{\ell}(U,V,\theta,\varphi) := \frac{1}{r} \sum_{m=-\ell}^{\ell} \psi_{\ell m,0}(U,V) Y_{\ell m}(\theta,\varphi), \tag{6.23}$$

and we obtain their LLT behaviour along Γ. Mode-sum regularisation is then used to obtain the ℓ-mode contributions of the LLT, LH scalar field to the Detweiler-Whiting regular field. As a final step, we perform the sum over ℓ analytically, finding that the LLT, LH scalar field does not contribute to the regular field.

6.3.1 Derivation of ψ_0

The retarded solution to Eq. (6.10) can be written in terms of the retarded Green's function,

$$\begin{aligned} \psi_0(U,V) &= \int_{-\infty}^{U} dU' \int_{-\infty}^{V} dV' G(U;U',V') S(U') \delta(V' - V_p(V')) \\ &= \psi_0^{\mathrm{I}} + \psi_0^{\mathrm{II}} + \psi_0^{\mathrm{III}}, \end{aligned} \tag{6.24}$$

where ψ_0^{X} represents the contribution to the double integral from region X ($X \in \{\mathrm{I}, \mathrm{II}, \mathrm{II}\}$). Note that we have suppressed the explicit ℓm labels in Eq. (6.24) for the purposes of notational compactness, so that $\psi_0 \equiv \psi_{\ell m,0}$, $S(U) \equiv S_{\ell m}(U)$ etc. We will continue with this convention, reintroducing mode labels only when necessary for clarity.

Which source regions X contribute significantly to $\psi_0(U,V)$ depends on whether the field evaluation point (U,V) lies in the external zone outside the cutoff, $V - U \geq 2R$, or in the internal zone, $V - U < 2R$. We consider the two cases separately below.

6.3.1.1 External evaluation point

By construction, the geodesic trajectory lies entirely outside the cutoff, and hence does not intersect region III for an external evaluation point. This means that the source has no support in region III, immediately giving

$$\psi^{\rm III}_{0>} \equiv 0 \tag{6.25}$$

for any external evaluation point.

We see from Fig. 6.3 that in region II, the source is supported only in the subregion with $U' < \bar{U}(U)$, where $\bar{U}$ is the solution of

$$V_p(\bar{U}) = U + 2R. \tag{6.26}$$

The contribution from region II is thus given by

$$\psi^{\rm II}_{0>}(U,V) = \int_{-\infty}^{\bar{U}(U)} dU' \int_{\bar{V}(U')}^{\bar{V}(U)} dV' G^{\rm II}_{>}(U;U',U') S(U') \delta(V' - V_p(U')), \tag{6.27}$$

where

$$\bar{V}(U) := U + 2R. \tag{6.28}$$

Performing the integral over V', and substituting the Green's function from Eq. (6.18), we arrive at

$$\psi^{\rm II}_{0>}(U,V) = \sum_{n,j=0}^{\ell} \sum_{i=1}^{\ell+1} \beta_{nji} \left(\frac{R}{r_*}\right)^{\ell-n} \int_{-\infty}^{\bar{U}(U)} dU' \left(1 - \frac{R}{r'_{*p}}\right)^{\ell-j} \left(\frac{R}{r'_{*p}}\right)^{j} E_i(U - V_p(U') + 2R)\, S(U'). \tag{6.29}$$

Finally, for region I, the relevant domain of integration depends on whether $V \geq V_p(U)$ (i.e. the evaluation point is outside the scatter geodesic Γ) or $V < V_p(U)$ (the evaluation point lies between R and Γ); the two scenarios are illustrated in Fig. 6.3. The contributions in each case are

$$\begin{aligned}
\psi^{\rm I}_{0>}(U, V \geq V_p(U)) &= \int_{\bar{U}(U)}^{U} dU' \int_{\bar{V}(U)}^{V_p(U)} dV' G^{\rm I}_{>}(U;U',V') S(U') \delta(V' - V_p(U')), \\
\psi^{\rm I}_{0>}(U, V < V_p(U)) &= \int_{\bar{U}(U)}^{U_p(V)} dU' \int_{\bar{V}(U)}^{V} dV' G^{\rm I}_{>}(U;U',V') S(V') \delta(V' - V_p(U')).
\end{aligned} \tag{6.30}$$

Upon integrating over V', we have for either scenario

$$\psi^{\rm I}_{0>}(U,V) = \int_{\bar{U}(U)}^{\tilde{U}(U,V)} dU'\, G^{\rm I}_{>}(U;U',V_p(U')) S(U'), \tag{6.31}$$

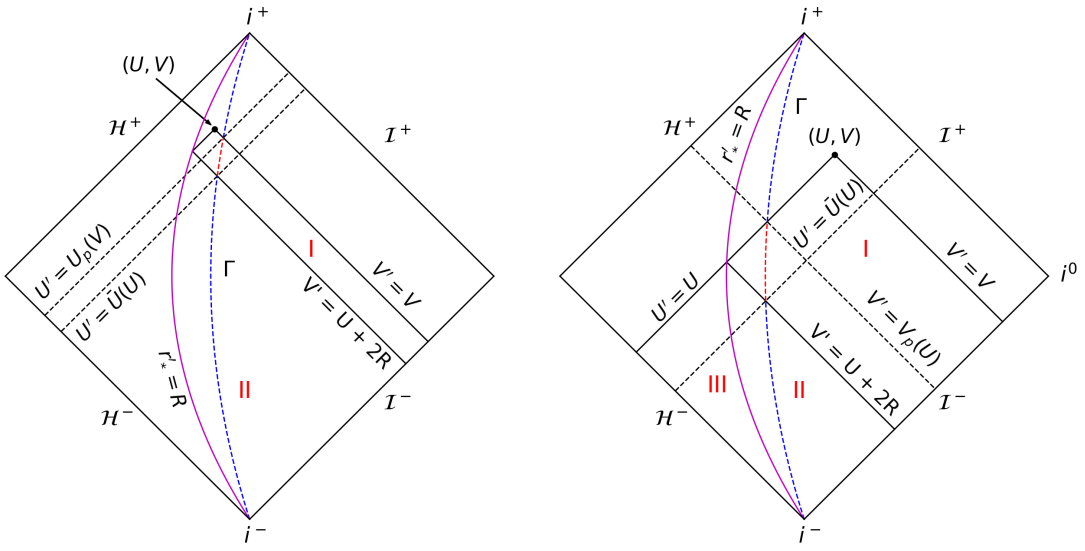

FIGURE 6.3: Two scenarios for an external evaluation point. *Left panel:* the case $2R+U<V<V_p(U)$, in which the support of the scatter geodesic Γ in region I is $\bar{U}(U)\leq U'\leq U_p(V)$. *Right panel:* the case $V>V_p(U)$, in which the support of Γ in region I is $\bar{U}(U)\leq U'\leq U$. Solid lines denote the boundaries of the Green's function regions I-III (region III omitted for clarity in left panel). The section of Γ lying in region I is highlighted in red for both cases. Note the support in region II is the same ($U'\leq\bar{U}$) for both, and there is no support in region III for either.

where we have introduced

$$\tilde{U}(U,V)=\begin{cases} U & \text{for } V\geq V_p(U),\\ U_p(V) & \text{for } V<V_p(U).\end{cases} \tag{6.32}$$

Substituting from Eqs. (6.7) and (6.14), this becomes

$$\psi^{\mathrm{I}}_{0>}(U,V)=\sum_{n=0}^{\ell}\frac{A_n^\ell}{\ell!(2r_*)^{\ell-n}}\int_{\bar{U}(U)}^{\tilde{U}(U,V)}dU'\,\frac{S(U')}{(2r'_{*p})^\ell}\,\partial_U^n\left[(V_p(U')-U)(U-U')\right]^\ell. \tag{6.33}$$

6.3.1.2 Internal evaluation point

For an internal field evaluation point, $V-U<2R$, the situation reverses. The geodesic Γ no longer intersects regions I or II (see Fig. 6.4), so that

$$\psi^{\mathrm{I}}_{0<}\equiv 0\equiv\psi^{\mathrm{II}}_{0<} \tag{6.34}$$

for any internal evaluation point. The sole contribution to $\psi_{0<}$ thus comes from region III, and, using the Green's function from Eq. (6.22), it reads

$$\psi^{\mathrm{III}}_{0<}(U,V)=\int_{-\infty}^{U_p(V)}dU'\int_{\bar{V}(U')}^{V}dV'G^{\mathrm{III}}_{<}(U,V;U',V')S(U')\delta(V'-V_p(U'))$$

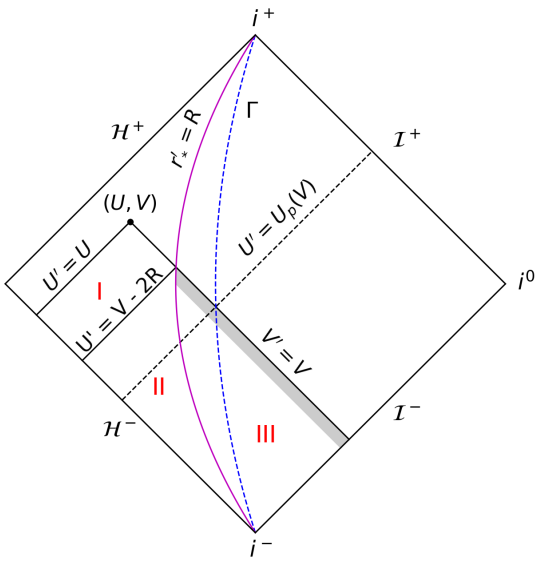

FIGURE 6.4: For an internal evaluation point, with $V-U<2R$, the integration has support only in region III. Recall from Eq. (6.22) that the Green's function in this region is exponentially suppressed to the past of $V'=V$, so that the primary support lies in the shaded band. Solid lines denote the boundaries of the Green's function regions I-III.

$$= \sum_{j=0}^{\ell} \sum_{i=1}^{\ell+1} \beta_{ji} \int_{-\infty}^{U_p(V)} dU' \left(1-\frac{R}{r'_{*p}}\right)^{\ell-j} \left(\frac{R}{r'_{*p}}\right)^{j} E_i(V-V_p(U'))\, S(U'). \tag{6.35}$$

We note that a calculation of the ψ_0 contribution to the self-force requires only the value of ψ_0 in a neighbourhood of the worldline Γ, which lies entirely in the external zone. Consequently, we will not need to make use of Eq. (6.35) in the remainder of this section, or in the next. One will however require the value of ψ_0 at internal evaluation points if one wishes to solve Eq. (6.11) for ψ_1, for example using the strategy we propose in Sec. 6.5.

6.3.2 Late time expansions

We want to evaluate $\psi_0(U,V)$ for $V=V_p(U)$, and then take the limit $U\to\infty$. To that end, in this section we will collect large-U expressions for the source $S(U)$ and other relevant functions evaluated along the orbit.

Our first goal is to obtain large-U expansions for the geodesic trajectory. Using Eq. (2.27),

$$r_p(t) \sim vt \tag{6.36}$$

as $t \to \infty$, so that

$$U_p(t) \sim (1-v)t, \tag{6.37}$$

and hence

$$r_p^*(U) \sim r_p(U) \sim \frac{v}{1-v}U \tag{6.38}$$

at leading order in $1/U$ as $U \to \infty$. Writing $V_p = U_p + 2r_*^p$ and substituting Eq. (6.38), we arrive at

$$V_p(u) \sim \alpha U, \tag{6.39}$$

where we have introduced

$$\alpha := \frac{1+v}{1-v}. \tag{6.40}$$

We will also find it convenient to invert relation (6.39):

$$U_p(V) \sim V/\alpha, \tag{6.41}$$

and to rewrite Eq. (6.38) in terms of α, in which case it becomes

$$r_p^*(U) \sim r_p(U) \sim \left(\frac{\alpha-1}{2}\right) U. \tag{6.42}$$

Furthermore, substituting Eq. (6.42) into Eq. (2.28), we get

$$\varphi_p(U) \sim \varphi_\infty + O\left(1/U\right)) \tag{6.43}$$

as $U \to \infty$.

We also have

$$\bar{V}(U) \sim U \tag{6.44}$$

as $U \to \infty$, a result which follows trivially from Eq. (6.28). The expansion for $\bar{U}$ is also readily obtained by combining Eq. (6.39) with the equation defining $\bar{U}$, Eq. (6.26), yielding

$$\bar{U}(U) \sim U/\alpha \tag{6.45}$$

as $U \to \infty$.

As a final step to obtain the large-U asymptotics of $S(U)$, we need to expand $\dot{U}_p$. Using Eqs. (2.1) and (2.10),

$$\begin{aligned}\dot{U}_p = \dot{t}_p - \dot{r}^*_p &= \left[E \mp \sqrt{E^2 - f(r_p)(1 + L^2/r_p^2)}\right] / f(r_p) \\ &= \left[E \mp \sqrt{E^2 - f(r_p)(1 + v^2E^2b^2/r_p^2)}\right] / f(r_p) \\ &= \frac{E}{f(r_p)}\left[1 \mp \sqrt{v^2\left(1 - \frac{b^2}{r_p^2} + \frac{2Mb^2}{r_p^3}\right) + \frac{2M}{E^2 r_p}}\right]. \end{aligned} \tag{6.46}$$

Here the upper sign is for the outbound leg of the orbit, and the lower sign is for inbound. Taking the $r_p \to \infty$ limit, we obtain

$$\dot{U}_p(U \to \infty) = E(1 - v). \tag{6.47}$$

Substituting Eqs. (6.38), (6.43) and (6.47) into Eq. (6.7) thus gives

$$S_{\ell m}(U \to \infty) \sim \frac{\sigma_{\ell m}}{U}, \tag{6.48}$$

where

$$\sigma_{\ell m} := \frac{2\pi q}{vE} Y^*_{lm}(\pi/2, \varphi_\infty). \tag{6.49}$$

6.3.3 The retarded field Φ_0

We are now in a position to evaluate the fields ψ_0 on the orbit and obtain their LLT behaviour. As any point $(U, V_p(U))$ lies in the external evaluation zone $V_p(U) - U > 2R$, we need to consider the two contributions $\psi^{\rm II}_{0>}$ and $\psi^{\rm I}_{0>}$ defined in Eqs. (6.29) and (6.33) respectively.

6.3.3.1 Contribution from $\psi^{\rm II}_{0>}$

Evaluating (6.29) on Γ gives

$$\begin{aligned}\psi^{\rm II}_{0\Gamma}(U) &:= \psi^{\rm II}_{0>}(U, V_p(U)) \\ &= \sum_{n,j=0}^{\ell} \sum_{i=1}^{\ell+1} \beta_{nji} \left(\frac{R}{r_{*p}}\right)^{\ell-n} \int_{-\infty}^{\bar{U}(U)} dU' \left(1 - \frac{R}{r'_{*p}}\right)^{\ell-j} \left(\frac{R}{r'_{*p}}\right)^{j} E_i(U - V_p(U') + 2R)\, S(U'),\end{aligned} \tag{6.50}$$

where $r_{*p} = r_{*p}(U) = (V_p(U) - U)/2$ and $r'_{*p} = r_{*p}(U')$. We will now show this contribution decays to zero as $U \to \infty$.

To do this, we make use of a bounding argument. Since $r_{*p}(U) > R$ for all U, we have the upper bounds

$$0 < \left(\frac{R}{r_{*p}}\right)^{\ell-n} < 1, \qquad 0 < \left(\frac{R}{r'_{*p}}\right)^{j} < 1, \qquad 0 < \left(1 - \frac{R}{r'_{*p}}\right)^{\ell-j} < 1 \tag{6.51}$$

for all ℓ, n, j and U, and hence we may bound

$$|\psi^{\rm II}_{0\Gamma}(U)| < \sum_{n,j=0}^{\ell} \sum_{i=1}^{\ell+1} |\beta_{nji}| \int_{-\infty}^{\bar{U}(U)} dU' \Big| E_i(U - V_p(U') + 2R)\, S(U') \Big| \,. \tag{6.52}$$

Recall now that $V_p(U')$ increases monotonically with U' [approximately as $\sim \alpha U'$ at large U'], so that when U' is large, the support of the integral in Eq. (6.52) decreases exponentially in U' away from its upper boundary. Also, recall from Eq. (6.48) that near the upper boundary the source function is approximately $S(U') \sim \sigma_{lm}/U'$ when U is large. The combination of these two facts ensures that the integral vanishes in the limit $U \to \infty$. To prove this, we split each of the integrals on the right hand side of Eq. (6.52) into two pieces, in the form

$$\int_{-\infty}^{\bar{U}} dU' = \int_{-\infty}^{\bar{U}/2} dU' + \int_{\bar{U}/2}^{\bar{U}} dU', \tag{6.53}$$

and consider the limit $U \to \infty$ (in which $\bar{U} \to \infty$ also) of each part separately.

To tackle the first integral in (6.53), we introduce the function

$$K(U) := \begin{cases} 1 & |U| \le U_0, \\ U_0/|U| & \text{else}, \end{cases} \tag{6.54}$$

where $U_0 > 0$ is some arbitrary cut-off, and then consider

$$E_i(U - V_p(U') + 2R)/K(aU') \tag{6.55}$$

for some constant $a > 0$. The derivative of this function is

$$\begin{aligned} &\frac{d}{dU'}\Big(E_i(U - V_p(U') + 2R)/K(aU')\Big) \\ &\qquad = \left[\kappa_i \frac{dV_p}{dU'} - a\frac{d}{d\tilde{U}} \log(K(\tilde{U}))\Big|_{\tilde{U}=aU'}\right] \frac{E_i(U - V_p(U') + 2R)}{K(aU')}. \end{aligned} \tag{6.56}$$

Note that there exists a constant $\lambda > 0$ such that $dV_p/dU > \lambda$ for all U.[3] Furthermore,

$$\frac{d}{dU} \log K(U) := \begin{cases} 0 & |U| \le U_0, \\ -1/U & \text{else}, \end{cases} \qquad \le \frac{1}{U_0}, \tag{6.57}$$

[3]This can be proved simply by noting $dV_p/dU = (1+\rho)/(1-\rho)$, where $\rho := \dot{r}_p/E$ is bounded strictly away from unity, i.e. $|\rho| \le \rho_{\max}$ for some $\rho_{\max} < 1$.

hence

$$\frac{d}{dU'}\Big(E_i(U - V_p(U') + 2R)/K(aU')\Big) \geq (\kappa_i\lambda - a/U_0)\frac{E_i(U - V_p(U') + 2R)}{K(aU')}, \quad (6.58)$$

which we can make > 0 by choosing some $0 < a < \kappa_i\lambda U_0$ (noting that κ_i, λ and U_0 are all strictly positive themselves). With this choice, the function (6.55) is monotonically increasing in U', so we may bound

$$\int_{-\infty}^{\bar{U}/2} dU' \Big|E_i(U - V_p(U') + 2R)\, S(U')\Big| < \frac{E_i(U - V_p(\bar{U}/2) + 2R)}{K(a\bar{U})} \int_{-\infty}^{\bar{U}(U)} dU' \big|S(U')K(aU')\big| \quad (6.59)$$

$$\leq \frac{E_i(U - V_p(\bar{U}/2) + 2R)}{K(a\bar{U})} \int_{-\infty}^{+\infty} dU' \big|S(U')K(aU')\big|. \quad (6.60)$$

Note that the combination $S(U')K(aU') \sim 1/U'^2$ as both $U' \to \pm\infty$, so that the integral in the second line of Eq. (6.60) converges. Recalling Eqs. (6.39) and (6.45),

$$U - V_p(\bar{U}/2) + 2R \sim U/2 + 2R \to \infty \quad (6.61)$$

as $U \to \infty$, and hence

$$\frac{E_i(U - V_p(\bar{U}/2) + 2R)}{K(a\bar{U})} \sim U \exp\left[-\kappa_i(U/2 + 2R)\right] \to 0. \quad (6.62)$$

It thus follows that

$$\int_{-\infty}^{\bar{U}/2} dU' \Big|E_i(U - V_p(U') + 2R)\, S(U')\Big| \longrightarrow 0 \quad (6.63)$$

as $U \to \infty$.

We bound the second integral in (6.53) in the following manner. Since $S(U') \sim \sigma_{\ell m}/U'$ as $U \to \infty$, there exist suitable positive constants U_1 and C such that $|S_{\ell m}(U')| < C/\sqrt{U'}$ for all $U > U_1$. From Eq. (6.45), we have $\bar{U} \sim U/\alpha \to \infty$ as $U \to \infty$, so that $\bar{U}/2 > U_1$ whenever U is sufficiently large. In this case, we may bound

$$\begin{aligned}\int_{\bar{U}/2}^{\bar{U}} dU' \Big|E_i(U - V_p(U') + 2R)\, S(U')\Big| &< C\int_{U/(2\alpha)}^{U/\alpha} dU' \frac{E_i(U - \alpha U')}{\sqrt{U'}} \\ &< \frac{\sqrt{2\alpha}\,C}{\sqrt{U}} \int_{U/(2\alpha)}^{U/\alpha} du' E_i(U - \alpha U') \\ &= \frac{\sqrt{2}CR}{\kappa_i\sqrt{\alpha U}}\left[1 - e^{-\kappa_i U/(2R)}\right] \\ &\to 0 \quad \text{as } U \to \infty. \end{aligned} \quad (6.64)$$

In summary, we have established that

$$\psi^{\rm II}_{0\Gamma}(U\to\infty)=0. \tag{6.65}$$

6.3.3.2 Contribution from $\psi^{\rm I}_{0>}$

Evaluating (6.33) on Γ gives

$$\psi^{\rm I}_{0\Gamma}(U)=\sum_{n=0}^{\ell}\frac{A_n^\ell}{\ell!(2r_{*p})^{\ell-n}}\int_{\bar U(U)}^{U}dU'\frac{S(U')}{(2r'_{*p})^\ell}\,\partial_U^n\big[(V_p(U')-U)(U-U')\big]^\ell. \tag{6.66}$$

Using Eqs. (6.42) and (6.48), this becomes

$$\psi^{\rm I}_{0\Gamma}(U\to\infty)=\ \frac{\sigma_{\ell m}}{\ell!}\sum_{n=0}^{\ell}\frac{A_n^\ell}{(\alpha-1)^{2\ell-n}U^{\ell-n}}\int_{U/\alpha}^{U}dU'\,\frac{\partial_U^n\big[(\alpha U'-U)(U-U')\big]^\ell}{(U')^{\ell+1}} \tag{6.67}$$

at leading order in $1/U$. To simplify the integrand, we make a change of integration variable $U'\to x(U')$, where $x:=U/U'$. Under this transformation we have $dU'=-(U/x^2)dx$ and $\partial_U^n=(x/U)^n\partial_x^n$, so that the integral becomes

$$\psi^{\rm I}_{0\Gamma}(U\to\infty)=\frac{\sigma_{\ell m}}{\ell!}\sum_{n=0}^{\ell}\frac{A_n^\ell}{(\alpha-1)^{2\ell-n}}\int_1^\alpha dx\,\frac{\partial_x^n\big[(\alpha-x)^\ell(x-1)^\ell\big]}{x^{\ell-n+1}}. \tag{6.68}$$

With n sucessive applications of integration by parts, this becomes

$$\psi^{\rm I}_{0\Gamma}(U\to\infty)=\sigma_{\ell m}\sum_{n=0}^{\ell}\frac{A_n^\ell}{(\alpha-1)^{2\ell-n}(\ell-n)!}\int_1^\alpha dx\,\frac{(\alpha-x)^\ell(x-1)^\ell}{x^{\ell+1}}. \tag{6.69}$$

Substituting A_n^ℓ from Eq. (6.16), we may write this as

$$\psi^{\rm I}_{0\Gamma}(U\to\infty)=\frac{\sigma_{\ell m}}{(\alpha-1)^{2\ell}}\,H_\ell(\alpha)\,I_\ell(\alpha), \tag{6.70}$$

where

$$H_\ell(\alpha):=\sum_{n=0}^{\ell}\frac{(2\ell-n)!}{n![(\ell-n)!]^2}(\alpha-1)^n,\qquad I_\ell(\alpha):=\int_1^\alpha\frac{(\alpha-x)^\ell(x-1)^\ell}{x^{\ell+1}}\,dx\,. \tag{6.71}$$

Both $H_\ell(\alpha)$ and $I_\ell(\alpha)$ can be expressed in terms of simple hypergeometric functions, which in turn are simply related to Legendre functions P_ℓ and Q_ℓ in the variable $(\alpha+1)/(\alpha-1)=1/v$. Specifically,

$$H_\ell(\alpha)=F_{2\rm F1}(-\ell,-\ell,1,\alpha)=(\alpha-1)^\ell\,P_\ell(1/v), \tag{6.72}$$

and

$$I_\ell(\alpha) = \frac{(\ell!)^2}{(2\ell+1)!}(\alpha-1)^{2\ell+1}\, F_{2\mathrm{F}1}(\ell+1,\ell+1,2\ell+2,1-\alpha)$$
$$= 2(\alpha-1)^\ell\, Q_\ell(1/v). \tag{6.73}$$

Thus, Eq. (6.70) reduces to

$$\psi^{\mathrm{I}}_{0\Gamma}(U\to\infty) = 2\sigma_{\ell m} P_\ell(1/v) Q_\ell(1/v). \tag{6.74}$$

6.3.3.3 The retarded field Φ_0^ℓ

Our final step in this section is to obtain the LLT behaviour of the ℓ-mode contributions to the LH retarded scalar field evaluated on the worldline,

$$\Phi^\ell_{0\Gamma}(t) := \frac{1}{r}\sum_{m=-\ell}^{\ell} \psi^{0\Gamma}_{\ell m}(t) Y_{\ell m}(\theta_p(t),\varphi_p(t)). \tag{6.75}$$

Substituting the LLT result from Eq. (6.74), making use of the definition of $\sigma_{\ell m}$ in Eq. (6.49), and expanding $Y_{\ell m}(\theta_p,\varphi_p)$ at leading order as $t\to\infty$, we obtain

$$\lim_{t\to\infty}\left[r_p(t)\Phi^\ell_{0\Gamma}(t)\right] = \frac{4\pi q}{vE} P_\ell\left(\frac{1}{v}\right) Q_\ell\left(\frac{1}{v}\right) \sum_{m=-\ell}^{\ell} Y_{\ell m}\left(\frac{\pi}{2},\varphi_\infty\right) Y_{\ell m}\left(\frac{\pi}{2},\varphi_\infty\right). \tag{6.76}$$

Performing the sum over m using the addition theorem for spherical harmonics,

$$\sum_{m=-\ell}^{\ell} Y^*_{\ell m}(\theta,\varphi)\, Y_{\ell m}(\theta,\varphi) = \frac{2l+1}{4\pi}, \tag{6.77}$$

we finally obtain

$$\lim_{t\to\infty}\left[r_p(t)\Phi^\ell_{0\Gamma}(t)\right] = (2\ell+1)\frac{q}{vE}\, P_\ell(y)\, Q_\ell(y), \tag{6.78}$$

where

$$y := \frac{1}{v} (> 1). \tag{6.79}$$

6.3.4 The Detweiler-Whiting regular field Φ_0^R

In this section we will consider the Detweiler-Whiting regular piece Φ_0^R of the LH scalar field Φ_0, evaluated on the worldline Γ at late times. We will calculate Φ_0^R using a mode-sum regularisation procedure analogous to that introduced for the self-force in Sec. 2.2.2.

In the present case, the regular field on Γ is obtained via the mode-sum formula

$$\Phi^R_{0\Gamma}(t) = \sum_{\ell=0}^{\infty} \left(\Phi^\ell_{0\Gamma}(t) - B(t) \right), \tag{6.80}$$

where the regularisation parameter $B(t)$ is given by [63, 169]

$$B(t) = \frac{2q}{\pi\sqrt{L^2 + r_p^2}} \, \mathsf{El}_1 \left(\frac{\pi}{2}, \frac{L^2}{L^2 + r_p^2} \right), \tag{6.81}$$

and El_1 is defined in Eq. (2.24). As $r_p \to \infty$, B has leading-order behaviour

$$B(t) \sim \frac{q}{r_p}. \tag{6.82}$$

Substituting Eqs. (6.78) and (6.82) into Eq. (6.80), we arrive at

$$\lim_{t\to\infty} \left[r_p(t) \Phi^R_{0\Gamma}(t) \right] = \frac{q}{vE} \sum_{\ell=0}^{\infty} \left[(2\ell+1) P_\ell(y) Q_\ell(y) - \frac{1}{\sqrt{y^2-1}} \right], \tag{6.83}$$

where, recall, $y = 1/v$ and we used $vE = (y^2-1)^{-1/2}$.

6.3.4.1 Explicit summation over ℓ

We denote the sum in Eq. (6.83) by $\Lambda(y)$:

$$\Lambda(y) := \sum_{\ell=0}^{\infty} \left[(2\ell+1) P_\ell(y) Q_\ell(y) - \frac{1}{\sqrt{y^2-1}} \right], \tag{6.84}$$

and perform the sum over ℓ analytically. Intuition strongly suggests that $\Lambda(y) = 0$. To see why, note that the mass M of the central black hole did not enter our previous calculation – the Green's function does not depend on M, and neither did the source at LLT order (recall Eq. (6.48)). The LLT source, in particular, is equivalent to that of a particle moving along a straight line described exactly by Eq. (6.36). We are therefore effectively calculating the regular field sourced by a particle moving in a straight line in flat spacetime, which is known to vanish (along with the self-force).

To prove $\Lambda = 0$, we write it as

$$\Lambda(y) = \lim_{n\to\infty} \lim_{x\to y} \sum_{l=0}^{n} \left[(2l+1) P_l(x) Q_l(y) - \frac{1}{\sqrt{y^2-1}} \right] \tag{6.85}$$

and make use of Christoffel's partial sum formula (see e.g. Eq. 4.18.6 in Ref. [190]),

$$\sum_{\ell=0}^{n} (2l+1) P_\ell(x) Q_\ell(y) = \frac{(n+1)\left[P_{n+1}(x) Q_n(y) - P_n(x) Q_{n+1}(y) \right] - 1}{x - y}, \tag{6.86}$$

to give

$$\Lambda(y) = \lim_{n\to\infty}\lim_{x\to y}\left[\frac{(n+1)\left[P_{n+1}(x)Q_n(y) - P_n(x)Q_{n+1}(y)\right]-1}{x-y} - \frac{n+1}{\sqrt{y^2-1}}\right]. \quad (6.87)$$

Replacing $P_{n+1}(x)$ and $Q_{n+1}(y)$ using the identity

$$(n+1)P_{n+1}(x) = (x^2-1)P_n'(x) + (n+1)xP_n(x), \quad (6.88)$$

which also applies for $Q_n(x)$, we get

$$\Lambda(y) = \lim_{n\to\infty}\lim_{x\to y}\left[\frac{(x^2-1)P_n'(x)Q_n(y) - (y^2-1)P_n(x)Q_n'(y) - 1}{x-y} + (n+1)P_n(x)Q_n(y) - \frac{n+1}{\sqrt{y^2-1}}\right]. \quad (6.89)$$

Note that the first fraction in the above gives rise to an indeterminate limit of the form $0/0$, since

$$\begin{aligned}\lim_{x\to y}\Big[(x^2-1)P_n'(x)Q_n(y) - (y^2-1)P_n(x)Q_n'(y) - 1\Big] &= (y^2-1)\Big[P_n'(y)Q_n(y) - P_n(y)Q_n'(y)\Big] - 1\\ &= (y^2-1)W(y) - 1\\ &= 0,\end{aligned} \quad (6.90)$$

where $W(y) = (y^2-1)^{-1}$ is the Wronskian of P_n and Q_n. Applying l'Hopital's rule and taking $x \to y$, we obtain

$$\Lambda(y) = \lim_{n\to\infty}\Big[\big[(y^2-1)P_n''(y) + 2yP_n'(y)\big]Q_n(y) - (y^2-1)Q_n'(y)P_n'(y) + (n+1)P_n(y)Q_n(y) - \frac{n+1}{\sqrt{y^2-1}}\Big] \quad (6.91)$$

Eliminating the second derivative using Legendre's equation,

$$(1-y^2)P_n''(y) - 2yP_n'(y) + n(n+1)P_n(y) = 0, \quad (6.92)$$

and simplifying, this becomes

$$\Lambda(y) = \lim_{n\to\infty}\Big[(n+1)^2P_n(y)Q_n(y) - (y^2-1)Q_n'(y)P_n'(y) - \frac{n+1}{\sqrt{y^2-1}}\Big]. \quad (6.93)$$

We have thus reduced the problem to an evaluation of the single limit in Eq. (6.93). We note the asymptotic leading-order large-n scalings $P_n, Q_n \sim n^{-1/2}$ and $P_n', Q_n' \sim n^{+1/2}$, so a priori each of the 3 terms in Eq. (6.93) is of $O(n)$. As a result, we need to know the

asymptotic forms of P_n and Q_n to $O(n^{-3/2})$, i.e., to first subleading order. For $y > 1$, these are

$$P_n(y) = \Big(\frac{x}{\sinh x}\Big)^{1/2}\left[I_0\Big((n+\frac{1}{2})x\Big) - \frac{1}{4(2n+1)}\left(\frac{1}{x}-\coth x\right)I_1\Big((n+\frac{1}{2})x\Big) + O(n^{-5/2})\right],$$
$$Q_n(y) = \Big(\frac{x}{\sinh x}\Big)^{1/2}\left[K_0\Big((n+\frac{1}{2})x\Big) + \frac{1}{4(2n+1)}\left(\frac{1}{x}-\coth x\right)K_1\Big((n+\frac{1}{2})x\Big) + O(n^{-5/2})\right], \tag{6.94}$$

where $x = \cosh^{-1} y$, and I_k and K_k are the modified Bessel functions of the first and second kind, themselves admitting the expansions

$$\begin{aligned} I_k(z) &= \frac{e^z}{\sqrt{2\pi z}}\left(1 - \frac{4k^2-1}{8z} + O(z^{-2})\right), \\ K_k(z) &= \frac{\pi e^{-z}}{\sqrt{2\pi z}}\left(1 + \frac{4k^2-1}{8z} + O(z^{-2})\right). \end{aligned} \tag{6.95}$$

The leading-order terms in (6.94) and high-order expansions for the Bessel functions are widely available in standard texts [see e.g. Sections 10.40(i) and 14.15(iii) of Ref. [190]]. For the subleading terms in Eq. (6.94), we used expressions from Ref. [191], given only for $0 < y < 1$, and analytically continued them to $y > 1$, carefully checking the resulting expressions numerically in Mathematica.

Using the above asymptotic expressions, we obtain

$$\begin{aligned} P_n(y)Q_n(y) &= \frac{2n-1}{4n^2\sqrt{y^2-1}} + O(n^{-3}), \\ P'_n(y)Q'_n(y) &= -\frac{2n+1}{4(y^2-1)^{3/2}} + O(n^{-1}), \end{aligned} \tag{6.96}$$

which, substituted in Eq. (6.93), gives

$$\Lambda = \frac{1}{\sqrt{y^2-1}}\lim_{n\to\infty}\left[\frac{(n+1)^2(2n-1)}{4n^2} + \frac{2n+1}{4} - (n+1) + O(n^{-1})\right] = 0. \tag{6.97}$$

In conclusion, we have demonstrated that

$$\lim_{t\to\infty}\Big[r_p(t)\Phi_0^{\rm R}(r_p(t))\Big] = 0\,. \tag{6.98}$$

6.4 Evaluating the self-force F^0_α near i^+

In this section we will calculate the contribution that the LLT piece of ψ_0 makes to the self-force, confirming that this too vanishes. We begin by considering the φ-component of the force, before moving on to consider the U and V components, from which we finally

construct the t and r components of the force. We conclude the section by comparing our analytical results to numerical results for the ℓ-modes of the full force.

The self-force will be calculated using mode-sum regularisation as usual, using only the one-sided derivative from $r > r_p$ for simplicity. Concretely, this means we take $\tilde{U} = U$ in Eq. (6.33).

6.4.1 The azimuthal component F^0_φ

Taking the φ derivative of Eq. (6.23) and evaluating on the geodesic Γ,

$$\begin{aligned} r_p(t)\left[\partial_\varphi \Phi_0^\ell\right]_\Gamma(t) &= \sum_{\ell=0}^{\infty}\sum_{m=-\ell}^{\ell} \psi_{0\Gamma}(t)\partial_\varphi Y_{\ell m}\left(\frac{\pi}{2}, \varphi_p(t)\right) \\ &= i\sum_{\ell=0}^{\infty}\sum_{m=-\ell}^{\ell} m\, \psi_{0\Gamma}(t) Y_{\ell m}\left(\frac{\pi}{2}, \varphi_p(t)\right). \end{aligned} \tag{6.99}$$

We consider the contribution from region II first. At late times along Γ, we have

$$\lim_{t\to\infty} r_p\left[\partial_\varphi \Phi_0^{\mathrm{II},\,\ell}\right]_\Gamma = i\sum_{\ell=0}^{\infty}\sum_{m=-\ell}^{\ell} m\, \psi^{\mathrm{II}}_{0\Gamma}(U\to\infty) Y_{\ell m}\left(\frac{\pi}{2}, \varphi_\infty\right) = 0, \tag{6.100}$$

since, by virtue of Eq. (6.65), each of the ℓm modes here vanishes individually. For the contribution from region I, we substitute Eq. (6.74) into Eq. (6.99), giving

$$\lim_{t\to\infty} r_p\left[\partial_\varphi \Phi_0^{\mathrm{II},\,\ell}\right]_\Gamma = \frac{4\pi q i}{vE}\sum_{\ell=0}^{\infty}\sum_{m=-\ell}^{\ell} m\, P_\ell(1/v) Q_\ell(1/v) Y^*_{\ell m}\left(\frac{\pi}{2}, \varphi_\infty\right) Y_{\ell m}\left(\frac{\pi}{2}, \varphi_\infty\right). \tag{6.101}$$

The individual ℓm terms on the right hand side are non-zero, so that ψ_0 would appear to contribute to the self-force initially at $1/r_p$ order at late times. But the sum over m here is, in fact, exactly zero. This can be seen by noting

$$\sum_{m=-\ell}^{\ell} m\, Y^*_{\ell m}\left(\frac{\pi}{2}, \varphi_\infty\right) Y_{\ell m}\left(\frac{\pi}{2}, \varphi_\infty\right) = \sum_{m=-\ell}^{\ell} m \left|Y_{\ell m}\left(\frac{\pi}{2}, \varphi_\infty\right)\right|^2 = 0, \tag{6.102}$$

because $|Y_{\ell,m}|^2 = |Y_{\ell,-m}|^2$ and hence the terms are antisymmetric in m. Thus, we have established that

$$\lim_{t\to\infty} r_p(t)\left[\partial_\varphi \Phi_0^\ell\right]_\Gamma = 0. \tag{6.103}$$

Finally, we substitute Eq. (6.103) into the mode-sum formula (2.49), confirming that there is no $1/r_p$ contribution to the self-force. For the φ component of the force, the regularisation parameters (recall Eq. (2.53)) decay as $1/r_p^3$ at large r_p, so that Eq. (2.49)

reads

$$F^0_\varphi = \frac{q^2}{r_p}\sum_{\ell=0} r_p \partial^+_\varphi(\Phi^\ell_0/q)\Big|_\Gamma, \tag{6.104}$$

at $O(1/r_p)$, where ∂^+_α indicates the one-sided derivative from $V > V_p(U)$. It then follows from Eq. (6.103) that

$$\lim_{t\to\infty} r_p(t) F^0_\varphi(t) = 0, \tag{6.105}$$

consistent with the empirical $F^{\rm self}_\varphi \sim 1/r_p^2$ decay found in numerical tests.

6.4.2 The components F^0_U and F^0_V: contribution from region II

It is easier to first take the U and V derivatives of the field, and then obtain the t and r derivatives from these using the chain rule. To take U and V derivatives of $\psi^{\rm II}_{0>}$ we need to go back to Eq. (6.29), whose restriction to $V \geq V_p(U)$ is

$$\psi^{\rm II}_{0>}(U,V) = \sum_{n,j=0}^{\ell}\sum_{i=1}^{\ell+1}\beta_{nji}\left(\frac{R}{r_*}\right)^{\ell-n}\int_{-\infty}^{\bar U(U)} dU'\left(1-\frac{R}{r'_{*p}}\right)^{\ell-j}\left(\frac{R}{r'_{*p}}\right)^{j} E_i(U-V_p(U')+2R)\,S(U'). \tag{6.106}$$

This depends on V only through r_*, so taking the V derivative is simple:

$$\begin{aligned}&\partial_V\left[r_{*p}(U)\psi^{\rm II}_{0\Gamma}(U)\right]\\ &\quad= \sum_{n,j=0}^{\ell}\sum_{i=1}^{\ell+1}\tilde\beta_{nji}\left(\frac{R}{r_{*p}}\right)^{\ell-n}\int_{-\infty}^{\bar U(U)} dU'\left(1-\frac{R}{r'_{*p}}\right)^{\ell-j}\left(\frac{R}{r'_{*p}}\right)^{j} E_i(U-V_p(U')+2R)\,S(U'),\end{aligned} \tag{6.107}$$

where $\tilde\beta_{nji}$ are some other coefficients. It is easy to see that the bounding argument presented between Eqs. (6.51) and (6.64) holds unchanged, leading to

$$\partial_V\left(r_p\psi^{\rm II}_{0\Gamma}\right)_{U\to\infty} = 0. \tag{6.108}$$

The expression for the U derivative is a bit more involved:

$$\begin{aligned}r_{*p}\partial_U\psi^{\rm II}_{0\Gamma}(U) = &\sum_{n,j,i}\beta_{nji}\frac{d\bar U}{dU}\left(\frac{R}{r_{*p}}\right)^{\ell-n}\left(1-\frac{R}{\bar r_*}\right)^{\ell-j}\left(\frac{R}{\bar r_*}\right)^{j} r_{*p}(U)\,S(\bar U)\\ &-\sum_{n,j,i}\left(\frac{R}{r_p}\right)^{\ell-n}\left(\tilde\beta_{nji}R+\beta_{nji}\kappa_i\frac{r_{*p}}{R}\right)\end{aligned}$$

$$\times \int_{-\infty}^{\bar{U}(U)} dU' \left(1-\frac{R}{r'_{*p}}\right)^{\ell-j} \left(\frac{R}{r'_{*p}}\right)^{j} E_i(U-V_p(U')+2R)\, S(U') \tag{6.109}$$

where $\bar{r}_* = r_{*p}(\bar{U}) = (U+2R-\bar{U}(U))/2$. The term proportional to $\tilde{\beta}_{nji}$ contains the same integral as in Eq. (6.50), and can thus be bounded and shown to vanish in the limit $U\to\infty$ in the same way. Using the asymptotic relations

$$\bar{U}\sim U/\alpha, \qquad V_p(U')\sim \alpha U', \qquad \bar{r}_*\sim\left(\frac{\alpha-1}{2\alpha}\right)U, \qquad r_{*p}\sim\left(\frac{\alpha-1}{2}\right)U \tag{6.110}$$

the rest of the expression becomes, at large U,

$$\begin{aligned} r_{*p}\partial_U\psi^{\rm II}_{0\Gamma} \;\sim\; & -\frac{\alpha-1}{2}\sum_{j,i}\beta_{\ell ji}\kappa_i\frac{U}{R}\int_{-\infty}^{U/\alpha} dU'\left(1-\frac{R}{r'_{*p}}\right)^{\ell-j}\left(\frac{R}{r'_{*p}}\right)^{j} E_i(U-\alpha U')\, S(U') \\ & +\frac{\alpha-1}{2}\sigma_{\ell m}\sum_i \beta_{\ell 0 i}. \end{aligned} \tag{6.111}$$

As observed previously, at large U the support of the integral is concentrated near its upper end, so it suffices for us to truncate the integration from below at, say, $U' = U/(2\alpha)$, and then consider the leading term of the integrand at large U':

$$\begin{aligned} r_{*p}\partial_U\psi^{\rm II}_{0\Gamma} &\sim \frac{\alpha-1}{2}\sigma_{\ell m}\sum_i\beta_{\ell 0 i}\left[1-\kappa_i\frac{U}{R}\int_{U/(2\alpha)}^{U/\alpha}\frac{dU'}{U'}e^{-\kappa_i(U-\alpha U')/R}\right] \\ &\longrightarrow 0 \end{aligned} \tag{6.112}$$

as $U\to\infty$. It follows also that $\partial_U\psi^{\rm II}_{0\Gamma}\to 0$, and that

$$\partial_U\left(r_p\psi^{\rm II}_{0\Gamma}\right)\Big|_{U\to\infty} = 0. \tag{6.113}$$

Since the r and t derivatives are linear combinations of U and V derivatives, we find, in conclusion,

$$\partial_t(r_p\psi^{\rm II}_{0\Gamma})\big|_{U\to\infty}=0, \qquad \partial_r(r_p\psi^{\rm II}_{0\Gamma})\Big|_{U\to\infty}=0, \tag{6.114}$$

We can therefore focus on the contribution from region I.

6.4.3 The components F^0_U and F^0_V: contribution from region I

6.4.3.1 V derivative

To take the derivatives of $\psi^{\rm I}_{0>}$ we return to Eq. (6.33),

$$\psi^{\rm I}_{0>}(U,V) = \sum_{n=0}^{\ell}\frac{A^\ell_n}{\ell!(2r_*)^{\ell-n}}\int_{\bar{U}(U)}^{U} dU'\frac{S(U')}{(2r'_{*p})^\ell}\,\partial_U^n\left[(V_p(U')-U)(U-U')\right]^\ell. \tag{6.115}$$

The right hand side depends on V only through r_*, so taking ∂_V is particularly simple:

$$r_{*p}\left[\partial_V \psi^{\rm I}_{0>}\right]_\Gamma = -\frac{1}{2}\sum_{n=0}^{\ell}\frac{(\ell-n)A^\ell_n}{\ell!(2r_{*p})^{\ell-n}}\int_{\bar U(U)}^{U} dU'\,\frac{S(U')}{(2r'_{*p})^\ell}\,\partial_U^n\left[(V_p(U')-U)(U-U')\right]^\ell. \tag{6.116}$$

The calculation then proceeds along the lines of Eqs. (6.66)–(6.70), leading to

$$\lim_{U\to\infty} r_{*p}\left[\partial_V \psi^{\rm I}_{0>}\right]_\Gamma = -\frac{1}{2}\frac{\sigma_{\ell m}}{(\alpha-1)^{2\ell}}\,\tilde H_\ell(\alpha)\,I_\ell(\alpha), \tag{6.117}$$

where

$$\tilde H_\ell(\alpha) := \sum_{n=0}^{\ell}\frac{(2\ell-n)!(\ell-n)}{n![(\ell-n)!]^2}(\alpha-1)^n. \tag{6.118}$$

We can express this as a derivative of $H_\ell(\alpha)$:

$$\begin{aligned}\tilde H_\ell(\alpha) &= -(\alpha-1)^{\ell+1}\frac{d}{d\alpha}\left[(\alpha-1)^{-\ell}H_\ell(\alpha)\right]\\ &= -(\alpha-1)^{\ell+1}\frac{d}{d\alpha}\left[P_\ell(1/v)\right] = (\alpha-1)^\ell(y-1)P'_\ell(y),\end{aligned} \tag{6.119}$$

where, recall, $y=1/v$, and a prime now denotes d/dy. The rest of the calculation is similar to the one leading to Eq. (6.78), instead of which we now obtain

$$\begin{aligned}\lim_{U\to\infty} r_p\Big[\partial_V\left(r\Phi^\ell_0\right)\Big]_\Gamma &= -\frac{q}{2vE}(2\ell+1)(y-1)P'_\ell(y)Q_\ell(y)\\ &= -\frac{q(1-v)}{2v^2E}(2\ell+1)P'_\ell(y)Q_\ell(y),\end{aligned} \tag{6.120}$$

The mode-sum formula (2.49) requires as input the derivatives of the scalar field Φ_0, given by

$$\begin{aligned}\lim_{U\to\infty} r_p^2(t)\Big[\partial_V\Phi^\ell_0\Big]_\Gamma &= \lim_{U\to\infty}\Big\{r_p(t)\Big[\partial_V\left(r\Phi^\ell_0\right)\Big]_\Gamma - \frac{1}{2}r_p(t)\,\Phi^\ell_{0\Gamma}\Big\}\\ &= -\frac{q(1-v)}{2v^2E}(2\ell+1)P'_\ell(y)Q_\ell(y) - \frac{q}{2vE}(2\ell+1)P_\ell(y)Q_\ell(y),\end{aligned} \tag{6.121}$$

where we have made use of Eq. (6.78) in the second line.

6.4.3.2 U derivative

Taking the U derivative of Eq. (6.115) and evaluating on Γ we get

$$\begin{aligned}&r_{*p}\left[\partial_U\psi^{\rm I}_{0>}\right]_\Gamma\\ &\quad= -r_{*p}\left[\partial_V\psi^{\rm I}_{0>}\right]_\Gamma\\ &\qquad+\frac{1}{2}\sum_{n=0}^{\ell}\frac{A^\ell_n}{\ell!(2r_{*p})^{\ell-n-1}}\int_{\bar U(U)}^{U}dU'\,\frac{S(U')}{(2r'_{*p})^\ell}\,\partial_U^{n+1}\left[(V_p(U')-U)(U-U')\right]^\ell\end{aligned}$$

$$+ r_{*p}\left[A^\ell_\ell S(U) - \sum_{n=0}^{\ell} \frac{A^\ell_n}{\ell!(2r_*)^{\ell-n}} \frac{d\bar{U}}{dU} \frac{S(\bar{U})}{(V_p(\bar{U})-\bar{U})^\ell}\, \partial_U^n \left[(V_p(\bar{U})-U)(U-\bar{U})\right]^\ell\right]. \tag{6.122}$$

The second line here comes from differentiating the r_{*p}-dependent factor outside the integral. The third line comes from differentiating the U-dependent expression in the integrand, and the fourth line comes from differentiating the integration boundaries. In the second surface term on the fourth line, we note that, at large U,

$$V_p(\bar{U}) \sim \alpha\bar{U} \sim \alpha(U/\alpha) = U, \tag{6.123}$$

so all the terms in the sum over n vanish except the one with $n = \ell$, which gives $-A^\ell_\ell S(U)$, precisely cancelling the first boundary term.

The expression in the third line of Eq. (6.122) becomes, at leading order in $1/U$,

$$\frac{1}{2}\frac{\sigma_{\ell m}}{\ell!} \sum_{n=0}^{\ell} \frac{A^\ell_n}{(\alpha-1)^{2\ell-n-1}U^{\ell-n-1}} \int_{U/\alpha}^{U} dU' \, \frac{\partial_U^{n+1}\left[(\alpha U'-U)(U-U')\right]^\ell}{(U')^{\ell+1}}, \tag{6.124}$$

or, after transforming $U' \to x$ as in Eq. (6.68) and then performing $n+1$ successive integrations by parts,

$$\begin{aligned}
&\frac{1}{2}\frac{\sigma_{lm}}{l!} \sum_{n=0}^{l} \frac{A^l_n}{(\alpha-1)^{2l-n-1}} \int_1^\alpha dx \, \frac{\partial_x^{n+1}\left[(\alpha-x)^\ell (x-1)^\ell\right]}{x^{\ell-n}} \\
&= \frac{1}{2}\sigma_{\ell m} \sum_{n=0}^{\ell-1} \frac{A^\ell_n(\ell-n)}{(\alpha-1)^{2\ell-n-1}(\ell-n)!} \int_1^\alpha dx \, \frac{\partial_x\left[(\alpha-x)^\ell (x-1)^\ell\right]}{x^{\ell+1}} \\
&= \frac{1}{2}\frac{\sigma_{\ell m}}{(\alpha-1)^{2\ell+1}}\, \tilde{H}_\ell(\alpha)\, I_\ell(\alpha) \\
&= -(\alpha-1) \lim_{U\to\infty} r_{*p}\left[\partial_V \psi^{\rm I}_{0>}\right]_\Gamma .
\end{aligned} \tag{6.125}$$

Here the first integration by parts produces (for $n = \ell$) two non-zero surface terms identical to the ones in the 3rd line of Eq. (6.122), which, however, cancel each other as above. In the last equality we have recalled Eq. (6.117). Putting this back in Eq. (6.122) we find, for $U \to \infty$,

$$\begin{aligned}
\lim_{U\to\infty} r_{*p}\left[\partial_U \psi^{\rm I}_{0>}\right]_\Gamma &= -\lim_{U\to\infty} r_{*p}\left[\partial_V \psi^{\rm I}_{0>}\right]_\Gamma - (\alpha-1)\lim_{U\to\infty} r_{*p}\left[\partial_V \psi^{\rm I}_{0>}\right]_\Gamma \\
&= -\alpha \lim_{U\to\infty} r_{*p}\left[\partial_V \psi^{\rm I}_{0>}\right]_\Gamma ,
\end{aligned} \tag{6.126}$$

so the U derivative is just $(-\alpha)$ times the V derivative. Recalling Eq. (6.120) we thus immediately have

$$\lim_{U\to\infty} r_p(t)\left[\partial_U\left(r\Phi^\ell_0\right)\right]_\Gamma = \frac{q(1+v)}{2v^2E}(2\ell+1)P'_\ell(y)Q_\ell(y), \tag{6.127}$$

and hence

$$\lim_{U\to\infty} r_p^2(t)\partial_U \Phi^\ell_{0\Gamma} = \frac{q(1+v)}{2v^2E}(2\ell+1)P'_\ell(y)Q_\ell(y) + \frac{q}{2vE}(2\ell+1)P_\ell(y)Q_\ell(y). \qquad (6.128)$$

6.4.4 The components F^0_t and F^0_r

We now derive the t and r derivatives of Φ^ℓ_0, evaluated on the worldline at late times, and hence write down the corresponding self-force mode-sum. Using the chain rule, we have

$$\partial_r \sim \partial_{r_*} = \partial_V - \partial_U, \qquad \partial_t = \partial_V + \partial_U. \qquad (6.129)$$

Substituting for the U and V derivatives from Eqs. (6.121) and (6.128), we thus obtain

$$\begin{aligned}
\lim_{U\to\infty} r_p^2(t)\Big[\partial_r\Phi^\ell_0\Big]_\Gamma &= -\frac{q}{v^2E}(2\ell+1)P'_\ell(y)Q_\ell(y) - \frac{q}{vE}(2\ell+1)P_\ell(y)Q_\ell(y), \\
\lim_{U\to\infty} r_p^2(t)\Big[\partial_t\Phi^\ell_0\Big]_\Gamma &= \frac{q}{vE}(2\ell+1)P'_\ell(y)Q_\ell(y). \qquad (6.130)
\end{aligned}$$

Finally, we construct the self-force mode-sum for this contribution. From Eqs. (2.51) and (2.52), the t and r component regularisation parameters decay like $1/r_p^2$ at large r_p, with leading-order forms

$$A^\pm_\alpha = \pm\frac{q^2\bar{A}_\alpha}{r_p^2} \qquad \text{and} \qquad B_\alpha = \frac{q^2\bar{B}_\alpha}{r_p^2}, \qquad (6.131)$$

for $\alpha = t, r$, where

$$\bar{A}_\alpha = E(v,-1) \qquad \text{and} \qquad \bar{B}_\alpha = \frac{1}{2}E^2(-v, 2v^2-1) \qquad [\alpha = t, r]. \qquad (6.132)$$

The mode-sum (2.49) can thus be written

$$F^0_\alpha = \frac{q^2}{r_p^2}\sum_{\ell=0}\Big[r_p^2\partial^+_\alpha(\Phi^\ell_0/q)\Big|_\Gamma - (\ell+1/2)\bar{A}_\alpha - \bar{B}_\alpha\Big] \qquad (\alpha = t, r) \qquad (6.133)$$

at (leading) $1/r_p^2$ order. Substituting from Eqs. (6.130) and (6.132), we obtain

$$\begin{aligned}
\lim_{t\to\infty}\Big[r_p^2(t)F^0_r(r_p(t))\Big] = -\frac{q^2}{v^2E}\sum_{\ell=0}^{\infty}\Big[&(2\ell+1)P'_\ell(y)Q_\ell(y) + v(2\ell+1)P_\ell(y)Q_\ell(y) \\
&- \frac{1}{2}(2l+1)E^2v^2 + \frac{1}{2}E^3v^2(2v^2-1)\Big], \qquad (6.134)
\end{aligned}$$

$$\lim_{t\to\infty}\Big[r_p^2(t)F^0_t(r_p(t))\Big] = \frac{q^2}{vE}\sum_{\ell=0}^{\infty}\left[(2\ell+1)P'_\ell(y)Q_\ell(y) - \frac{1}{2}(2\ell+1)E^2v^2 + \frac{1}{2}E^3v^2\right]. \qquad (6.135)$$

We now demonstrate that both of these sums equal 0, so that there is no $1/r_p^2$ contribution to the self-force.

6.4.4.1 Explicit summation over ℓ

Define the sum

$$\tilde{\Lambda}(y) = \sum_{\ell=0}^{\infty} \left[(2\ell+1) P'_\ell(y) Q_\ell(y) - \frac{2\ell+1}{2(y^2-1)} + \frac{y}{2(y^2-1)^{3/2}} \right]. \tag{6.136}$$

Provided $\tilde{\Lambda}(y)$ converges, we may write Eqs. (6.134) and (6.135) as

$$\lim_{t\to\infty} \left[r_p^2(t) F_r^0(r_p(t)) \right] = -\frac{q^2}{v^2 E} \left[\tilde{\Lambda}(y) + v\Lambda(y) \right] \tag{6.137}$$

and

$$\lim_{t\to\infty} \left[r_p^2(t) F_t^0(r_p(t)) \right] = \frac{q^2}{vE} \tilde{\Lambda}(y). \tag{6.138}$$

Recalling Eq. (6.97), $\Lambda(y) = 0$ and we need only consider $\tilde{\Lambda}(y)$:

$$\begin{aligned} \tilde{\Lambda}(y) &= \lim_{n\to\infty} \sum_{\ell=0}^{n} \left[(2\ell+1) P'_\ell(y) Q_\ell(y) - \frac{2\ell+1}{2(y^2-1)} + \frac{y}{2(y^2-1)^{3/2}} \right] \\ &= \lim_{n\to\infty} \left\{ \sum_{\ell=0}^{n} (2\ell+1) P'_\ell(y) Q_\ell(y) - \frac{(n+1)^2}{2(y^2-1)} + \frac{y(n+1)}{2(y^2-1)^{3/2}} \right\} \end{aligned} \tag{6.139}$$

Notice that

$$\begin{aligned} \sum_{\ell=0}^{n} (2\ell+1) P'_\ell(y) Q_\ell(y) &= \frac{1}{2} \sum_{\ell=0}^{n} (2\ell+1) \left[P'_\ell(y) Q_\ell(y) + P_\ell(y) Q'_\ell(y) \right] \\ &\qquad + \frac{1}{2} \sum_{\ell=0}^{n} (2\ell+1) \left[P'_\ell(y) Q_\ell(y) - P_\ell(y) Q'_\ell(y) \right] \qquad (6.140) \\ &= \frac{1}{2} \frac{d}{dy} \sum_{\ell=0}^{n} (2\ell+1) P_\ell(y) Q_\ell(y) + \frac{(n+1)^2}{2(y^2-1)}, \qquad (6.141) \end{aligned}$$

where we made use of the Wronskian $W(y) = (y^2-1)^{-1}$. We can then rewrite

$$\tilde{\Lambda}(y) = \frac{1}{2} \lim_{n\to\infty} \left\{ \frac{d}{dy} \sum_{\ell=0}^{n} (2\ell+1) P_\ell(y) Q_\ell(y) + \frac{y(n+1)}{(y^2-1)^{3/2}} \right\}. \tag{6.142}$$

In Sec. 6.3.4 we found that

$$\sum_{\ell=0}^{n} (2\ell+1) P_\ell(y) Q_\ell(y) = \frac{1}{\sqrt{y^2-1}} \left[\frac{(n+1)^2(2n-1)}{4n^2} + \frac{2n+1}{4} + O\left(n^{-1}\right) \right] \tag{6.143}$$

as $n \to \infty$. Assuming that we may differentiate this series term-by-term with respect to y, we get

$$\frac{d}{dy}\sum_{\ell=0}^{n}(2\ell+1)P_\ell(y)Q_\ell(y) = -\frac{(n+1)y}{(y^2-1)^{3/2}}\left[1+O\left(n^{-2}\right)\right], \tag{6.144}$$

and hence it follows from Eq. (6.142) that $\tilde{\Lambda}(y) = 0$. Thus we have established

$$\lim_{t\to\infty} r_p^2(t)F_r^0(t) = 0 = \lim_{t\to\infty} r_p^2(t)F_t^0(t). \tag{6.145}$$

6.4.5 Numerical validation

We saw in the previous section that the leading term ψ_0 in our hierarchical expansion (6.9) gives rise to terms of order $1/r_p^2$ in the mode-sum for the t and r components of the self-force, which then sum to zero. As well as establishing consistency with the numerical results, which suggest a $1/r_p^3$ decay in those components of the self-force at large radius, achieving the necessary cancellation with the regularisation parameters provides useful validation for expressions (6.134) and (6.135).

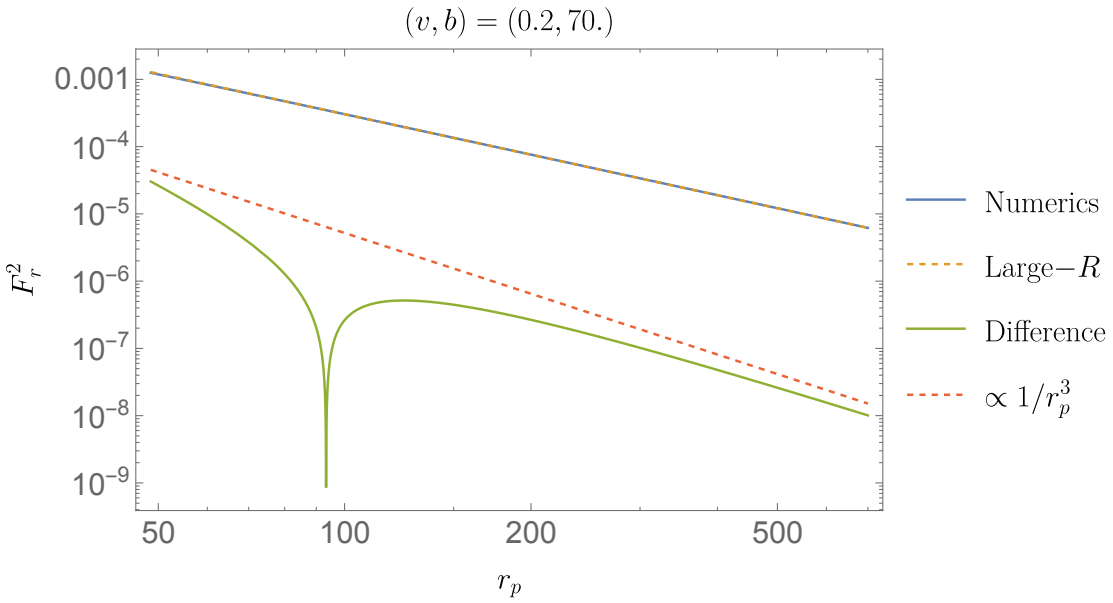

FIGURE 6.5: Comparison between the numerical (solid blue) and leading-order analytical (dashed orange) results for the regularised $\ell = 2$ contribution to the r-component of the self-force along the orbit with parameters $b = 70M$ and $v = 0.2$. The analytical result is from Eq. (6.147), and the numerical self-force data was obtained using the time-domain code of Ref. [149]. The numerical and analytical results are visually coincident. Subtracting the analytical result from the numerical data, the residual is several orders of magnitude smaller throughout the domain, and decays as $1/r_p^3$. Image credit: O. Long [192]

Our leading-late-time calculation of ψ_0 is not able to provide us with the leading term in the late-time expansion of $F_\alpha^{\rm self}$ for comparison with numerical data, but we can

compare the regularised ℓ-mode contributions to the self-force, which are individually non-zero for the t and r components. In particular, Fig. 6.5 displays the regularised $\ell = 2$ contribution to the r component of the self-force at late times along an example orbit, i.e the term in the self-force mode-sum (2.49),

$$F^{\text{full}+}_{r,\ell} - (\ell + 1/2)A^{+}_{r} - B_r, \tag{6.146}$$

with $\ell = 2$, as well as the term in the leading-order approximation (6.133),

$$q\partial^{+}_{r}\Phi^{\ell}_{0}\Big|_{\Gamma} - (\ell + 1/2)\frac{q^2\bar{A}_r}{r_p^2} - \frac{q^2\bar{B}_r}{r_p^2}. \tag{6.147}$$

Excellent agreement is observed between the two results, which are visually indistinguishable from at least $r_p = 50M$ onwards. Furthermore, subtracting (6.147) from (6.146), the residual is $O(1/r_p^3)$ – one order faster than (6.146), and the same order as the empirical fall-off in F_r^{self}. Altogether this serves as strong evidence in favour of the correctness of our calculation so far. In particular, it strongly suggests that (6.147) gives the exact $O(1/r_p^2)$ term in (6.146), and hence that none of the $n > 0$ terms in the hierarchical expansion (6.9) contribute to the mode-sum for F_r^{self} at $O(1/r_p^2)$ at late times (or, at the very least, that any such contributions are numerically much smaller than the $O(1/r_p^3)$ terms during the time range displayed in Fig. 6.5).

6.5 Calculation of ψ_1: setup and outlook

In this final section we consider the calculation of the leading-late-time piece of ψ_1, the next-to-leading order term in the hierarchical expansion (6.9). The calculation of this term remains at a preliminary stage, so we will present only the basic outline of our strategy, concluding with a discussion of our progress to date and the outlook for the analytical large-r_p calculation as a whole.

6.5.1 Strategy

The retarded solution to Eq (6.11) is given in terms of the Green's function (6.13) by

$$\begin{aligned}\psi_1(x) &= -\int_{-\infty}^{U} dU' \int_{-\infty}^{V} dV'\, G(x;x')\delta V(r')\psi_0(x') \\ &= -\int_{-\infty}^{U} dU' \int_{-\infty}^{V} dV' \int_{-\infty}^{U'} dU'' \int_{-\infty}^{V'} dV''\, G(x;x')\delta V(r')G(x';x'')S(U'')\delta(V'' - V_p(U'')),\end{aligned} \tag{6.148}$$

where $x := \{U, V\}$ and $x' := \{U', V'\}$. In the second line we have substituted for ψ_0 in terms of the Green's function from Eq. (6.24). In practice, we find it more convenient

to change the integration order, simplifying the form of the integration limits:

$$\psi_1(x) = -\int_{-\infty}^{\tilde{U}(U,V)} dU'' \int_{U''}^{U} dU' \int_{V_p(U'')}^{V} dV'\, G(x;x')\delta V(r')G(x';x_p'')S(U''), \qquad (6.149)$$

where $x_p'' = \{U'', V_p(U'')\}$ and so forth, and [recalling Eq. (6.32)] $\tilde{U} = U$ for $V \geq V_p(U)$ and $\tilde{U} = U_p(V)$ for $V < V_p(U)$. For each source point $(U'', V_p(U''))$ we now have a rectangular integration domain over U', V', and the field is then obtained by integrating over the source retarded time U''. We will be interested primarily in the value of ψ_1 on the particle,

$$\psi_1(U, V_p(U)) = \int_{-\infty}^{U} dU'' \int_{U''}^{U} dU' \int_{V_p(U'')}^{V_p(U)} dV'\, G(x_p;x')\delta V(r')G(x';x_p'')S(U'')\,, \qquad (6.150)$$

which we seek to evaluate at $U \gg R$.

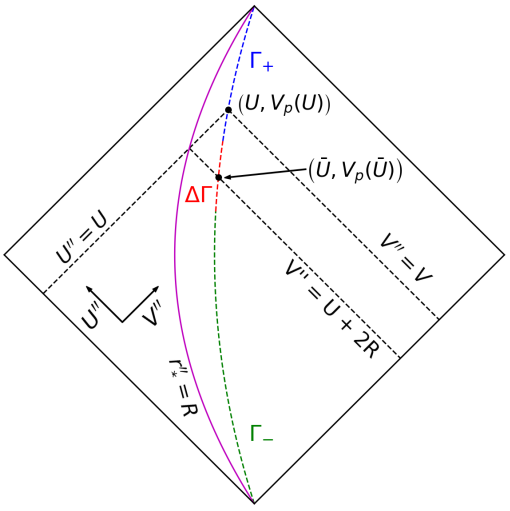

FIGURE 6.6: The division (6.151) of the worldline into early (Γ_-, green), strong-field ($\Delta\Gamma$, red) and late (Γ_+, blue) portions.

The next step in our strategy is to split the worldline integral over U'' into three different segments,

$$\begin{aligned}
\Gamma_+ :&\quad \bar{U}(U) + \Delta < U'' \leq U &&\text{(recent, weak field)},\\
\Delta\Gamma :&\quad \bar{U}(U) - \Delta < U'' \leq \bar{U}(U) + \Delta &&\text{(strong field)},\\
\Gamma_- :&\quad -\infty < U'' \leq \bar{U}(U) - \Delta &&\text{(early, weak field)},
\end{aligned} \qquad (6.151)$$

where Δ is some constant retarded-time interval satisfying

$$R \ll \Delta \ll U, \qquad (6.152)$$

and U is assumed sufficiently large to enable this. This split is illustrated in Fig. 6.6. We then split $\psi_1(U, V_p(U))$ into corresponding contributions,

$$\psi_1 = \psi_1^+ + \Delta\psi_1 + \psi_1^-, \tag{6.153}$$

and evaluate each contribution separately.

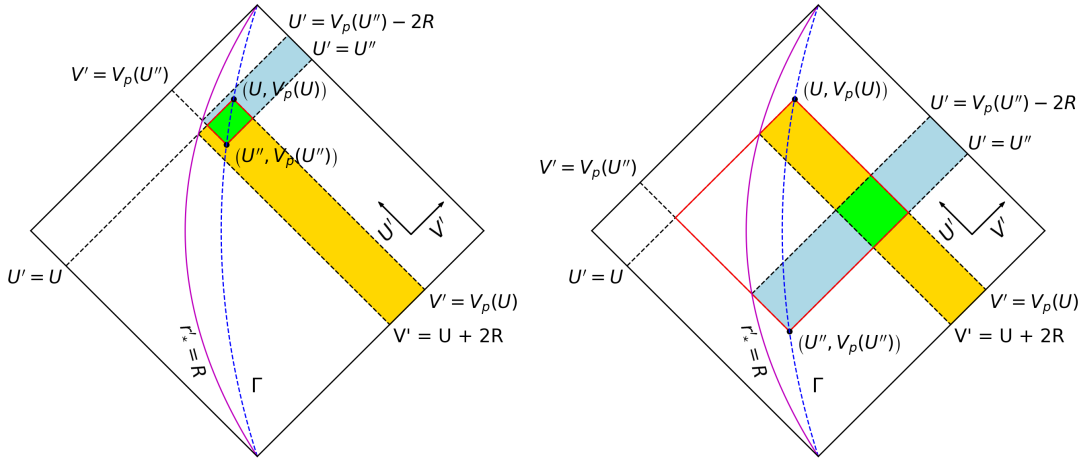

FIGURE 6.7: Support of (U', V') integration in Eq. (6.150) for fixed U and U'' in the two cases $U'' \in \Gamma_+$ (*left panel*) and $U'' \in \Gamma_-$ (*right panel*). The red lines indicate the borders of the integration region $U < U' < U''$, $V_p(U) < V' < V_p(U'')$. The regions for which the Green's functions $G(x_p; x')$ and $G(x'; x''_p)$ are of region-I type are shaded yellow and blue respectively; the integrand has significant support only in the overlap region, shaded in green. At late retarded times U, the entire integration region lies in the weak-field $r'_* \gg R$ when $U'' \in \Gamma_+$. For $U'' \in \Gamma_-$, the integration region notionally extends to the strong-field, but the region of effective support remains entirely in the weak-field.

To understand why the split (6.151) is useful, note that in order to obtain the large-r_p expansion of ψ_1, we wish to expand the factor $\delta V(r')$ in Eq. (6.150) in r'_* at $r'_* \gg R$. As may be seen from the left panel of Fig. 6.7, for $U'' \in \Gamma_+$, the (U', V') integration region in Eq. (6.150) is confined to

$$r'_* \geq \frac{1}{2}\left[V_p(\bar{U} + \Delta) - U\right] \sim \frac{1}{2}\alpha\Delta \gg R, \tag{6.154}$$

as $U \to \infty$, where we made use of $V_p(U) \sim \alpha U$ and $\bar{U} \sim U/\alpha$ from Eqs. (6.39) and (6.45) respectively. We may therefore freely use weak-field, large-r' expansions of $\delta V(r')$ whenever $U'' \in \Gamma_+$. The situation is less clear when $U \in \Gamma_-$, however. The right panel of Fig. 6.7 demonstrates that the integration region always extends down into the strong-field $r'_* < R$ region when $U'' \in \Gamma_-$. Fortunately, however, we recall from Fig. 6.2 that the Green's function only has significant support in region I, decaying exponentially to the past of the region I boundary. This means that the support of the integrand in Eq. (6.150) is effectively restricted to the region where the $G(x_p; x')$ and $G(x'; x''_p)$ Green's functions are both of region-I type. This region is shaded green in the right

panel of Fig. 6.7, and for large U it always lies in the strong-field:

$$r'_* \geq \frac{1}{2}\left[(U+2R) - (V_p(\bar{U}-\Delta) - 2R)\right] \sim \frac{1}{2}(\alpha\Delta + 4R) \gg R. \tag{6.155}$$

We are therefore able to expand $\delta V(r')$ when $U'' \in \Gamma_-$ too.

The calculation of ψ_1^- can also be aided by the following observation. Suppose the point-particle source on the right hand side of Eq. (6.6) is truncated to the future of some finite retarded time U_0, i.e. replacing $S(U) \to S(U)\Theta(U_0 - U)$. Near to past null infinity, $U \to -\infty$, we expect that the scalar field ψ will be static, due to the absence of incoming radiation [note this is consistent with the static leading-order early-time result for ψ_0 obtained by substituting $v \to -v$ in Eq. (6.74)]. If this is correct, Eq. (89) of Ref. [189] tells us that the resulting solution to the field equation with future-truncated source decays like

$$\psi(t,r) \sim \frac{1}{t^{2\ell+2}} r P_\ell\left(\frac{r-M}{M}\right) \qquad (t \gg |r_*|), \tag{6.156}$$

at late times, and hence $\psi \sim U^{-(\ell+1)}$ when evaluated along the orbit as $U \to \infty$. Put another way, the error in ψ from truncating the source to the *past* of U_0 decays at the same rate; given that ψ_1 is expected to decay as $1/U$ along the orbit, the error will be at a subdominant order for any $\ell > 0$ (but not, necessarily, for $\ell = 0$). This means that for $\ell > 0$, we may truncate the worldline integral in Eq. (6.150) to the past of $U'' = U_0$, where U_0 is a finite constant, without affecting the leading late-time result for ψ_1. The case $\ell = 0$ would need to be considered separately.

Finally, when $U'' \in \Delta\Gamma$, the integrand *is* supported in the strong-field $r'_* \sim R$, and it is not possible to make use of any large-r' expansions for $\delta V(r')$ during this portion of the worldline integral. Intuitively, however, the piece $\Delta\psi_1$ from $U'' \in \Delta\Gamma$ may not contribute to the leading-late-time behaviour of ψ_1, arising as it does from a constant, finite retarded-time interval, which becomes arbitrarily distant as $U \to \infty$. Establishing whether this holds true – using a bounding argument, for example – is an important aim of our approach.

6.5.2 Outlook

Our calculation of ψ_1 remains at a preliminary stage, and we opt not to present detailed results. We will, however, note several features we have observed thus far. Our initial results are consistent with $\psi_1 \sim 1/r_p$, i.e. ψ_1 is suppressed by a factor of $1/r_p$ relative to ψ_0 as expected, and will contribute to all components of the self-force at their empirical leading late time orders: $1/r_p^3$ for the t and r components, and $1/r_p^2$ for the φ component. We have also tentatively established that the contribution $\Delta\psi$ is, indeed, subdominant at late times.

In order to complete the calculation of $F_\alpha^{\rm self}$ at leading late time order, we must also include the next-to-leading late time terms from ψ_0, at least some of which are expected to contribute to $F_t^{\rm self}$ and $F_r^{\rm self}$ at $O(1/r_p^3)$, and to $F_\varphi^{\rm self}$ at $O(1/r_p^2)$. We remarked in Sec. 6.3.4 that the LLT ψ_0 calculation is effectively performed in flat spacetime with a particle moving along the asymptotic straight line trajectory, and hence does not give rise to a contribution to the self-force. At the first post-LLT order, ψ_0 will have a contribution from terms arising from the next-to-leading asymptotic expansions of the geodesic trajectory; such terms describe an accelerated trajectory, which will feel a self-force, even in flat spacetime.

Chapter 7

Conclusions

This work has produced three primary outputs. Firstly, we successfully accomplished our goal of developing the first frequency-domain method for calculating the scalar-field self-force along hyperbolic geodesics in Schwarzschild spacetime. To do this, we had to develop solutions to several significant numerical challenges, most notably the development of the tail correction and IBP schemes in Chapter 3 to minimise the error from truncating the slowly-convergent oscillatory integrals $C^{-}_{\ell m\omega}$ at finite radius, as well as the use of sinusoid-weighted Clenshaw-Curtis quadrature to accelerate their evaluation. As we saw in Chapter 4, our frequency-domain method can significantly exceed the precision of Ref. [149]'s time-domain platform in the strong-field region near periapsis, and has unique access to angular modes with $\ell > 15$ there.

Despite these achievements, several limitations of our frequency-domain approach do remain, with the most significant ones arising from the use of extended homogeneous solutions. There is no known method for reconstructing the time-domain field from an EHS in the external region $r \geq r_p(t)$ for a scattering source, and presently we are restricted to a one-sided regularisation procedure in which the self-force is calculated using the limit of the field from the $r < r_p(t)$ direction alone. Even more significantly, in Chapter 4 the cancellation between low-frequency modes of the EHS was found to seriously impede the reconstruction of the time-domain modes of the scalar field away from periapsis. Compared to bound orbits, the degree of cancellation faced is intrinsically more severe for scatter orbits due to the greater eccentricity, and the errors in the calculation of the frequency-domain quantities are larger and more numerous. Currently, our only solution to this challenge is a gradual, adaptive, reduction in the value of the mode-sum truncation $\ell_{\max}$ as the radius is increased.

Our second output is a method for resumming the post-Minkowskian expansion of the scatter angle using the singular structure of the self-force scatter angle correction $\delta\varphi^{(1)}$ in the limit of the transition to plunge, $b \to b_c(v)$. As seen in Chapter 5, the resulting model has the correct asymptotics to 4PM order as $b \to \infty$, and to 1SF order as $b \to b_c(v)$, but

is also uniformly accurate in between. The key advantage of this semi-analytic approach is that the resummed angle can be rapidly evaluated once given the self-force singularity coefficient $A_1(v)$. We saw in Sec. 5.2 that $A_1(v)$ can in principle be obtained from a calculation of the self-force along the critical orbits $b = b_c(v)$ alone, and calculating the self-force at nodes along the 1-dimensional separatrix $b = b_c(v)$ is computationally much cheaper than populating the full 2-dimensional (v, b) parameter space. In our case, however, we did not calculate $A_1(v)$ by integrating along the critical orbit itself, preferring instead to fit the coefficient numerically to values of the scatter angle along sequences of near-critical geodesics. Performing the calculation in this manner remains significantly faster than populating the full parameter space, but also allowed us to make use of our exisiting time- and frequency-domain numerical methods without the need for lengthy modifications. Our frequency-domain code proved extremely valuable to this effort, despite its issues away from periapsis. The frequency-domain method's access to modes with $\ell > 15$ near to periapsis led to the discovery of the high-velocity, large-ℓ features which we attributed to likely relativistic beaming in Sec. 5.4.1, and was crucial for capturing their large contribution to the self-force as part of the hybrid method described in Sec. 5.4.2.3.

Finally, in Chapter 6 we initiated an analytical calculation for the scalar-field self-force at early and late times along a hyperbolic scatter orbit, and obtained initial results for the leading-order piece of the scalar-field evaluated on the particle. Such analytical results, once fully developed, will be critical for supplementing both time- and frequency-domain numerical approaches, and potentially for providing initial data for time-domain simulations.

7.1 Outlook

The emphasis of this thesis has been primarily on the development of the numerical method, and its subsequent application in the strong-field region ($r_{\min} \lesssim 6M$) of orbital parameter space. Ongoing work aims to expand these boundaries, exploring the scattering parameter space at large. Particular attention should be paid to the limit of large $r_{\min}$, a regime which is crucial for comparisons with post-Minkowskian results. Part of the challenge in the PM domain is the need to increase the radial truncation $r_{\max}$ used in the integrals $C^{-}_{\ell m\omega}$ as $r_{\min}$ increases, and we need to understand the implications of this on the accuracy, and particularly the efficiency, of the code. Preliminary results suggest that our IBP and tail correction schemes remain effective at suppressing high-frequency noise in the tails of the $C^{-}_{\ell m\omega}$ spectra, but the overall level of decay we can achieve before the onset of noise is less than for the strong-field orbits considered previously. Some degradation in our method's performance is thus expected in the PM regime.

In addition to continued exploration of the current numerical code, we highlight several directions in which this research should be developed in the future.

7.1.1 Large radius asymptotics of the self-force

Work is ongoing to complete the calculation of the leading-order, $1/r_p$ term in ψ_1, using the strategy described in Sec. 6.5. Once complete, and supplemented by the next-to-leading-order piece of ψ_0, we will have the necessary ingredients to calculate the scalar-field self-force correct at leading order in $1/r_p$ at early and late times along the orbit. This can be compared to numerical self-force results, validating both approaches. The leading-order self-force can also be immediately incorporated into scatter angle calculations, complementing or replacing numerical extrapolations for the $r \to \infty$ tail of the scatter angle integral, a significant source of error in existing calculations. Ideally, the domain of validity of the leading-order analytical self-force will already overlap with that of the frequency-domain numerical approach, so that we can perform complete scatter angle calculations without needing to hybridise with self-force data from a time-domain code. Nonetheless, should this fail to happen, our analytical framework extends to higher orders. Future work will also aim to extend the calculation away from the particle's orbit, so that we may obtain the early-time scalar-field at generic spatial positions, suitable for use as initial data for time-domain evolutions. The analytical approach taken in Chapter 6 can also be extended to gravity once required, as in Ref. [193], for example.

7.1.2 Self-force calculations along the critical orbit

To properly exploit the PM resummation technique developed in Chapter 5, we need to be able to calculate the coefficients $A_1(v)$ as accurately as possible, at a sufficiently dense grid of velocities. We established in Sec. 5.2 that $A_1(v)$ may be expressed as an integral of the self-force along the critical orbit, but we actually calculated $A_1(v)$ using extrapolation from $b > b_c(v)$ instead. This ensured we could make use of our existing self-force code, but it required us to calculate the self-force along ~ 10 orbits (rather than just the 2 branches of the critical orbit), and introduced additional error from the fit to numerical data. Moving forward, therefore, there is a strong incentive to develop methods that can calculate the self-force along the critical orbits directly. From the frequency-domain perspective, an initial analysis found that the variation of parameters solution analogous to Eq. (2.106) for a critical orbit is divergent at $\omega = m\omega_{\rm circ}$, where $M\omega_{\rm circ} = (M/r_{\rm min})^{3/2}$ is the frequency of the circular orbit of radius $r_{\rm min}$. Further investigation identified the presence of both a δ-function and a *pole* in the scalar-field's frequency spectrum, arising from the asymptotic circular whirl along the critical orbit. An approach which subtracts the distributional piece of the spectrum, leaving behind a residual field which we can calculate numerically, is under development, and we expect to begin numerical trials soon.

7.1.3 Extension to gravity

We have made good use of a scalar-field toy model to develop solutions to some of the problems facing self-force calculations along scatter orbits, but our ultimate goal is to calculate the gravitational self-force. One approach to gravitational SF calculations is based upon metric reconstruction from curvature scalars [148, 194], which may be implemented in either the time or frequency domains. A frequency-domain method to solve the Teukolsky equation with scatter orbit source would build very naturally on the techniques developed in this thesis, but would also inherit many of the same limitations. Any approach based on the EHS method would continue to suffer from the severe cancellation problem we have observed, and would still be restricted to a one-sided mode-sum regularisation procedure based on the field in $r \leq r_p(t)$ alone. The latter is particularly problematic for the conventional approach, in which the self-force is calculated from the modes of the metric perturbation in a so-called "radiation" gauge, using a two-sided regularisation procedure; one-sided regularisation would be much more complicated in radiation gauge, and has never been attempted. There is no such issue in Lorenz gauge, however, where one-sided regularisation may be readily applied [195]. Lorenz gauge metric reconstruction is less well developed than its radiation gauge counterpart, particularly in Kerr, but progress has been made in recent years [196–198]. In principle, one may also calculate the components of the Lorenz gauge metric perturbation directly. This path was taken in Ref. [199], which worked in the frequency-domain to find the tensor spherical harmonic modes of the metric perturbation in Lorenz gauge, and hence the self-force. This code – which once again relies on EHS – may also be extended quite naturally to scatter orbits using our techniques. A Lorenz gauge time-domain code was also used in Ref. [200] to calculate the self-force along the $v = 0$ critical orbit, and it may be possible to extend this to generic scatter orbits. In principle, a frequency-domain variant could also be developed, incorporating some of the techniques developed herein.

We note also that there is ongoing work to develop a modern time-domain solver for the Teukolsky equation with a scatter orbit source, utilising hyperboloidal slicing and compactification [184]. These techniques have previously been applied to frequency-domain self-force calculations for bound orbits also [183], so a frequency-domain variant of this solver may also be possible in the future.

7.1.4 Alternatives to the use of EHS

It is clear that the use of EHS is a limiting factor in frequency-domain self-force calculations for scatter orbits. In the conclusion of Sec. 4.6, we considered the idea of reconstructing the time-domain modes of the scalar field using the variation of parameters formula (2.106) directly, possibly using spectral filtering and/or extrapolation. As well

as circumventing the EHS cancellation problem, if successful, such an approach would enable the calculation of the field in $r > r_p(t)$, simplifying radiation gauge gravitational SF calculations. Furthermore, the computational building blocks of the variations of parameter solution (i.e. the homogeneous solutions and the integrands of the different integrals) are the same as for the EHS approach, so that existing EHS codes will require minimal modification. The techniques developed in Chapter 3 to accelerate the convergence and evaluation of the radial integrals, in particular, could immediately be applied to the integral with upper limit ∞ in formula (2.106).

A more radical suggestion is to abandon both EHS and mode-sum regularisation together, and make use of a *puncture* instead [201, 202]. In this approach, rather than using the local expansion of Φ^S in the vicinity of the worldline to obtain regularisation parameters, one instead uses it to devise a puncture field $\Phi^{\mathcal{P}} \approx \Phi^S$ which approximates the local singularity at the particle, such that the *residual* field $\Phi^{\mathcal{R}} := \Phi - \Phi^{\mathcal{P}} \approx \Phi^R$ is regular (at least C^1) on the worldline. Using Eq. (2.30), $\Phi^{\mathcal{R}}$ obeys

$$\nabla_\mu \nabla^\mu \Phi^{\mathcal{R}} = -4\pi T - \nabla_\mu \nabla^\mu \Phi^{\mathcal{P}} := -4\pi T_{\text{eff}}, \tag{7.1}$$

where the term on the right-hand side, which is regular (at least C^3) at the worldline, is known as the effective source. The self-force can be obtained by solving Eq. (7.1) for $\Phi^{\mathcal{R}}$, and then using Eq. (2.34) with the replacement $\Phi^R \to \Phi^{\mathcal{R}}$. The residual field $\Phi^{\mathcal{R}}$ is smoother than the retarded field Φ at the worldline, mitigating the Gibbs phenomenon somewhat: the spherical-harmonic frequency modes of the residual field decay as ω^{-k}, where $k > 1$ increases with the order of the puncture. While still only a polynomial decay, for a sufficiently high-order puncture, k may be large enough to render a variations of parameter based calculation practical. The puncture approach has been applied in the frequency-domain previously for the scalar-field [203] and gravitational [204] SF along circular orbits in Schwarzschild, and more recently for eccentric orbits in Schwarzschild using a scalar-field model [205]. An extension to scatter orbits may also be possible, but further work is needed to understand the scale of the technical challenges.

7.1.5 Beyond

Once a calculation of the gravitational SF is at hand, we will be able to attack our ultimate objectives. A first-order gravitational SF calculation of the scatter angle will allow us to validate and benchmark the state of the art 4PM and 5PM-1SF analytical results. The self-force scatter angle will also be incorporated into EOB models, enhancing their performance at extreme mass ratios (and even equal mass ratios, if SF-informed, mass-symmetric, PM results are used), and thus benefit waveform modelling for compact binary gravitational wave sources. It may also be possible to compare self-force scatter angle results, or EOB resummations thereof, to numerical relativity scatter simulations. Initial gravitational SF calculations are expected to be restricted to the case

of a primary Schwarzschild black hole, so an extension to Kerr is essential if we are to accurately represent the astrophysical population of black holes. Such an extension is likely to be easiest if we use an approach based on radiation gauge metric reconstruction. Finally, we remark that in the more distant future it may be possible to extend scatter orbit calculations to second self-force order, giving access to 6PM terms in the conservative Hamiltonian (potentially for the first time) and, using EOB or boundary-to-bound relations, contributing to efforts to obtain post-adiabatic EMRI waveforms. Such calculations are likely to face many computational and theoretical hurdles, some of which may be currently unknown, so that it is hard to gauge accurately the possible timescales. It is safe to say, however, that scattering calculations will continue to develop and make significant contributions to the field of gravitational wave astronomy in coming years.

Appendix A

Expansion of geodesic quantities at large radius

We collect here expressions for the coefficients that occur in the large-radius expansions of the geodesic quantities in Eqs. (2.27) and (2.28). To obtain large-r expansions for $t_p(r)$ and $\varphi_p(r)$ along the outbound leg of the orbit, we rewrite the equations of motion in terms of the parameter r, and then expand in powers of $1/r$. In order to do this, we first expand

$$\left(\frac{dr_p}{d\tau}\right)^{-1} = \sum_{n=0}^{\infty} U_n \left(\frac{2M}{r}\right)^n, \tag{A.1}$$

where the first few coefficients work out to be

$$U_0 = \frac{1}{\sqrt{E^2-1}}, \tag{A.2}$$

$$U_1 = -\frac{1}{2\left(E^2-1\right)^{3/2}}, \tag{A.3}$$

$$U_2 = \frac{3-4\tilde{L}^2+4E^2\tilde{L}^2}{8(E^2-1)^{5/2}}, \tag{A.4}$$

$$U_3 = \frac{-5+4\tilde{L}^2+4E^2\tilde{L}^2-8E^4\tilde{L}^2}{16(E^2-1)^{7/2}}, \tag{A.5}$$

$$U_4 = \frac{1}{128\left(E^2-1\right)^{9/2}}\Big[48E^4\tilde{L}^4+96E^4\tilde{L}^2-96E^2\tilde{L}^4 - 72E^2\tilde{L}^2+48\tilde{L}^4-24\tilde{L}^2+35\Big], \tag{A.6}$$

$$U_5 = \frac{1}{256\left(E^2-1\right)^{11/2}}\Big[-63-192E^6\tilde{L}^4+336E^4\tilde{L}^4 - 240E^4\tilde{L}^2-96E^2\tilde{L}^4+200E^2\tilde{L}^2-48\tilde{L}^4+40\tilde{L}^2\Big], \tag{A.7}$$

with $\tilde{L} := L/(2M)$. Writing

$$\frac{dt_p}{dr} = \frac{dt_p}{d\tau}\left(\frac{dr_p}{d\tau}\right)^{-1}, \tag{A.8}$$

we expand $dt_p/d\tau$, given in Eq. (2.1), and combine with (A.1) to obtain

$$\frac{dt_p}{dr} = A + \frac{2MB}{r} - \sum_{n=1}^{\infty} nC_n \left(\frac{2M}{r}\right)^{n+1}, \tag{A.9}$$

and therefore

$$t_p(r) = t_0 + Ar + 2MB\log\left(\frac{r}{2M}\right) + 2M\sum_{n=1}^{\infty} C_n\left(\frac{2M}{r}\right)^n. \tag{A.10}$$

The dimensionless coefficients A and B work out as

$$A = \frac{E}{\sqrt{E^2-1}} = \frac{1}{v}, \tag{A.11}$$

$$B = \frac{E(2E^2-3)}{2(E^2-1)^{3/2}} = \frac{3v^2-1}{2v^3}, \tag{A.12}$$

and the first few dimensionless coefficients C_n are

$$C_1 = -\frac{E\left[4E^2\left(\tilde{L}^2-5\right)+8E^4-4\tilde{L}^2+15\right]}{8(E^2-1)^{5/2}}, \tag{A.13}$$

$$C_2 = -\frac{E\left[-35+70E^2-56E^4+16E^6-12(E^2-1)\tilde{L}^2\right]}{32(E^2-1)^{7/2}}, \tag{A.14}$$

$$\begin{aligned} C_3 = -\frac{E}{384(E^2-1)^{9/2}}\Big[&315-840E^2+1008E^4-576E^6 \\ &+128E^8+120(E^2-1)\tilde{L}^2+48(E^2-1)^2\tilde{L}^4\Big], \end{aligned} \tag{A.15}$$

$$\begin{aligned} C_4 = \frac{E}{1024(E^2-1)^{11/2}}\Big[&693-2310E^2+3696E^4-3168E^6 \\ &+1408E^8-256E^{10}+280(-1+E^2)\tilde{L}^2 \\ &+48(-1+E^2)^2(3+2E^2)\tilde{L}^4\Big], \end{aligned} \tag{A.16}$$

$$\begin{aligned} C_5 = -\frac{E}{5120\,(E^2-1)^{13/2}}\Big[&64E^6\left(5\tilde{L}^6+15\tilde{L}^4-429\right) \\ &+1024E^{12}-6656E^{10}+18304E^8-1260\tilde{L}^2+3003 \\ &-24E^4\left(40\tilde{L}^6+50\tilde{L}^4-1001\right)+720\tilde{L}^4 \\ &+12E^2\left(80\tilde{L}^6-40\tilde{L}^4+105\tilde{L}^2-1001\right)-320\tilde{L}^6\Big]. \end{aligned} \tag{A.17}$$

In Eq. (A.10) t_0 is a constant of integration, whose value is fixed by the initial condition imposed on t_p. In practice we determine t_0 by comparing the expansion (A.10) to a numerical integration of Eq. (2.19) at large radii.

Similarly, we can express $\varphi_p(r)$ along the outbound leg of the orbit as an expansion in $1/r$ at large r. The result is

$$\varphi_p(r) = \varphi_\infty + \sum_{n=1}^{\infty} D_n \left(\frac{2M}{r}\right)^n, \tag{A.18}$$

where $\varphi_\infty := \varphi_p(\chi_\infty)$ and the first few coefficients are

$$D_1 = -\frac{\tilde{L}}{\sqrt{E^2-1}}, \tag{A.19}$$

$$D_2 = \frac{\tilde{L}}{4\left(E^2-1\right)^{3/2}}, \tag{A.20}$$

$$D_3 = \frac{\tilde{L}\left(-4E^2\tilde{L}^2 + 4\tilde{L}^2 - 3\right)}{24\left(E^2-1\right)^{5/2}}, \tag{A.21}$$

$$D_4 = \frac{\tilde{L}\left[8E^2\left(E^2-1\right)\tilde{L}^2 + 4\left(E^2-1\right)\tilde{L}^2 + 5\right]}{64\left(E^2-1\right)^{7/2}}, \tag{A.22}$$

$$D_5 = -\frac{\tilde{L}}{1920\left(E^2-1\right)^{9/2}}\Big[144\left(E^2-1\right)^2\tilde{L}^4 + 288E^2\left(E^2-1\right)\tilde{L}^2 + 72\left(E^2-1\right)\tilde{L}^2 + 105\Big]. \tag{A.23}$$

Appendix B

Post-Minkowskian expansion of the scalar-field scatter angle correction

In analogy with Eq. (2.74), the conservative and dissipative scatter angle corrections admit PM expansions

$$\delta\varphi^{(1)}_{\rm cons/diss} = \sum_{k=2}^{\infty} \delta\varphi^{(1,k)}_{\rm cons/diss}(v) \left(\frac{GM}{b}\right)^k, \tag{B.1}$$

where the total coefficient is given by $\delta\varphi^{(1,k)} = \delta\varphi^{(1,k)}_{\rm cons} + \delta\varphi^{(1,k)}_{\rm diss}$. In the conservative sector, the known coefficients are:

$$\delta\varphi^{(1,2)}_{\rm cons} = -\frac{\pi}{4}, \tag{B.2}$$

$$\delta\varphi^{(1,3)}_{\rm cons} = -\frac{4E\left(3-v^2\right)}{3v^2}, \tag{B.3}$$

$$\begin{aligned}
\delta\varphi^{(1,4)}_{\rm cons} =& \frac{\pi}{32v^5E^4}\Bigg[-6(95E+82)v\,\mathsf{El}_1\left(\frac{\pi}{2},\frac{E-1}{E+1}\right)^2 - 36E^6v^7\log^2\left(\frac{1+E}{2}\right) \\
&+ 6(E(100E+177)+79)v\,\mathsf{El}_1\left(\frac{\pi}{2},\frac{E-1}{E+1}\right)\mathsf{El}_2\left(\frac{\pi}{2},\frac{E-1}{E+1}\right) \\
&- 3(E+1)\left(100E^2+79\right)v\,\mathsf{El}_2\left(\frac{\pi}{2},\frac{E-1}{E+1}\right)^2 + 9E^6v\left(1-3v^2\right)^2\operatorname{arccosh}^2(E) \\
&+ E^6\left(1-3v^2\right)\left(36v^4\log\left(\frac{Ev}{2}\right) - 29\left(2-v^2\right)v^2 - 16\right)\operatorname{arccosh}(E) \\
&+ 48E^4v^5\log\left(b/M\right) + 2E^6v^3\left((38-24E)v^4 + (24E-58)v^2 - 16\right)\log\left(\frac{Ev}{2}\right) \\
&+ 6E^6v^3\left((8E-27)v^4 + 12v^4\log\left(\frac{Ev}{2}\right) - 8(E-4)v^2 - 8\right)\log\left(\frac{1+E}{2}\right)
\end{aligned}$$

$$- v\left[18E^6 + 252E^5 - 216E^3 + 463E^2 - 348E + E^4\left(12v^4 + 8v^2 - 223\right) + 110\right]\Bigg], \tag{B.4}$$

In the dissipative sector, the known coefficients are:

$$\delta\varphi^{(1,2)}_{\rm diss} = 0, \tag{B.5}$$

$$\delta\varphi^{(1,3)}_{\rm diss} = \frac{2E}{3}\frac{(1+v^2)^2}{v^3}, \tag{B.6}$$

$$\delta\varphi^{(1,4)}_{\rm diss} = \frac{\pi E}{8v}\left[\frac{3E\left(1-3v^2\right)\left(1+5v^2\right)}{2v^3}\operatorname{arccosh}(E) + 3E\left(1+5v^2\right)\log\left(\frac{1+E}{2}\right)\right.$$
$$\left. + \frac{24E + (61E+18)v^6 + 2(75-52E)v^4 + (19E+84)v^2}{6v^4}\right]. \tag{B.7}$$

In the above expressions, El_1 is the incomplete elliptic integral of the first kind [previously defined in Eq. (2.24)], and El_2 is the incomplete elliptic integral of the second kind [previously defined in Eq. (2.54)].

The leading PM term $\delta\varphi^{(1,2)}_{\rm cons}$ was first obtained in [150], and the leading term $\delta\varphi^{(1,3)}_{\rm diss}$ was first obtained in [149] (using results from [150]). The terms $\delta\varphi^{(1,3)}_{\rm cons}$, $\delta\varphi^{(1,4)}_{\rm cons}$ and $\delta\varphi^{(1,4)}_{\rm diss}$ were derived in [151] using Amplitude methods, except for certain pieces of the polynomial expression in the last line of Eq. (B.4) for $\delta\varphi^{(1,4)}_{\rm cons}$, associated with undetermined Wilson coefficients. These have more recently been determined through two independent methods: Matching of amplitude calculations in effective-field theory and black hole perturbation theory [177]; and a double PM/post-Newtonian expansion of the self-force [178].

Appendix C

Boundary conditions for homogeneous solutions

To obtain boundary conditions for the homogeneous solution $\psi^{+}_{\ell\omega}(r)$ in the limit $r \to \infty$, we make the ansatz [152]

$$\psi^{+}_{\ell\omega}(x) = e^{i\omega r_*} \sum_{k=0}^{k_{\rm out}} c_k^{\infty} \left(\frac{2M}{r}\right)^k, \tag{C.1}$$

and substitute into the homogeneous equation (2.94). This yields the recurrence relation

$$\sum_{i=0}^{3} f_i^{\infty} c_{k-i}^{\infty} = 0, \tag{C.2}$$

where the coefficients are given by

$$f_0^{\infty} = -2i\tilde{\omega}k, \tag{C.3}$$
$$f_1^{\infty} = k(k-1) + 2i\tilde{\omega}(k-1) - l(l+1), \tag{C.4}$$
$$f_2^{\infty} = -2k^2 + 5k - 3 + l(l+1), \tag{C.5}$$
$$f_3^{\infty} = (k-2)^2, \tag{C.6}$$

with $\tilde{\omega} := 2M\omega$.

Near the horizon we have a similar expansion for $\psi^{-}_{\ell\omega}(r)$,

$$\psi^{-}_{\ell\omega}(x) = e^{-i\omega r_*} \sum_{k=0}^{k_{\rm in}} c_k^{\rm eh} y^k, \tag{C.7}$$

where $y := r/2M - 1$. Again substituting into Eq. (2.94), we arrive at a recurrence relation for the coefficients,

$$\sum_{i=0}^{3} d_i^{\rm eh} c_{k-i}^{\rm eh} = 0, \tag{C.8}$$

with

$$d_0^{\rm eh} = -2i\tilde{\omega}k + k^2, \tag{C.9}$$

$$d_1^{\rm eh} = -6i\tilde{\omega}(k-1) - 1 - l(l+1) + (k-1)(2k-3), \tag{C.10}$$

$$d_2^{\rm eh} = (k-2)(k-3) - l(l+1) - 6i\tilde{\omega}(k-2), \tag{C.11}$$

$$d_3^{\rm eh} = -2i\tilde{\omega}(k-3). \tag{C.12}$$

The recurrence relations (C.2) and (C.8) admit solutions with $c_{k<0}^{\infty/{\rm eh}} = 0$, $c_0^{\infty/{\rm eh}} = 1$, and $c_{k>0}^{\infty/{\rm eh}}$ determined recursively. The number of terms, and hence accuracy of the approximation, may be controlled by varying the truncation parameters $k_{\rm out}$ and $k_{\rm in}$.

Appendix D

Constants appearing in the tail correction scheme

In this appendix we collect the various coefficients that appear in the expansions that make up the tail correction scheme described in Section 3.1.2. The first 5 coefficients $\hat{c}_n^\infty$ appearing in Eq. (3.5) are given in terms of the coefficients c_n^∞ of Eq. (2.99) by

$$\hat{c}_1^\infty := c_1^\infty - i\tilde{\omega}, \tag{D.1}$$

$$\hat{c}_2^\infty := c_2^\infty - i\tilde{\omega}c_1^\infty + \frac{1}{2}(-i\tilde{\omega} - \tilde{\omega}^2), \tag{D.2}$$

$$\begin{aligned}\hat{c}_3^\infty := \frac{1}{6}\big[&- 3c_1^\infty\tilde{\omega}^2 - 3ic_1^\infty\tilde{\omega} - 6ic_2^\infty\tilde{\omega} + 6c_3^\infty + i\tilde{\omega}^3 \\ &- 3\tilde{\omega}^2 - 2i\tilde{\omega}\big],\end{aligned} \tag{D.3}$$

$$\begin{aligned}\hat{c}_4^\infty := \frac{1}{24}\Big[&4i\tilde{\omega}^3c_1^\infty - 12\tilde{\omega}^2c_1^\infty - 12\tilde{\omega}^2c_2^\infty - 8i\tilde{\omega}c_1^\infty - 12i\tilde{\omega}c_2^\infty \\ &- 24i\tilde{\omega}c_3^\infty + \tilde{\omega}^4 + 6i\tilde{\omega}^3 - 11\tilde{\omega}^2 - 6i\tilde{\omega} + 24c_4^\infty\Big],\end{aligned} \tag{D.4}$$

$$\begin{aligned}\hat{c}_5^\infty := \frac{1}{120}\Big[&5\tilde{\omega}^4c_1^\infty + 30i\tilde{\omega}^3c_1^\infty + 20i\tilde{\omega}^3c_2^\infty - 55\tilde{\omega}^2c_1^\infty \\ &- 60\tilde{\omega}^2c_2^\infty - 60\tilde{\omega}^2c_3^\infty - 30i\tilde{\omega}c_1^\infty - 40i\tilde{\omega}c_2^\infty \\ &- 60i\tilde{\omega}c_3^\infty - 120i\tilde{\omega}c_4^\infty - i\tilde{\omega}^5 + 10\tilde{\omega}^4 + 35i\tilde{\omega}^3 \\ &- 50\tilde{\omega}^2 - 24i\tilde{\omega} + 120c_5^\infty\Big].\end{aligned} \tag{D.5}$$

The first 5 coefficients $H_{n\sigma}$ appearing in Eq. (3.9) are given in terms of the quantities Δ_n of Eq. (3.7) by

$$H_{1,\sigma} := i\sigma\Delta_\infty^{(1)}, \tag{D.6}$$

$$H_{2,\sigma} := \frac{1}{2}\left[-\left(\Delta_1\right)^2 + 2i\sigma\Delta_2\right] \tag{D.7}$$

$$H_{3,\sigma} := \frac{i}{6}\left[-\sigma\left(\Delta_1\right)^3 + 6\sigma\Delta_3 + 6i\Delta_2\Delta_1\right], \tag{D.8}$$

$$\begin{aligned} H_{4,\sigma} := \frac{1}{24}\Big[&- 12i\sigma\Delta_2\left(\Delta_1\right)^2 + 24i\sigma\Delta_4 + \left(\Delta_1\right)^4 \\ &- 24\Delta_3\Delta_1 - 12\left(\Delta_2\right)^2\Big], \end{aligned} \tag{D.9}$$

$$\begin{aligned} H_{5,\sigma} := \frac{i}{120}\Big[&\sigma\left(\Delta_1\right)^5 - 20i\Delta_2\left(\Delta_1\right)^3 \\ &- 60\sigma\Delta_3\left(\Delta_1\right)^2 - 60\sigma\left(\Delta_2\right)^2\Delta_1 \\ &+ 120i\Delta_4\Delta_1 + 120i\Delta_2\Delta_3 + 120\sigma\Delta_5\Big]. \end{aligned} \tag{D.10}$$

Appendix E

Near-separatrix behaviour of $\delta\varphi^{(0)}$

In this appendix we derive Eq. (5.5) for the logarithmic divergence of the geodesic scatter angle $\delta\varphi^{0)}$ in the near-separatrix limit.

Starting with the expression (2.26) for $\delta\varphi^{(0)}$ in terms of an elliptic function, we expand in p about $p_c(e) = 6 + 2e$ (at fixed e), to find

$$\delta\varphi^{(0)} \simeq -\left(\frac{6+2e}{e}\right)^{1/2} \ln\left(\delta p/p_c\right) + \text{const}, \tag{E.1}$$

where $\delta p := p - p_c(e)$. We need now to (i) express the e-dependent coefficient in terms of v on the separatrix, and (ii) express $\delta p/p_c$ (fixed e) in terms of $\delta b/b_c$ (fixed v) inside the logarithm. For (i), we use Eq. (2.16) to write

$$L_c(e)/M = \frac{p_c(e)}{\sqrt{p_c(e) - 3 - e^2}} = \frac{6+2e}{\sqrt{(3-e)(1+e)}}; \tag{E.2}$$

then invert to obtain e in terms of L_c on the separatrix. This yields

$$\begin{aligned} -\left(\frac{6+2e}{e}\right)^{1/2} &= -2\left(1 - \frac{12M^2}{L_c^2}\right)^{-1/4} \\ &= -2\left(1 - \frac{12M^2(1-v^2)}{v^2 b_c^2}\right)^{-1/4}, \end{aligned} \tag{E.3}$$

where in the second equality we have used Eqs. (2.5) and (2.8). Note that $1 < e < 3$ for critical scatter geodesics, so expressions like those in (E.2) make sense.

To achieve goal (ii) above, we write

$$\delta b = b - b_c(v) = \frac{L}{\sqrt{E^2 - 1}} - b_c(v(E)), \tag{E.4}$$

again using Eqs. (2.5) and (2.8), then substitute for $b_c(v(E))$ from Eq. (5.2), and finally for E and L in terms of p and e from Eq. (2.16). The resulting function of p and e we

expand in p about $p_c(e) = 6 + 2e$ at fixed e. We find

$$\delta b = \frac{e(3+e)^{3/2}M}{16(1+e)^3(e-1)^{1/2}}(\delta p)^2 + O(\delta p^3), \tag{E.5}$$

noting the linear term vanishes. Hence

$$\ln(\delta p/p_c) = \frac{1}{2}\ln(\delta b/b_c) + \text{const}, \tag{E.6}$$

and Eq. (E.1) produces Eq. (5.5), with the coefficient $A_0(v)$ given in Eq. (5.6).

References

[1] B. P. Abbott et al. Observation of Gravitational Waves from a Binary Black Hole Merger. *Phys. Rev. Lett.*, 116(6):061102, 2016.

[2] Albert Einstein. Feldgleichungen der Gravitation. *Sitzungsber. Preuss. Akad. Wiss. Berlin (Math. Phys.)*, 1915:844–847, 1915.

[3] Albert Einstein. Näherungsweise Integration der Feldgleichungen der Gravitation. *Sitzungsber. K. Preuss. Akad. Wiss.*, pages 688–696, 1916.

[4] Albert Einstein. Über Gravitationswellen. *Sitzungsber. K. Preuss. Akad. Wiss.*, pages 154–167, 1918.

[5] Hermann Weyl. *Space - Time - Matter*. Methuen and Co., London, 1922.

[6] Arthur Stanley Eddington. The propagation of gravitational waves. *Proc. Roy. Soc. Lond. A*, 102:268–282, 1922.

[7] Alexander Blum. Einstein's second-biggest blunder: the mistake in the 1936 gravitational-wave manuscript of Albert Einstein and Nathan Rosen. *Arch. Hist. Exact. Sci.*, 76:623–632, 2022.

[8] Albert Einstein and N. Rosen. On Gravitational waves. *J. Franklin Inst.*, 223:43–54, 1937.

[9] F. A. E. Pirani. On the Physical significance of the Riemann tensor. *Acta Phys. Polon.*, 15:389–405, 1956.

[10] Jorge Cervantes-Cota, Salvador Galindo-Uribarri, and George Smoot. A brief history of gravitational waves. *Universe*, 2(3):22, September 2016.

[11] R. A. Hulse and J. H. Taylor. Discovery of a pulsar in a binary system. *Astrophys. J. Lett.*, 195:L51–L53, 1975.

[12] J. H. Taylor, R. A. Hulse, L. A. Fowler, G. E. Gullahorn, and J. M. Rankin. Further observations of the binary pulsar PSR 1913+16. *Astrophys. J. Lett.*, 206:L53–L58, 1976.

[13] Joel M. Weisberg and Joseph H. Taylor. Relativistic binary pulsar B1913+16: Thirty years of observations and analysis. *ASP Conf. Ser.*, 328:25, 2005.

[14] J. H. Taylor, L. A. Fowler, and P. M. McCulloch. Measurements of general relativistic effects in the binary pulsar PSR 1913+16. *Nature*, 277:437–440, 1979.

[15] J. H. Taylor and J. M. Weisberg. A new test of general relativity - Gravitational radiation and the binary pulsar PSR 1913+16. *Astrophys. J.*, 253:908–920, 1982.

[16] J. Weber. Evidence for discovery of gravitational radiation. *Phys. Rev. Lett.*, 22:1320–1324, 1969.

[17] J. Weber. Anisotropy and polarization in the gravitational-radiation experiments. *Phys. Rev. Lett.*, 25:180–184, 1970.

[18] J. J. Giganti, J. V. Larson, J. P. Richard, R. L. Tobias, and J. Weber. Lunar surface gravimeter experiment. Final Report Maryland Univ., College Park. Dept. of Physics and Astronomy, January 1977.

[19] D. W. Sciama, G. B. Field, and M. J. Rees. Upper Limit to Radiation of Mass Energy Derived from Expansion of Galaxy. *Phys. Rev. Lett.*, 23:1514–1515, 1969.

[20] Peter Kafka. Are Weber's pulses illegal? Gravity Research Foundation, 1972.

[21] M. E. Gertsenshteĭn and V. I. Pustovoĭt. On the Detection of Low-Frequency Gravitational Waves. *Soviet Journal of Experimental and Theoretical Physics*, 16:433, January 1963.

[22] Vladimir B Braginskiĭ. Gravitational radiation and the prospect of its experimental discovery. *Soviet Physics Uspekhi*, 8(4):513, 1966.

[23] Rainer Weiss. Electromagnetically Coupled Broadband Gravitational Antenna. MIT Research Laboratory of Electronics, Quarterly Progress Report, No. 105, 1972.

[24] GEO600 website. https://www.geo600.org/.

[25] LIGO website. https://www.ligo.caltech.edu/.

[26] Virgo website. https://www.virgo-gw.eu/.

[27] B. P. Abbott et al. Characterization of transient noise in Advanced LIGO relevant to gravitational wave signal GW150914. *Class. Quant. Grav.*, 33(13):134001, 2016.

[28] B. P. Abbott et al. Tests of general relativity with GW150914. *Phys. Rev. Lett.*, 116(22):221101, 2016. [Erratum: Phys.Rev.Lett. 121, 129902 (2018)].

[29] B. P. Abbott et al. GW151226: Observation of Gravitational Waves from a 22-Solar-Mass Binary Black Hole Coalescence. *Phys. Rev. Lett.*, 116(24):241103, 2016.

[30] B. P. Abbott et al. GWTC-1: A Gravitational-Wave Transient Catalog of Compact Binary Mergers Observed by LIGO and Virgo during the First and Second Observing Runs. *Phys. Rev. X*, 9(3):031040, 2019.

[31] B. P. Abbott et al. GW170814: A Three-Detector Observation of Gravitational Waves from a Binary Black Hole Coalescence. *Phys. Rev. Lett.*, 119(14):141101, 2017.

[32] B. P. Abbott et al. GW170817: Observation of Gravitational Waves from a Binary Neutron Star Inspiral. *Phys. Rev. Lett.*, 119(16):161101, 2017.

[33] A. Goldstein et al. An Ordinary Short Gamma-Ray Burst with Extraordinary Implications: Fermi-GBM Detection of GRB 170817A. *Astrophys. J. Lett.*, 848(2):L14, 2017.

[34] B. P. Abbott et al. Gravitational Waves and Gamma-rays from a Binary Neutron Star Merger: GW170817 and GRB 170817A. *Astrophys. J. Lett.*, 848(2):L13, 2017.

[35] B. P. Abbott et al. Multi-messenger Observations of a Binary Neutron Star Merger. *Astrophys. J. Lett.*, 848(2):L12, 2017.

[36] B. P. Abbott et al. GW170817: Measurements of neutron star radii and equation of state. *Phys. Rev. Lett.*, 121(16):161101, 2018.

[37] R. Abbott et al. GWTC-2: Compact Binary Coalescences Observed by LIGO and Virgo During the First Half of the Third Observing Run. *Phys. Rev. X*, 11:021053, 2021.

[38] R. Abbott et al. GWTC-2.1: Deep extended catalog of compact binary coalescences observed by LIGO and Virgo during the first half of the third observing run. *Phys. Rev. D*, 109(2):022001, 2024.

[39] R. Abbott et al. GWTC-3: Compact Binary Coalescences Observed by LIGO and Virgo during the Second Part of the Third Observing Run. *Phys. Rev. X*, 13(4):041039, 2023.

[40] R. Abbott et al. Observation of Gravitational Waves from Two Neutron Star–Black Hole Coalescences. *Astrophys. J. Lett.*, 915(1):L5, 2021.

[41] R. Abbott et al. GW190521: A Binary Black Hole Merger with a Total Mass of $150M_{\odot}$. *Phys. Rev. Lett.*, 125(10):101102, 2020.

[42] R. Abbott et al. GW190814: Gravitational Waves from the Coalescence of a 23 Solar Mass Black Hole with a 2.6 Solar Mass Compact Object. *Astrophys. J. Lett.*, 896(2):L44, 2020.

[43] B. P. Abbott et al. GW190425: Observation of a Compact Binary Coalescence with Total Mass $\sim 3.4M_{\odot}$. *Astrophys. J. Lett.*, 892(1):L3, 2020.

[44] Kagra website. https://gwcenter.icrr.u-tokyo.ac.jp/en/.

[45] LIGO Scientific Collaboration, Virgo Collaboration, KAGRA Collaboration. Observation of Gravitational Waves from the Coalescence of a $2.5-4.5\ M_\odot$ Compact Object and a Neutron Star. arXiv:2404.04248 [gr-qc], 4 2024.

[46] LIGO India website. https://www.ligo-india.in/.

[47] M. Saleem et al. The science case for LIGO-India. *Class. Quant. Grav.*, 39(2):025004, 2022.

[48] Rana X. Adhikari et al. LIGO Voyager Upgrade: Design Concept. Technical Report LIGO-T1400226-v9, LIGO Scientific Collaboration, 2024.

[49] Cosmic Explorer website. https://cosmicexplorer.org/.

[50] Einstein Telescope website. https://www.et-gw.eu/.

[51] Matthew Evans et al. A Horizon Study for Cosmic Explorer: Science, Observatories, and Community. Technical Report CE–P2100003–v7, National Science Foundation, 2021.

[52] Gabriella Agazie et al. The NANOGrav 15 yr Data Set: Evidence for a Gravitational-wave Background. *Astrophys. J. Lett.*, 951(1):L8, 2023.

[53] Christopher Moore, Robert Cole, and Christopher Berry. Gravitational wave detectors and sources. https://gwplotter.com, 2024.

[54] LISA consortium website. https://www.lisamission.org/.

[55] Monica Colpi et al. LISA Definition Study Report. Technical Report ESA-SCI-DIR-RP-002, European Space Agency, 2023.

[56] Seiji Kawamura et al. Current status of space gravitational wave antenna DECIGO and B-DECIGO. *PTEP*, 2021(5):05A105, 2021.

[57] Jun Luo et al. TianQin: a space-borne gravitational wave detector. *Class. Quant. Grav.*, 33(3):035010, 2016.

[58] Wen-Hong Ruan, Zong-Kuan Guo, Rong-Gen Cai, and Yuan-Zhong Zhang. Taiji program: Gravitational-wave sources. *Int. J. Mod. Phys. A*, 35(17):2050075, 2020.

[59] Lorenzo Speri, Nikolaos Karnesis, Arianna I. Renzini, and Jonathan R. Gair. A roadmap of gravitational wave data analysis. *Nature Astron.*, 6(12):1356–1363, 2022.

[60] Niayesh Afshordi et al. Waveform Modelling for the Laser Interferometer Space Antenna. arXiv:2311.01300 [gr-qc], 11 2023.

[61] Michael Pürrer and Carl-Johan Haster. Gravitational waveform accuracy requirements for future ground-based detectors. *Phys. Rev. Res.*, 2(2):023151, 2020.

[62] Pau Amaro Seoane et al. Astrophysics with the Laser Interferometer Space Antenna. *Living Rev. Rel.*, 26(1):2, 2023.

[63] Black Hole Perturbation Toolkit. (bhptoolkit.org).

[64] Tanja Hinderer and Éanna É. Flanagan. Two-timescale analysis of extreme mass ratio inspirals in Kerr spacetime: Orbital motion. *Phys. Rev. D*, 78(064028), Sep 2008.

[65] Stanislav Babak, Jonathan Gair, Alberto Sesana, Enrico Barausse, Carlos F. Sopuerta, Christopher P. L. Berry, Emanuele Berti, Pau Amaro-Seoane, Antoine Petiteau, and Antoine Klein. Science with the space-based interferometer LISA. V: Extreme mass-ratio inspirals. *Phys. Rev. D*, 95(10):103012, 2017.

[66] Matthew D. Duez and Yosef Zlochower. Numerical Relativity of Compact Binaries in the 21st Century. *Rept. Prog. Phys.*, 82(1):016902, 2019.

[67] Luc Blanchet. Gravitational Radiation from Post-Newtonian Sources and Inspiralling Compact Binaries. *Living Rev. Rel.*, 17:2, 2014.

[68] Luc Blanchet and Thibault Damour. Radiative gravitational fields in general relativity I. general structure of the field outside the source. *Phil. Trans. Roy. Soc. Lond. A*, 320:379–430, 1986.

[69] Michael Boyle et al. The SXS Collaboration catalog of binary black hole simulations. *Class. Quant. Grav.*, 36(19):195006, 2019.

[70] Carlos O. Lousto and Yosef Zlochower. Orbital Evolution of Extreme-Mass-Ratio Black-Hole Binaries with Numerical Relativity. *Phys. Rev. Lett.*, 106:041101, 2011.

[71] Carlos O. Lousto and James Healy. Study of the intermediate mass ratio black hole binary merger up to 1000:1 with numerical relativity. *Class. Quant. Grav.*, 40(9):09LT01, 2023.

[72] Mekhi Dhesi, Hannes R. Rüter, Adam Pound, Leor Barack, and Harald P. Pfeiffer. Worldtube excision method for intermediate-mass-ratio inspirals: Scalar-field toy model. *Phys. Rev. D*, 104(12):124002, 2021.

[73] Leor Barack. Gravitational self force in extreme mass-ratio inspirals. *Class. Quant. Grav.*, 26:213001, 2009.

[74] Eric Poisson, Adam Pound, and Ian Vega. The Motion of point particles in curved spacetime. *Living Rev. Rel.*, 14:7, 2011.

[75] Leor Barack and Adam Pound. Self-force and radiation reaction in general relativity. *Rept. Prog. Phys.*, 82(1):016904, 2019.

[76] Adam Pound and Barry Wardell. *Black Hole Perturbation Theory and Gravitational Self-Force*, page 1–119. Springer Singapore, 2021. arXiv:2101.04592 [gr-qc].

[77] Ryuichi Fujita. Gravitational Waves from a Particle in Circular Orbits around a Schwarzschild Black Hole to the 22nd Post-Newtonian Order. *Prog. Theor. Phys.*, 128:971–992, 2012.

[78] Donato Bini and Thibault Damour. High-order post-Newtonian contributions to the two-body gravitational interaction potential from analytical gravitational self-force calculations. *Phys. Rev. D*, 89(6):064063, 2014.

[79] Abhay G. Shah, John L Friedman, and Bernard F Whiting. Finding high-order analytic post-Newtonian parameters from a high-precision numerical self-force calculation. *Phys. Rev. D*, 89(6):064042, 2014.

[80] Chris Kavanagh, Adrian C. Ottewill, and Barry Wardell. Analytical high-order post-Newtonian expansions for extreme mass ratio binaries. *Phys. Rev. D*, 92(8):084025, 2015.

[81] Erik Forseth, Charles R. Evans, and Seth Hopper. Eccentric-orbit extreme-mass-ratio inspiral gravitational wave energy fluxes to 7PN order. *Phys. Rev. D*, 93(6):064058, 2016.

[82] Soichiro Isoyama, Ryuichi Fujita, Alvin J. K. Chua, Hiroyuki Nakano, Adam Pound, and Norichika Sago. Adiabatic Waveforms from Extreme-Mass-Ratio Inspirals: An Analytical Approach. *Phys. Rev. Lett.*, 128(23):231101, 2022.

[83] Parameswaran Ajith et al. Phenomenological template family for black-hole coalescence waveforms. *Class. Quant. Grav.*, 24:S689–S700, 2007.

[84] Geraint Pratten, Sascha Husa, Cecilio Garcia-Quiros, Marta Colleoni, Antoni Ramos-Buades, Hector Estelles, and Rafel Jaume. Setting the cornerstone for a family of models for gravitational waves from compact binaries: The dominant harmonic for nonprecessing quasicircular black holes. *Phys. Rev. D*, 102(6):064001, 2020.

[85] Cecilio García-Quirós, Marta Colleoni, Sascha Husa, Héctor Estellés, Geraint Pratten, Antoni Ramos-Buades, Maite Mateu-Lucena, and Rafel Jaume. Multimode frequency-domain model for the gravitational wave signal from nonprecessing black-hole binaries. *Phys. Rev. D*, 102(6):064002, 2020.

[86] Geraint Pratten et al. Computationally efficient models for the dominant and subdominant harmonic modes of precessing binary black holes. *Phys. Rev. D*, 103(10):104056, 2021.

[87] A. Buonanno and T. Damour. Effective one-body approach to general relativistic two-body dynamics. *Phys. Rev. D*, 59:084006, 1999.

[88] Thibault Damour. Introductory lectures on the Effective One Body formalism. *Int. J. Mod. Phys. A*, 23:1130–1148, 2008.

[89] Alessandra Buonanno and B. S. Sathyaprakash. Sources of Gravitational Waves: Theory and Observations. arXiv:1410.7832 [gr-qc], Oct 2014.

[90] Angelica Albertini, Alessandro Nagar, Adam Pound, Niels Warburton, Barry Wardell, Leanne Durkan, and Jeremy Miller. Comparing second-order gravitational self-force and effective one body waveforms from inspiralling, quasicircular and nonspinning black hole binaries. II. The large-mass-ratio case. *Phys. Rev. D*, 106(8):084062, 2022.

[91] Alessandro Nagar and Simone Albanesi. Toward a gravitational self-force-informed effective-one-body waveform model for nonprecessing, eccentric, large-mass-ratio inspirals. *Phys. Rev. D*, 106(6):064049, 2022.

[92] Nicolás Yunes, Alessandra Buonanno, Scott A. Hughes, Yi Pan, Enrico Barausse, M. Coleman Miller, and William Throwe. Extreme Mass-Ratio Inspirals in the Effective-One-Body Approach: Quasi-Circular, Equatorial Orbits around a Spinning Black Hole. *Phys. Rev. D*, 83:044044, 2011. [Erratum: Phys.Rev.D 88, 109904 (2013)].

[93] Nicolas Yunes, Alessandra Buonanno, Scott A. Hughes, M. Coleman Miller, and Yi Pan. Modeling Extreme Mass Ratio Inspirals within the Effective-One-Body Approach. *Phys. Rev. Lett.*, 104:091102, 2010.

[94] Thibault Damour. Gravitational Self Force in a Schwarzschild Background and the Effective One Body Formalism. *Phys. Rev. D*, 81:024017, 2010.

[95] Maarten van de Meent, Alessandra Buonanno, Deyan P. Mihaylov, Serguei Ossokine, Lorenzo Pompili, Niels Warburton, Adam Pound, Barry Wardell, Leanne Durkan, and Jeremy Miller. Enhancing the SEOBNRv5 effective-one-body waveform model with second-order gravitational self-force fluxes. *Phys. Rev. D*, 108(12):124038, 2023.

[96] Enrico Barausse, Alessandra Buonanno, and Alexandre Le Tiec. The complete non-spinning effective-one-body metric at linear order in the mass ratio. *Phys. Rev. D*, 85:064010, 2012.

[97] Sarp Akcay, Leor Barack, Thibault Damour, and Norichika Sago. Gravitational self-force and the effective-one-body formalism between the innermost stable circular orbit and the light ring. *Phys. Rev. D*, 86:104041, 2012.

[98] Andrea Antonelli, Maarten van de Meent, Alessandra Buonanno, Jan Steinhoff, and Justin Vines. Quasicircular inspirals and plunges from nonspinning effective-one-body Hamiltonians with gravitational self-force information. *Phys. Rev. D*, 101(2):024024, 2020.

[99] Angelica Albertini, Alessandro Nagar, Adam Pound, Niels Warburton, Barry Wardell, Leanne Durkan, and Jeremy Miller. Comparing second-order gravitational self-force, numerical relativity, and effective one body waveforms from inspiralling, quasicircular, and nonspinning black hole binaries. *Phys. Rev. D*, 106(8):084061, 2022.

[100] Thibault Damour. Gravitational scattering, post-Minkowskian approximation and Effective One-Body theory. *Phys. Rev. D*, 94(10):104015, 2016.

[101] Thibault Damour. High-energy gravitational scattering and the general relativistic two-body problem. *Phys. Rev. D*, 97(4):044038, 2018.

[102] Andrea Antonelli, Alessandra Buonanno, Jan Steinhoff, Maarten van de Meent, and Justin Vines. Energetics of two-body Hamiltonians in post-Minkowskian gravity. *Phys. Rev. D*, 99(10):104004, 2019.

[103] Thibault Damour and Piero Rettegno. Strong-field scattering of two black holes: Numerical relativity meets post-Minkowskian gravity. *Phys. Rev. D*, 107(6):064051, 2023.

[104] Mohammed Khalil, Alessandra Buonanno, Jan Steinhoff, and Justin Vines. Energetics and scattering of gravitational two-body systems at fourth post-Minkowskian order. *Phys. Rev. D*, 106(2):024042, 2022.

[105] Poul H. Damgaard and Pierre Vanhove. Remodeling the effective one-body formalism in post-Minkowskian gravity. *Phys. Rev. D*, 104(10):104029, 2021.

[106] Peter D. D'Eath. Dynamics of a small black hole in a background universe. *Phys. Rev. D*, 11:1387–1403, 1975.

[107] Robert P. Geroch and Jennie H. Traschen. Strings and Other Distributional Sources in General Relativity. *Conf. Proc. C*, 861214:138–141, 1986.

[108] Marco Bruni, Sabino Matarrese, Silvia Mollerach, and Sebastiano Sonego. Perturbations of space-time: Gauge transformations and gauge invariance at second order and beyond. *Class. Quant. Grav.*, 14:2585–2606, 1997.

[109] Steven Detweiler and Bernard F. Whiting. Self-force via a Green's function decomposition. *Phys. Rev. D*, 67(024025), Jan 2003.

[110] Yasushi Mino, Misao Sasaki, and Takahiro Tanaka. Gravitational radiation reaction to a particle motion. *Phys. Rev. D*, 55:3457–3476, 1997.

[111] Theodore C. Quinn and Robert M. Wald. An Axiomatic approach to electromagnetic and gravitational radiation reaction of particles in curved space-time. *Phys. Rev. D*, 56:3381–3394, 1997.

[112] Adam Pound. Second-order gravitational self-force. *Phys. Rev. Lett.*, 109:051101, 2012.

[113] Maarten van de Meent. Gravitational self-force on eccentric equatorial orbits around a Kerr black hole. *Phys. Rev. D*, 94(044034), Aug 2016.

[114] Maarten van de Meent. Gravitational self-force on generic bound geodesics in Kerr spacetime. *Phys. Rev. D*, 97(104033), May 2018.

[115] Adam Pound, Barry Wardell, Niels Warburton, and Jeremy Miller. Second-Order Self-Force Calculation of Gravitational Binding Energy in Compact Binaries. *Phys. Rev. Lett.*, 124(2):021101, 2020.

[116] Niels Warburton, Adam Pound, Barry Wardell, Jeremy Miller, and Leanne Durkan. Gravitational-Wave Energy Flux for Compact Binaries through Second Order in the Mass Ratio. *Phys. Rev. Lett.*, 127(15):151102, 2021.

[117] Barry Wardell, Adam Pound, Niels Warburton, Jeremy Miller, Leanne Durkan, and Alexandre Le Tiec. Gravitational Waveforms for Compact Binaries from Second-Order Self-Force Theory. *Phys. Rev. Lett.*, 130(24):241402, 2023.

[118] Andrew Spiers, Adam Pound, and Jordan Moxon. Second-order Teukolsky formalism in Kerr spacetime: Formulation and nonlinear source. *Phys. Rev. D*, 108(6):064002, 2023.

[119] Patrick Bourg, Benjamin Leather, Marc Casals, Adam Pound, and Barry Wardell. Implementation of a GHZ-Teukolsky puncture scheme for gravitational self-force calculations. arXiv:2403.12634 [gr-qc], Mar 2024.

[120] C. P. L. Berry and J. R. Gair. Expectations for extreme-mass-ratio bursts from the Galactic Centre. *Mon. Not. Roy. Astron. Soc.*, 435:3521–3540, 2013.

[121] C. P. L. Berry and J. R. Gair. Extreme-mass-ratio-bursts from extragalactic sources. *Mon. Not. Roy. Astron. Soc.*, 433:3572–3583, 2013.

[122] Thibault Damour. Classical and quantum scattering in post-Minkowskian gravity. *Phys. Rev. D*, 102(024060), Jul 2020.

[123] Donato Bini, Thibault Damour, Andrea Geralico, Stefano Laporta, and Pierpaolo Mastrolia. Gravitational scattering at the seventh order in G: nonlocal contribution at the sixth post-Newtonian accuracy. *Phys. Rev. D*, 103(044038), Feb 2021.

[124] Zvi Bern, Lance Dixon, David C. Dunbar, and David A. Kosower. One-loop n-point gauge theory amplitudes, unitarity and collinear limits. *Nuclear Physics B*, 425(1-2):217–260, Aug 1994.

[125] Zvi Bern, Lance Dixon, David C. Dunbar, and David A. Kosower. Fusing gauge theory tree amplitudes into loop amplitudes. *Nuclear Physics B*, 435(1-2):59–101, Feb 1995.

[126] H. Kawai, D. C. Lewellen, and S. H. H. Tye. A Relation Between Tree Amplitudes of Closed and Open Strings. *Nucl. Phys. B*, 269:1–23, 1986.

[127] Z. Bern, J. J. M. Carrasco, and H. Johansson. New relations for gauge-theory amplitudes. *Phys. Rev. D*, 78:085011, Oct 2008.

[128] Zvi Bern, John Joseph M. Carrasco, and Henrik Johansson. Perturbative quantum gravity as a double copy of gauge theory. *Phys. Rev. Lett.*, 105:061602, Aug 2010.

[129] Zvi Bern, Clifford Cheung, Radu Roiban, et al. Scattering Amplitudes and the Conservative Hamiltonian for Binary Systems at Third Post-Minkowskian Order. *Phys. Rev. Lett.*, 122(201603), May 2019.

[130] Zvi Bern, Clifford Cheung, Radu Roiban, Chia-Hsien Shen, Mikhail P. Solon, and Mao Zeng. Black Hole Binary Dynamics from the Double Copy and Effective Theory. *JHEP*, 206, Oct 2019.

[131] Zvi Bern, Andres Luna, Radu Roiban, Chia-Hsien Shen, and Mao Zeng. Spinning Black Hole Binary Dynamics, Scattering Amplitudes and Effective Field Theory. *Phys. Rev. D*, 104(065014), Sep 2021.

[132] Zvi Bern, Julio Parra-Martinez, Radu Roiban, Eric Sawyer, and Chia-Hsien Shen. Leading Nonlinear Tidal Effects and Scattering Amplitudes. *JHEP*, 188, May 2021.

[133] Zvi Bern, Julio Parra-Martinez, Radu Roiban, et al. Scattering Amplitudes and Conservative Binary Dynamics at $\mathcal{O}(G^4)$. *Phys. Rev. Lett.*, 126(171601), Apr 2021.

[134] Mathias Driesse, Gustav Uhre Jakobsen, Gustav Mogull, Jan Plefka, Benjamin Sauer, and Johann Usovitsch. Conservative Black Hole Scattering at Fifth Post-Minkowskian and First Self-Force Order. *Phys. Rev. Lett.*, 132(24):241402, 2024.

[135] Gregor Kälin and Rafael A. Porto. Post-Minkowskian Effective Field Theory for Conservative Binary Dynamics. *JHEP*, 11:106, 2020.

[136] Gregor Kälin, Zhengwen Liu, and Rafael A. Porto. Conservative Dynamics of Binary Systems to Third Post-Minkowskian Order from the Effective Field Theory Approach. *Phys. Rev. Lett.*, 125(261103), Dec 2020.

[137] Zhengwen Liu, Rafael A. Porto, and Zixin Yang. Spin Effects in the Effective Field Theory Approach to Post-Minkowskian Conservative Dynamics. *JHEP*, 06:012, 2021.

[138] Christoph Dlapa, Gregor Kälin, Zhengwen Liu, and Rafael A. Porto. Dynamics of binary systems to fourth Post-Minkowskian order from the effective field theory approach. *Phys. Lett. B*, 831:137203, 2022.

[139] Christoph Dlapa, Gregor Kälin, Zhengwen Liu, and Rafael A. Porto. Conservative dynamics of binary systems at fourth post-minkowskian order in the large-eccentricity expansion. *Phys. Rev. Lett.*, 128:161104, Apr 2022.

[140] Gregor Kälin, Jakob Neef, and Rafael A. Porto. Radiation-reaction in the effective field theory approach to post-minkowskian dynamics. *Journal of High Energy Physics*, 2023(1), Jan 2023.

[141] Thibault Damour. Radiative contribution to classical gravitational scattering at the third order in G. *Phys. Rev. D*, 102(12):124008, 2020.

[142] Paolo Di Vecchia, Carlo Heissenberg, Rodolfo Russo, and Gabriele Veneziano. The eikonal approach to gravitational scattering and radiation at $\wr(g^3)$, 2021.

[143] Gregor Kälin and Rafael A. Porto. From Boundary Data to Bound States. *JHEP*, 72, Jan 2020.

[144] Gihyuk Cho, Gregor Kälin, and Rafael A. Porto. From boundary data to bound states. Part III. Radiative effects. *JHEP*, 04:154, 2022. [Erratum: JHEP 07, 002 (2022)].

[145] Tim Adamo, Riccardo Gonzo, and Anton Ilderton. Gravitational bound waveforms from amplitudes. *JHEP*, 05:034, 2024.

[146] Riccardo Gonzo and Canxin Shi. Boundary to bound dictionary for generic Kerr orbits. *Phys. Rev. D*, 108(8):084065, 2023.

[147] Jack Lewis, Adam Pound, and Riccardo Gonzo. (in preparation).

[148] Oliver Long and Leor Barack. Time-domain metric reconstruction for hyperbolic scattering. *Phys. Rev. D*, 104:024014, Jul 2021.

[149] Leor Barack and Oliver Long. Self-force correction to the deflection angle in black-hole scattering: A scalar charge toy model. *Phys. Rev. D*, 106:104031, Nov 2022.

[150] Samuel E. Gralla and Kunal Lobo. Self-force effects in post-Minkowskian scattering. *Class. Quant. Grav.*, 39(9):095001, 2022.

[151] Leor Barack et al. Comparison of post-Minkowskian and self-force expansions: Scattering in a scalar charge toy model. *Phys. Rev. D*, 108(2):024025, 2023.

[152] Leor Barack, Amos Ori, and Norichika Sago. Frequency-domain calculation of the self force: The High-frequency problem and its resolution. *Phys. Rev. D*, 78:084021, 2008.

[153] Niels Warburton and Leor Barack. Self force on a scalar charge in Kerr spacetime: circular equatorial orbits. *Phys. Rev. D*, 81:084039, 2010.

[154] Niels Warburton and Leor Barack. Self force on a scalar charge in Kerr spacetime: eccentric equatorial orbits. *Phys. Rev. D*, 83:124038, 2011.

[155] Niels Warburton. Self force on a scalar charge in Kerr spacetime: inclined circular orbits. *Phys. Rev. D*, 91(2):024045, 2015.

[156] Zachary Nasipak, Thomas Osburn, and Charles R. Evans. Repeated faint quasi-normal bursts in extreme-mass-ratio inspiral waveforms: Evidence from frequency-domain scalar self-force calculations on generic Kerr orbits. *Phys. Rev. D*, 100(064008), Sep 2019.

[157] Seth Hopper and Vitor Cardoso. Scattering of point particles by black holes: gravitational radiation. *Phys. Rev. D*, 97(044031), Feb 2018.

[158] Seth Hopper. Unbound motion on a Schwarzschild background: Practical approaches to frequency domain computations. *Phys. Rev. D*, 97(064007), Mar 2018.

[159] Christopher Whittall and Leor Barack. Frequency-domain approach to self-force in hyperbolic scattering. *Phys. Rev. D*, 108(6):064017, 2023.

[160] Oliver Long, Christopher Whittall, and Leor Barack. Black hole scattering near the transition to plunge: Self-force and resummation of post-Minkowskian theory. arXiv:2406.08363 [gr-qc], Jun 2024.

[161] Maarten van de Meent. unpublished.

[162] Charles Darwin. The Gravity Field of a Particle. *Proceedings of the Royal Society of London Series A*, 249(1257):180–194, January 1959.

[163] Charles Darwin. The Gravity Field of a Particle. II. *Proceedings of the Royal Society of London Series A*, 263(1312):39–50, August 1961.

[164] Theodore C. Quinn. Axiomatic approach to radiation reaction of scalar point particles in curved spacetime. *Phys. Rev. D*, 62:064029, Aug 2000.

[165] Leor Barack and Amos Ori. Mode sum regularization approach for the self-force in black hole space-time. *Phys. Rev. D*, 61(6061502(R)), Feb 2000.

[166] Leor Barack. Gravitational self-force by mode sum regularization. *Phys. Rev. D*, 64:084021, Sep 2001.

[167] Leor Barack and Amos Ori. Regularization parameters for the self-force in Schwarzschild spacetime: Scalar case. *Phys. Rev. D*, 66(084022), 2002.

[168] Steven Detweiler, Eirini Messaritaki, and Bernard F. Whiting. Self-force of a scalar field for circular orbits about a schwarzschild black hole. *Phys. Rev. D*, 67:104016, May 2003.

[169] Anna Heffernan, Adrian Ottewill, and Barry Wardell. High-order expansions of the Detweiler-Whiting singular field in Schwarzschild spacetime. *Phys. Rev. D*, 86(104023), Nov 2012.

[170] Anna Heffernan, Adrian Ottewill, and Barry Wardell. High-order expansions of the Detweiler-Whiting singular field in Kerr spacetime. *Phys. Rev. D*, 89(2):024030, 2014.

[171] Leor Barack. Gravitational self force in extreme mass-ratio inspirals. *Class. Quant. Grav.*, 26(213001), Oct 2009.

[172] Yasushi Mino. Perturbative approach to an orbital evolution around a supermassive black hole. *Phys. Rev. D*, 67(8), Apr 2003.

[173] Leor Barack and Norichika Sago. Gravitational self-force correction to the innermost stable circular orbit of a schwarzschild black hole. *Phys. Rev. Lett.*, 102:191101, May 2009.

[174] Donato Bini and Thibault Damour. Gravitational radiation reaction along general orbits in the effective one-body formalism. *Phys. Rev. D*, 86:124012, 2012.

[175] Donato Bini, Thibault Damour, and Andrea Geralico. Radiative contributions to gravitational scattering. *Phys. Rev. D*, 104(8):084031, 2021.

[176] Leor Barack and Norichika Sago. Beyond the geodesic approximation: conservative effects of the gravitational self-force in eccentric orbits around a Schwarzschild black hole. *Phys. Rev. D*, 83:084023, 2011.

[177] Mikhail M. Ivanov, Yue-Zhou Li, Julio Parra-Martinez, and Zihan Zhou. Gravitational Raman Scattering in Effective Field Theory: A Scalar Tidal Matching at O(G3). *Phys. Rev. Lett.*, 132(13):131401, 2024.

[178] Donato Bini, Andrea Geralico, Chris Kavanagh, Adam Pound, and Davide Usseglio. Post-Minkowskian self-force in the low-velocity limit: scalar field scattering. arXiv:2406.15878 [gr-qc], Jun 2024.

[179] GNU Scientific Library. https://www.gnu.org/software/gsl/.

[180] Jonathan Thornburg, Barry Wardell, and Maarten van de Meent. Excitation of Kerr quasinormal modes in extreme–mass-ratio inspirals. *Phys. Rev. Res.*, 2(013365), 2020.

[181] Leonardo Dagum and Ramesh Menon. OpenMP: an industry standard API for shared-memory programming. *Computational Science & Engineering, IEEE*, 5(1):46–55, 1998.

[182] Roland Haas. Scalar self-force on eccentric geodesics in Schwarzschild spacetime: A time-domain computation. *Phys. Rev. D*, 75(124011), Jun 2007.

[183] Rodrigo Panosso Macedo, Benjamin Leather, Niels Warburton, Barry Wardell, and Anıl Zenginoğlu. Hyperboloidal method for frequency-domain self-force calculations. *Phys. Rev. D*, 105(104033), May 2022.

[184] Rodrigo Panosso Macedo, Oliver Long, and Leor Barack. (in preparation).

[185] David Gottlieb and Chi-Wang Shu. On the Gibbs Phenomenon and its Resolution. *SIAM Review*, 39(4):644–668, 1997.

[186] Leor Barack and Norichika Sago. Gravitational self-force on a particle in eccentric orbit around a Schwarzschild black hole. *Phys. Rev. D*, 81:084021, 2010.

[187] Enrico Barausse, Emanuele Berti, Vitor Cardoso, Scott A. Hughes, and Gaurav Khanna. Divergences in gravitational-wave emission and absorption from extreme mass ratio binaries. *Phys. Rev. D*, 104(6):064031, 2021.

[188] Samuel E. Gralla, Scott A. Hughes, and Niels Warburton. Inspiral into Gargantua. *Class. Quant. Grav.*, 33(15):155002, 2016. [Erratum: Class.Quant.Grav. 37, 109501 (2020)].

[189] Leor Barack. Late time dynamics of scalar perturbations outside black holes. 2. Schwarzschild geometry. *Phys. Rev. D*, 59:044017, 1999.

[190] *NIST Digital Library of Mathematical Functions*. https://dlmf.nist.gov/, Release 1.2.1 of 2024-06-15. F. W. J. Olver, A. B. Olde Daalhuis, D. W. Lozier, B. I. Schneider, R. F. Boisvert, C. W. Clark, B. R. Miller, B. V. Saunders, H. S. Cohl, and M. A. McClain, eds.

[191] Leonid Bakaleinikov and Alexander Silbergleit. Uniform asymptotic expansion of Legendre functions. *J. Math. Phys.*, 61(8):083503, 08 2020.

[192] Oliver Long. Personal correspondence.

[193] Leor Barack. Late time decay of scalar, electromagnetic, and gravitational perturbations outside rotating black holes. *Phys. Rev. D*, 61:024026, 2000.

[194] Adam Pound, Cesar Merlin, and Leor Barack. Gravitational self-force from radiation-gauge metric perturbations. *Phys. Rev. D*, 89(2):024009, 2014.

[195] Leor Barack, Yasushi Mino, Hiroyuki Nakano, Amos Ori, and Misao Sasaki. Calculating the gravitational self-force in Schwarzschild space-time. *Phys. Rev. Lett.*, 88:091101, 2002.

[196] Sam R. Dolan, Chris Kavanagh, and Barry Wardell. Gravitational Perturbations of Rotating Black Holes in Lorenz Gauge. *Phys. Rev. Lett.*, 128(15):151101, 2022.

[197] Sam R. Dolan, Leanne Durkan, Chris Kavanagh, and Barry Wardell. Metric perturbations of Kerr spacetime in Lorenz gauge: circular equatorial orbits. *Class. Quant. Grav.*, 41(15):155011, 2024.

[198] Barry Wardell, Chris Kavanagh, and Sam R. Dolan. Sourced metric perturbations of Kerr spacetime in Lorenz gauge. arXiv:2406.12510 [gr-qc], Jun 2024.

[199] Sarp Akcay, Niels Warburton, and Leor Barack. Frequency-domain algorithm for the Lorenz-gauge gravitational self-force. *Phys. Rev. D*, 88(10):104009, 2013.

[200] Leor Barack, Marta Colleoni, Thibault Damour, Soichiro Isoyama, and Norichika Sago. Self-force effects on the marginally bound zoom-whirl orbit in Schwarzschild spacetime. *Phys. Rev. D*, 100(12):124015, 2019.

[201] Leor Barack and Darren A. Golbourn. Scalar-field perturbations from a particle orbiting a black hole using numerical evolution in 2+1 dimensions. *Phys. Rev. D*, 76:044020, 2007.

[202] Ian Vega and Steven L. Detweiler. Regularization of fields for self-force problems in curved spacetime: Foundations and a time-domain application. *Phys. Rev. D*, 77:084008, 2008.

[203] Niels Warburton and Barry Wardell. Applying the effective-source approach to frequency-domain self-force calculations. *Phys. Rev. D*, 89(4):044046, 2014.

[204] Barry Wardell and Niels Warburton. Applying the effective-source approach to frequency-domain self-force calculations: Lorenz-gauge gravitational perturbations. *Phys. Rev. D*, 92(8):084019, 2015.

[205] Benjamin Leather and Niels Warburton. Applying the effective-source approach to frequency-domain self-force calculations for eccentric orbits. *Phys. Rev. D*, 108(8):084045, 2023.